

**Fatigue Stiffness Loss and Life
Prediction Technique Development of a
Real Rubber Automotive Component
by means of Finite Element Analysis**

Mikel Isasi Iriondo

Lea Artibai Ikastetxea S. Coop.

and

London Metropolitan University

PhD - Doctor Europaeus

2018

Date	30/04/2018
Fund	
Control no	HR
Collection/ Loan type	Store Theraps
Class no	[678.4 IR17
Accession no	3011809655

Abstract

The main aim of the study has been to investigate the potential of providing a complete rubber fatigue behaviour predictions. The work explores the nucleation and growth of cracks, but including stiffness loss and damage evolution. It has been performed in two filled rubbers, one natural rubber and one blend of Styrene-Butadiene (SBR) with polibutadiene (BR). Such techniques involve various topics to be analyzed: material monotonic and cyclic deformation behaviours, knowledge of stress/strain histories, the fatigue life and failure plane associated with the nucleation of cracks and their subsequent growth, fatigue damage quantification parameters, cycling control type, influence of density and size of cracks. Material characterization is designed to be economically and feasible in time limits. An industrialization of procedures has been carried out in our facilities for a complete material characterization, with high automation on test executions and data processing.

Fatigue life prediction methods are studied by means of computer aided analytical techniques. Fatigue crack nucleation and growth life prediction approaches are studied. The equivalence criteria selected for life predictions, the cracking energy density, is adequate for multiaxial and variable amplitude loadings. Similarly, critical plane approach is used for identifying the failure plane. Although in the scope of the project there are only uniaxial and fully relaxing strain conditions.

The major research potential is directed to develop stiffness loss and damage evolution prediction capacity. A damage function is defined to contemplate the effect of stiffness loss and crack size on the strain energy density. The parameter that quantifies the damage is the normalized stiffness. In rubber fatigue the strain energy density may depend not only on the instantaneous strain or stress, but also on damage state of material. The stiffness loss approach relates the differentiated particular damage developments of different loading modes (strain, stress or energy) in a function. Additionally, the damage function can be fitted by a constitutive model for stiffness loss computations, and using this model additionally the influence of size of the crack and its density are considered. The approaches are implemented in Endurica CL solver for rubber fatigue analysis. The characterization and prediction capabilities are settled at Leartiker facilities, and operative for giving a reasonable fatigue damage and stiffness loss predictions.

Acknowledgements

This dissertation is dedicated to my family.

The only people that can understand the exhaustion I feel at the end of writing the dissertation are my parents, Nerea and Javier, my brother Asier, and my wife, Larraitz. They have never stopped encouraging me. This has been of vital importance for me.

I have received great help and collaboration internally at Leartiker in Lea-Artibai Ikastetxea S.Coop. I am especially grateful to Aitor Arriaga for his support at every stage of the project, and for believing in me from the beginning. Zorion Kareaga, Jon Anakabe and Joana Kano, I am very glad of have been your fellow traveller on this tough journey. Thanks to Asier Retolaza and Rikardo Pagaldai for your assistance with mathematical algorithms and convergence difficulties in finite element analysis. Alex Arrillaga, Nerea Bastida, Ane Miren Zaldua helped debug the specimen manufacturing process. Sincere thanks to my former and actual managers for supporting this research: Jose Javier Egurrola, Amaia Egia, Ainara Basurko and Rafael Atxurra.

I cannot find words to express the gratefulness I owe to my advisor Will Mars, with his selfless aid, has influenced this work in many significant ways. The opportunity to enjoy each one of his trainings of “theory and application of fatigue analysis” and “characterizing elastomer fatigue behavior for analysis and engineering” has been decisive in the consecution of the dissertation. I am also grateful for his willingness and patience attending any of my inquiries.

I especially want to express my gratitude to my supervisors Ricardo Hernandez, and Aitor Arriaga at Leartiker, and Mathew Philip in London Metropolitan University for their helpful comments, suggestions and corrections.

Thanks to the company Cikautxo for being the first interested in the project, especially to Iñigo Aspiazu, Ernesto Jimenez and Jon Plaza for their kind assistance at the experimental testing phase. Cikautxo has been also provided significant financial support for this work.

I would like to thanks also to James Busfield from the Queen Mary University of London, Zoltan Major, from the Polymer Competence Centre of Leoben, for allowing me to carry out an internship in your facilities. Consequently, I am grateful

for provided assistance in the rubber fatigue testing to Samuel Asare, in Queen Mary University of London, and to Blaz Likozar, in Polymer Competence Centre of Leoben.

Eskerrik asko bihotzez danori!

Table of Contents

Abstract	ii
Acknowledgements	iii
Table of Contents	v
List of Figures	xi
List of Tables	xxii
1. Introduction	1
1.1. Objectives	2
1.2. Structure of the thesis	2
2. Rubber Material Comprehension	6
2.1. General Rubber Characteristics	6
2.2. Rubber-Like Elasticity	8
2.2.1. Elastic Properties at Small Strains	8
2.2.2. Elastic Properties at Large Strains	10
2.2.2.1. Molecular Theory of Rubber-Like Elasticity	10
2.2.2.2. General Theory of Rubber-Like Elasticity	14
2.2.3. Strain Energy Functions for use at Hyperelastic Constitutive Models	19
2.3. Imperfect Elasticity	22
2.3.1. Mullin's Effect	22
2.3.2. Hysteresis	26
2.3.3. Stress Relaxation and Creep	27
2.3.4. Dynamic Behaviour	28
2.3.5. Temperature Effect	29
2.3.6. Summary of the effect of imperfect elasticity	29
2.4. Elastomer Materials	30
2.4.1. Material	30
2.4.2. Vulcanisation Processes and Test Specimen Manufacture	32

2.4.2.1.	Crosslink Density Measurement.....	33
2.4.2.2.	Test Samples and Exhaust Mounts Moulding Process	35
2.5.	Material Stress Strain Behaviour	38
2.5.1.	Test Procedure for Monotonic Characterization.....	38
2.5.2.	Stress Strain Behaviour	44
2.6.	Materials Constitutive Models Curve Fitting.....	48
2.6.1.	Hyperelasticity	48
2.6.2.	Mullin's Effect Model Fitting	49
3.	Rubber Fatigue	56
3.1.	Fatigue Life Approaches of Rubber.....	57
3.1.1.	Crack Nucleation Approach.....	57
3.1.1.1.	Maximum stretch ratio.....	59
3.1.1.2.	Maximum principal Cauchy stress	59
3.1.1.3.	Strain Energy Density.....	60
3.1.1.4.	Critical Plane Approach and Equivalent Parameters.....	61
3.1.1.4.1.	Cracking Energy Density	61
3.1.1.4.2.	Cauchy Stress Based Equivalent Quantity	63
3.1.1.4.3.	Configurational Stress Tensor	65
3.1.2.	Crack Growth Approach	68
3.1.2.1.	An Energy Criterion for Fracture.....	69
3.1.2.2.	Test Specimens for Rubber.....	70
3.1.2.3.	Regimes of Fatigue Crack Growth	74
3.1.2.4.	J-integral and Crack Tip Conditions.....	76
3.1.2.5.	Threshold strain energy release rate	78
3.1.3.	A Crack Growth Model for Crack Nucleation.....	79
3.1.3.1.	Intrinsic Flaws in Rubber.....	80
3.1.3.2.	Integrated Power-Law Model	84

3.1.4.	Summary and Applications of Analysis Approaches.....	86
3.2.	Fatigue Life Determination.....	92
3.2.1.	Energy Release Rate Computed by Cracking Energy Density	94
3.2.2.	Fatigue Life Computation	96
3.2.3.	Crack Closure Effect.....	98
3.2.4.	Crack Orientation Effect.....	99
3.3.	Factors that Affect the Fatigue Life of Rubber.....	100
3.3.1.	Mechanical Loading.....	100
3.3.1.1.	Maximum Load and Fluctuating Loading	101
3.3.1.2.	Minimum Load, Mean Load, and R-Ratio	102
3.3.1.3.	Annealing and Dwell Periods	104
3.3.1.1.	Multiaxiality.....	106
3.3.1.2.	Loading Frequency and Waveform	107
3.3.1.3.	Loading Sequence.....	108
3.3.1.4.	Duty Cycle	108
3.3.2.	Environmental Conditions	109
3.3.2.1.	Temperature	109
3.3.2.2.	Ozone.....	109
3.3.2.3.	Oxygen.....	111
3.3.3.	Rubber Formulation	112
3.3.3.1.	Polymer type.....	112
3.3.3.2.	Filler.....	114
3.3.3.3.	Antidegradants	116
3.3.3.4.	Vulcanization.....	116
3.3.4.	Dissipative Effects	117
3.3.4.1.	The Mullins Effect.....	118
3.3.4.2.	Strain-Crystallization.....	118

3.3.4.3.	Rate Independent Hysteresis.....	119
3.3.4.4.	Viscoelasticity.....	119
4.	Material Fatigue Behaviour Characterization	120
4.1.	Fatigue Crack Growth Testing.....	121
4.1.1.	Fatigue Crack Growth Characterization Tests	122
4.1.1.1.	Monotonic Crack Growth Test to Break.....	126
4.1.1.2.	Short Fatigue Crack Growth Test	128
4.1.1.3.	Fully Relaxing Fatigue Crack Growth Test Experiments.....	130
4.1.1.4.	Non-Relaxing Fatigue Crack Growth Test Experiments.....	140
4.1.1.5.	Effect of R-ratio on Fatigue Crack Growth	145
4.2.	Fatigue Crack Nucleation Testing.....	155
4.2.1.	Fatigue Crack Nucleation Characterization Tests.....	155
4.2.1.1.	Monotonic Strain to Break of Simple Tension	155
4.2.1.2.	Cycling to Break of Simple Tension.....	158
4.2.2.	Material Intrinsic Flaw Size Determination.....	163
4.2.3.	Volume Density of Crack Precursors.....	167
4.3.	Summary of Material Characterization	170
5.	Component Fatigue Life Predictions	171
5.1.	Prediction of Component Stress Strain Behaviour.....	171
5.1.1.	Material Characterization.....	172
5.1.2.	Finite Element Model Construction.....	173
5.1.2.1.	Abaqus Model.....	175
5.1.2.2.	Ansys Model	176
5.1.2.2.1.	APDL of Ansys to output the strain history	177
5.1.3.	Finite Element Model and Material Verification	179
5.1.3.1.	Correlation of Material Model.....	179
5.1.3.2.	Correlation of Finite Element Model.....	183

5.2.	Component Fatigue Experiments	187
5.2.1.	Fatigue Test Experiment Conditions and Results	188
5.2.2.	Localization of First Nucleated Cracks	191
5.3.	Component Crack Nucleation Life Prediction	195
5.3.1.	Fatigue Crack Nucleation Life Prediction	197
5.3.2.	Identify the Fatigue Critical Location	200
5.4.	Summary of Component Fatigue Life Predictions	202
6.	Component Stiffness Loss Prediction	205
6.1.	Loss of Stiffness and Development of Crack Precursors during Fatigue	206
6.1.1.	Crack Precursors	206
6.1.2.	Cyclic Stiffness Loss	208
6.1.3.	Theory	209
6.1.3.1.	Crack Precursor Development	209
6.1.3.1.	Stiffness Loss Theory	210
6.1.4.	Experimental	213
6.1.5.	Results and Discussion	213
6.1.6.	Summary of Development of Crack Precursors Influence	215
6.2.	Cycling Control Type Influence on Stiffness Loss	215
6.2.1.	Theory	216
6.2.2.	Stiffness Loss Characterization of Material	220
6.2.3.	Component Fatigue Experiments	222
6.2.4.	Analysis Procedure	224
6.2.5.	Results and Discussion	227
6.2.5.1.	Stiffness Loss Tendency on Graphical Representation	228
6.2.5.2.	Stiffness Loss Quantitative Results	231
6.2.5.1.	Cracking Zone Identification	232

6.2.5.2. Study of Parameters that Influence on Stiffness Loss Predictions	233
6.2.5.2.1. The Flaw Size	234
6.2.5.2.2. The Percentile	235
6.2.5.2.3. The Lookup Table	237
6.2.6. Summary of Control Type Influence	239
7. Conclusions and Future Works	244
7.1. Conclusions	244
7.2. Directions for Future Works	248
8. Publications and Communications	250
9. References	251
Appendix I	267
Appendix II	290
Appendix III	297

List of Figures

Figure 2.1 Diagram of the three reasons, from any of which deviations from this ideal model could result from. [8]	14
Figure 2.2 Initial transient softening of filled rubber due to the Mullin's effect [3]	23
Figure 2.3 Hysteresis loops for natural rubber taken from Lindley [38]. (a) The first cycle loops for unfilled natural rubber extended to various strains and (b) first second and tenth cycle loops for a natural rubber that contains 50 phr of carbon black.	27
Figure 2.4 A plot taken from Deeprasertkul [42] to demonstrate that the measured strain lags behind the applied stress for a visco-elastic material	29
Figure 2.5. Swelling measurement results are plotted for pure shear test sample at different curing times and exhaust mount component, along with sample obtained from ODR test used as pattern of optimum curing level. There are plotted the results of both materials: A) MCN material; B) MSB material	35
Figure 2.6 Oscillating Disk Rheometer (ODR) test, according to the ASTM D2084 standard, for both A) MCN and B) MSB materials.	37
Figure 2.7 Equivalence of stress states shown by superposition of hydrostatic pressure. Adapted from Bhashyam [46]	39
Figure 2.8 Schematics of uniaxial tension/compression, equibiaxial tension/compression and pure shear. Adapted from Bhashyam [46]	40
Figure 2.9 Test Samples and gripping of each strain state characterization testing set-up: A) Planar tension. B) Simple Tension. C) Simple compression.	43
Figure 2.10. Monotonic stress-strain behaviour curves in simple Tension, Planar Tension and Simple Compression	45

Figure 2.11. Stabilization of stress-strain curves after five cycles. Results generated in planar tension at 75% strain.	45
Figure 2.12 Cyclically stable stress-strain curves in progressively increasing: A.1) Uniaxial Tension (Simple Tension and Simple Compression), MCN material; A.2) Planar Tension, MCN material; B.1 Uniaxial Tension (Simple Tension and Simple Compression), MSB material; B.2) Planar Tension, MSB material.	47
Figure 2.13 Schematic loading-unloading curves in simple tension (Mullins effect) [32]	50
Figure 2.14 Fit of Mullins law to a series of cyclic stabilized unloading curves in planar tension, simple tension and simple compression. Data for both materials: A.1) Uniaxial Tension (Simple Tension and Simple Compression) of MCN material; A.2) Planar Tension of MCN material; B.1 Uniaxial Tension (Simple Tension and Simple Compression) of MSB material; B.2) Planar Tension of MSB material.	54
Figure 3.1 Crack growth test pieces for which the stored energy release rate T can be easily calculated: (a) trousers (b) pure shear (c) angled (d) split and (e) edge crack.	71
Figure 3.2 Greensmith's [86] data for variation of k with maximum principal stretch λ , in $T = 2kWc$. This relationship gives the energy release rate T of a crack in the simple tension specimen shown. Different data point types are for different rubber compounds.	74
Figure 3.3 Regimes of fatigue crack growth behaviour in unfilled rubber, under $R = 0$ loading (X = SBR, O = NR). Mcycle = Megacycles = 10^6 cycles. [54] Based on [122]	76
Figure 3.4 Schematic representation and real image capture of fatigue crack initiation mechanism around a carbon black agglomerate [150]	83
Figure 3.5. Crack nucleation and growth phases during a typical fatigue failure case.	93

Figure 3.6 Energy release rate evolution during fatigue crack nucleation and growth as the crack is growing, represented by the crack size	93
Figure 3.7 The crack growth per cycle, dc/dN , as a function of maximum strain energy release rate, T , for different minimum tearing energies, T_{min} . T_{min} equal to zero and T_{min} equal to about 6% of the maximum (Lake and Lindley [89])	104
Figure 3.8 $R = 0$ fatigue crack growth behaviour for 8 elastomer types. Results for unfilled, and two filler types are shown [200]. \circ Gum; \bullet Filled with 50 phr N300 carbon black (fine) Filled with; $+$ Filled with 50 phr N900 carbon black (coarse)	114
Figure 4.1 Strain – Displacement relationship for Planter Tension sample up to 100% strain	124
Figure 4.2 Sequence of pictures to explain the Image J image processing system work process. A) Uploaded raw picture, then the model is converted in binary, and at last step a Line Graph operation is executed to obtain (x,y) coordinates of the crack edge, and B) finally crack edge coordinates are plotted in a spreadsheet program like Excel.	125
Figure 4.3 Engineering stress-strain curve of monotonic tensile to break test of pre-cracked planar tension test sample. A) MSB (Specimen P3 was selected). B) MCN (Specimen P2 was selected.)	127
Figure 4.4 Test scheme showing history of peak strain (top), and history of crack length (bottom)	129
Figure 4.5 Graph of crack growth as a function engineering strain. Power regression fitting curve is plotted, which defines the crack growth law. MCN Material results are shown.	130
Figure 4.6 Test scheme designed to start crack growth at the minimum observable rate and end at targeted maximum crack length	132
Figure 4.7 Plot of experimentally determined and fitted crack lengths as function of performed cycles. A) is the plot of the MCN	

- material behaviour and B) is the plot of the MSB material behaviour. 134
- Figure 4.8 Plot in logarithmic values of crack growth rate versus energy release rate. The linear regression equation is also shown. A) is the plot of the MCN material behaviour and B) is the plot of the MSB material behaviour. 135
- Figure 4.9 Plot in logarithmic scale of crack growth rate versus energy release rate. The linear regression equation is also shown. A) is the plot of the MCN material behaviour and B) is the plot of the MSB material behaviour. 137
- Figure 4.10 Plot of the Lake and Lindley [122] model, with four regimes of fatigue crack growth behaviour and their correspondent descriptive equations. The plot have been taken from Endurica user manual [217] 138
- Figure 4.11 Plot of the fatigue crack growth behaviour based on Lake and Lindley model [122]. A) is the plot of the MSB material behaviour and B) is the plot of the MCN material behaviour. 139
- Figure 4.12 Overall test scheme for characterizing crack retardation with nonrelaxing cycles 141
- Figure 4.13 Representative scheme of a hypothetical test conditions for a single peak strain level. 142
- Figure 4.14 Plot of stress-strain loop for a fully relaxing test cycle and a non fully relaxing cycle. Area under the curve is drawn to show the strain energy density that has to be computed. 145
- Figure 4.15 Crack length measurement in function of performed cycles. The fitted crack length is superimposed over experimental results, which shows an appropriate fitting. A) is the plot of the MCN material behaviour and B) is the plot of the MSB material behaviour. 146
- Figure 4.16 A plot of the crack arrest effect. Fitting of crack growth law tendency lines (solid line), and experimental results or

- observations (dots) are plotted. Observations and fitted curves are marked according to the R ratio. The graph shown in A) is from the MCN material, and the B) is from the MSB material. 149
- Figure 4.17 A Plot of the effect of R_7 ratio on fatigue crack growth exponent $F(R)$. The graph shown in A) is from the MCN material, and the B) is from the MSB material. 150
- Figure 4.18 Observations of strain crystallization function $x(R)$ for crack growth under nonzero minimum strain. The obtained results for first replicate of test conditions with first sample are in hollow circle, for second replicate are in hollow diamond, for the third replicate are in hollow rectangle, and all of them are compared with tabulated crystallization function, marked with 'x'. The graph shown in A) is of the MCN material, and the B) is of the MSB material. 153
- Figure 4.19 Simple tension stress-strain curves to break for MSB and MCN materials. A) is the plot of the MCN material behaviour and B) is the plot of the MSB material behaviour. 157
- Figure 4.20 Simple tension test sample and gripping configuration for the cycling test. The camera is use to capture the crack growth. 158
- Figure 4.21 Strain-displacement relationship for simple tension specimen at uniaxial tensile test. 159
- Figure 4.22 Typical stiffness loss behaviour until break at two strain levels is represented. Stress in plotted against the number of cycles in logarithmic scale. A) is the plot of the MCN material, and B) is the plot of the MSB material. 162
- Figure 4.23 Elastic behaviour of material as a function of strain obtained from Planar Tension test sample. A) is the plot of the MSB material behaviour and B) is the plot of the MCN material behaviour. 165
- Figure 4.24. Fatigue life dependence in flaw size at various strain levels (ranging from 25% to 400% peak strain). A) is the plot of MSB

- material, assuming a flaw size of 0.03 mm; and B) is the plot of MSB material, assuming a flaw size of 0.04 mm. 166
- Figure 4.25 Strain-life calibration curve with experimentally obtained fatigue life and computed strain-life curves. A) is the plot of the MSB material (continuous line is for flaw size of 0.022); and B) is the plot of the MCN material. (continuous line is for flaw size of 0.08) 166
- Figure 4.26. Images of cracks developing in the surface of each specimen are shown. The pictured specimen is almost failed, and is shown as slightly strained to permit observation of the cracks. Images are in order from first to third replicate. 168
- Figure 5.1. Exhausts mount component dimensions in mm, and gripping system for fatigue and stiffness loss experimental tests 173
- Figure 5.2. Left side image show the CAD model of the exhausts mount component. Right side image is a quarter-symmetric of Abaqus finite element model. 176
- Figure 5.3 Left side image show the CAD model of the exhausts mount component. Right side image is a quarter-symmetric of Ansys finite element model. 177
- Figure 5.4. Fatigue nucleation life vs. element number is plotted for the simple tension specimen in MCN material. Fatigue life is computed in Endurica from Strain history results obtained from Ansys (hollow circle) and Abaqus (filled circle), modelled in both Ansys and Abaqus for the MCN material. 178
- Figure 5.5 Stress vs. strain plot of three specimen geometries, and for MCN material. The graphs show the experimentally obtained results in dot line, and. the simulation results at 50 and 100 % strain in solid circle and solid diamond respectively. In the Figure 5.5.A) is for the simple tension, Figure 5.5.B) is for the planar tension, Figure 5.5.C) is for the simple compression. 181

Figure 5.6. Stress vs. strain plot of three specimen geometries, and for MCN material. The graphs show the experimentally obtained results in dot line, and. the simulation results at 50 and 100 % strain in solid circle and solid diamond respectively. In the Figure 5.6.A) is for the simple tension, Figure 5.6.B) is for the planar tension, Figure 5.6.C) is for the simple compression. 182

Figure 5.7. Force vs. displacement (F-D) plot of an exhaust mount made of MCN material. The graph represents the simulation results by F-D plot for two peak displacements 20mm in solid square, 30 mm in solid circle; and three experimental results at 20, 30 and 50 mm in hollow square, circle and triangle respectively, for three cycling peak displacements: 5, 85, 1200. In the Figure 5.7 A) is represented the case considering no friction, and in the Figure 5.7 B) is represented the case considering rubber to metal friction. 185

Figure 5.8. Force vs. displacement (F-D) plot of an exhaust mount made of MCN material. The graph represents the simulation results by F-D plot for two peak displacements 20mm in solid square, and 30 mm in solid circle; three experimental results at 20, 30 and 50 mm in hollow square, circle and triangle respectively, for three cycling peak displacements: 5, 85, 1200. In the Figure 5.8 A) is represented the case considering there is no friction, and in the Figure 5.8 B) is represented the case considering rubber to metal friction. 186

Figure 5.9 Component fatigue life test set-up with two cameras installed in front of the MTS Bionix Servo-hydraulic test machine to acquire images of the first visual crack during the testing. 188

Figure 5.10. Entire fatigue nucleation life results at all replicates of each initial peak displacement conditions, commanded at both, force and displacement. Figure 5.10. A) Results for exhaust mount made by MCN material. Figure 5.10. B) Results for exhaust mount made by MSB material. 191

- Figure 5.11. Representative image of the cycling fatigue test of MCN material made exhaust mount, which is amplified in the typical fatigue crack nucleation zone to better see the crack. 193
- Figure 5.12. The fatigue life in logarithmic scale vs. The initial peak displacement are shown in the following graph. Fatigue life predictions (hollowed symbols) are correlated with carried out experimental results (full symbols) for the exhaust mount made by MCN material. Circles are for displacement control loadings, while triangles are for force control loadings. 199
- Figure 5.13. The fatigue life in logarithmic scale vs. The initial peak displacement are shown in the following graph. Fatigue life predictions (hollowed symbols) are correlated with carried out experimental results (full symbols) for the exhaust mount made by MSB material. The circles are for displacement control loadings, while the triangles are for force control loadings. 200
- Figure 5.14. Comparative image of simulation results in a quarter part of entire model (left side) and a capture of the component during the fatigue test in the instant that a crack is nucleated. Prediction and experimental components shown in the pictures are both made of MCN material. 201
- Figure 5.15. The finite element models of fatigue life prediction results at three different peak displacement levels simulated for the MCN material made exhaust mount component. Fatigue Life distribution (in log₁₀ scale) for a displacement of 20 mm between pins. 202
- Figure 6.1 Microscope image showing typical microstructure of subject material 206
- Figure 6.2. Stress drop history during a fatigue test with a cycling peak strain of 150%. 214
- Figure 6.3. Relative contribution of the “large” defect and “all other” defect terms in Eq. 6-12. 215

- Figure 6.4 Graphical representation of the softening function $h=E/E_0$ versus the normalized fatigue life N/N_f 219
- Figure 6.5. Evolution of reaction variables strain, energy, and stress for control under strain, energy, and stress. Each plot corresponds to a different value of initial amplitude. 220
- Figure 6.6. Normalized stiffness loss curve derived from simple tension strip experiment in displacement control, presented in a graph as a function of normalized life, N/N_f . 222
- Figure 6.7. Evolution of normalized stiffness with regard to cycles, for displacement controlled mode tests. Two peak displacement value results are shown: Blue hollow circle is for 20 mm, and green hollow circle is for 30 mm. 223
- Figure 6.8. Evolution of normalized stiffness with regard to cycles, for force controlled tests. Two peak force value results are shown: Blue hollow circle is for 885 N, equivalent to 20 mm peak displacement, and green hollow circle is for 1280 N, equivalent to 30 mm peak displacement. 224
- Figure 6.9. Schematic representation of analysis workflow to predict the rubber components stiffness loss. 225
- Figure 6.10. Graphical representation of predicted number of cycles in function of programmed percentile values for the exhaust mount made by MCN material. 226
- Figure 6.11. Computed graphical evolution of stiffness loss, for strain and stress controlled conditions. Normalized stiffness is plotted against life cycles. Solid lines are for strain control cases and dashed lines for stress control cases. Figure 6.11.A) is for exhaust mount made by MCN material and Figure 6.11.B) for the one made by MSB. 229
- Figure 6.12. Computed and experimentally obtained evolution of stiffness loss at strain control conditions. Normalized stiffness is plotted against life cycles. Solid lines are for simulations of strain

control, and symbols for experimental strain control tests. The Blue coloured are for 20 mm peak displacements and green coloured one for 30 mm peak displacements. Shown results are of MCN material.

231

Figure 6.13. Predicted and experimentally obtained stiffness loss curves commanded at stress. Simulation has been carried out to a peak displacement, but cycling conditioning has been considered at stress control. Normalized stiffness is plotted against life cycles. Solid lines are for simulations of stress control, and symbols for experimental stress control tests. The Blue coloured are for first small force and green coloured for a second higher force. Figure 6.13.A) is for exhaust mount made by MCN material.

231

Figure 6.14. Comparison of fatigue crack nucleation point observed experimentally and obtained analytically

233

Figure 6.15. Normalized stiffness vs. stiffness loss life prediction results for four different initial flaw sizes for MSB material made exhaust mount simulation are plotted. The percentile value is kept constant at a value of 0.02. The four flaw sizes defined for simulations are: 0.009 (circle), 0.015 (square), 0.05 (triangle), and 0.08 (diamond), all of them in mm.

235

Figure 6.16. Normalized stiffness vs. stiffness loss life prediction results for four different percentile values for MSB material made exhaust mount simulation are plotted. The four different percentile values have been defined for simulations are: 0.01 (circle), 0.02 (square), 0.05 (triangle), 0.1 (diamond).

236

Figure 6.17. Normalized stiffness versus the ratio of life divided by the final life, N/N_f is plotted by the data of the lookup table, and thus the stiffness loss behaviour for the MSB material is represented. Two look up tables are shown: The number one (circle) is obtained from the mean values of all experimental test replicates, and the number two (square) from the replicate that showed the greatest stiffness loss.

238

Figure 6.18. Normalized stiffness vs. stiffness loss life prediction results for two different lookup tables of MSB material made exhaust mount are plotted. Lookup Table 1 (circle) is related with experimentally obtained material data. Lookup Table 2 (square) obtained from the same MSB material experimental tests, but from the replicate that presented the greatest.

238

Figure 6.19. Comparison of stiffness loss rates experimentally obtained and computed by Endurica code, under displacement and force control tests over MCN material exhaust mount component. Experimental test results are shown in hollow symbols, while prediction results are shown by dashed and continuous lines.

240

Figure 6.20. The normalized stiffness values are plotted in function of the ratio of current life divided by the final life N/N_f . The following stiffness loss results are plotted in a single graph: predictions on the exhaust mount model (dashed lines), experimental cycle to failure test on simple tension specimen at two peak levels (full symbols), and experimental cycle to stiffness loss test on real exhaust mount component (hollow symbol). Results for both materials are plotted: Figure 6.20. A) is for MCN material and Figure 6.20. B) is for MSB material.

242

List of Tables

Table 2.1 Strain Energy Density Functions for Hyperelastic Constitutive Models.	22
Table 2.2 Recipe for both rubber compounds: MCN (Natural Rubber) and MSB (SBR + BR).	32
Table 2.3 It is summarized in a table the sulfur and accelerant relationship that defines the type of sulphur vulcanization system of a rubber compound.	32
Table 2.4 ODR measurement results to determine specimen and component curing time, to define transformation process curing time.	37
Table 2.5. Planar tension sample injection moulding process conditions.	38
Table 2.6. Compression moulding process conditions for simple compression samples.	38
Table 2.7. Car exhaust mount, real component, injection moulding process conditions.	38
Table 2.8 Stretch states used in stress-strain characterization of rubber	40
Table 2.9 Yeoh 3 rd Order material model functions coefficients for MCN and MSB materials	49
Table 2.10 Mullin's law parameters obtained by modified Ogden-Roxburgh damage function parameters r , m , and β that defines the Mullin's effect behaviour of both materials, MCN and MSB	55
Table 3.1 Summary of reported initial flaw size values that have been taken from Lake and Lindley [89], Lake [158] and Choi and Roland [139] for different types of elastomers.	83
Table 3.2 Geometric features of filled rubber [37].	84
Table 4.1 Strength parameters derived from edge cracked planar tension tests	127
Table 4.2 Parameter values which define the fatigue crack growth behaviour by Lake and Lindley [122] model.	140

Table 4.3 Value of F_0 and F_1 parameters that define the exponential function Eq. 4-40, which define the dependence of materials on the R ratio in non-relaxing strain conditions.	150
Table 4.4 Tabular data of crystallization law of both MSB and MCN material	154
Table 4.5 Simple tension strain at break results ($\epsilon_{ST,b}$) for MSB and MCN materials	158
Table 4.6 Fatigue cycling test conditions in displacement and strain values.	159
Table 4.7 Fatigue nucleation experiment conditions defined for material intrinsic flaw size determination tests	161
Table 4.8 Simple tension cycling strain to break test results for two materials, MSB and MCN; Results are given for two peak strain tests.	163
Table 4.9. Parameter values of the power law function shown in Eq. 4-53	165
Table 4.10 Fatigue crack nucleation life experimental results, and computed initial flaw size.	167
Table 4.11 Fatigue test results with peak strain of 150% for MCN material.	169
Table 5.1. Fatigue testing operating conditions and obtained fatigue life average results for exhaust mount made by MCN material.	189
Table 5.2. Fatigue testing operating conditions and obtained fatigue life average results for exhaust mount made by MSB material.	190
Table 5.3.A Table of pictures at fatigue crack nucleation instant for MCN material made exhaust mounts. The images are cut in the nucleation zone. Pictures have been presented for each control type, loading level and replicate.	194
Table 5.3.B Table of pictures at fatigue crack nucleation instant for MSB material made exhaust mounts. The images are cut in the nucleation zone. Pictures have been presented for each control type, loading level and replicate.	195

Table 5.4. Fatigue life prediction conditions and obtained results for the exhaust mount made by MCN material.	198
Table 5.5. Fatigue life prediction conditions and obtained results for the exhaust mount made by MSB material.	198
Table 6.1. Experimental operating conditions for exhaust mount fatigue testing.	223
Table 6.2. Numerical results of computed stiffness loss and fatigue life at that stiffness drop, for strain and stress controlled conditions.	232
Table 6.3. Numerical mean value results of experimental stiffness loss and fatigue life at that stiffness drop, for strain and stress controlled conditions.	232
Table 8.1 List of publications	250
Table 8.2 List of communications	250

1. Introduction

The work described in the thesis arises from the need of a rubber parts manufacturing company on developing a material fatigue characterization method for stiffness loss and fatigue life prediction, in order to take into consideration cyclic loading effects on an early stage on the design process. Rubber components are subjected to large static loads upon which are superimposed cyclic loads over a long time. As a result, the material in the component is subjected to complex non-uniform stresses. Rubber has a set of unusual physical properties, such as large strain elasticity, incompressibility, internal damping and high strength, which makes it appropriate for a series of applications, such as tyres, conveyor belts, automotive components, rubber tracks, hoses, sport goods, and medical devices. Therefore, develop or design more durable or higher strength materials are of great importance for research engineers, as well as how to predict the stiffness loss and fatigue life of products. Long-term durability is a critical issue.

In the automotive industry, in many design scenarios of rubber components, as it is observed on spec sheets, loss of stiffness is what determines the end of life. Fatigue damage in elastomer causes gradual degradation of the stiffness prior to rupture. The mechanism of this degradation seems to have origins in both molecular and mesoscopic processes in the material [1,2]. The first few loading cycles applied in a test are known to cause a rapid transient decrease in stiffness, as demonstrated by Mullins [3]. When cracks start to grow, the rate of stiffness loss increases until the test is stopped or complete stiffness loss occurs due to the specimen rupture. Given the role of crack precursors in determining fatigue life, their tendency to grow, and their abundant presence in rubber's microstructure, their contribution to cyclic softening effects is clear.

To address the issue effectively and economically is needed to model and design for mechanical fatigue early in the product development process. This need has partially been addressed by the development of simulation software capable of predicting stress and strain histories. It has been of great importance to incorporate finite element analysis (FEA) software in the design processes; and then identify the

suitable energy criterion to represent the stress-strain behaviour of rubber, at least until 100% strains that are frequently encountered in engineering applications.

1.1.Objectives

The objectives of this research project have been:

- 1) To identify existing approaches for multiaxial fatigue analysis in rubber. Identify and implement the material characterization procedure and simulation methodology, considering that those have to be practical in time, and thus feasible in costs.
- 2) To thoroughly evaluate the analysis approach for its ability to predict observed effects of loading histories on fatigue crack nucleation and growth in rubber. The evaluation will be run over a real component and for two materials: a strain crystallizing material (NR) and a non-strain-crystallizing material (SBR + BR).
- 3) To identify existing approaches for stiffness loss analysis in rubber components under fatigue loading, and in case of being necessary to develop a new one. The predictions have to consider the influence of cracks size and density in the fatigue damage, and fatigue loading control type in the stiffness loss rate. Then, to feed the simulation method, material characterization procedure is to be implemented or to be developed.
- 4) To evaluate the analysis approach for its ability to predict the stiffness loss in a real component for two materials, a strain crystallizing material (NR) and a non-strain-crystallizing material (SBR + BR)

1.2.Structure of the thesis

In the rubber component manufacturing industry there is a lack of centres offering the complete fatigue life prediction service, from the specific full material characterization to computer aided fatigue life simulations. This prediction service has to include all life predictions, the fatigue life prediction, crack nucleation life prediction and the stiffness loss life prediction. The determination of critical zones in the finite element component model through the identification of most damaged element has also to be possible. To industrialize the process it has to be automated and shortened. Therefore, the strength of carried out research and implementation

work resides in the uniqueness on being able to perform the complete process of rubber fatigue behaviour prediction. Thus, in the thesis are detailed all steps of the procedure, from the material characterization tests to the finite element simulations and life predictions with the specific solver for fatigue analysis.

Chapter 2 is an introduction to rubber elasticity and general rubber characteristics. A set of imperfect elasticity effects that reduces the accuracy of stiffness calculations are introduced. Then, a review of different approaches that can be adopted to model the behaviour of a rubber and establish a reliable technique to predict stiffness behaviour is presented. Correlation results between numerical calculations and experimental test results at static loading conditions are presented finally on this chapter.

During the project, has been validated an approach by which experimental data measured under simplified tests would be used to predict fatigue life and loss of stiffness of rubber under arbitrary, more complex strain states. In Chapter 3 the application of crack nucleation and crack growth approaches to the analysis of fatigue life in rubber components are detailed. Existing theories are explained for each approach, strengths and limitations are remarked, and examples of how this are applied in engineering analysis are presented. The fatigue life determination is detailed considering the cracking energy density as damage measuring parameter, to take into account the crack closure and crack orientation effects. Then, factors that are known to influence the fatigue life of rubber are reviewed: mechanical loading history, environment, rubber formulation, and dissipative aspects of the constitutive response of material.

In Chapter 4 crack nucleation and growth testing procedures are detailed for either uniaxial or multiaxial conditions. The characterization of material to crack growth behaviour provides a crack growth rate data in function of a parameter independent of specimen geometry and loading history. By fatigue crack nucleation characterization the number of cycles to specimen failure at different peak strains is tabulated. From the combined data of crack growth and nucleation tests the intrinsic flaw size of material is determined. The material intrinsic flaw size is the principal data to predict the nucleation and fatigue life. Additionally, in the simple tension cycling to break test has been installed a system for automatically take pictures of the situation of the crack during the testing. Thus, the volume density of crack precursors

can be measured and classified by size. The measured stiffness in function of number of cycles is then used to construct the damage function that defines the stiffness loss of a rubber component used for computations of Chapter 6.

The complete material fatigue behaviour data under uniaxial conditions is used to predict the fatigue life of a complex geometry component. In chapter 5 the simulation process to predict the fatigue life of an exhausts mount is detailed. First, the uniaxial static simulations by the finite element analysis software Abaqus and Ansys, are done. The material virgin monotonic stress-strain behavior is modeled for the simulations using a conventional hyperelastic strain energy density function of reduced polynomial, Yeoh third order, whereas the Mullins Effect is modeled by the Ogden and Roxburgh approach. The static FEA simulation is used to transform the loading history, either force or displacement, to be applied over the real component, into a strain history that each element on the model bears. Thus, the Endurica CL solver for elastomer fatigue analysis is fed by strain history data per element in the model. For the nucleation life and fatigue life computations additional specific material fatigue behaviour data is required by the solver. The fatigue nucleation life is defined as the number of cycles required the crack to grow from its initial flaw size until a specified critical crack size, depends on the initial size of the flaw and is determined by the fatigue crack growth rate law. The crack nucleation is the principal phase in the fatigue life. The 80 % of the total life is consumed propagating the flaw from an initial size of 20 to 200 μm until a critical crack size, usually defined on 1 mm. For correlation with prediction results component fatigue life experimental tests have been carried out to analyse the crack nucleation location, the crack nucleation life and the fatigue life of the real component, the car exhaust mount. Tests conditions have been defined on three peak levels for each of two control types, and all of them have been run for each of two materials, the NR and the SBR+BR.

In many design scenarios in the automotive industry of rubber and rubber to metal bonded components the loss of stiffness is the parameter determining the end of life. In Chapter 6 the approach for stiffness loss calculation of rubber components is detailed. In rubber fatigue the strain energy density may depend not only on the instantaneous strain or stress, but also on damage state of material, and on the mode of control imposed in the fatigue test. The stiffness loss approach relates the

differentiated particular damage developments of different loading modes in a function. The parameter that quantifies the damage is the normalized stiffness, and a function has been defined that contemplates the effect of stiffness loss and crack size on the strain energy density. The approach has been implemented in Endurica CL solver for rubber fatigue analysis. There are two options to feed the solver with specific stiffness loss material data. The first input option is a tabular data of the damage function, which relates the normalized stiffness loss as a function of the normalized fatigue life. It has been assumed that all strain amplitudes produce the same identical stiffness loss characteristic curve. The parameter that quantifies the damage is the normalized stiffness, and the defined function contemplates the effect of stiffness loss and crack size on the strain energy density. The second input considers additionally the size of cracks and density of each defect in the surface of component with a constitutive model. Given the role of crack precursors in determining fatigue life, due to their abundant presence in rubber's microstructure and tendency to grow, their contribution on cyclic softening has been incorporated into a constitutive model.

2. Rubber Material Comprehension

2.1. General Rubber Characteristics

Rubber materials occur both in a natural and synthetic forms. Natural rubber (NR) is extracted from the sap of the tree *Hevea Braziliensis*. The main chemical constituent of natural rubber is the hydrocarbon $(C_5H_8)_n$ ($n \sim 10^5$) or polyisoprene (IR) which is a polymer of isoprene consisting of a continuous chain. The use of the term rubber is not limited to naturally occurring rubber but as Treloar [4] points out in his work the term is applied indiscriminately to any material having similar mechanical properties to those of natural rubber. Synthetic rubbers are available in a wide variety since United States had to start developing them during Second World War (1940's). Currently, synthetic rubbers are derived from the oil and gas industry. General-purpose rubbers include styrene-butadiene rubber (SBR), butadiene rubber (BR) and polyisoprene – both natural rubber (NR) and its synthetic equivalent (IR).

The most significant physical property of a rubbery material is the high extensibility that exhibit even with the application of relatively small stresses. The long chain molecules are a common characteristic of all polymeric materials including rubbers. Rubber materials have the following distinct features: (i) The polymer contains very long and flexible molecules, which are arranged in amorphous polymers with a random-coil. (ii) The polymer operates above the glass transition temperature, T_g which is the temperature at which the polymer changes from the glassy state to the rubbery state. (iii) The polymer should exhibit limited crystallinity.

In engineering applications, it is necessary rubber to be in its cross-linked or vulcanised state. Since the forces between the molecules are weak and chains have freely rotating links the material behaves like a viscous liquid. The introduction of crosslinks converts a rubber material into an elastic material. The vulcanized rubbers are commonly known as elastomers. Vulcanization or cross-linking is the process in which the chains are chemically linked together to form a network.

The vulcanization process requires curatives, such as sulphur or peroxide, in order to introduce the cross-links between the large polymer chains. The work in this thesis is concerned with sulphur vulcanised elastomers. The process is carried out at an

elevated constant temperature (typically 140 -185°C) in a mould that is kept at high pressure in a hydraulic press to achieve good conformation to the mould shape. Sulphur based vulcanising systems require long curing times. It is therefore common practice to speed up the vulcanising process, by using chemical accelerators which are added during the mixing process. Other vulcanising ingredients for a sulphur based system include zinc oxide and stearic acid. After its polymer chains have been cross-linked, the stiffness of the elastomer increases. There is a reduction in the creep and slippage of the chains of the elastomer. Vulcanisation improves greatly the durability and utility while the permanent set after loading and unloading and hysteresis in the material decrease.

In practice, in addition to vulcanising ingredients, other additives such as antioxidants and fillers are usually added to compound engineering elastomers. These additives modify the mechanical, chemical and physical properties to a much greater degree than is possible by the simple alteration of the fundamental molecular structure. The more common types of reinforcing fillers are carbon-black and silica which are widely used in the rubber industry. In this work the filler introduced in the elastomers have been carbon black. It is the most commonly used filler and it is available in a wide range of particle sizes, shapes and structures. The specific grade used depends upon the specific engineering application.

Rubber's ability to withstand very large strains without permanent deformation or fracture makes it ideal for many applications. Elastomers have a wide range of applications such as tyres, vibration isolation components and earthquake bearings. These applications impose large static and time-varying strains over a long time. Long-term durability is therefore a critical issue. While many factors contribute to long-term durability, mechanical fatigue is often the primary consideration. To address the issue effectively and economically, engineers need to model and design for mechanical fatigue early in the product development process.

There are different theories that describe the stress-strain behaviour of elastomers depending on the extent of deformation and the presence (or absence) of fillers. These theories and their applicability are presented in detail in section 2.2 since they are essential to analyse the behaviour of material. The principles of Finite Element Analysis which form the basis of the analytical modelling work carried out are presented also at the end of the chapter.

2.2. Rubber-Like Elasticity

Elastomers can undergo large extensions, normally within the range of 200% to 1000% for most engineering elastomers. The engineering stress versus strain behaviour during large tensile extensions is non-linear, and as a consequence a single value for the Young's modulus is inappropriate.

It is possible to define two different approaches to analyse the material deformation behaviour. If the maximum extension ratio found in a component is below 1.1 the strains in an elastomer are considered small. Thus, the deformed geometry can be considered to be unchanged in shape by the action of the applied forces, and it would therefore be possible to apply linear elasticity theory. This approach is discussed in section 2.2.1. When the extension ratios in the elastomer become greater than 1.1, as is frequently the case with elastomeric components, strains are considered large. Then, recourse to the conventional theory of rubber-like elasticity discussed in section 2.2.2 would be required. This theory can be derived from a consideration of the behaviour of individual molecules in the elastomer. This approach works reasonably well for most unfilled elastomers, however for engineering applications elastomers frequently incorporate reinforcing particles, such as carbon black, dispersed throughout the material. This composite of elastomer and reinforcing particles cannot be accurately described by this molecular based theory of rubber-like elasticity. So, some of the alternative phenomenological strain energy functions that have been used in the past to describe rubber-like elasticity are examined in section 2.2.2. A simple strain energy density function that can be used to describe the behaviour for applications loaded in the engineering strain range (defined as components subjected to extension ratios less than 2) is discussed in section 2.2.3. The limitations of using an elastic theory to represent the behaviour of real elastomers, which experience imperfect elastic behaviour, such as stress relaxation, creep, hysteresis, and other are discussed in section 2.3.

2.2.1. *Elastic Properties at Small Strains*

There are two fundamental elastic constants, specifically the bulk modulus K and shear modulus G that can be used to describe the behaviour of isotropic elastic materials. Those describe the resistance of material to different kind of strain states. The bulk modulus K deals with the resistance to compression in volume under a

hydrostatic pressure. It is defined as the ratio of the applied pressure to the volumetric strain. The shear modulus, G deals with the resistance to a simple shearing stress. It is defined as the ratio of the applied shear stress, τ , required to produce a shear strain, γ . There is a third elastic modulus, the Young's modulus, E , which can be measured and it is related (at small strains) to the other two modulus values as shown [5]:

$$K = \frac{E}{3(1 - 2\nu)} \quad \text{Eq. 2-1}$$

$$G = \frac{E}{2(1 + \nu)} \quad \text{Eq. 2-2}$$

Where ν is the Poisson's ratio. The shear and tensile moduli of rubber solids are low, in the range of 0.05 – 10 MPa. On the other hand, the bulk modulus is relatively large, of the order of 1.0 – 2.0 GPa. The resulting value of Poisson's ratio is close to 0.5 (0.4995) which therefore gives a small strain tensile modulus E of approximately $3G$. As a result, elastomers are frequently regarded as being incompressible in bulk, being a reasonable approximation for many engineering applications. This implies that Poisson's ratio would be of the value of 0.5 and that the elastic behaviour at small strains (<20% strain) can be described by a single elastic constant such as G .

This significantly larger bulk modulus gives high compression stiffness with low shear stiffness when the elastomer is constrained in shape for example by bonding the elastomer between rigid plates. This exceptional behaviour is widely exploited and applied in the design of vibration isolation compression mounts, such as earthquake or bridge bearings as well as the mounting systems used in automotive applications. Simple analytical relationships, which allow stiffness values to be calculated for some of these standard shape components, have been derived using a linear elasticity theory. However, when the geometry becomes complex or the deformations large, this theory becomes difficult to use and recourse has to be made to finite element analysis techniques. These initial gradients of the load-deflection curve calculations can use either a small strain elasticity theory or, with a suitable approach adopted, a large deformation non-linear rubber-like elasticity theory. Theory of large strain rubber-like elasticity is discussed next.

2.2.2. *Elastic Properties at Large Strains*

Large strain behaviour of rubber material is not easy to describe. The mechanical response of elastomeric is complicated by material non-linearity. There are two main approaches that attempt to describe that behaviour.

First the molecular theory will be explained, which is based on the concept of the mechanical work done to increase the configurational entropy of the elastomer network when is deformed. The derivations and the related background to the general expressions are commonly called the simple statistical theory owing to the statistical treatment of the probable end-to-end distance of a typical single molecule; or alternatively the kinematic theory, owing to the analogy with the kinetic theory of gases, deriving from the consideration of thermal motions of molecular segments. It is also known as Neo-Hookean network theory. The application of this approach is restricted to simple unfilled elastomers loaded to moderate strains. As it has no practical application in our project will be shortly explained in order to develop a physical understanding for the phenomenological approach that is discussed later.

The phenomenological approach that is based on classical mechanics will be explained next. The approach attempts to fit the measured experimental stress strain relationship behaviour by the judicious selection of an appropriate mathematical form for the strain energy function. Both approaches can result in the derivation of a strain (sometimes also referred to as stored) energy density function. This is a measure of the amount of energy stored elastically in a unit volume of the material having been subjected to a specific state of strain.

2.2.2.1. *Molecular Theory of Rubber-Like Elasticity*

The molecular theory of rubber-like elasticity was a development of the work carried out by James and Guth [6]. Treloar [4] reviewed the derivations of the original molecular theory, the basis of which is the behaviour of a single randomly configured elastomer chain. The theory assumes that the network contains N chains per unit volume each containing n identical, freely jointed links of length, l_m , and that a chain is defined as a segment of molecule between successive crosslinks.

The rubber deforms in a manner which causes the configurational entropy of the chains to alter, without a change in the internal energy. The distribution of distance

between crosslinks, r , follows a Gaussian distribution in the unstrained state described by a probability density function:

$$P(r) = \left(\frac{b^3}{\pi^{\frac{3}{2}}}\right) \exp(-b^2 r^2) \quad \text{Eq. 2-3}$$

Where

$$b^2 = \frac{3}{2nl^2} \quad \text{Eq. 2-4}$$

And it is assumed that distance between the chain ends, r , is smaller than the fully extended length of the chain nl . The volume doesn't change on deformation and is considered incompressible. It is possible to derive from Eq. 2-3 the mean square distance between the ends of the chain, denoted by \bar{r}^2 as nl^2 .

The move on deformation of crosslinks is assumed will be like embedded in an elastic continuum. The components in each chain change in the same ratio as in the bulk rubber. This assumption is known as of affine deformation.

The entropy of the network is the sum of the entropies of the individual chains between each crosslink. The entropy of the individual chains is given by:

$$S = C_A - \frac{3kr^2}{2nl_m^2} \quad \text{Eq. 2-5}$$

C_A is an arbitrary constant, and k is the Boltzmann constant. The entropy change associated with deforming a chain is calculated using Eq. 2-5 and summing over all chains yields on:

$$\Delta S = -\frac{1}{2} Nk(\lambda_1^2 + \lambda_2^2 + \lambda_3^2 - 3) \quad \text{Eq. 2-6}$$

Where ΔS is the change in entropy of the network per unit volume under a deformation, and λ_1 , λ_2 , and λ_3 are the three principal extension ratios (the ratios of stretched to unstretched length) along three mutually perpendicular axes. Thus a unit cube would be deformed into a cuboid with edges of length λ_1 , λ_2 , and λ_3 .

For a reversible deformation, the work of deformation is equal to the change in the Helmholtz free energy. The Helmholtz free energy, A_H , is defined as:

$$A_H = U - T_A S \quad \text{Eq. 2-7}$$

where U is the internal energy and T_A is the absolute temperature. Hence, for an isothermal deformation, the work of deformation for a unit volume, W , is given by:

$$W = \Delta A_H = \Delta U - T_A \Delta S \quad \text{Eq. 2-8}$$

By applying the second assumption given above that there is no change in internal energy under deformation, Eq. 2-8 simplifies to:

$$W = -T_A \Delta S \quad \text{Eq. 2-9}$$

where T_A is the absolute temperature. Hence, from Eq. 2-6:

$$W = \frac{1}{2} NkT_A (\lambda_1^2 + \lambda_2^2 + \lambda_3^2 - 3) \quad \text{Eq. 2-10}$$

W represents the elastically stored energy per unit volume and is equivalent to the strain energy function described earlier. It is convenient to write:

$$G = NkT_A \quad \text{Eq. 2-11}$$

Hence,

$$W = \frac{1}{2} G (\lambda_1^2 + \lambda_2^2 + \lambda_3^2 - 3) = \frac{1}{2} G (I_1 - 3) \quad \text{Eq. 2-12}$$

Thus, the strain energy function represented by Eq. 2-12 involves only one physical constant, G , which may be determined from the degree of crosslinking in the rubber. It follows from the assumption of constant volume relation that:

$$\lambda_1 \lambda_2 \lambda_3 = 1 \quad \text{Eq. 2-13}$$

So, Eq. 2-12 may thus be rewritten as:

$$W = \frac{1}{2} G (\lambda_1^2 + \lambda_2^2 + [\lambda_1 \lambda_2]^{-2}) \quad \text{Eq. 2-14}$$

Thus, for an incompressible material, W is a function of two independent variables, in this case they λ_1 and λ_2 are chosen.

For an incompressible material the state of deformation is unaffected by the imposition of a hydrostatic pressure, $-p$. It follows that the stresses are indeterminate to the extent of an arbitrary hydrostatic stress, $+p$:

$$t_i = \lambda_i \frac{\partial W}{\partial \lambda_i} + p \quad \text{Eq. 2-15}$$

Where t_i is the true (or Cauchy) stress, defined as the force per unit area in the deformed state and i takes the values 1, 2 or 3. However, the differences between any two principal stresses may be determined absolutely. Assuming the Strain Energy Function given in Eq. 2-16, then those are given as:

$$\begin{aligned} t_1 - t_2 &= G(\lambda_1^2 - \lambda_2^2) \\ t_2 - t_3 &= G(\lambda_2^2 - \lambda_3^2) \\ t_3 - t_1 &= G(\lambda_3^2 - \lambda_1^2) \end{aligned} \quad \text{Eq. 2-16}$$

The stress-strain behaviour for particular modes of deformation may be determined from Eq. 2-16 by substitution of appropriate relationship for the stresses and extension ratios. It is interesting to note that, in simple shear, the shear stress is given by:

$$t_3 - t_1 = G(\lambda_3^2 - \lambda_1^2) \quad \text{Eq. 2-17}$$

in which γ is the shear strain. Thus the material constant, G is equivalent to the shear modulus. It is observed that Hooke's law is obeyed for some simple unfilled elastomers up to reasonable strains in simple shear (through not in other deformations) and Rivlin [7] showed that the statistical theory was a natural extension of Hooke's law to large deformations, thus a material obeying it was called Neo-Hookean.

There are deviations from theory even for unfilled elastomers, especially in uniaxial extension, where at low strains (below about 50%), the measured modulus is higher than that anticipated from the theory. Flory [8] reported that these deviations from this ideal model could result from any of these three reasons:

- a) Loose-ends: a free loose end to the molecular chain connected to the network at only one end and making no contribution to the material's modulus.
- b) Closed looping: a molecular chain curls around and crosslink with itself, again making no contribution to the material's modulus.

c) Inter-looping: physical entanglement of the chains restricting the number of available configurations.

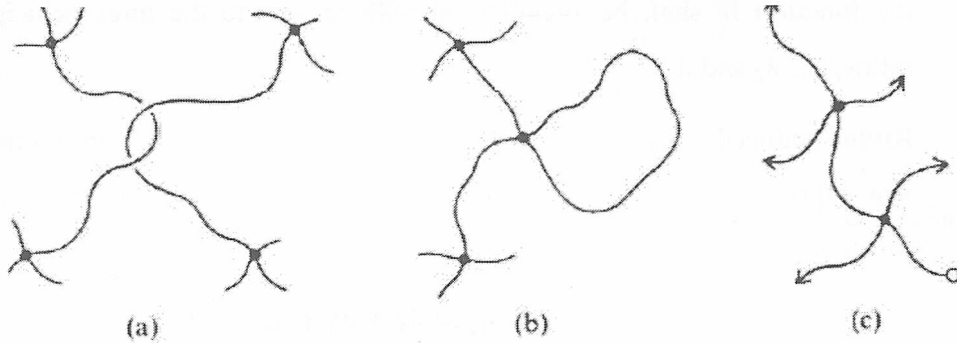


Figure 2.1 Diagram of the three reasons, from any of which deviations from this ideal model could result from. [8]

At relatively high strains, greater than 300%, a rapidly rising modulus, stiffening, is seen experimentally which is not predicted by the theory. This increment of stiffness is assigned to the finite extensibility of the molecular network. It results from the network of polymer chains becoming somewhat aligned by the application of the strain, and the molecules that make up the material are no longer being simply reoriented but are starting to become stretched by the application of the load. Gent [9] proposed an empirical equation to describe this behaviour, given as:

$$W = -\frac{1}{2}G(I_m - 3)\ln\left(1 - \frac{I_1 - 3}{I_m - 3}\right) \quad \text{Eq. 2-18}$$

where $I_1 = \lambda_1^2 + \lambda_2^2 + \lambda_3^2$ and I_m is the value of I_1 when this limited extensibility is reached.

The main benefits of statistical theory are that requires a single material constant and that it can explain the behaviour based upon an examination of the molecular structure alone.

2.2.2.2. General Theory of Rubber-Like Elasticity

The general theory of rubber-like elasticity is a phenomenological approach that employs mathematical reasoning to derive an appropriate function to fit the experimentally observed stress versus strain behaviour of rubber. This general treatment of the stress-strain relations of rubber-like solids began with Mooney [10] before the derivation of the Gaussian statistical theory and was further developed by

Rivlin [11]. Rivlin's large strain elasticity theory assumes that (i) The rubber is incompressible in bulk, and isotropic in elastic behaviour in the unstrained state. (ii) No volume change occurs on deformation. The condition for isotropy requires that the function W shall be symmetrical with respect to the three principal extension ratios, λ_1 , λ_2 and λ_3 .

Rivlin deduced, based on symmetry considerations, that the strain energy function was expressible in terms of the three strain invariants, I_1 , I_2 and I_3 , independently of the choice of axes, which are defined as:

$$\begin{aligned} I_1 &= \lambda_1^2 + \lambda_2^2 + \lambda_3^2 \\ I_2 &= \lambda_1^2 \lambda_2^2 + \lambda_2^2 \lambda_3^2 + \lambda_1^2 \lambda_3^2 \\ I_3 &= \lambda_1 \lambda_2 \lambda_3 \end{aligned} \quad \text{Eq. 2-19}$$

Three strain invariants, I_1 , I_2 and I_3 arise naturally as coefficients in the characteristic equation for solving for the eigenvalues ($\lambda_1^2, \lambda_2^2, \lambda_3^2$) of both the left and right Cauchy Green stretch tensors. Mooney derived, using mathematical reasoning, the following strain energy function

$$W = C_1(\lambda_1^2 + \lambda_2^2 + \lambda_3^2) + C_2 \left(\frac{1}{\lambda_1^2} + \frac{1}{\lambda_2^2} + \frac{1}{\lambda_3^2} - 3 \right) \quad \text{Eq. 2-20}$$

For an incompressible material I_3 is unity; hence, can be rewritten for incompressible materials in terms of the two strain invariants I_1 and I_2 defined in Eq. 2-19 as,

$$W = C_1(I_1 - 3) + C_2(I_2 - 3) \quad \text{Eq. 2-21}$$

The Mooney Strain Energy Function contains two elastic constants C_1 and C_2 and simplifies to the Neo-Hookean equation, as given in Eq. 2-12, when $C_1 = G/2$ and $C_2 = 0$ or in terms of the strain invariants, as

$$W = C_1(I_1 - 3) \quad \text{Eq. 2-22}$$

Rivlin [12] showed that for a pure homogenous strain, a set of relations exist between the principal extension ratios λ_1 , λ_2 and λ_3 and the true principal stresses referred to the deformed dimensions t_1 , t_2 and t_3 , and the partial derivatives of W with respect to the two strain invariants I_1 and I_2 . These relations are given in Eq. 2-21, where the left hand side is defined as the reduced stress term σ^* .

$$\begin{aligned}\frac{t_1 - t_2}{\lambda_1^2 - \lambda_2^2} &= 2 \left(\frac{\partial W}{\partial I_1} + \lambda_3^2 \frac{\partial W}{\partial I_2} \right) \\ \frac{t_1 - t_2}{\lambda_1^2 - \lambda_2^2} &= 2 \left(\frac{\partial W}{\partial I_1} + \lambda_3^2 \frac{\partial W}{\partial I_2} \right) \\ \frac{t_1 - t_2}{\lambda_1^2 - \lambda_2^2} &= 2 \left(\frac{\partial W}{\partial I_1} + \lambda_3^2 \frac{\partial W}{\partial I_2} \right)\end{aligned}\quad \text{Eq. 2-23}$$

The engineering stress σ_i , which relates to the undeformed dimensions, is related to the true stress t_i by

$$\sigma_i = \frac{t_i}{\lambda_i} \quad \text{Eq. 2-24}$$

Using these relationships, specific expressions for the reduced stress term σ^* for the simple homogenous deformation modes shown below are derived. The reduced stress term for a uniaxial deformation, such as that shown in Figure 2.2 (a), is given by,

$$\sigma^* = \frac{\sigma}{(\lambda - \lambda^{-2})} = 2 \left[\left(\frac{\partial W}{\partial I_1} \right) + \frac{1}{\lambda} \left(\frac{\partial W}{\partial I_2} \right) \right] \quad \text{Eq. 2-25}$$

On the other hand, in pure shear, as shown in Figure 2.2(c), the reduced stress is given by,

$$\sigma^* = \frac{\sigma}{(\lambda - \lambda^{-3})} = 2 \left[\left(\frac{\partial W}{\partial I_1} \right) + \left(\frac{\partial W}{\partial I_2} \right) \right] \quad \text{Eq. 2-26}$$

The simple shear deformation shown in Figure 2.2(b) cannot be evaluated directly using the framework of the principal extensions. However, Rivlin [12] showed that in simple shear, the reduced stress term, σ^* was the shear stress, τ divided by the shear strain γ thus,

$$\sigma^* = \frac{\tau}{\gamma} = 2 \left[\left(\frac{\partial W}{\partial I_1} \right) + \left(\frac{\partial W}{\partial I_2} \right) \right] \quad \text{Eq. 2-27}$$

In simple shear the shear strain γ is related to the strain invariants I_1 and I_2 thus,

$$\gamma^2 = (I_1 - 3) = (I_2 - 3) \quad \text{Eq. 2-28}$$

Rivlin [12] proposed a general strain energy function using only mathematical argumentation. The work dealt with large elastic deformations and proposed that the strain energy density W is a symmetric function of the three strain invariants given in Eq. 2-19:

$$W = \sum_{i+j+k=1}^{\infty} C_{ijk} (I_1 - 3)^i (I_2 - 3)^j (I_3 - 3)^k \quad \text{Eq. 2-29}$$

For an incompressible material where $I_3 = 1$, the equation may be reduced to,

$$W = \sum_{i+j=1}^{\infty} C_{ij} (I_1 - 3)^i (I_2 - 3)^j \quad \text{Eq. 2-30}$$

C_{00} is usually set equal to zero to reflect zero stored energy in the unstrained state. Eq. 2-30 is a power series, usually truncated to the first few terms. When only the first term ($i=1, j=0$) of this expression is adopted, it yields the Neo-Hookean Strain Energy Function, given earlier in Eq. 2-12; whereas the first two terms ($i=1, j=1$) yield the Mooney Strain Energy Function given in Eq. 2-21.

Ogden [13] proposed an alternative type of Strain Energy Function, expressed in terms of the principal extension ratios, λ_i , instead of strain invariants, I_i and wrote the strain energy function for an incompressible rubber in the form,

$$W = \sum_{i=1}^n \frac{2\mu_i}{\alpha_i^2} (\lambda_1^{\alpha_i} + \lambda_2^{\alpha_i} + \lambda_3^{\alpha_i} - 3) \quad \text{Eq. 2-31}$$

Where n is the order of the energy function and the coefficients α_i and μ_i can again be fitted from experimental data to predict the stress versus strain behaviour.

According to Busfield [14] the derivation of the coefficients for a Rivlin function which includes both I_1 and I_2 terms is difficult. It is necessary to measure the stress terms independently in two orthogonal directions in order to calculate both the $\partial W/\partial I_1$ and $\partial W/\partial I_2$ terms. Evaluation of the relationship between these two functions requires the tests to be performed over a wide range of values of I_1 and I_2 . Such an evaluation is not a straight forward procedure but it can be achieved by allowing λ_1 and λ_2 to vary independently as in the biaxial straining of a thin sheet. The equations

required to determine the values of $\partial W/\partial I_1$ and $\partial W/\partial I_2$ independently of each other are given below,

$$\frac{\partial W}{\partial I_1} = \frac{\frac{\lambda_1^2 \sigma_1}{\lambda_1^{2-1}/\lambda_1^2 \lambda_2^2} - \frac{\lambda_1^2 \sigma_1}{\lambda_2^{2-1}/\lambda_1^2 \lambda_2^2}}{2(\lambda_1^2 - \lambda_2^2)} \quad \text{Eq. 2-32}$$

$$\frac{\partial W}{\partial I_2} = \frac{\frac{\sigma_1}{\lambda_1^{2-1}/\lambda_1^2 \lambda_2^2} - \frac{\sigma_2}{\lambda_2^{2-1}/\lambda_1^2 \lambda_2^2}}{2(\lambda_1^2 - \lambda_2^2)}$$

However, their approach is limited by experimental difficulties as it requires the calculation of the differences between the strains and the stresses, which serves to amplify any experimental errors. Moreover, the experiment is complicated by the fact that rubber is not perfectly elastic. Therefore as Treloar [4] had shown, an inherent lack of reproducibility exists. These effects meant that much of this earlier work completely disregards the small strain behaviour with many workers having measured contradicting data at extension ratios below 4.

In the case of filled materials, the experimental difficulties are more evident due to the phenomenon of imperfect elasticity. James and Green [15] confirmed this for filled elastomers, by showing that $\partial W/\partial I_1$ was much greater than $\partial W/\partial I_2$. The examination of data published by Fukahori and Seki [16] also supports the contention that for filled elastomers $\partial W/\partial I_2$ by comparison with $\partial W/\partial I_1$ was nearly zero. Gregory [17] suggested an approach whereby $\partial W/\partial I_2$ was assumed to be equal to zero. Davies et al. [18] confirmed this observation on a range of carbon black filled materials (Eq. 2-4).

The first condition was not satisfied for unfilled elastomers as Obata et al [19] and Jones and Treloar [20] demonstrated. However, for filled elastomers as Gregory [17], Davies et al. [18], Gough et al [21], and Yeoh and Fleming [22] have all shown, it appears that both conditions were approximately satisfied and a simple relationship between the reduced stress term σ^* and the first strain invariant I_1 exists. Yeoh [23] adopted this approach and proposed the following strain energy function for filled elastomers:

$$W = C_{10}(I_1 - 3) + C_{20}(I_1 - 3)^2 + C_{30}(I_1 - 3)^3 \quad \text{Eq. 2-33}$$

It is well known that this approach predict well the stress strain behaviour of filled elastomers at large strains. Besides, the ability of the function to model large strain behaviour makes it suitable for use in the fracture analysis.

In this section, the methodology for the mechanical characterization of filled elastomer materials has been reviewed. It can be seen that the real problem of materials characterization consist on a simple curve fitting exercise. Power series stored energy functions in both I_1 and I_2 are unsuitable for prediction of the following two particular extension levels: at low extensions ratios below 1.3, where the material becomes progressively softer as the strain is increased; and for extension ratios greater than 2, where the effects of finite extensibility makes the material behaviour stiffen with an increase in the applied strain, without recourse to a large number of terms.

2.2.3. *Strain Energy Functions for use at Hyperelastic Constitutive Models*

This section reviews existing hyperelastic constitutive models, and their ability to capture stress-strain behaviour of rubber. How functions were developed and their basis has been explained in the section 2.2.2. In present section we will focus on the applicability and drawbacks. The most commonly used strain energy density functions [9–11,23–27] have been listed in Table 2.1 (only perfectly incompressible models are included).

The unifying hypothesis of hyperelasticity is the acceptance of the existence of a scalar-valued potential function, the strain energy density function W , which is a function of the strain state, and whose derivative with respect to a particular strain component gives the corresponding stress component. A general approach to hyperelasticity is to assume that the strain energy density is an arbitrary function of the three strain state invariants. Assuming perfect incompressibility of the material, only two of the invariants need be considered. This function may be approximated with a polynomial expansion in two variables. This has been called the Generalized Polynomial model [10,11]. The approach admits a range of complex nonlinear elastic behaviours, but in contrast it has some drawbacks. First, a satisfactory curve fit to find the coefficients C_{ij} is heavily dependent upon data that covers the entire range of multiaxial stress/strain states to be represented, and require a large number of coefficients that have no physical meaning. Second, when the model is used to

predict stresses under conditions not represented in the original experimental data, the results can be highly inaccurate. The model admits unstable strain energy density functions, where an increase in strain results in a decrease in strain energy [1].

Some special cases of the Generalized Polynomial model are quite useful. The Neo-Hookean model is the simplest, with a single term of the polynomial model. Its accuracy is not as great as other models, particularly at large strain levels. A significant advantage is that this model is unconditionally stable. A fit of the model to the stress-strain curve in one strain state is often adequate for predicting stress-strain curves in other strain states, at least for small and moderate strains. In terms of engineering stress and strain, the Neo-Hookean model exhibits a softening curve, typically exhibited by rubbers at low and moderate strains. At large strains, however, the rubber stress-strain curve exhibits stiffening, that model cannot capture [1].

Several models simultaneously exhibit unconditional stability, and capture both the initial softening and subsequent stiffening that is typical of rubber. These include the Arruda-Boyce [25], and Gent [9] models. It is also known the stability of the Yeoh [23,26], model. These models share the assumption that the strain energy density function depends only on I_1 . The Yeoh model is a cubic function in I_1 . There is no physical basis for this model, but fits to observed data from multiple strain states can be achieved quite readily. The Arruda-Boyce model is based on the mechanics of a representative volume element composed of eight non-Gaussian polymer chains. The form is shown in Table 2.1 is a five-term series expansion of the Arruda-Boyce model. This model has two curve fit constants – the initial shear modulus G , and the locking stretch λ_m . The locking stretch is the stretch at which the stress goes to infinity because polymer network chains are fully extended and rigid. The Gent model was also developed to capture phenomenologically the stiffening at high strains due to the finite chain extensibility, and is quite similar in response to the Arruda-Boyce model. A practical disadvantage of the Arruda-Boyce and Gent models is that the precise shape of the stress-strain curve may not be accurately represented, particularly in the case of filled elastomers.

Two final models are the Mooney-Rivlin [10,11] and Ogden [24] models. The Mooney-Rivlin model is a special case of the Generalized Polynomial model, retaining the linear terms in both I_1 and I_2 . The Ogden model is not written explicitly in terms of the invariants. Instead, it is written directly in terms of the principal

stretches. Neither of these models is unconditionally stable, and care must be exercised to check the stability of potential curve-fits. Both models are entirely empirical in nature. When using these models, it is again fundamental that data from multiple strain states be included in the curve fit.

A volume on the subject of rubber constitutive modelling [27] shows that many researchers continue to search for a hyperelastic model that: (i) gives a good fit to observed stress-strain behaviour under multiple strain states, (ii) minimizes the number of curve fit parameters required, and (iii) is physically meaningful. Quite good curve fits can be obtained with existing models, particularly in light of the fact that the resulting residual errors are often smaller than observed inelastic effects that can't be captured by hyperelastic models.

From a phenomenological viewpoint, the differences between hyperelastic models consist in how well each conforms to a particular nonlinear stress-strain curve. A significant problem with these models is that they do not address certain types of history dependence that significantly affect the stress-strain behaviour of rubber. A convincing demonstration of this limitation was reported by Ahmadi et al [28].

Table 2.1 Strain Energy Density Functions for Hyperelastic Constitutive Models.

Constitutive Model Name	Strain Energy Density Function
Neo – Hookean	$W = \frac{1}{2}G(I_1 - 3)$
Mooney – Rivlin	$W = C_{10}(I_1 - 3) + C_{01}(I_2 - 3)$
Generalized Polynomial	$W = \sum_{i=1}^N \sum_{j=1}^N C_{ij} (I_1 - 3)^i (I_2 - 3)^j$
Ogden	$W = \sum_{i=1}^n \frac{2\mu_i}{\alpha_i^2} (\lambda_1^{\alpha_i} + \lambda_2^{\alpha_i} + \lambda_3^{\alpha_i} - 3)$
Gent	$W = -\frac{G}{2} \lambda_m \ln \left(1 - \frac{I_1 - 3}{\lambda_m} \right)$
Arruda – Boyce	$W = G \left\{ \begin{aligned} &\frac{1}{2}(I_1 - 3) + \frac{1}{20\lambda_m^2}(I_1^2 - 9) + \frac{11}{1050\lambda_m^4}(I_1^3 - 27) \\ &+ \frac{19}{7000\lambda_m^6}(I_1^4 - 81) + \frac{519}{673750\lambda_m^8}(I_1^5 - 243) + \dots \end{aligned} \right\}$
Yeoh	$W = C_{10}(I_1 - 3) + C_{20}(I_1 - 3)^2 + C_{30}(I_1 - 3)^3$

* All Models given in this table are incompressible models

2.3. Imperfect Elasticity

The theories discussed earlier assume that rubber is a perfectly elastic material. However, in several cases a significant departure from perfect elasticity takes place. The material shows then a range of imperfect elasticity effects that reduces the accuracy of a stiffness calculation by describing the mechanical behaviour of the elastomer by simple strain energy density function. It is interesting when using strain energy density function to predict the behaviour of a component using a finite element analysis programme to be aware of the significance of the complications. The effects associated with imperfect elasticity are reviewed in this section.

2.3.1. Mullin's Effect

The largest history-dependent effect in most rubber compounds is the Mullins Effect. Mullins [3] studied the transient stress-strain response of rubber under cyclic loading.

Starting with a virgin specimen, Mullins applied a cyclic, quasi-static deformation and recorded the stress-strain response shown in Figure 2.2. On the initial loading, the virgin material exhibits a relatively stiff response. When the material is subsequently unloaded, then reloaded, the stress-strain curve follows a significantly softer path. (In Figure 2.2, loading paths are solid lines; unloading paths are dashed lines.) After several cycles, the stress-strain response stabilizes, and additional cycles follow the same path of the stabilized stress-strain curve. If the previous maximum strain is not exceeded, the effect once it is stabilized will get relatively permanent.

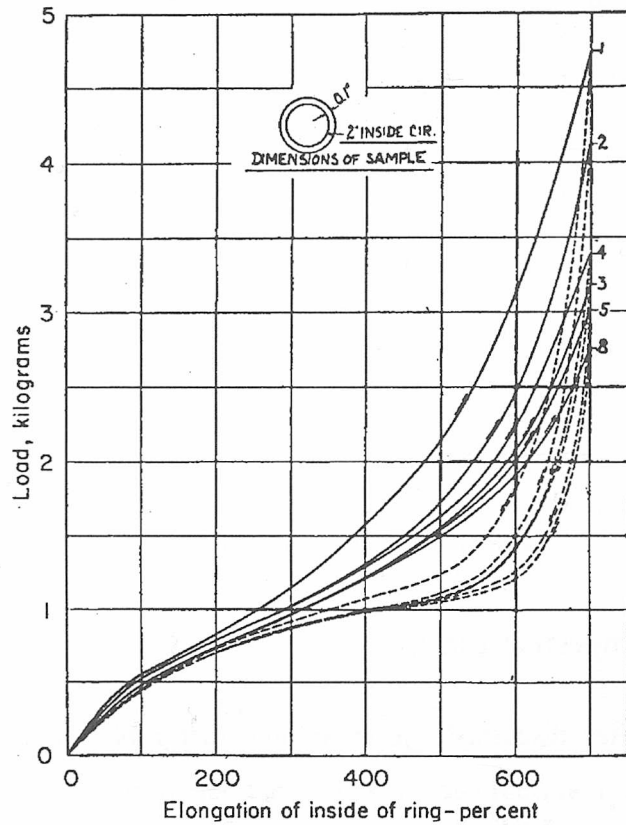


Figure 2.2 Initial transient softening of filled rubber due to the Mullin's effect [3]

It has been reported that leaving it in the unstrained state for a long period, part of the original stress-strain properties can be recovered. Recovery of the Mullins effect has not been properly addressed. The physical phenomena taking place during the Mullin's softening can be recovered with a high temperature [29,30] or a solvent exposure [31]. At room temperature, this healing can be neglected and the Mullin's effect can be considered as a damaging process, as it is introduced in the phenomenological models.

Due to the considerable softening of the nonlinear elastic response, the hysteresis during the first few cycles of loading to a new maximum strain level is much greater than the hysteresis under subsequent steady state cyclic loading. The large initial hysteresis is associated with dissipation of strain energy due to the irreversible break of polymer chains in the elastomer network. As discussed in section 3.2.4, it is believed that this transient dissipative mechanism is beneficial to the strength and fatigue properties of filled rubbers.

When a rubber is characterized for Mullins effect, it is highly important to define maximum strain levels at which will be stabilized. The degree to which rubber is softened depends on the maximum value of the strain experienced during the complete loading history. The larger the maximum strain experienced, the softer the stabilized response.

The importance of the Mullins Effect in the rubber's mechanical response, motivate several researchers to model it in a way suitable for use in continuum mechanics or Finite Element Analysis [32,33]. For example, Simo [34] and Miehe [35] have both introduced the concept of a damage parameter to reduce the stress in a second cycle by a magnitude that reflects the amount of strain seen in the previous loading cycle. Ogden and Roxburgh [32] developed later this idea to produce an isotropic model based upon a strain energy density function. The function is modified by a term that contains a damage parameter to model the softening behaviour. The softener parameter only operates whilst the material is being unloaded, and subsequent loading curves follow the previous unloading path until the previous unloading is exceeded. Once the previous maximum loading is exceeded, the behaviour is described by the unmodified strain energy density function.

The model proposed by Ogden and Roxburgh [32,36] is the widest accepted, having the acceptance of the finite element analysis software's industry and being already implemented in the most popular software (Abaqus, Ansys, LS-Dyna, Nastran). On the approach, the virgin monotonic stress-strain behaviour is modelled using a conventional hyperelastic strain energy density function $\tilde{W}(\lambda_1)$. The Mullins effect is then described as a modification of the monotonic curve, according to:

$$W(\lambda_1, \eta) = \eta \tilde{W}(\lambda_1) + \phi(\eta) \quad \text{Eq. 2-34}$$

$$\eta = 1 - \frac{1}{m} \operatorname{erf} \left[\frac{1}{m} (\tilde{W}_{\max} - \tilde{W}) \right] \quad \text{Eq. 2-35}$$

Where, W is the deviatoric part of the strain energy function of the material. \tilde{W} is the deviatoric strain energy function that arises by regarding the stress-strain curve resulting from monotonic loading of the material (prior to any preconditioning) as non-linear elastic. The maximum value of \tilde{W} achieved in all prior history is denoted \tilde{W}_{\max} .

$\phi(\eta)$ is called the damage function. When solving for the stresses, $\phi(\eta)$ vanishes, leaving only the multiplicative factor η . η scales the monotonic stress to its corresponding steady state cyclic value. The parameters r and m are material constants determined by best fit and subject to the constraints $r > 1, m > 0$.

FEA software developers found interesting to implement the model on their codes. Mars [37] highlighted the interesting features of the model why to work with it on finite element computations:

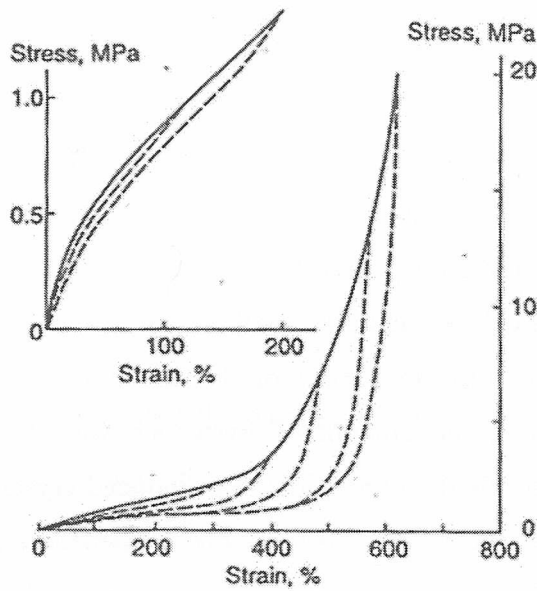
- (i) Simple base hyperelastic model $\tilde{W}(\lambda_1)$ for the monotonic response (i.e. Neo-Hookean), without missing qualitatively realistic, including the stiffening that occurs as the strain approaches its previous maximum value.
- (ii) Only two additional parameters are required, r and m , beyond the base hyperelastic constants, making it interesting to automate the curve fitting.
- (iii) The multiplicative structure of the resulting stress-strain relations seems susceptible to efficient use in a Finite Element implementation.
- (iv) The using of other existing base hyperelastic model of higher accuracy is possible on this model, when additional accuracy would be required.

In contrast, several issues regarding this model remain not resolved. First, the model is based on the assumption that equivalent softening for 3D strain states is achieved according to a criterion of total strain energy density on the monotonic curve. Second, the model assumes that softening occurs isotropically, when stretching a reinforced rubber produces an uneven softening in all directions, and thus creates some anisotropy.

2.3.2. *Hysteresis*

The phenomenon of hysteresis results from the energy loss on stretching and relaxing rubber during a loading cycle. Hysteresis is another complication that is related to the relaxation processes. The energy dissipated during a loading cycle is considered as the area between the loading and the unloading cycle. Examples of which are shown in Figure 2.3, taken from Lindley [38]. For an unfilled elastomer, the magnitude of the energy loss at extension ratios below 3 is quite small. Payne and Whittaker [39] showed that at higher extension ratios in excess of 4 with strain crystallising elastomers, such as natural rubber, the amount of hysteresis was dramatically increased due to the formation and the dissolution of strain induced crystals during the loading cycle. The magnitude of the energy loss is greater in filled elastomers and the amount of hysteresis (energy loss) increases as the amount of particulate filler is increased.

A)



B)

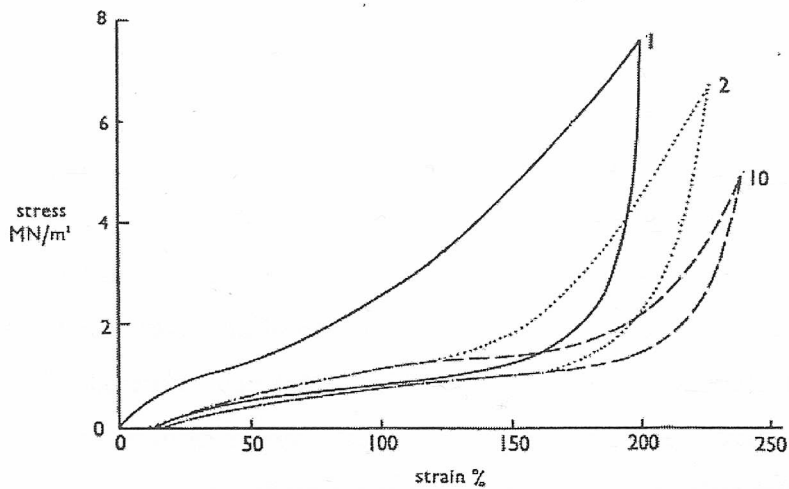


Figure 2.3 Hysteresis loops for natural rubber taken from Lindley [38]. (a) The first cycle loops for unfilled natural rubber extended to various strains and (b) first second and tenth cycle loops for a natural rubber that contains 50 phr of carbon black.

2.3.3. Stress Relaxation and Creep

Stress relaxation is the phenomenon that occurs when an extended vulcanised elastomer sample is maintained at a constant length, and the measured stress in the sample decreases with time. Creep, conversely, is where the elastomer continues to extend under a given load as a function of time. Gent [40] showed that for unfilled natural rubber, similar mechanisms are responsible for both stress relaxation and creep. These mechanisms are also partially responsible for the delayed recovery following the removal of an imposed extension or load. A small proportion of this

recovery is instantaneous, but the remaining small portion takes much longer and may never be complete. The amount of non-recovered deformation is known as permanent set.

These relaxation processes are associated with the internal viscosity of the material, which is a measure of the frictional forces that have to be overcome to make the elastomer molecules slide over each other. These frictional forces introduce a time delay. These creep or stress relaxation phenomena introduce time dependence into the measurement of the mechanical behaviour of an elastomer. It is therefore important that the loading for both tests is applied at roughly equivalent strain rates.

2.3.4. *Dynamic Behaviour*

As has been mentioned due to the imperfect elasticity of material, the strain resultant to an applied force always shows a retarded response. An applied sinusoidal force will result in a measured sinusoidal strain of the same frequency, but displaced in terms of time by a phase shift known as the loss angle. The scale of this phase shift, or loss angle value, depends on the elastomer composition and both the strain amplitude and the test frequency. Figure 2.4 shows mentioned effect, where both the imposed sinusoidal stress functions and the measured strain are plotted along the time axis. The conventional approach which has been reviewed by Kramer, Hvidt, and Ferry [41] to describe this effect is to consider this total response to be represented by an elastic in phase response plus a viscous out of phase response. In shear, for example, both of these terms are then combined to define the complex modulus G^* ,

$$G^* = G' + jG'' \quad \text{Eq. 2-36}$$

where G' is the in phase, 'storage' modulus and G'' is the out of phase, 'loss' modulus. The ratio of these two values is a measure of the phase angle, δ , which is given by,

$$\tan \delta = G''/G' \quad \text{Eq. 2-37}$$

The two Moduli are functions of the frequency. At low frequencies G' approaches the equilibrium shear modulus and G'' becomes very small. This means that the rubber is nearly perfectly elastic at low frequencies. In the case of fatigue it is important to characterize the effect at suitably slow test rates in order to minimise the complications caused by these dynamic effects.

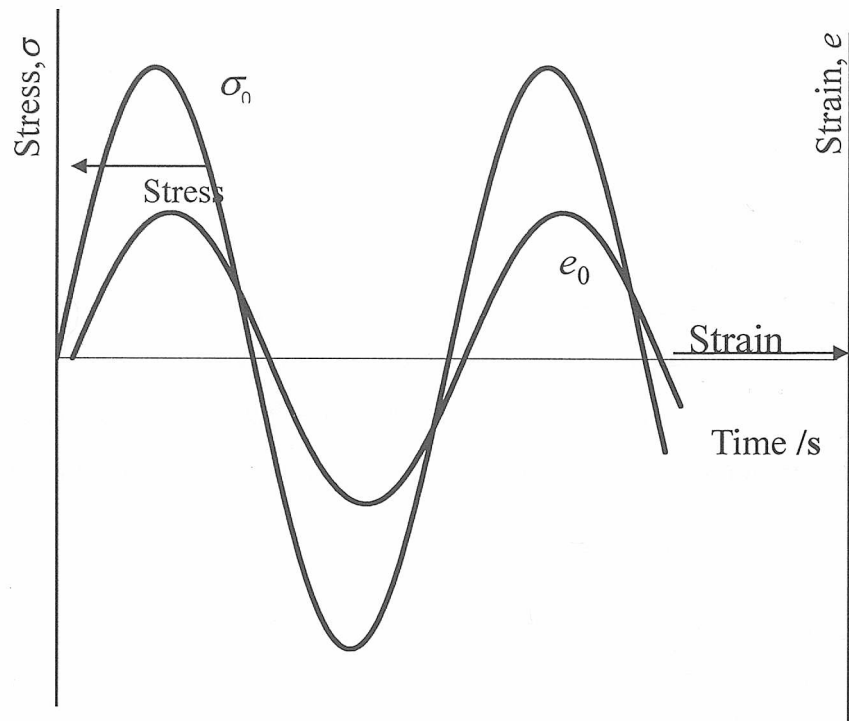


Figure 2.4 A plot taken from Deeprasertkul [42] to demonstrate that the measured strain lags behind the applied stress for a visco-elastic material

2.3.5. Temperature Effect

Rubber materials are sensitive to temperature and this is particularly evident at low temperatures. Like every polymeric material, as the glass transition temperature point, T_g is approached the elastomer becomes harder and more viscoelastic. For unvulcanized natural rubber T_g occurs at around -70°C and at about 1 to 2°C higher for vulcanized natural rubber. This is a reversible situation as the temperature is increased well above the glass transition temperature the material recovers its elastomeric characteristics. Therefore, rubber has the advantage that usage temperature is above its T_g , but in some extreme cases at very low or high temperatures can show a rigid or plastic behaviour respectively [43].

2.3.6. Summary of the effect of imperfect elasticity

It is very difficult to take into account analytically all the complications caused by the imperfect elasticity of the elastomer in a straightforward manner when using a finite element analysis package. However, it is possible to minimise some of the effects remembering mainly following advices. Firstly, ensure that the strain rate of

the test during materials characterization is equivalent to the strain rate applied in the test of the actual component. It is clear that the peak stresses under a displacement controlled cyclic fatigue test will be decreased with the number of cycles, due to the effect called Mullin's. For this reason the approach proposed by Ogden and Roxburgh [32] is applied to quantify the effect of cyclic stress softening. In the present thesis failure due to crack growth phenomena is considered and it is necessary to characterize the behaviour of a filled elastomer as it undergoes a cyclic fatigue test.

2.4. Elastomer Materials

The elastomer materials that are used throughout this thesis are all carbon black filled elastomers. The amount of carbon black is between 60 and 61 parts per hundred of elastomer (phr). The additives incorporated into the elastomer mix during the material compounding process are presented first. This is followed by a discussion of the vulcanisation process for both the material characterization specimens and the components such as the bushes that are going to be tested. It is important that the degree of crosslinking is consistent between the test piece and the actual component. The equilibrium swelling techniques used to measure the degree of crosslinking are reviewed. Finally the test methods that are adopted to measure the material properties and the actual component stiffness values are described.

2.4.1. Material

The materials used in this study were carbon black filled elastomers. One is natural cis-polyisoprene (NR) and the other one is a blend of SBR and BR, we will name them respectively as MCN and MSB. Those Compounds are typically used in engineering anti-vibration applications and were provided by CIKAUTXO S.Coop. The recipes were designed to withstand fatigue loading and present good behaviour against the growth of the crack. In the two materials selection similar stress versus strain behaviour was sought, and was achieved. Both compounds are materials that incorporate relatively high tear resistance carbon black N-539. This filler is added primarily to increase the stiffness, the strength and the tear resistance of the resulting compound. The fatigue life is increased with the carbon black structure size, and with the decrease of specific surface area. The amount of carbon black almost doesn't

vary from one compound to other with the objective to obtain a resultant material with similar strength and hardness, varying from 60 to 61 phr. This allowed a evaluation between different materials but with similar stiffness and static behaviour. The compounding formulations including the mass fractions of carbon black are given for each elastomer used in this thesis in Table 2.2.

The compounds presented in this work were vulcanised with sulphur crosslinking systems. A vulcanisation system between conventional and semi-efficient was adopted, which uses adequate accelerators to increase the rate of the cross-linking process and reduces the amount of elemental sulphur. This is commonly used in commercial compounds as it is suitable for injection moulding components. The addition of the accelerator has the dual effect of increasing the scorch time, defined as the time before the vulcanisation process begins and reducing the time to achieve a state of optimum cure. This allows the material to be heated up prior to injection for a sensible length of time to facilitate the polymer flow during the injection cycle without the material crosslinking before it reaches the mould cavity. A reduction in the amount of sulphur in the system reduces the amount of compound degradation, named as reversion effect. Reversion occurs when the elastomer is cured beyond the optimum cure time. The optimum fatigue life is obtained with a 2.5 sulphur/accelerant ratio. Nevertheless, this optimum ratio is not a universal value, and is slightly variable with the recipe, antidegradant type, rubber type and additive type.

The other additives incorporated during the mixing phase include: antioxidants, that provide resistance to oxidation and heat; antiozonants, that provided resistance to ozone induced surface cracks; and plasticisers that can be incorporated to either facilitate processing or to impart some particular physical property in the vulcanised part. The formulations for each of the materials used here are given in Table 2.2 (some specific and special ingredients have been omitted).

Table 2.2 Recipe for both rubber compounds: MCN (Natural Rubber) and MSB (SBR + BR).

Ingredient	MCN (PHR)*
NR (10CV60)	100
Carbon Black N539	60
Zinc Oxide (Reaction activator)	
Antiozonant	10
Sulfur, elemental (Cross linking agent)	4

Ingredient	MSB (PHR)*
SBR 21% styrenic content	70
BR 97% CIS	30
Carbon Black N539	61
Zinc Oxide (Reaction activator)	3
Rubber Antioxidant	
Antiozonant	7
Sulfur, elemental (Cross linking agent)	4

*Parts per hundred rubber, by weight

Table 2.3 It is summarized in a table the sulfur and accelerant relationship that defines the type of sulphur vulcanization system of a rubber compound.

Sulfur Vulcanization System	SULFUR (PHR)*	ACCELERANT (PHR)*
Conventional	2.0 - 3.5	0.3 - 1
Semi-Efficient	1.0 - 2.0	1.0 - 2.5
Efficient	0.25 - 0.7	2.5 - 5

*Parts per hundred rubber, by weight

2.4.2. Vulcanisation Processes and Test Specimen Manufacture

Transformation process used for material vulcanization was injection moulding for the pure shear sample and real component. On the other hand, uniaxial compression specimens were transformed by compression mould process.

The vulcanisation time for each compound was extrapolated from curing time determination test, Oscillating Disk Rheometer (ODR), which works according to the ASTM D2084 standard [29]. As a result we get a chart where the vertical axis is a measure of the torque required to oscillate a rotating disk in a heated rubber filled cavity, and the horizontal axis is the time. From these charts the vulcanisation time for each compound was derived as the time required for the torque to reach its maximum value for the temperature at which the test was undertaken. These chosen vulcanisation times are given in Table 2.5, Table 2.6, Table 2.7. Car exhaust mount, real component, injection moulding process conditions.

After vulcanization the crosslink density is measured to ensure we have get during transformation process the desired crosslink density in the rubber. Test samples are used to test and characterize the material that feed finite element analysis softwares to give prediction of the real component. It is of great importance to have the confidence of have been working with samples of same crosslink density than real component.

2.4.2.1. Crosslink Density Measurement

Crosslink density measurement has a dual objective, to check the material consistency within a mix batch, between batches, or between different samples. In our case, principally the objective is to check consistency between samples and components, as all have been obtained from the same batch. In a cross-linked polymer the presence of an interconnected network make impossible the permeability of a solution, but immersion in a 'solvent' result in swelling. This equilibrium swelling in cyclohexane solvent had been used to determine the crosslink density.

The determination of equilibrium swelling volumes is one of the best methods for characterizing cross-linked structure. The rate of swell, as well as the equilibrium swell of a vulcanized in a solvent has been seen to be function of cure state. Either the molecular weight between crosslinks or its reciprocal, the number of effective network chains per unit rubber volume may be used as cure state index. The cure degree is usually determined applying the Flory-Rehner formula [44]:

$$\overline{M}_c = \frac{\rho V_0 (V_r^{1/3} - V_r/2)}{-\ln(1 - V_r) - V_r - \mu V_r^2} \quad \text{Eq. 2-38}$$

where ρ is the density of the material (rubber formulation), V_0 is the molar volume of solvent, μ is the value of the rubber-solvent interaction parameter and V_r is the polymer volume fraction in the swollen vulcanize, which is a function of the swollen rubber mass, dried rubber mass, density of the formulation and density of the solvent used to swollen the sample.

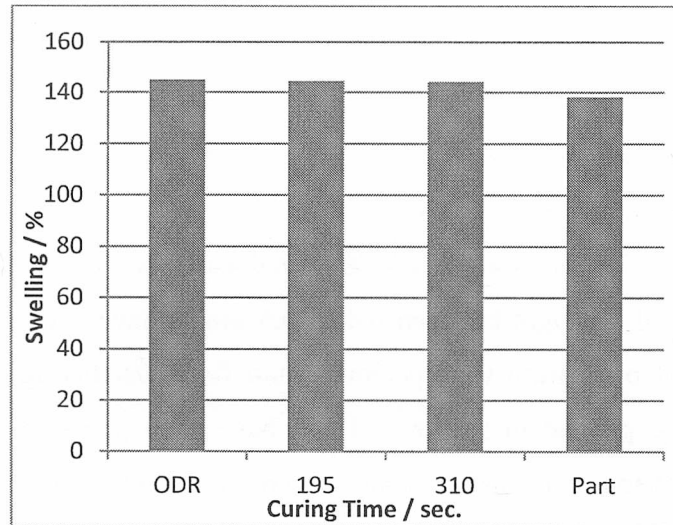
Due to the complexity of above mentioned procedure has been decided to use only the value of the swelling degree [45], which can be calculated from the weight of the

sample (m_0) before immerse it into the solvent, and after the immersion of them into a solvent for a period of time (m_1). For measuring the m_1 , samples have been taken out from the solvent, and the outer surface of the sample has been dried in a tissue paper before measuring its weight. Thus, swelling degree has been defined as:

$$\% \text{ swelling} = [(m_1 - m_0)/m_0] * 100 \quad \text{Eq. 2-39}$$

Samples of a weight between 0.4 to 0.5 grams have been cut from the component. Then, cut parts from test specimens and from Oscillating Disk Rheometer (ODR) sample (explained in section 2.4.2.2) have been prepared. All of them have been immersed into 6 ml ciclohexane solvent, and kept there for 24 hours. To properly work this technique a thermodynamically good solvent is required, and is recommendable to use a common solvent for both materials. The samples were weight before and after immersion into the solvent. From the weight difference the swelling degree is computed using the Eq. 2-39. Results have been considered adequate resulting in a minimum swelling rate in the range of 90-100% and a low evaporation rate.

A)



B)

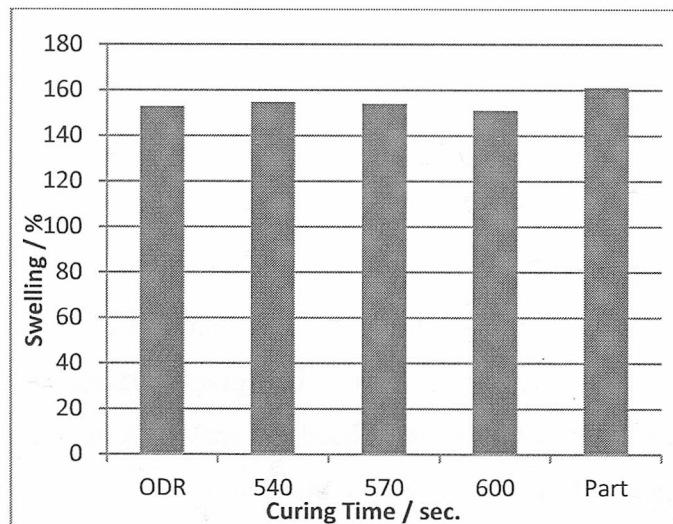


Figure 2.5. Swelling measurement results are plotted for pure shear test sample at different curing times and exhaust mount component, along with sample obtained from ODR test used as pattern of optimum curing level. There are plotted the results of both materials: A) MCN material; B) MSB material

2.4.2.2. Test Samples and Exhaust Mounts Moulding Process

Planar tension test pieces are obtained by injection moulding. The sample is a rectangular flat sheet with thick round ears on long length edges to facilitate the clamping system. Simple tension specimens were die cut from the flat area of the planar tension sample. The main advantage of getting both test specimens from the same pure shear sheet is to ensure we will have same cure degree in both testing geometries. Compression test sample have been manufactured by compression

moulding system. Platens were electrically heated to a temperature that was maintained by a temperature controller. Transformation process conditions are detailed in Table 2.5, Table 2.6.

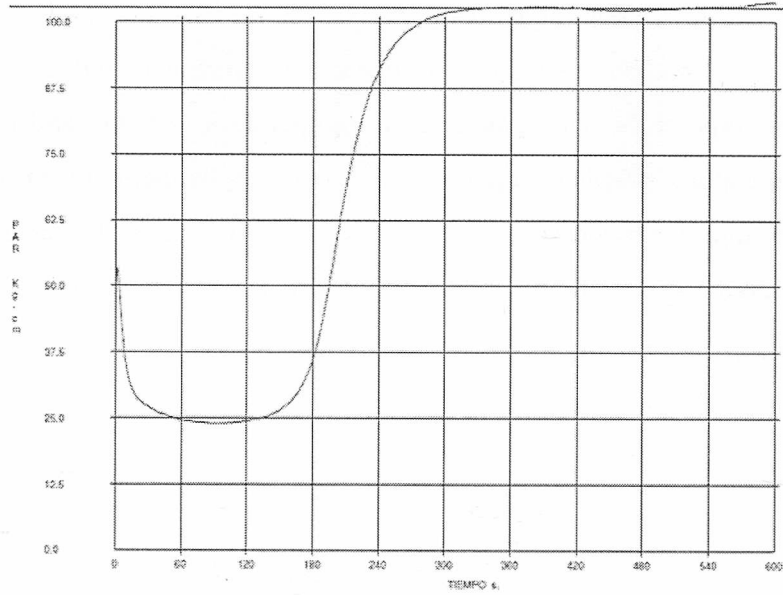
The real components worked with on this PhD thesis, the exhaust mount, have been transformed by injection moulding process. The injection has been performed over a prototyping mould under very precise control of injection parameters. The most important parameters to get a proper and homogeneous vulcanization are curing time and temperature. The mould cavity temperature is critic, and apart of programmed temperature of plates operator controls the temperature in the cavity at every injection. The residence time is defined depending of the measured temperature in the cavity. Injection process conditions are detailed in Table 2.7.

Defining the manufacture process parameters for a rubber material from which we do not have any information or experience requires additional information. We can get the required information from the Oscillating Disk Rheometer (ODR) test. The ODR works according to the ASTM D2084 standard [29]. The sample is located into a temperature controlled die cavity, where a bi-conical disk is located. A rotor oscillates the disk working in a sinusoidal way, at a frequency of 1.57 Hz and amplitude of 3 degrees. The opposition to the torque that suffers the oscillating disk due to the rubber material in between two sides is monitored over time. ODR measures not only the scorch or induction period, also the state and rate of cure, the torque versus time graph show how cure is proceeding. The torque level can be correlated to the degree of crosslinking. The test output TC (90) defines the optimum cure time, as the time required for the torque to reach 90% of the maximum achievable torque and relates to the time necessary for the cured rubber to achieve optimal properties. The conventional vulcanization system shows reversion in all the cases, while the torque force for semi-efficient vulcanization system shows a plateau. In the case of both materials we are working with on the project have shown a plateau (Figure 2.6). Not showing any reversion, the definition of curing time of material for different thickness geometries has been simplified. Knowing there is not risk of reversion, vulcanization time has been lengthened enough to ensure we haven't got miss-vulcanized component or specimen. Table 2.5 to Table 2.7 show the principal transformation process parameters for specimens and component.

Table 2.4 ODR measurement results to determine specimen and component curing time, to define transformation process curing time.

	Temperature (°C)	TC(90) (sec.)	Reversion
MCN	160	253	No
MSB	170	362	No

A)



B)

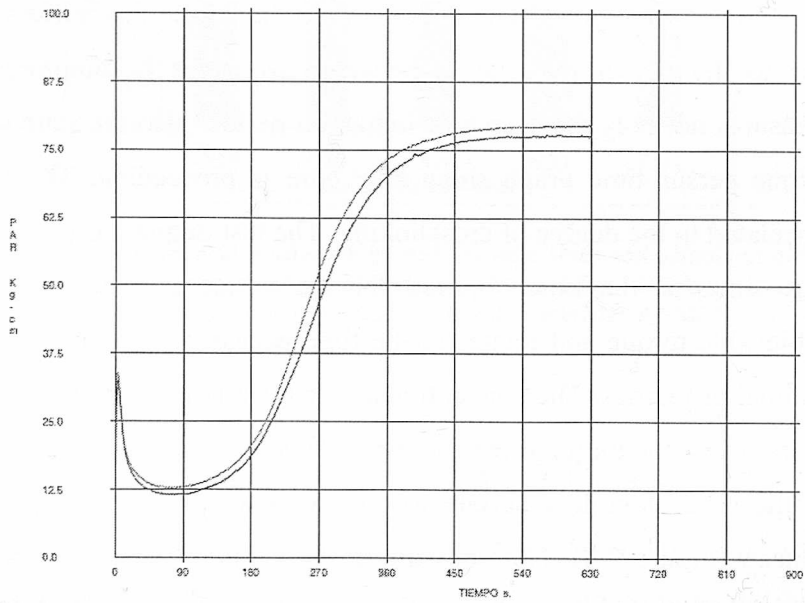


Figure 2.6 Oscillating Disk Rheometer (ODR) test, according to the ASTM D2084 standard, for both A) MCN and B) MSB materials.

Table 2.5. Planar tension sample injection moulding process conditions.

	Programmed Mould Temp. Upper Plate (°C)	Programmed Mould Temp. Lower Plate (°C)	Measured Mould Temp. Upper Plate (°C)	Measured Mould Temp. Lower Plate (°C)	Curing Time (sec.)
MCN	170	170	162	162	300
MSB	180	180	170	170	500

Table 2.6. Compression moulding process conditions for simple compression samples.

	Programmed Mould Temp. Upper Plate (°C)	Programmed Mould Temp. Lower Plate (°C)	Measured Mould Temp. Upper Plate (°C)	Measured Mould Temp. Lower Plate (°C)	Curing Time (sec.)
MCN	170	170	160	160	420
MSB	180	180	170	170	600

Table 2.7. Car exhaust mount, real component, injection moulding process conditions.

	Programmed Mould Temp. Upper Plate (°C)	Programmed Mould Temp. Lower Plate (°C)	Measured Mould Temp. Upper Plate (°C)	Measured Mould Temp. Lower Plate (°C)	Curing Time (sec.)
MCN	162	160	150	152	600
MSB	182	182	170	171	600

2.5. Material Stress Strain Behaviour

2.5.1. Test Procedure for Monotonic Characterization

Multiple modes of deformation are required to assess the material constants that define the hyperelastic stress-strain relationship in quasi-static conditions, Figure 2.8. Nevertheless, monotonic characterization has been performed over three samples from where can readily be achieved three independent strain states like simple tension, planar tension (sometimes also called “pure shear”), and simple compression. In the case of incompressible materials, some modes of deformation theoretically provide the same information. In particular, the following modes of deformation:

- Uniaxial Tension and Equibiaxial Compression
- Uniaxial Compression and Equibiaxial Tension
- Planar Tension and Planar Compression

These equivalences hold as long as any hydrostatic pressure superimposed to any stress field arising in the specimen does not affect the deformation field. The concept is shown in Figure 2.7. It is interesting the point that the equivalence between equibiaxial tests and compression tests when an equibiaxial test rig is not available.

Treloar[4] observed the equivalence of uniaxial tension and equibiaxial compression states. Since rubber is, to a reasonable approximation, incompressible, hydrostatic stress does not affect the state of strain, and hence can be added arbitrarily to enforce boundary conditions without affecting equilibrium. For uniaxial compression tests, sample dimensions should be chosen to minimize any bulging (edge effects) of the rubber disc, which would indicate a non-uniform strain state. Bulging is further minimized by the lubrication (for example by silicone based grease) of the two horizontal platens used in this test. The dimensions of the simple compression rubber disc used in the project are 17mm diameter and 25 mm height. To achieve the simple compression state, the test specimen needs to be compressed between two platens without any friction effects between the platens and the specimen. ASTM D395 type specimen is used in ASTM 575 Standard Test Methods for Rubber Properties in Compression.

Table 2.8 summarize the stress and stretch states associated with each specimen used. In addition, Figure 2.8 illustrates each specimens stress and stretch states.

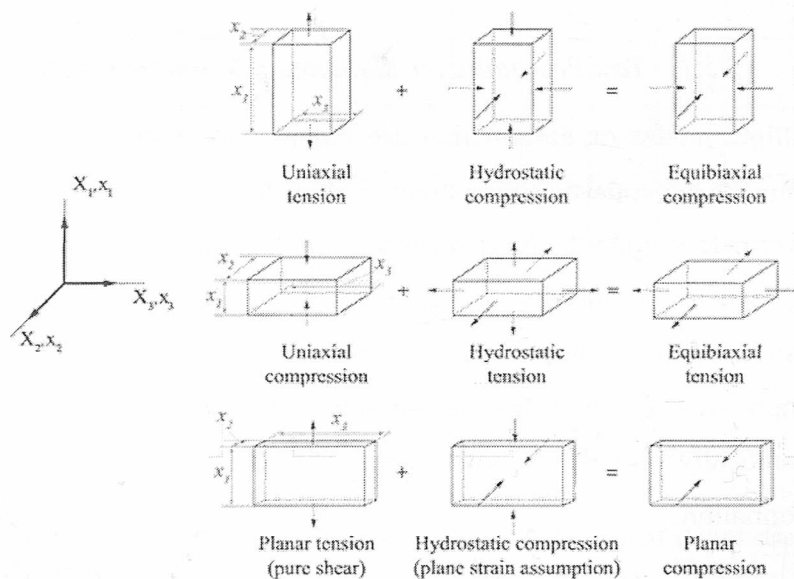


Figure 2.7 Equivalence of stress states shown by superposition of hydrostatic pressure. Adapted from Bhashyam [46]

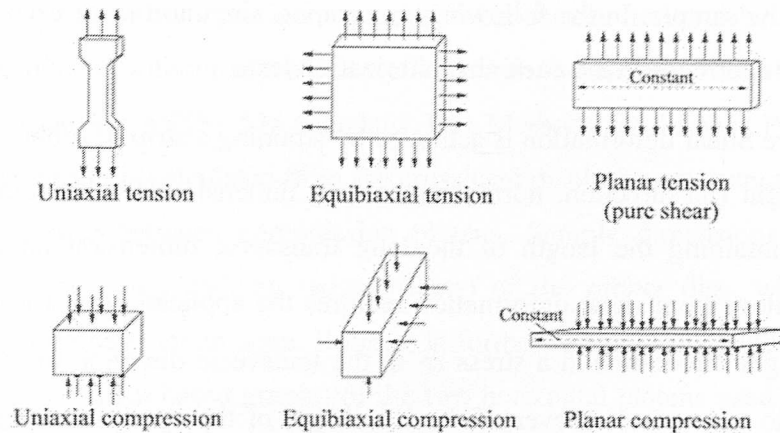


Figure 2.8 Schematics of uniaxial tension/compression, equibiaxial tension/compression and pure shear. Adapted from Bhashyam [46]

Table 2.8 Stretch states used in stress-strain characterization of rubber

	λ_1	λ_2	λ_3
Simple Tension	λ	$\lambda^{-1/2}$	$\lambda^{-1/2}$
Planar Tension	λ	1	$1/\lambda$
Simple Compression	λ^{-2}	λ	λ

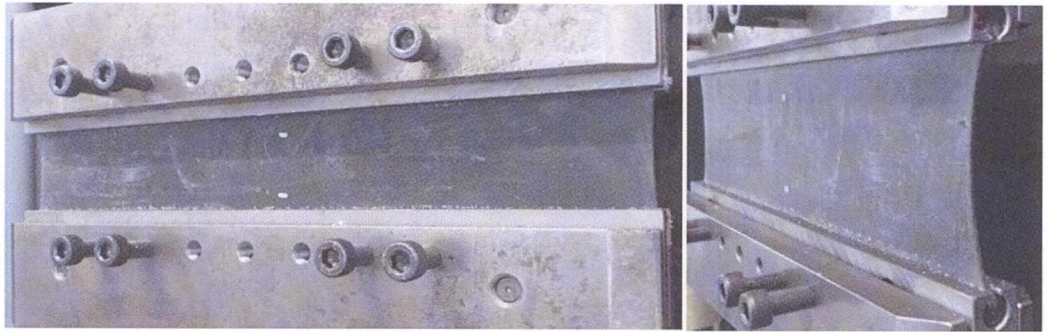
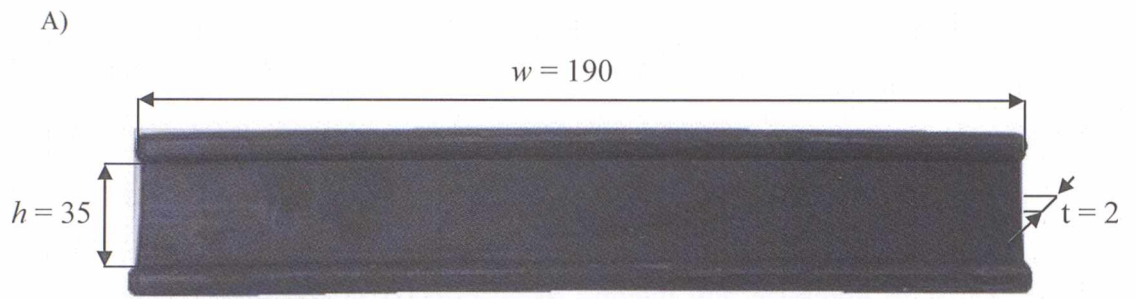
In the monotonic characterization testing initial, transient, and cyclically stable stress-strain responses were recorded at eight levels of peak strain, at each of the three strain states. All testing, for both monotonic and cyclic loading, were conducted in strain control at a strain rate of 1% strain/sec. Reflective tape affixed to specimen surfaces or white marks were used to mark the gauge length in simple and planar tension, and strains were measured continuously via video-extensometer. In planar tension has been verified that crosshead movement and strain suffered by component are linearly related during first 100% strain. Nevertheless, characterizing above 100% strain requires mandatorily the strain to be measured by an extensometer. In case of simple compression, strain is calculated from the crosshead displacement output divided by the initial gauge length measured between compression platens. The test fixtures and gripping arrangements are shown in Figure 2.9. Tests were conducted at lab temperature, nominally 20°C. For cyclic material relaxation tests, a fully relaxing straining condition was used ($R_\epsilon = \epsilon_{\min}/\epsilon_{\max} = 0$). Actually, the unloading is performed until a negligible positive force value to avoid the buckling

of the sample. In the following paragraphs, singularities of each test will be detailed to better understand each characterization test.

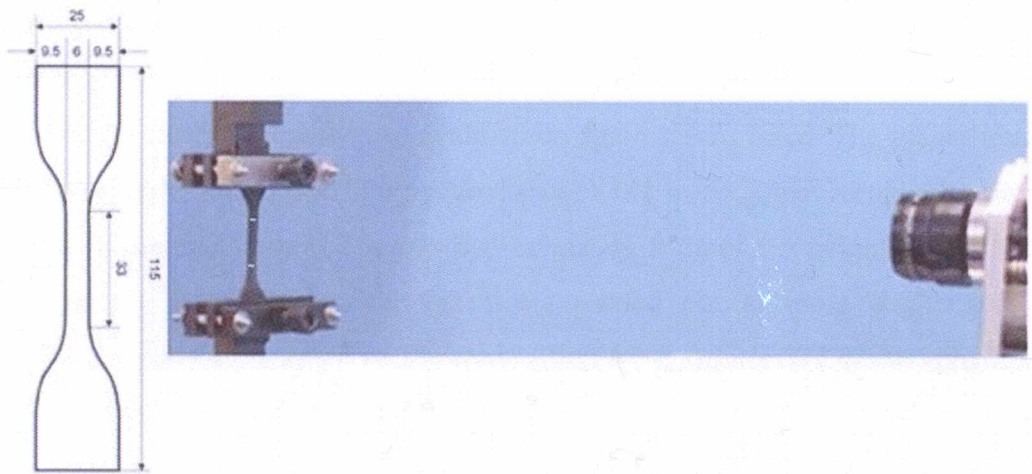
Pure Shear deformation is achieved by straining a strip of rubber (Figure 2.9.A) in its height (l_0) direction, normal to its long dimension, to an extension ratio λ_1 , while maintaining the length of the long transverse dimension unchanged ($\lambda_2=1$). To achieve pure shear deformation requires the application of a tensile stress σ_1 in the height direction and a stress σ_2 in the transverse direction to maintain an extension ratio of $\sigma_2=1$. However, if the length (w) of the specimen is more than 6 times its height, then the direct application of a transverse stress is not required, as the required stresses are automatically generated as a result of the restraints induced by the specimen grips. Except in the vicinity of the free edges, the state of strain in such a test piece is one of substantially uniform homogeneous pure shear. To avoid any slippage, the grips had to be carefully tightened. This tightening is always accompanied by a small change in the zero force due to a compressive force on the elastomer generated by the grips. This compressive force was balanced off by moving the cross-head slowly to again attain again a zero force. The planar tension test-pieces were vulcanized into nominal size of $188 \times 35 \times 2$ mm rectangular shapes. Therefore the specimen width was approximately 8 times the height of the rubber between the grips. Monotonic tests were carried out at room temperature by imposing extension at a rate of 1%/strain using MTS Bionix 370.02 Servohydraulic Test Machine with a 15 kN load cell.

Simple tensile test-pieces were stamped from flat part of planar tensile specimens using an ASTM D412, type C dumbbell die. As mentioned previously reflective tape affixed to specimen surfaces of white marks were inserted on the reduced section of the specimen, equidistant from the centre and perpendicular to the longitudinal axis, as shown in Figure 2.9.B. The specimen is marked under zero tension, at a gauge length of 25 mm. The thickness was taken as the average of 3 measurements by Vernier caliper. The range of the thickness measurement was typically 2.0 mm. The width of the specimen was typically 6.0 mm. The tensile tests to acquire stress versus strain curves at the 5th cycle were performed on an MTS Bionix 370.02 Servohydraulic Test Machine with 500 N load-cell. The strain is homogeneous in the central parallel portion of the dumbbell and care should be taken to grip the dumbbell. A video-extensometer was used to measure the strain.

To achieve the simple compression state, the test specimen needs to be compressed between two platens without any friction effects with the platens. ASTM D395 type specimen is used for ASTM 575 Standard Test Methods for Rubber Properties in Compression. Strain is calculated from the crosshead displacement output divided by the initial distance between compression platens. Sample dimensions should be chosen to minimize any bulging (edge effects) of the rubber disc, which would indicate a non-uniform strain state. Bulging is further minimized by the lubrication (for example by silicon based grease) of the two horizontal platens used in this test. The dimensions of the simple compression rubber disc used in the project are 17mm diameter and 25 mm height as can be shown in Figure 2.9.C. Tests were performed on an MTS Bionix 370.02 Servo-hydraulic Test Machine with 15 KN load-cell.



B)



C)

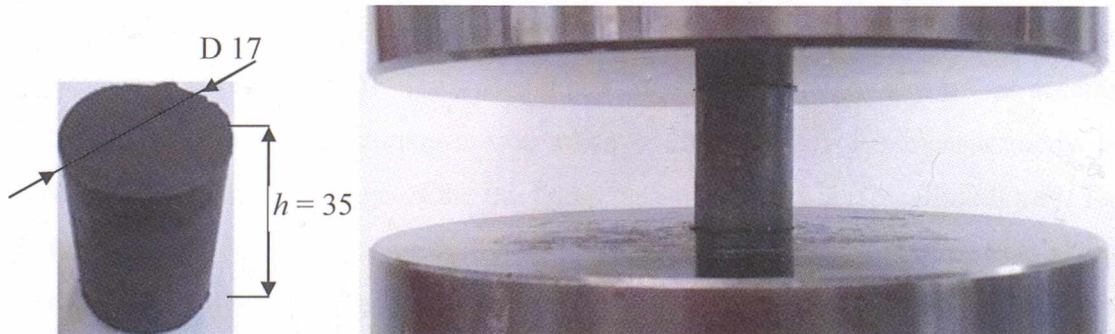


Figure 2.9 Test Samples and gripping of each strain state characterization testing set-up: A) Planar tension. B) Simple Tension. C) Simple compression.

2.5.2. Stress Strain Behaviour

The monotonic loading curves obtained in simple tension, planar tension, and simple compression tests are observed in Figure 2.10. The observed ranking at a given strain is a bit below the typical, that can be predicted from linear elasticity, where $\nu=0.5$, $\sigma_{ST}/\sigma_{ST}=1$, $\sigma_{PT}/\sigma_{ST}=1/(1-\nu^2)=1.333$, and $\sigma_{SC}/\sigma_{ST}=1/(1-\nu)=2$. σ_{ST} is the stress in simple tension, σ_{PT} is the stress in planar tension, and σ_{SC} is the stress in simple compression. The resulting sets of stress-strain curves in simple tension, planar tension, and simple compression, for cyclically stable conditions ($N = 5$) at eight peak strain levels are shown in Figure 2.12. The Mullins effect has a similar influence in all three strain states. A reduction in peak stress can be observed from the initial loop and the remaining reloading loops. It is interesting to note that, at lower strain levels, the softened curve go close to the virgin curve. At higher strain levels, the peak cyclic stress of the softened curve at $N = 5$ is lower than the monotonic loading curve. The physical meaning or reason should be the rapid initial growth of pre-existing flaws at high strain level and/or enhanced viscoelastic stress relaxation at large strains.

Another peculiarity is the small residual strain that remains after unloading the sample. The residual strain appears to depend on the peak strain achieved during the loading, and is stabilized typically after the first three to ten loadings of each level. The residual strain effect may have similar origins of strain softening, as it is suggested to be induced during the same loading events that result in strain softening. It is believed that the strain softening effect is associated with the presence of fillers in the rubber, and their influence on network chain breakage (section 2.3.3).

In the case of cyclic loading, the stress-strain curve does not follow a unique path, as predicted by perfect hyperelastic theories. Depending on the maximum strain experienced on the previous strain the subsequent loading follows the previous unloading path. All reloads show a double curvature which initially starts to soften and then stiffen. Then unload starts in an almost vertical manner, in an immediate drop in stress at the beginning. Anyway, the relative ranking on cycling loading of simple, planar, and compression, or equivalent biaxial, results are similar to the previously described monotonic case, which is shown in the graph of Figure 2.10.

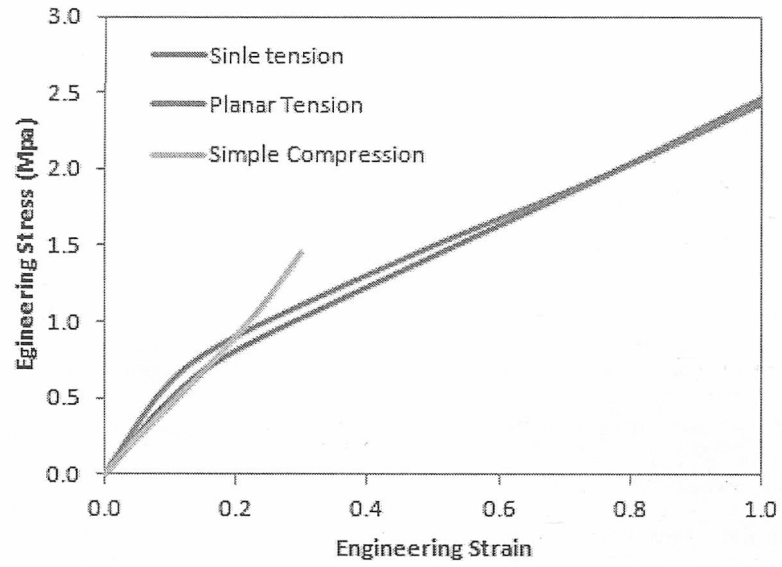


Figure 2.10. Monotonic stress-strain behaviour curves in simple Tension, Planar Tension and Simple Compression

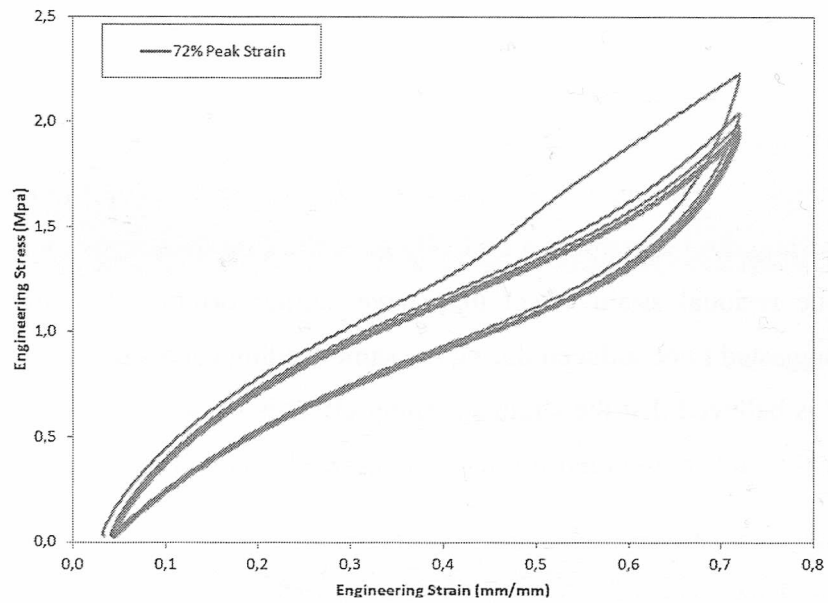
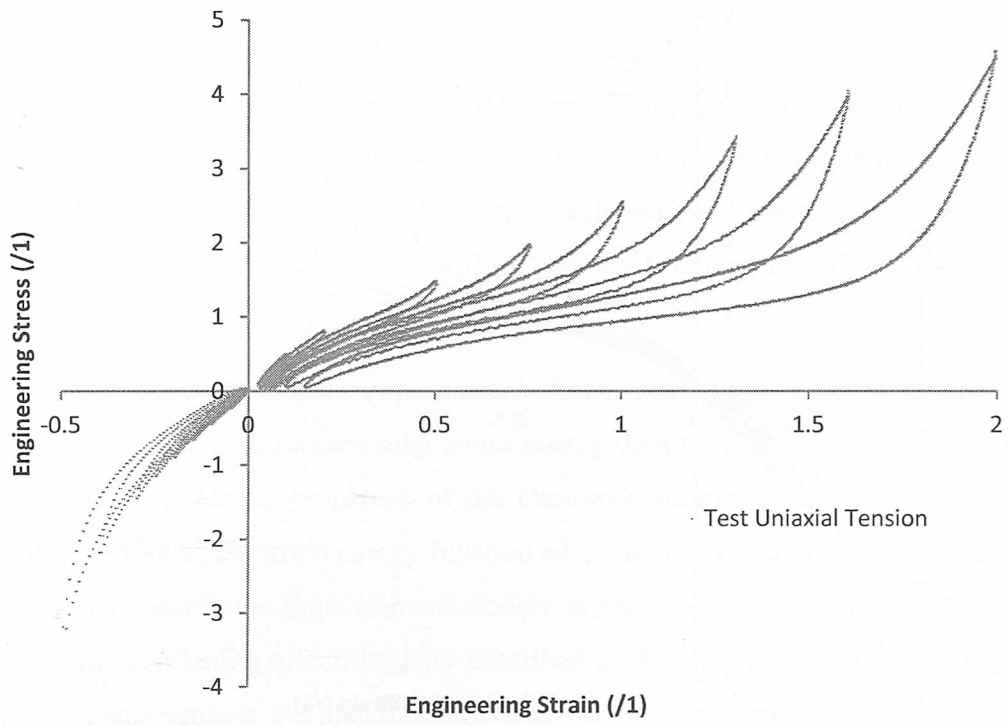
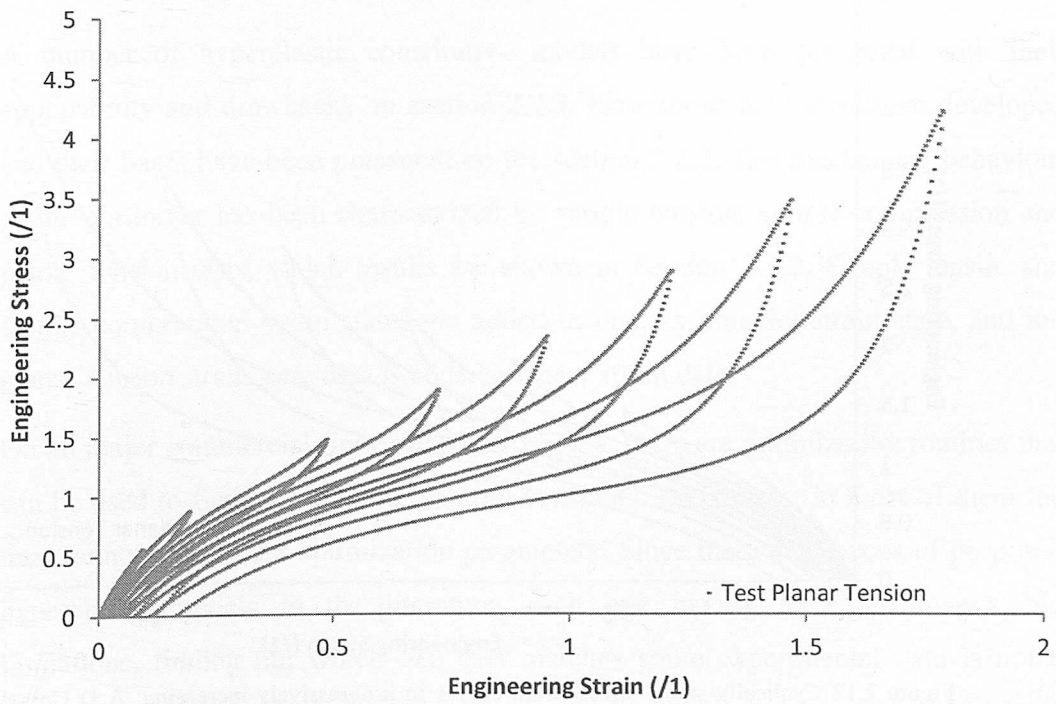


Figure 2.11. Stabilization of stress-strain curves after five cycles. Results generated in planar tension at 75% strain.

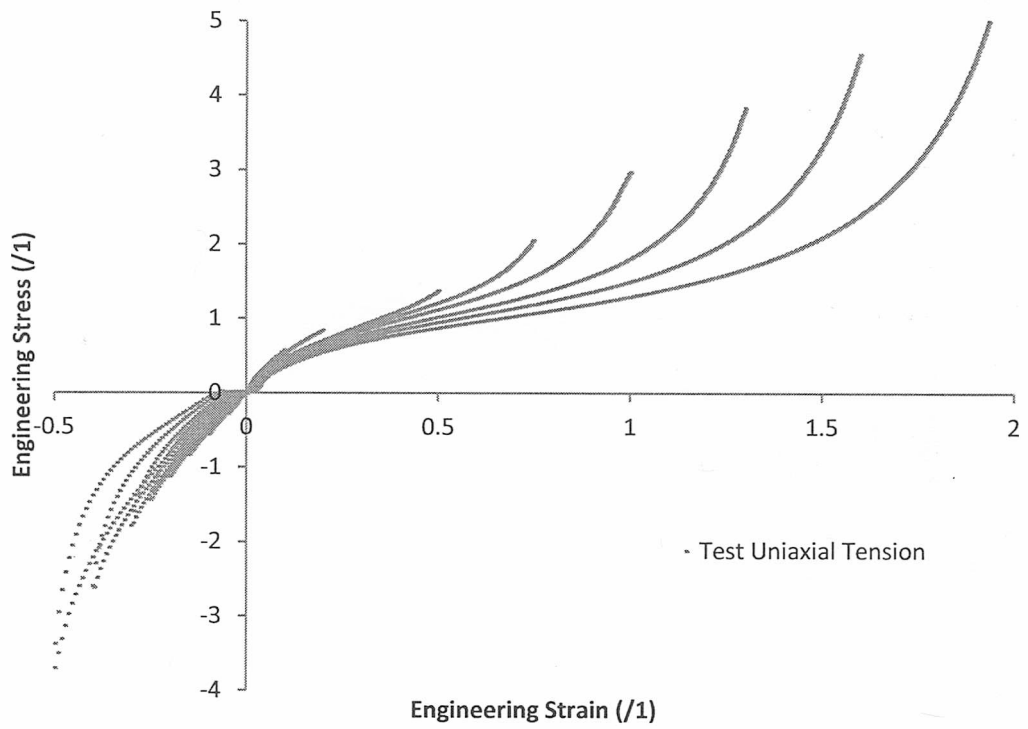
A.1)



A.2)



B.1)



B.2)

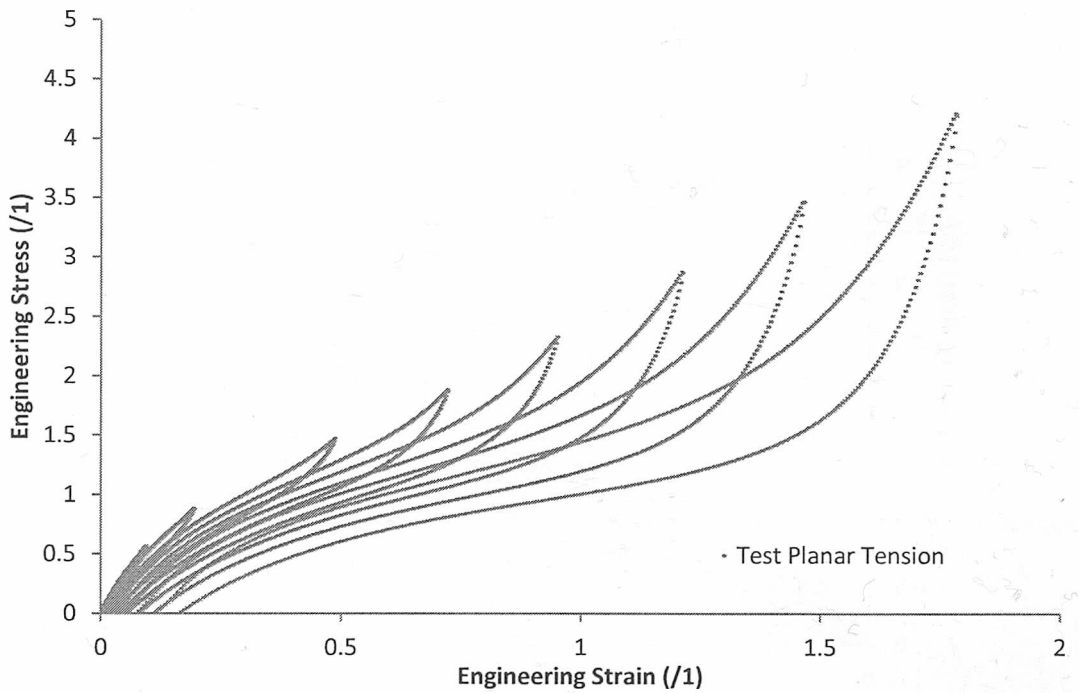


Figure 2.12 Cyclically stable stress-strain curves in progressively increasing: A.1) Uniaxial Tension (Simple Tension and Simple Compression), MCN material; A.2) Planar Tension, MCN material; B.1) Uniaxial Tension (Simple Tension and Simple Compression), MSB material; B.2) Planar Tension, MSB material.

2.6. Materials Constitutive Models Curve Fitting

The rubber materials modelling present a challenge because of the characteristic large strain behaviour of the material. At large strains, geometric and material non-linearity exists. Several constitutive theories for large elastic deformations based on strain energy density function have been developed for hyperelastic materials as mentioned in Section 2.2.3: the Neo-Hookean, the Mooney, the Rivlin, the Ogden and the Yeoh strain energy density functions.

To run this type of analysis, experimental data is required in order to acquire the material coefficients for a particular strain energy density function. It is necessary to characterize the elastic properties of the elastomer appropriately. This has been a non-trivial task as the strain energy function adopted must be capable of handling the strains that occur in the finite element models. A second complication arises from the cyclic stress softening effect, initially described by Mullins [3], whereby during the cyclic fatigue process the material behaviour becomes progressively less stiff from cycle to cycle.

2.6.1. Hyperelasticity

A number of hyperelastic constitutive models have been presented with their applicability and drawbacks on section 2.2.3. How those functions were developed and their bases have been presented on the section 2.2.2. The mechanical behaviour of the elastomer has been characterized by simple tension, simple compression and planar tension tests, which results are shown in Section 2.5.2. Simple tensile and simple compression strain states are added in one, as uniaxial strain state, and the planar tension strain state data is added as shear strain data.

On all major commercial finite element software, there are optimization routines that can be used to find hyperelastic material constants. Regardless, in most of them the user cannot control the optimization parameters. Since there are dozens of proposed hyperelastic models in the literature, each one having their advantages and limitations, finding out which one best matches some experimental data is not a straightforward task. HyperFit is a software package developed under Matlab[®] whose objective is simplifying the choice of a hyperelastic model and the determination of its constants for a particular material. It consists on a number of routines that apply

non-linear least squares methods on experimental data to find optimized constants for a given model. Besides the standard curve fitting procedure, where the results of a single test are used to determine constants, HyperFit offers the possibility of multi-criteria optimization, meaning that different test results can be simultaneously used for optimization. The fitting of the data has been done by Hyperfit. After having checked the curve fitting plot of all models presented, Reduced Polynomial or Yeoh 3rd order model have been decided to use. This approach predicts the stress-strain behaviour of filled elastomers well at large strains, and the ability of the function to model large strain behaviour well makes it suitable for use in the fracture analysis problems.

The coefficients (C_{10} , C_{20} , C_{30} ,) obtained by the regression to experimental data, with the Eq. 2-40 for the two materials of the project are summarized in Table 2.9.

$$W = C_{10}(I_1 - 3) + C_{20}(I_1 - 3)^2 + C_{30}(I_1 - 3)^3 \quad \text{Eq. 2-40}$$

Table 2.9 Yeoh 3rd Order material model functions coefficients for MCN and MSB materials

	C_{10}	C_{20}	C_{30}
MCN	0.58279	0.036058	-0.0002158
MSB	0.7613	0.017187	-0.00010976

2.6.2. Mullin's Effect Model Fitting

The Mullins law is used to define how the elastomer material stress-strain behaviour depends on the most extreme prior loading event. Peak strain levels at which material will be stabilized have been defined first. Maximum strain value is of great importance. Softening occurs whenever the load increases beyond its prior peak value. The degree to which rubber is softened depends on the maximum value of the strain experienced during the complete loading history. The larger the maximum strain experienced, the softer the stabilized response.

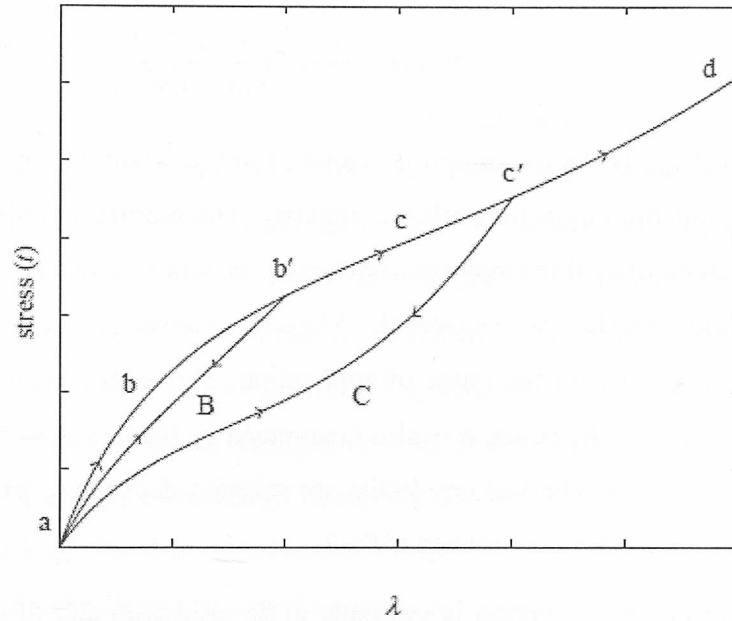


Figure 2.13 Schematic loading-unloading curves in simple tension (Mullins effect) [32]

The importance of the Mullins Effect in the rubber's mechanical response, cause several researchers to model it in a way suitable for use in continuum mechanics or Finite Element Analysis [32,34,47]. The model proposed by Ogden and Roxburgh [32,36] is the most accepted, and is implemented in all major commercial finite element analysis software (Abaqus, Ansys, LS-Dyna, Nastran). This kind of models has been classified as pseudo-elastics.

Ogden and Roxburgh [32] produced an isotropic model based upon a strain energy density function. The function is modified by a term that contains a damage parameter to model the softening behaviour. The softener parameter only operates whilst the material is being unloaded, and subsequent loading curves follow the previous unloading path until the previous unloading is exceeded. Once the previous maximum loading is exceeded, the behaviour is described by the unmodified strain energy density function. On the approach, the virgin monotonic stress-strain behaviour is modelled using a conventional hyperelastic strain energy density function $\tilde{W}(\lambda_1)$. The Mullins effect is then described as a modification of the monotonic curve, according to $W(\lambda_1, \eta)$, Eq. 2-34. The equation that is implemented in finite element software differs from original Ogden – Roxburgh in the damage variable, η . The equation implemented in Ansys is,

$$\eta = 1 - \frac{1}{r} \operatorname{erf} \left(\frac{\tilde{W}_{max} - \tilde{W}_0}{m + \beta \tilde{W}_{max}} \right) \quad \text{Eq. 2-41}$$

Where \tilde{W}_{max} is the maximum previous or initial strain energy, and W_0 is the strain energy for the virgin hyperelastic material. The modified Ogden-Roxburgh damage function requires three material constants r , m , and β . When $\beta=0$, the original Ogden-Roxburgh model is recovered. Material constants have to be selected to ensure $\eta \in (0,1)$ over the range of application. This condition is guaranteed for $r > 0$, $m > 0$, and $\beta \geq 0$; however, it is also guaranteed by the less strict limits $r > 0$, $m > 0$, and $(m + \beta W_m) > 0$. The last one limits are solution-dependent, have to be ensured that the limits for η are not violated if $\beta < 0$.

The Mullins effect option is available to be used with any of the nearly- and fully-incompressible isotropic hyperelastic constitutive models of Ansys (TB, HYPER options with the exception of TBOPT= BLATZ or TBOPT= FOAM), and modifies the behaviour of those models. Mullins effect option is claimed by command TB, and has to be set to TBOPT=PSE2, and three material parameters r , m , and β , are introduced as shown next.

```
TB,CDM,1,,3,PSE2      !Modified Ogden Roxburgh pseudo-elastic
TBDATA,1,1.5,1.0E6,0.2  !Define r, m, and beta
```

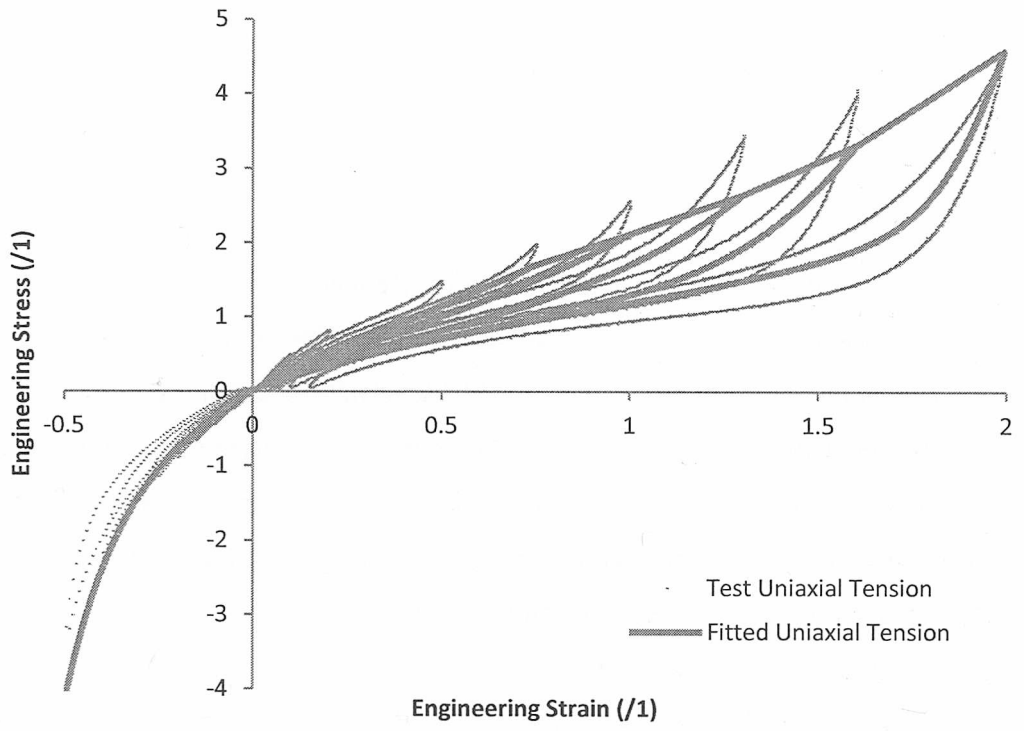
In the same way the Mullins effect option is also available in Abaqus. The Mullins effect model can be defined by specifying the Mullins effect parameters. The user subroutine UMULLINS can be used. The parameters r , m , and β of the Mullins effect can be given directly as functions of temperature and/or field variables.

- Input File Usage: *MULLINS EFFECT
- Abaqus/CAE Usage: Property module: material editor: Mechanical > Damage for Elastomers > Mullins Effect: Definition: Constants

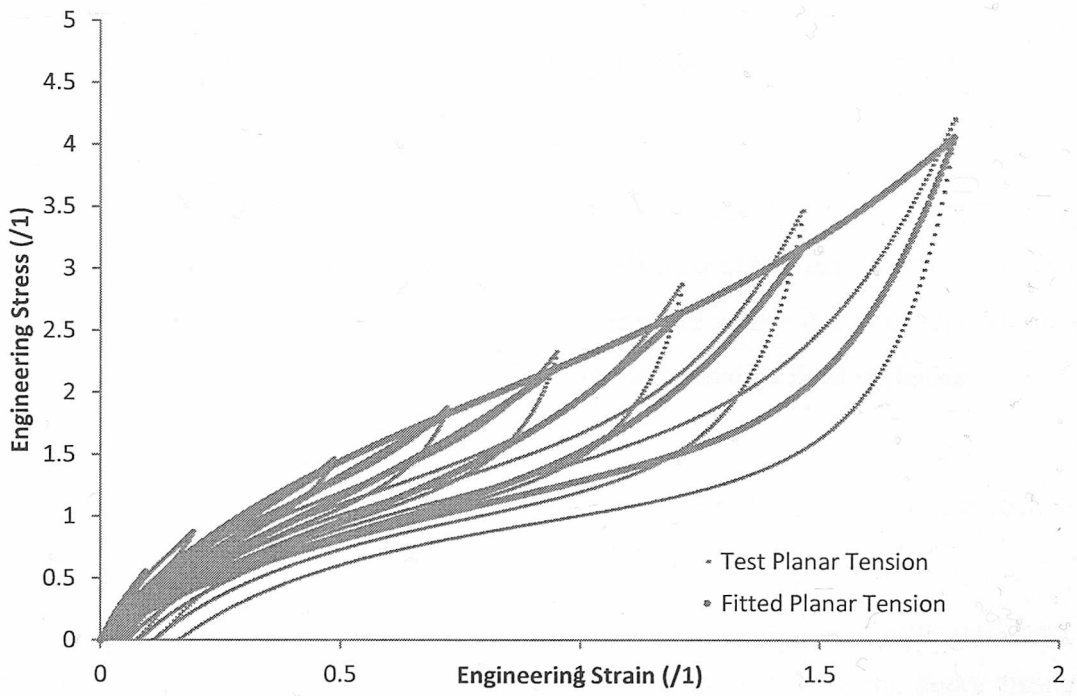
Routines dedicated to this task exist on all major finite element software packages. Nevertheless, in most cases the user has little or no control over the curve fitting process. Furthermore, those functionalities are often restricted to few pre-selected hyperelastic models, and there is no direct way of comparing the results yielded by different modelling choices. HyperFit is a code developed to help minimizing difficulties selecting the model that best fit a particular test curve. Non-linear least

squares methods are applied to match theoretical curves with user provided experimental data, resulting in optimized material constants. The code allows multi-criteria optimization, so that the analyst can optimize the constants against more than one type of experimental data. The fitting has been carried with the primary curve defined by the topmost stress strain data point for each stabilized peak strain level (the fifth cycle of each of eight strain levels). The three strain states at once have been fitted to Yeoh of third order or Reduced Polynomial constitutive model, computing from there the coefficients C_{10} , C_{20} , C_{30} . Once the hyperelastic behaviour has been fitted the dissipative term and softening parameter have been computed for the Ogden-Roxburgh model for considering the pseudoelasticity. The unloading data of the fifth stabilization cycles at each of strain level have been incorporated for the fitting. The multi-criteria optimization is run again to determine the Mullins parameters r , m , and β . Some restrictions have been enforced to the fitting process $r > 1$, $m > 0$, and $0 < \beta < 0.5$. The results of the fitting are plotted in the Figure 2.14 with their correlation with stabilized unloading curves of three strain states. Similarly, Mullin's law parameters obtained by modified Ogden-Roxburgh damage function parameters r , m , and β that define the Mullin's effect behaviour of both materials, MCN and MSB are summarized in the Table 2.10.

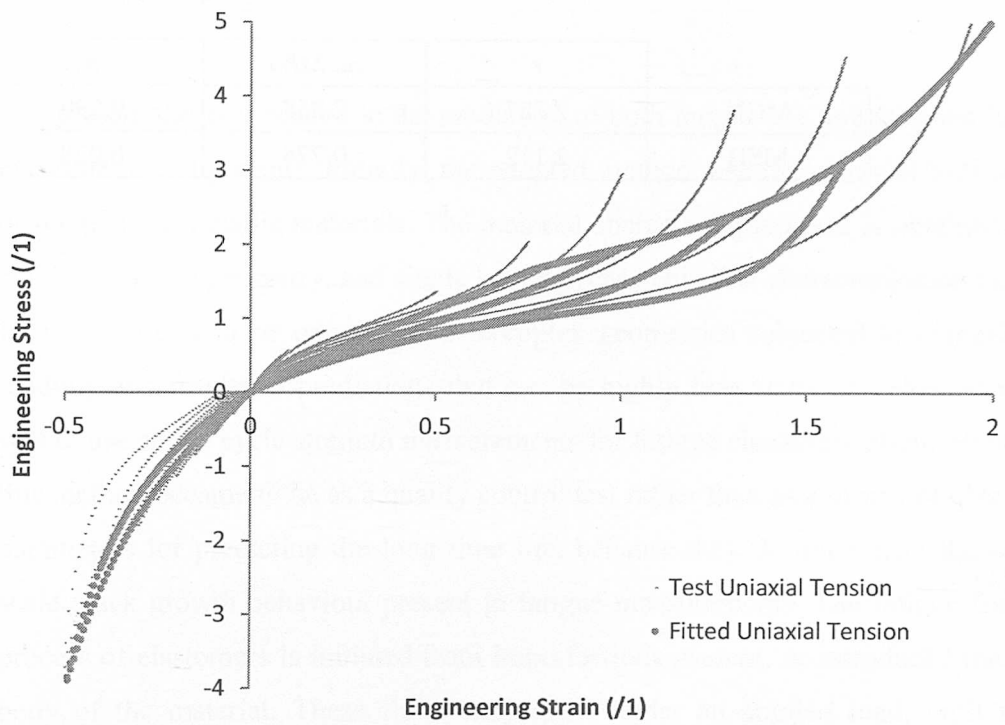
A.1)



A.2)



B.1)



B.2)

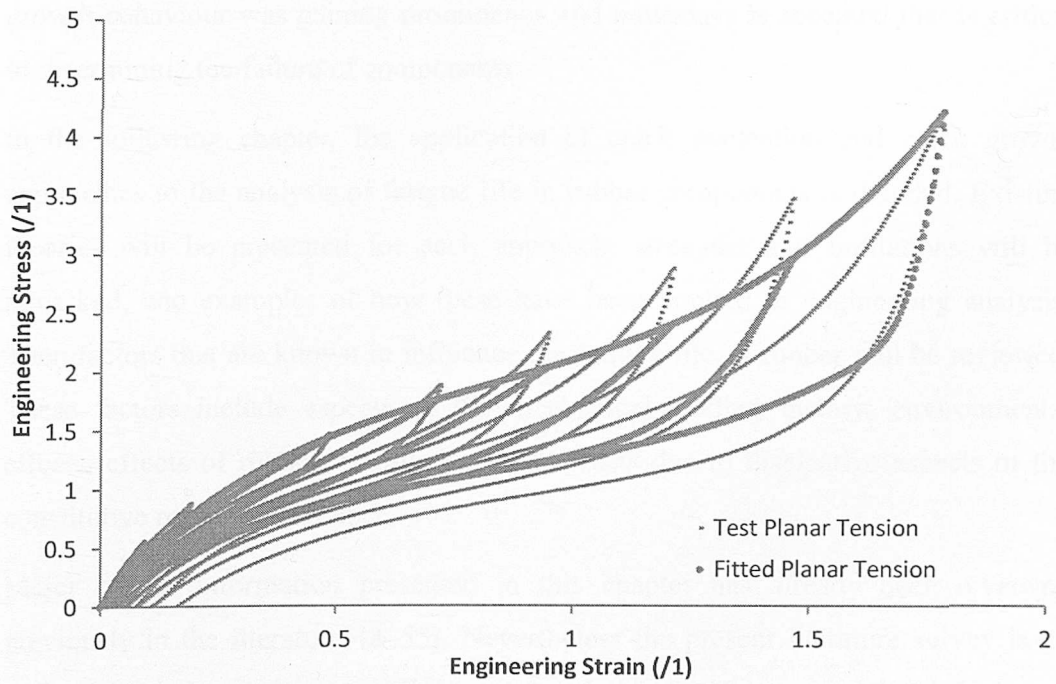


Figure 2.14 Fit of Mullins law to a series of cyclic stabilized unloading curves in planar tension, simple tension and simple compression. Data for both materials: A.1) Uniaxial Tension (Simple Tension and Simple Compression) of MCN material; A.2) Planar Tension of MCN material; B.1) Uniaxial Tension (Simple Tension and Simple Compression) of MSB material; B.2) Planar Tension of MSB material.

Table 2.10 Mullin's law parameters obtained by modified Ogden-Roxburgh damage function parameters r , m , and β that defines the Mullin's effect behaviour of both materials, MCN and MSB

	r	m, MPa	β
MCN	2.287	2.258	0.290
MSB	2.112	0.774	0.028

3. Rubber Fatigue

The present thesis is related to the prediction of both fatigue life and stiffness loss of elastomeric components. Initially, the adopted method was the classical S-N curves developed for metallic materials. The material characterization data is obtained from single test piece geometry, and single loading type. This first characterization method later was found to be unreliable for complex geometries subjected to complicated loading, and results in predictions that can be highly inaccurate. Another approach was to use single cycle strength measurements for fatigue characterization. Similarly, this method became to be as a quality control test rather than as a means of obtaining parameters for predicting the long time life, because they do not reflect the small-scale crack growth behaviour present in fatigue measurements. The fatigue fracture process of elastomers is initiated from imperfections present, or introduced into, the body of the material. These flaws may grow under an applied load, until a big fracture occurs, that leads to the component failure or fracture. Therefore, the crack growth behaviour was gaining prominence and nowadays is accepted that is critical in determining the failure of components.

In the following chapter, the application of crack nucleation and crack growth approaches to the analysis of fatigue life in rubber components is detailed. Existing theories will be presented for each approach, strengths and limitations will be remarked, and examples of how these have been applied in engineering analysis. Then factors that are known to influence the fatigue life of rubber will be reviewed. These factors include aspects of the mechanical loading history, environmental effects, effects of rubber formulation, and effects due to dissipative aspects of the constitutive response of rubber.

Major of the information presented in this chapter has already been reviewed previously in the literature[48–55]. Nevertheless the present literature survey is an update of existing reviews, to reflect recent and previously unnoticed developments.

3.1. Fatigue Life Approaches of Rubber

Engineers need to model fatigue life early in the design process. The development of finite element simulation software satisfied the necessity of calculation of stress and strain histories in complex geometries [56–58]. This section reviews analysis approaches that are currently available for predicting fatigue life in rubber. There are two general approaches. One, focused on predicting crack nucleation life, given the history of quantities that are defined at a material point, in the sense of continuum mechanics [59]. Stress and strain are examples of such quantities. Second, is based on ideas from fracture mechanics, focused on predicting the growth of a particular crack, given the initial geometry and energy release rate history of the crack [60].

3.1.1. Crack Nucleation Approach

Crack nucleation approach is based on quantities that are defined at each material point in the sense of Continuum Mechanics. Consider that a fatigue life of rubber material has an intrinsic life determined by the history of stresses or strains.

The nucleation life may be defined as well as the number of cycles required to a crack of certain size appears: Le Cam [61] has defined in 2 mm and 1 mm for Mars [54] Saintier [62], Ostoja-kuczynski [63]. Indeed, the stiffness decrease can be correlated with the number of cycles required to cause the appearance of a crack of a certain size. Saintier et al. [64] estimated the percentage of the fatigue life spent in propagating the fatigue crack from 100 - 200 μm initial flaw size to a critical size of 1 mm. The fatigue life spent is an 80% of total life.

The earliest known study of this type was August Wöhler's work with railroad axles in the 1867 [65]. A similar analysis approach was applied to rubber by Cadwell in 1940 [66], and remains in use today [67]. The approach is particularly appropriate in applications where the initial flaws are several orders of magnitude smaller than component features, and where the multiaxial stress state of the component can be appropriately related to the stress state under which material fatigue characterization tests were conducted. It is also appropriate when crack location is part of the unknowns. This implies to identify the pertinent mechanical parameters controlling multiaxial fatigue life.

The most used fatigue life parameters for rubber crack nucleation include maximum principal strain (or stretch), the maximum principal Cauchy stress and strain energy density, among others. Strain is a natural choice because it can be directly determined from displacements. When strain energy density is applied to fatigue analysis in rubber, it is often estimated from a hyperelastic strain energy density function, which is defined entirely in terms of strains. Nevertheless, the efficiency of those parameters unifying multiaxial fatigue data and modelling fatigue life reinforcement in rubber is considered limited [54]. Only scalar equivalence criteria had been applied in rubber, and being a scalar quantity, it does not provide a specific orientation of potentially occurring cracks. Mars [54] and Saintier [61,68] proposed at the same time, without knowing each other's work, two approaches extending the concept of critical plane, classically applied to metallic materials, to rubber fatigue.

Saintier considered both damage and reinforcement mechanisms observed in elastomers. More precisely, the maximum normal stress acting on the critical plane, defined by the plane experiencing the maximum principal stress over a cycle, was considered to control the fatigue damage evolution. Furthermore, the reinforcement mechanism was related to the minimum crystallinity level on the critical plane during a cycle.

Mars [37,69] proposed a new predictor, referred to as the cracking energy density, by considering that the nucleation of macroscopic fatigue cracks is the consequence of the propagation of microscopic defects initially present in the virgin material. The proposal emphasized two important features: critical plane and energy release rate.

In an attempt to improve Mars theoretical foundation, Verron and Andriyana [70] adopted the Configurational Mechanics theory; more precisely, authors related the energy released during defects growth to the properties of the configurational stress tensor. Nevertheless, further works are required in order to fully establish a rigorous connection between energy release rate and this continuum parameter.

In general, an ideal multiaxial fatigue model have to be robust, sensitive to load phasing and mean stress, and applicable to variable amplitude loading. Another important characteristic is the ability to consider crack closure effects. The mentioned parameters are briefly explained below. Parameters preferred for the critical plane approach are explained on the specifically developed section.

3.1.1.1. *Maximum stretch ratio*

Most of rubber fatigue experiments are conducted by displacement; therefore, is a natural choice to relate fatigue life to strain measurements. Furthermore, it was widely observed that cracks initiate in a plane normal to the maximum tensile strain. Cadwell et al., [66]; Fielding [71] investigated fatigue life of rubber for different stretch levels in both uniaxial extension and shear; they showed that for elastomers which crystallize under strain (such as natural rubber), increasing minimum stretch can significantly improve the fatigue life. The improvement goes to a maximum value at a moderately high strain level (200%), beyond which additional minimum strain decreased the life.

Fatigue life under conditions of simple and equibiaxial tension was investigated by Roberts and Benzies [72] and Roach [73]. They have shown an expected result, fatigue life, under maximum principal stretch (or strain), is longer in simple tension than in equibiaxial tension. Nevertheless, the difference was pronounced for Natural Rubber (NR), and much less pronounced in Styrene Butadiene Rubber (SBR). Ro [74] reanalysed the data from these studies, using other strain-based parameters, including octahedral shear strain, and maximum shear strain, concluding that none of these parameters is optimal for unifying simple and equibiaxial tension data.

3.1.1.2. *Maximum principal Cauchy stress*

Andre' et al. [75], Abraham et al. [76], Saintier et al. [64] correlated fatigue life with the maximum principal Cauchy stress. In fact, the authors adopted this predictor in order to investigate fatigue life improvement due to crystallization in rubber under non-relaxing tension cyclic loading condition. In general, for constant maximum stress level, fatigue life is observed to increase when the minimum stress is strictly positive. Under simple torsion, Andre' et al. [75] showed that cracks orientation is perpendicular to the direction of the largest principal Cauchy stress; consequently, they suggested that this predictor may be the appropriate local variable to describe multiaxial fatigue damage. Nevertheless, Abraham et al. [76] inferred that the maximum principal Cauchy stress cannot be used to predict fatigue life of elastomers.

3.1.1.3. *Strain Energy Density*

In the late 1950s and early 1960s, success with crack growth models [77–89] had a significant impact on the subsequent development of the nucleation life approach in rubber. After the development of fracture mechanics for rubber, strain energy density came into use as a parameter to predict fatigue crack initiation [53]. Previously, the independent variables in fatigue studies were alternating and minimum tensile strain, or stretch

Strain energy density may be considered as a measure of the energy release rate of naturally occurring flaws. The energy release rate is proportional to the product of strain energy density (far from the crack tip), and the crack size [88,90,91]. The conditions under which strain energy density may be uniquely related to the energy release rate of naturally occurring flaws are limited. For the relationship to hold, it is assumed that crack growth is self-similar, that the far-field strain gradient across the crack is negligible, and that the stress state is one of simple tension. The relationship can be understood as a crack that suddenly opens in an infinite medium, which is in a state of simple tension, and the energy released is proportional to the original strain energy density times the volume over which the strain energy is relieved due to the crack. However, the crack has to be aligned to the direction of straining or not more than one axis of straining has to be active, otherwise not all of the strain energy near the crack faces could be released.

Roberts and Benzies [72], and Roach [73], found that for both Natural Rubber and SBR, when compared based on equal strain energy density, equibiaxial tension fatigue life was longer than simple tension fatigue life. This ranking is opposite of that found when compared on the basis of maximum principal strain. Roach proposed a hypothesis that gave the best correlation between simple and equibiaxial tension fatigue data. He proposed that differences could be explained by considering only that portion of the strain energy density that was available for flaw growth. For simple tension, that all of the strain energy density is available. For equibiaxial tension, that only one half of the strain energy density is available for flaw growth.

From the theoretical standpoint, a scalar measure like strain energy density does not predict the fact that cracking appears in a specific orientation. In addition, the strain

energy density cannot be a general measure of energy release rate, since the energy released depends on how the flaw is oriented with respect to the strains.

3.1.1.4. Critical Plane Approach and Equivalent Parameters

The critical plane approach is based on physical observation that fatigue cracks initiate and grow within material on certain privileged planes called critical planes. The corresponding failure is supposed to be due to the stress, strain or energy histories acting on these planes. The critical plane is then determined by identifying material plane which maximizes the combination of relevant fatigue damage parameters, or results on a prediction of minimum life. This approach enjoyed a great deal of success in metals, but only few studies use the critical plane approach to predict fatigue failure in rubber materials. This is mainly due to the fact that multiaxial loading effects in rubber, which often undergoes large strain loading conditions, are not yet well understood, as concluded by Mars and Fatemi [54].

The efficiency of those fatigue life parameters unifying multiaxial fatigue data and modelling fatigue life reinforcement in rubber was revealed initially limited [54]. This was because only scalar equivalence criteria had been used in rubber, being a scalar quantity, they does not provide a specific orientation of potentially occurring cracks. Mars [54] and Saintier [62,68] to account the lack of the scalar parameters proposed, at same date but independently, two approaches based on the same concept. Classically applied to metallic materials, they extended the critical plane concept to rubber fatigue. Later, Verron and Andriyana [70] adopted the Configurational Mechanics theory in an attempt to improve Mars theoretical foundation; based on the same critical plane concept, authors related the energy released during defects growth to the properties of the configurational stress tensor (configuration mechanic criteria). More detailed explanation of last developed approaches and parameters are detailed in the following sections.

3.1.1.4.1. Cracking Energy Density

The inability of the strain energy density to unify multiaxial fatigue life predictions can be explained by the fact that, in complex loading and geometries only a portion of the strain energy density is available for flaw to grow. Approaches that attempt to take into account the energy release rate of microscopic defects in order to render microscopic phenomena were previously investigated by Rivlin and Thomas [77],

Greensmith [86], Lindley [92], Young [93]. They related the tearing energy, i.e. the energy release rate of Griffith [94], to the strain energy density for classical fracture mechanics of rubber test specimens. This approach was extended to multiaxial loading conditions by Mars [54] through the concept of cracking energy density. As mentioned previously, this parameter represents the portion of the total strain energy density that is available to be released. Mars [54] also introduced the critical plane concept in the context of elasticity, and postulated the increment of available energy to be released on a given material plane. The energy is defined as the dot product of the Cauchy traction vector σr (σ being the Cauchy stress tensor) with the increment of strain in the r -direction (direction of the normal vector of the critical plane). This strain increment vector is defined as the product of the increment of the strain tensor $d\varepsilon$ with the normal vector r . The increment of energy is given by:

$$dW_c = (\sigma r) \cdot (d\varepsilon r) = r \cdot \sigma d\varepsilon r = \vec{\sigma} \cdot d\vec{\varepsilon} \quad \text{Eq. 3-1}$$

It leads to the definition of an energetic tensor which increment is $\sigma d\varepsilon$. Then, the predictive parameter defined by Mars consists on accumulating this tensor over one cycle, and the critical material plane is determined.

Mars [37] proved that for all kind of tests conducted by axial/torsion specimens, peak cracking energy density exhibit slightly worse correlation than peak maximum principal strain. In contrast, the cracking energy density is the only parameter that correctly predicts the experimentally observed differences between simple and equibiaxial tension fatigue. It is believed that provides reasonable estimates of fatigue life under hydrostatic tension and simple compression. Cracking energy density is unique relative to scalar equivalence parameters. Nevertheless, it requires the use of an associated criterion for critical plane selection. Three kinds of criteria would be adequate: the plane of maximum peak cracking energy density, the plane of maximum cracking energy density range, and the plane of minimum life (including R ratio effects). The minimum life criterion will be used in our computations, as it gave the most accurate life correlation in Mars [37]. The cracking energy density methodology was also used by Zine et al. [95], and Martinovs and Gonca [96] on their computations. Zine et al. [95] applied the cracking energy density criterion in a finite element analysis code and found good agreement between numerical and analytical results for common strain states. Their

experiment results showed also the efficiency of this criterion to explain fatigue life of elastomers under multiaxial loading conditions.

3.1.1.4.2. *Cauchy Stress Based Equivalent Quantity*

The critical plane approach is based on the reality that fatigue cracks initiate and grow within material on certain preferred planes. The corresponding failure is supposed to be due to the stress, strain or energy histories acting on these planes. The critical plane is then determined by identifying material plane which maximizes the combination of relevant fatigue damage parameter.

To choose the mechanical fatigue damage parameter most of existing fatigue life models has been evaluated in the literature by Saintier, [64]. Models that are based on stress, strain, strain energy evolution or any combination of those quantities have been studied. Mars [69] recently proposed cracking energy density parameter for rubbery materials was also evaluated. Mars proposed that fatigue life could be related to an amount of energy ΔW_c , where W_c represents the so called cracking energy density. He considers the orientation of the plane of interest constant over a cycle and identify the plane of crack initiation as the plane which maximizes $\Delta W_c = W_{c,max} - W_{c,min}$. However, it was not clear how such a quantity could be computed with an incremental definition of W_c . The fatigue life is then related to ΔW_c via a power-law function.

Under large strain conditions, not taking into account material plane rotations can be hazardous when computing amplitudes of a given quantity. Let's assume a given mechanical quantity X (stress, strain or energy), of which to compute an amplitude and mean stress value on a particular material plane is wanted. Since X_{max} and X_{min} must be computed at two different times the corresponding material planes are different. So, their rotations have to be taken into account.

Saintier has developed a methodology to find fatigue crack orientation from the principal stress directions [64]. The methodology could be performed in the same way using principal strain directions since they coincide for an isotropic hyperelastic behaviour. The rubber is considered as isotropic incompressible hyperelastic material, so the strain tensor is only depending on the deviatoric part of the stress tensor. By definition of incompressibility, hydrostatic stress states do not induce any deformation. Thus, computing a damage parameter exclusively from the evolution of

a strain quantity imply that the hydrostatic part of the loading does not induce any damage. This was found to be experimentally wrong [97].

Damage parameters from energy based quantities show the same difficulties as strain based. When strain based tends toward zero, when stress state becomes close to a purely hydrostatic, the corresponding energy based quantity also tend to zero. As a conclusion, Cauchy stress tensor history over a cycle has to be named the preferred parameter to express de damage. As the maximal principal stress direction was found to correctly predict the fatigue crack orientations under non-proportional multiaxial loading, it is suggested that the maximum value of the first principal stress reached during a cycle drives the damage process.

It is well known that for uniaxial fatigue testing on natural rubber, running tests at non relaxing conditions ,positive loading ratio ($R = \sigma_{\min} / \sigma_{\max}$), induce a strong increase in the fatigue life. This reinforcement is often attributed to strain-induced crystallization of rubber (i.e. synthetic rubber which do not show such an ability do not present this reinforcement at $R>0$ either) [64,66,95]. In order to incorporate both fatigue damage and cyclic reinforcement mechanisms into the prediction of fatigue crack nucleation in rubber, [68] proposed a Cauchy stress-based equivalent quantity, σ_{eq} , defined as follow:

$$\sigma_{eq} = \frac{\Phi_{Damage}}{1 + \Phi_{Reinforcement}} \quad \text{Eq. 3-2}$$

where Φ_{Damage} (has stress units) and $\Phi_{Reinforcement}$ (dimensionless) are two quantities associated with damage and reinforcement mechanisms respectively and based on the Cauchy stress history. Φ_{Damage} is the driving force of the damage process. $\Phi_{Reinforcement}$ in positive under reinforcing loading condition and null otherwise. While the condition for having reinforcement under uniaxial loading is simple ($R>0$), it becomes much more complex under multiaxial loading.

The number of cycles to crack initiation is correlated to the stress state via a power law function of an equivalent stress.

$$N_i = \left(\frac{\sigma_{eq}}{\sigma_0} \right)^\alpha \quad \text{Eq. 3-3}$$

σ_0 (Normative stress) and α (power law coefficient) are the material parameters to be identified.

3.1.1.4.3. *Configurational Stress Tensor*

There are several recent studies that consider the theory of Configurational Mechanics to predict rubber fatigue [98–100]. As they mentioned, they were motivated by the studies focused on the energy release rate of microscopic defects in rubber [77,86,93] and more especially the work of Mars [69], who attempted to determine the portion of the total strain energy density that is available to be released as microscopic defects grow under multiaxial fatigue loading conditions. In fact, his concept of energy release rate was rationalized in the framework of Configurational Mechanics.

The theory is based on the work of Eshelby [101], in 1951, who introduced the energy-momentum tensor (also called the Eshelby tensor) to study forces on elastic singularities and defects. This tensor was extended then to large strain by Eshelby [102], in 1975. More recently, Maugin [103] and Steinmann [104] have shown that the notion of body configurations is essential in the theory; the large strain framework will be adopted for application to rubber fatigue.

In the material space, rubber can be considered as a material with a uniform distribution of defects, which grow under mechanical loading. From a microscopic scale, these defects can be voids (pre-existing porosities and cavities), micro-cracks or rigid inclusions (filler agglomerates). Crack nucleation is assumed to be a consequence of the growth of these pre-existing small flaws as proposed by Mars [37]. In the case of macroscopic crack, the concept of fracture mechanics offers an efficient theoretical foundation. The crack growth is determined by the calculation of the energy release rate for given specimen and crack shapes and for prescribed loading conditions. Nevertheless in most cases, the shape and position of initial defects in rubber parts are not known and the definition of energy release rate is not straightforward. Thus, a continuum approach which accounts for existence of material inhomogeneities is more appropriate.

The general and efficient way to analyse different kinds of material inhomogeneities within the framework of continuum mechanics is provided by the theory of Configurational Mechanics [105] (also designated as the Eshelbian Mechanics by

Maugin [103]). While in classical Newtonian Mechanics focus on physical forces generated by displacements in physical space. In Configurational Mechanics deals with different class of forces, named configurational forces, which are generated by displacements not in the physical space but in the material space (or manifold), i.e. the abstract set of particles that constitute the body.

Generally, material motion in the physical space induces microstructural changes or rearrangements in the material, e.g. growth of microscopic defects, dislocation or displacement of boundary phases. Describing such rearrangement in the physical space is not an easy task [104]. Thus, the balance of physical linear momentum should be completely written onto the material space [100].

$$Div_X \Sigma + G = 0 \quad \text{Eq. 3-4}$$

In which X is the position of the particle in the reference configuration and Σ is the configurational stress tensor defined by:

$$\Sigma = WI - F^T P = WI - CS \quad \text{Eq. 3-5}$$

And G is the configurational vector

$$G = - \left. \frac{\partial W}{\partial X} \right|_{\text{expl}} \quad \text{Eq. 3-6}$$

In these equations, W is the strain energy density per unit of undeformed volume, I is the 3x3 identity tensor. S is the second Piola-Kirchhoff stress tensor and C is the right Cauchy-Green strain tensor equal to $F^T F$. Moreover, G is defined as the negative explicit differentiation of the strain energy with respect to the particle position in the material manifold (see the index $\cdot|_{\text{expl}}$). If the material is homogeneous, $G = 0$ and the configurational stress tensor satisfies a strict conservation law.

$$Div_X \Sigma = 0 \quad \text{Eq. 3-7}$$

In the majority of studies involving Configurational Mechanics, only configurational forces are investigated through the calculation of path-independent integrals around inhomogeneities. So, configurational stress only appears in the definition of surface tractions, i.e. after contraction with the outward normal of the contour. Most of these works focus on the application of Configurational Mechanics to Fracture Mechanics.

Only few studies are concerned with the peculiar properties of the configurational stress tensor, Σ . Having into consideration the geometrical definition and the physical significance of the Cartesian components of this tensor, it appears that the configurational stress is a continuum mechanics quantity associated with energy changes during local structural rearrangement of material under loading

As fatigue loading conditions induce significant microstructural rearrangements in rubber, Verron & Andriyana [70] and Andriyana & Verron [100] consider this tensor as an appropriate continuum mechanics quantity to derive a new predictor for rubber fatigue. By supposing that opening and closing of microscopic defects (cavities) in rubber are due to only material normal traction and not due to material shear, the authors proposed that microscopic defects growth can be predicted by considering the *smallest* eigenvalue of this tensor. Thus the predictor is given by:

$$\Sigma^* = \left| \min[(\Sigma_i)_{i=1,2,3}, 0] \right| \quad \text{Eq. 3-8}$$

When one (or more) principal stress is negative, the predictor is strictly positive, and the defect tends to grow and to turn into a plane crack orthogonal. When the three principal stresses are positive, the material tractions tend to shrink the flaw and the predictor is set to 0.

In order to incorporate non-proportional multiaxial loading conditions, the authors proposed to accumulate the increment of the configurational stress that contributes to flaw opening. In this case, the previous predictor becomes [99]

$$\Sigma^* = \left| \min[(\Sigma_i^d)_{i=1,2,3}, 0] \right| \quad \text{Eq. 3-9}$$

Where $(\Sigma_i^d)_{i=1,2,3}$ are the eigenvalues of the damage part of the configurational stress tensor Σ^d .

It is to note that for fully-relaxing proportional loading conditions, the integration over one cycle reduces to the determination of the instantaneous value of the configurational stress tensor for the maximum strain level. In this case, Eq. 3-9 reduces to Eq. 3-8.

Finally, the number of cycles to crack initiation N_f is correlated to Σ^* via a classical power law function:

$$N_f = \left(\frac{\Sigma^*}{\Sigma_0} \right)^\beta \quad \text{Eq. 3-10}$$

Where Σ_0 and β are the material parameters identified from uniaxial tension fatigue data.

The Configurational Mechanics approach presented is still in progress (Andriyana and Verron, [100]; Verron [106]). Further works are required in order to fully establish a rigorous connection between energy release rate and this continuum parameter [107].

3.1.2. Crack Growth Approach

There are basically two possible approaches to study the fracture mechanics analysis of crack growth in solid materials; a critical stress criterion or an energy balance technique. Both require the existence of a pre-existing flaw in the component that grows under a cyclic loading of sufficient magnitude and number of repetitions.

The critical stress criterion states that when a sample containing a flaw is subjected to a stress, the material in the region close to the crack tip is subjected to an intensified stress. When the stress at the crack tip exceeds a critical value the material at the tip will break and grow an amount. To predict when the crack will grow, is necessary to know the strength and stress distribution of material. It is difficult to describe mathematically stress situation around the crack tip, due to large strains and material non linearity. In consequence, was difficult to apply the stress intensity factor approach. However, the development of FEA technique permitted to solve the stress analysis problem in the region of the crack tip. For this reason, the fracture mechanics approach adopted for elastomers is based upon an energy approach that will be described in section 3.1.2.1.

Inglis [108] in 1913, and Griffith [94] in 1920 introduced the idea of focusing attention on individual flaws. Griffith proposed a fracture criterion based on an energy balance including both the mechanical energy of a cracked body, and the energy associated with the crack surfaces. Griffith's approach was further developed for rubber by Thomas, Greensmith, Lake, Lindley, Mullins, and Rivlin in the 1950s and 1960s [77–89]. Irwin [109–111], Rice [112], and others developed the approach in metals. The original application of this approach was to predict static strength

[77,113,114], but Thomas [81] extended the approach to analyse the growth of cracks under cyclic loads in natural rubber. He discovered a power-law relationship between peak energy release rate and crack growth rate for natural rubber. Paris et al [115] independently found a similar power-law relationship in metals. Thomas [81] predated Paris' work [115] by 3 years.

In his work on the J-integral, Rice [112] credits Thomas' [78] work for first showing the connection between the energy release rate and the strain concentration at the crack tip. A path independent contour integral (in two dimensions) is taken around the tip of the crack to calculate the energy release rate. The J-integral has the advantage that only one analysis model is necessary to calculate the stored energy release rate.

3.1.2.1. *An Energy Criterion for Fracture*

Griffith [94] suggested that the reason for the observed strength of glass being much lower than that expected from a consideration of the intermolecular forces was due to the presence of small flaws. In order to carry out a quantitative assessment of their influence he introduced a novel energetic approach. He was able to show that the surface energy associated with the crack faces of a broken glass filament was equal to the elastic energy released by the fracture. The failure criterion was expressed in a differential form like,

$$2S_E = -\frac{1}{t} \left(\frac{\partial U}{\partial c} \right)_l \quad \text{Eq. 3-11}$$

Where S_E is the surface free energy per unit area, U is the total elastic energy stored in the sheet, c is the crack length, t is the sheet thickness and the subscript l indicates that the differentiation is carried out at constant overall extension so that the externally applied forces do not work. Griffith used the elasticity solution due to Inglis [108] for the problem of the stress distribution in a loaded sheet containing an elliptical hole, to calculate the differential for a crack in an infinite sheet.

This approach was taken by Rivlin and Thomas [77], who modified the Griffith theory to take into account the irreversible energy dissipation which occurs in the highly strained regions close to the crack tip. In rubber, the potential energy released from surrounding material is spent on both reversible and irreversible changes to

create the new surfaces [48,77,116]. The magnitude of these losses is determined by the visco-elastic properties of the elastomer, the strain in the crack tip region of a given size and the crack growth rate. Thus the energy required to propagate the crack at a particular rate is a characteristic of a given elastomer, and is defined as the stored energy release rate which is also sometimes known as the tearing energy, T .

$$T = - \left(\frac{\partial U}{\partial A_c} \right)_v \quad \text{Eq. 3-12}$$

A_c is the area of the fracture surface of the crack. The value of T is determined by the viscous work that has to be done in the crack tip region. This approach for crack growth calculations has been reviewed by many authors like Lake and Thomas [51], Hamed [117,118] and Thomas [49]. The energy release rate was initially developed to analyse static loading of rubber specimens [77]. However, Thomas [81] realized that the concept was also applicable for cyclic loading. In that case, it was found that the maximum energy release rate achieved during a cycle determined the crack growth rate for $R=0$ cycles.

3.1.2.2. *Test Specimens for Rubber*

Thomas [77] showed that static crack growth occurs above a critical value of the energy release rate, which is independent of the type of test specimen used on experimental and argued that the critical energy release rate is a true material property. On this initial study he had worked three specimen types: a centre-cracked sheet, an edge-cracked sheet, and a “trouser” test piece (Figure 3.1). A subsequent study with three additional test specimen types confirmed the independence of the critical energy release rate from specimen geometry [82]. Other studies [81,88,89,93], using the same specimen types, showed that the fatigue crack growth rate is also uniquely determined by the energy release rate.

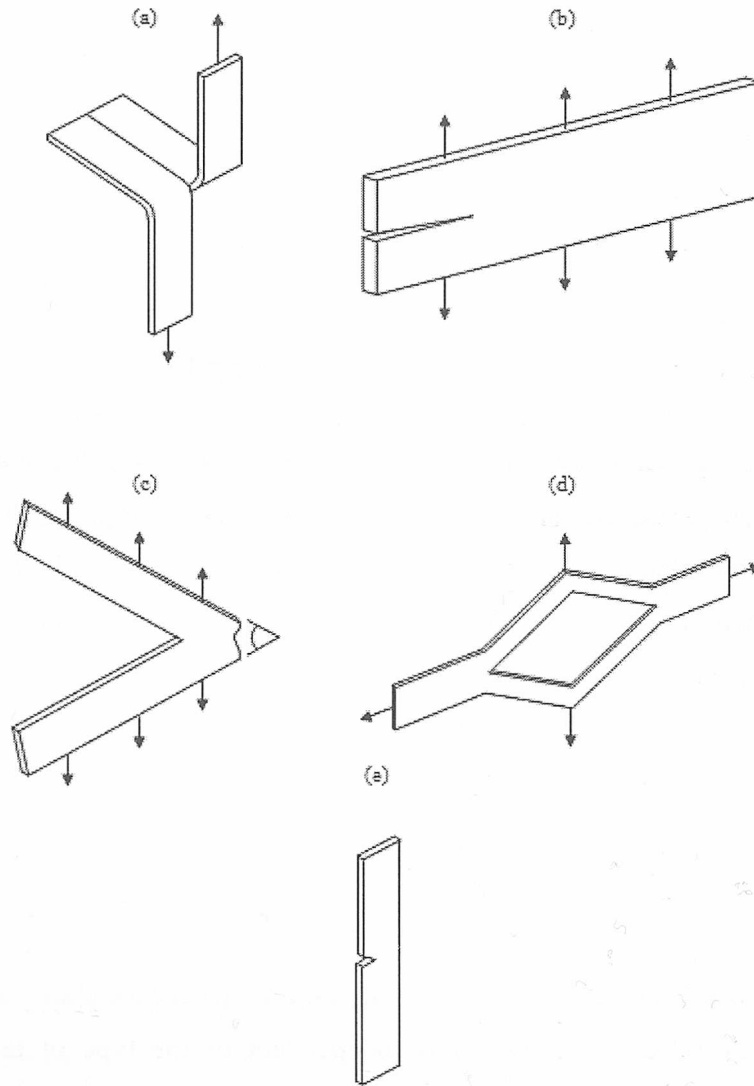


Figure 3.1 Crack growth test pieces for which the stored energy release rate T can be easily calculated: (a) trousers (b) pure shear (c) angled (d) split and (e) edge crack.

Specimen thickness has been shown to be an important aspect on the fatigue or fracture properties of the material. Thickness effects have been reported by Kadir and Thomas [119], and by Mazich et al [120]. Both of these studies were conducted with gum SBR. Kadir and Thomas showed that thickness dependence is related to the development of crack tip roughness. When the fracture surface remained smooth during growth, little dependence on specimen thickness was observed of the growth rate. When so called rough, or stick-slip crack growth occurs, however, the thickness effect has more influence. Thicknesses ranging from 0.1 mm to 10 mm were investigated. On a plot of crack growth rate, at constant energy release rate, as a function of specimen thickness, two plateaus were observed. Below 0.5 mm, and

above 5 mm, thickness had little effect. Between these thicknesses the crack growth rate changes by more than an order of magnitude. The crack growth rate for thin specimens was larger than for thick specimens. Mazich et al [120] looked at the influence of specimen thickness on the critical energy release rate for fracture. They found that, in the range from 1 mm to 3 mm, the critical energy release rate for crack growth increased by a factor of two. Note that these results are consistent with those of Kadir and Thomas, since higher crack growth rates are associated with lower critical energy release rates.

Following, stored energy release rate, T , calculation equations for most commonly use specimens in rubber fatigue crack growth studies will be shown. The stored energy release rate could be calculated from the measured specimen stored energy density determined from the measurable applied forces and strains. The relationships derived from these calculations are detailed next.

a) The trouser crack growth test.

$$T = \frac{2F\lambda}{t} - w_0W \quad \text{Eq. 3-13}$$

where F is the force applied to each leg, t is the initial test piece thickness and w_0 width, λ is the extension ratio and W the stored energy density in the legs.

It was used in early studies of fatigue crack growth in rubber [81] to demonstrate geometry independence of the relationship between the energy release rate and the fatigue crack growth rate. The energy release rate T depends on the applied force F , the extension ratio λ and strain energy density W in the 'legs' of the specimen, the specimen thickness t , and w_0 is the 'leg' width.

b) The pure shear crack growth test.

$$T = Wh_0 \quad \text{Eq. 3-14}$$

In the single edge cut pure shear specimen, the energy release rate T has a very simple form. It depends only in the strain energy density, W , remote from the crack and specimen edges; and the unstrained value of the height of the test piece h_0 . Note that the energy release rate for this specimen is independent of the crack size [77].

c) The angled crack growth test.

$$T = \frac{2F}{t} \sin\left(\frac{\theta}{2}\right) \quad \text{Eq. 3-15}$$

where F and t are again the applied force and the test piece thickness and θ is the angle between the separating legs.

d) The split crack growth test.

$$T = \{[F_A \lambda_A \sin \theta + F_B (\lambda_A \cos \theta - \lambda_B)]/t\} - w_0(W_A - W_B) \quad \text{Eq. 3-16}$$

where F_A and F_B are the forces applied to the respective pairs of legs, λ_A λ_B and W_A , W_B the corresponding extension ratios and stored energy densities in the legs. The angle of the opening is 2θ ($\tan \theta = F_A/F_B$) and w_0 and t are the initial width and thickness of the test piece.

e) The edge crack in a tensile crack growth test piece.

$$T = 2Wck(\lambda) \quad \text{Eq. 3-17}$$

the energy release rate, T , depends on the gauge section strain energy density, W , the crack length, c , and a slowly changing strain constant of proportionality, $k(\lambda)$. This relationship is different to the other relationships listed above, as it is derived from dimensional considerations and the stored energy release rate and the geometry change as the crack length increases.

Following the measurements by Greensmith [86] on the strain dependence of $k(\lambda)$ and using his own measurements, for the centre cracked specimens Lake [121] proposed an approximate relationship given as,

$$k(\lambda) = \pi / \sqrt{\lambda} \quad \text{Eq. 3-18}$$

Lindley [92] followed up Greensmith's work [86] with the first finite element analysis of the case of single edge notched tension specimen. They studied the dependence of the parameter k on strain for the case in which the crack is much smaller than the specimen width. A plot of Greensmith's data is shown in Figure 3.2. Their results were in a good agreement, and have been summarized with the following curve fit,

$$k = \frac{2.95 - 0.08(\lambda - 1)}{\lambda^{1/2}} \quad \text{Eq. 3-19}$$

In Eq. 3-19, $k=2.95$ for $\lambda=1$, which is less than theoretical value of π under infinitesimal strain assumption. Single edge cut, simple tension specimen, pictured is additionally shown in Figure 3.2 to illustrate the behaviour and tendency.

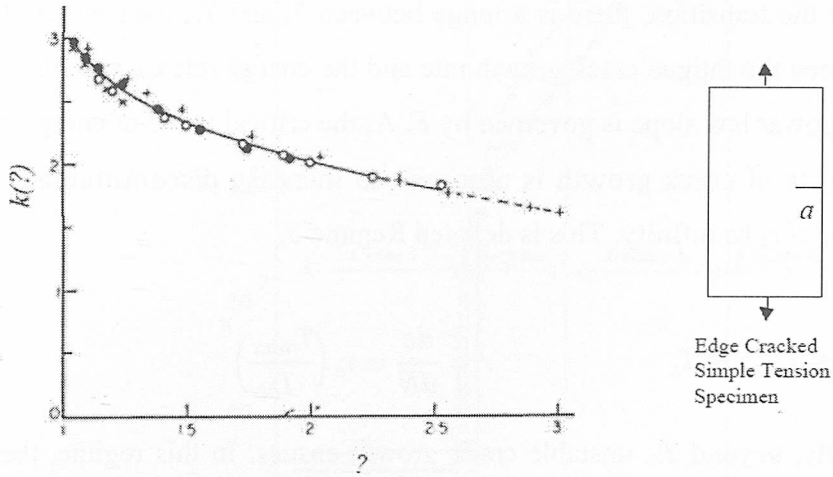


Figure 3.2 Greensmith's [86] data for variation of k with maximum principal stretch λ , in $T = 2kWc$. This relationship gives the energy release rate T of a crack in the simple tension specimen shown. Different data point types are for different rubber compounds.

3.1.2.3. Regimes of Fatigue Crack Growth

Lake and Lindley [122] identified four distinct regimes of fatigue crack growth behaviour, based on the maximum energy release rate per cycle, T , for $R = 0$ cycles in rubber. The full range of behaviour is shown in Figure 3.3, for unfilled Natural Rubber, and Styrene-Butadiene Rubber. Later the crack growth behaviour under fully relaxing conditions was parameterized, into a slightly modified lake and Lindley proposed scheme. The modification aimed at getting a parameter set that avoids the obscure units that arise with the original scheme [123].

So long as the peak energy release rate T remains below a threshold T_0 , crack growth proceeds at a constant rate r_0 , due solely to environmental attack. The crack growth rate dc/dN below T_0 is independent of the mechanical loading, and is denoted Regime 1.

$$T_{max} \leq T_0 \quad \frac{dc}{dN} = r_0 \quad \text{Eq. 3-20}$$

There is then a narrow range of T_{max} , between T_0 and T_t , over which there is a transition. The transition is described by the following relationship, in which A is a material property. This is denoted Regime 2.

$$T_0 \leq T_{max} \leq T_t \quad \frac{dc}{dN} = A(T_{max} - T_0) + r \quad \text{Eq. 3-21}$$

After the transition, there is a range between T_t and T_c , over which the relationship between the fatigue crack growth rate and the energy release rate obeys a power-law. The power law slope is governed by F . At the critical value of energy release rate, T_c , the rate of crack growth is assumed to increase discontinuously from a finite value of r_c to infinity. This is denoted Regime 3.

$$T_t \leq T_{max} \leq T_c \quad r = \frac{dc}{dN} = r_c \left(\frac{T_{max}}{T_c} \right)^F \quad \text{Eq. 3-22}$$

Finally, beyond T_c , unstable crack growth ensues. In this regime, the crack growth rate is essentially infinite. This is denoted Regime 4.

$$T_{max} = T_c \quad \frac{dc}{dN} = \infty \quad \text{Eq. 3-23}$$

Number of multi-regime models has been developed in the literature [124–131]. Nevertheless, it appears that no current multi-regime fatigue crack growth model is able to predict the observed $R > 0$ effects for an important class of rubbers [54]. When applied to strain-crystallizing rubbers, they predict increased crack growth rates for $R > 0$ conditions. In contrast, for strain-crystallizing rubbers, the crack growth rate is significantly retarded by $R > 0$ conditions, as discussed in section 3.3.1.2.

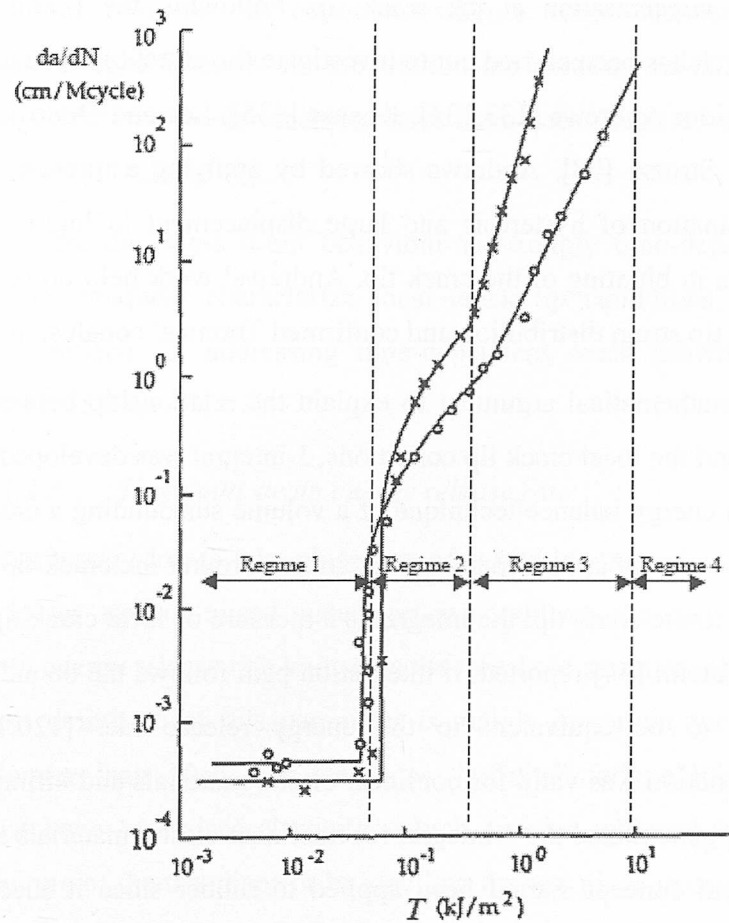


Figure 3.3 Regimes of fatigue crack growth behaviour in unfilled rubber, under $R = 0$ loading (X = SBR, O = NR). Mcycle = Megacycles = 10⁶ cycles. [54] Based on [122]

3.1.2.4. *J*-integral and Crack Tip Conditions

The morphology of the crack tip is another aspect affecting the crack growth behaviour and the strength of the material. Lake and Yeoh [132] reported that for very sharp cracks, tearing is found to occur on a small scale at very low energies not far above the threshold required for the onset of mechanical crack growth.

Thomas [78] demonstrated that energy release rate has a unique relationship to the local conditions at the crack tip, making it appropriate as a parameter for predicting fatigue crack growth and fracture. He studied the conditions for crack initiation, focussing on the strain distribution around the tip of a blunted crack in a sheet of rubber; he performed the same analysis over several specimen geometries. The energy release rate therefore gives a measure of local crack tip fields for a given material and crack tip geometry, and proves that is independent of the specimen type. This paper was an extension to the Rivlin and Thomas [77] work and considered the

strain concentration at the crack tip. Following the findings by Thomas much research has been carried out to investigate the effect of the crack tip on crack growth behaviour Andrews [133,134], Knauss [135], Lee and Donovan [136] and G. Medri & A. Strozzi [98]. Andrews showed by applying a microscopic technique, that a combination of hysteresis and large displacement in highly deformable materials results in blunting of the crack tip. Andrews' work help on better understanding the crack tip strain distribution and confirmed Thomas' conclusion.

The mathematical argument to explain the relationship between the energy release rate and the local crack tip conditions, J-integral was developed by Rice [112]. Based on an energy balance technique of a volume surrounding a crack tip, the calculation is made by a path independent integration around the crack tip. If the path is chosen close to the crack tip, the integral is a measure of local crack tip conditions. As Mars and Fatemi [54] reported, if integration path follows the boundaries of the specimen, turns to be equivalent to the energy release rate [120,136]. Rice's original formulation was valid for nonlinear elastic materials and infinitesimal strains. Chang [137] generalized the J-integral for nonlinear elastic materials at finite strains. The J-integral concept started been applied to rubber since it successfully characterizes ductile, highly dissipative fracture in metals and has been shown to satisfactorily characterize fracture in nonlinear, inelastic rubbers also.

A practical consequence of the J-integral is that the details of the processes occurring at the crack tip often do not need to be quantified in any way other than the J-integral in order to model crack growth. Instead, the details are accounted for by treating them as intrinsic to the material / crack-tip system. In this manner, nonlinearities due to finite network extensibility [4], strain crystallization [66,71,138,139], frictional losses due to filler interactions [140–142], and the Mullins effect [3,143,144] may be rolled into the fracture properties of the material [48,49]. Andrews [145] has proposed a theory to account for the effects of general nonlinear, dissipative constitutive behaviour on crack tip fields, under the assumption that crack propagates through an isotropic, homogeneous continuum. It is shown that the energy release rate approach avoids the necessity of modelling crack tip dissipative processes by focusing on where the energy for driving the cracks comes from (from strain energy stored beyond the J-integral boundary), instead of where that energy is spent (on dissipative processes near the crack tip).

Details of crack-tip processes are of interest when a deeper understanding of the failure process is sought. Theories for the relationship between the failure properties of rubber and rubber's molecular characteristics have been proposed and studied by several researchers [118,146,147].

In situations where the stress-strain behaviour is strongly time-dependent, the J-integral does not uniquely characterize local crack tip conditions. Lindley [38] presented an approach for addressing time-dependent crack growth in Styrene-Butadiene Rubber (SBR).

3.1.2.5. *Threshold strain energy release rate*

It is known that energy losses take place around a highly strained crack tip. When these energy losses are minimised under certain conditions the elastomer shows a minimum strain energy release rate known as the threshold strain energy release rate, T_0 . The correct definition of this parameter is mainly important for cases with a fatigue life longer than 10^6 , considered as "infinite" fatigue life. In case of elastomers that have low visco-elasticity, which can be achieved by raising the testing temperature of the test piece or by swelling the test piece in organic oils, it is possible to obtain a threshold energy release rate T_0 below which there is no crack growth. Lake and Thomas [146] carried out cyclic crack growth tests where they defined the minimum tearing limit at which cyclic crack growth will take place. They argued that below the T_0 crack growth was solely attributed to chemical attack by ozone. That work reported the principles they applied to get the threshold strain energy release rate. Their investigation deals with both crystalline and non-crystalline elastomers, where the tensile strength and tear strength is different. However, the magnitude of T_0 was found to be close to 50 Jm^{-2} for a range of elastomers, suggesting that this property could be related solely to the strength of the chemical bonds in the major polymer chains. Authors assumed that the tip diameter of the advancing crack, d , had the minimum possible value, d_0 , for rubber, when the elastic stored energy, W , had the minimum possible value, W_0 , which was determined by the bond strength. Thus, on a molecular scale becomes:

$$T_0 = W_0 d_0 \quad \text{Eq. 3-24}$$

Where W_0 is the minimum possible strain energy density at the tip and d_0 is the minimum possible tip diameter of the crack, which is the smallest and sharpest possible. In the case of rubber, the minimum distance possible is distance between adjacent cross-links in the unstrained state.

Mars has published on the Endurica LLC web page [148] that has developed a method to measure the elastomer's fatigue endurance limit. On the defence of the methodology Mars affirms that has overcome the inconvenient of existing procedures studied during decades, either exceptionally long testing periods (via a direct method of observation), or the use of potentially unsafe solvents (via an indirect method that involves swelling the elastomer and possibly changing the properties of interest). The approach is based on the principle that the endurance limit is set by the intrinsic strength of an elastomer's individual polymer network chains [149]. Developed test method determines the minimum energy required to cut or break each polymer chain that is reached by the crack tip, and it's associated critical stress and strain levels. The minimum energy is not easy to observe, due to the large amount of additional energy that is consumed simultaneously in viscoelastic processes occurring near the crack tip. Based on the procedure of lake and Yeoh [149], where the crack tip can be probed directly for the intrinsic strength and the effects of extraneous dissipated energy can be easily distinguished. The detailed procedure is still not published, but uses a series of carefully controlled cutting experiments, each made with a highly sharpened, instrumented blade. The procedure executes in less than a day, without the use of solvents. It seems that first results shown an acceptable correlation, up to 93% [148].

3.1.3. A Crack Growth Model for Crack Nucleation

Fatigue failure process consists on a gradual weakening of rubber specimens and consequent eventual fracture due to the repeated deformations even being much lower than the strain to break. This is attributed in the literature to the growth by repeated tearing of a small flaw, or number of flaws in the test piece. A crack growth approach has been successfully used to predict uniaxial fatigue crack nucleation life from fatigue crack growth measurements [88]. The approach is based on integration of the fatigue crack growth rate between two crack sizes, from the inherent flaw size to a size that would be considered as critical. Nevertheless, the growth from flaw size to small crack size often covers the most important portion of a component's life,

since the presence of a large crack usually means the component has already failed. Le Cam [61] has recently demonstrated experimentally that flaws grow from the very first loading cycle. Moreover, it was also shown that about 75% of the fatigue life of the part (defined by the number of cycles required to create a 1mm long crack on a diabolo sample) corresponds to the propagation of pre-existing flaws. Masquelier [150] realized a detailed study of the initiation of fatigue cracks in carbon black-filled natural rubber by interrupted fatigue tests. Fatigued samples were observed with a scanning electron microscope (SEM) and energy dispersive spectrometry of X-rays (EDS). The morphology, spatial distribution, and evolution of crack initiation sites for different strain levels were quantified, and the chemical natures of inclusions inducing crack initiations were identified. She found out that fatigue damage initially occurs generally on carbon black agglomerates. The obtained results strengthen the basis on which crack nucleation approach is based on.

In section 3.1.3.2 is presented the approach for computing the energy release rate of an assumed pre-existing flaw from the flaw size and the strain energy density. In cases where initial crack is of small size, the energy release rate may be factored into a product proportional to both, strain energy density, W , and crack size, c .

3.1.3.1. *Intrinsic Flaws in Rubber*

Initial flaw size is used as input of curve fit parameter to obtain agreement between crack nucleation and crack growth experiments [86,122,151]. In the subsequent theory it is suggested a way to estimate the size of naturally occurring flaws in rubber. The resulting flaw size is actually an effective flaw size, reflecting both the size and shape of the flaws [88]. Different initial flaw sizes in the range of 20×10^{-3} m to 50×10^{-3} mm were observed in a study by Lake and Lindley [122] for a variety of eight materials. Several publications have extended this range from 20×10^{-3} mm to 200×10^{-3} mm [152]. A summary of flaw sizes taken is shown in Table 3.1. Factors that may impact flaw size include polymer type, [122] crosslink density, [122,153] carbon black type, [122,154] degree of dispersion, [155] mould lubricants [37] and particulate compound ingredients [156]. Often, flaws can be imaged [37,102]. The flaw size can also be deduced from static strength measurements [1,157], and optical microscopy techniques [154] independent of fatigue measurements. The precise nature of such flaws remains obscure because it appears that there are multiple sources for flaws of the observed effective size. These sources

may include naturally occurring contaminants or voids in the base polymer, imperfectly dispersed compounding ingredients, filler agglomerates, mould lubricants, and imperfections in mould surfaces.

A basic assumption of fracture mechanics is continuity and homogeneity of the material. Nevertheless, depending on the initial flaw size of material, if they are enough small, the assumption is not true. In rubber, the intrinsic flaws are larger than features of the molecular network structure by a factor of more than 10.000, and larger than individual filler particles by a factor of more than 100. Agglomerations of carbon black particles can exhibit dimensions of the same scale of intrinsic flaws [154]. Mars [37] summarized the size scales of importance in filled rubber found in a number of publications on a table, Table 3.1. In contrast, the independent agreement of nucleation and growth approaches, using initial flaw size as the sole fitting parameter suggests that it is appropriate to assume that the initial flaws are embedded in continuous, homogeneous material.

Le Cam [61,99] research work clarified the obscure nature of crack initiation. Two main mechanisms were found to occur at crack initiation independently of the type of loading (i.e. uniaxial or multiaxial) but depending on the nature of the inclusion: decohesion and cavitation. Decohesion was mostly observed at rigid inclusions such as SiO₂ or CaCO₃ while cavitation, the spontaneous process of void nucleation, was found to occur in the neighbourhood of carbon black agglomerates. The distinction between decohesion and cavitation was made using SEM inspection at the crack initiation location. Specimen surfaces are systematically observed using a field effect scanning electron microscope (SEM) equipped with energy dispersive spectroscopy (EDS) analysis facilities. The EDS analysis system works as an integrated feature of a scanning electron microscope. The technique utilizes X-rays that are emitted from the sample during bombardment by the electron beam to characterize the elemental composition of the analysed volume. In addition, sections are cut using a cryogenic microtome (so that a perfect sectioning is ensured) to identify crack initiation mechanisms beneath the lateral surface.

Masquelier [150] performed a detailed study of the initiation of fatigue cracks in carbon black-filled natural rubber. She performed interrupted fatigue tests and fatigued samples were observed with a SEM. The morphology, spatial distribution, and evolution of crack initiation sites for different strain levels were quantified.

Additionally, by using EDS of X-rays the analysis of the chemical nature of inclusions inducing crack initiation were done. The chemical nature of inclusions were sorted in five categories: Carbon Black (CB), Zink Oxide (ZnO), Talc, other oxides (calcium/silicon oxides (SiO₂,CaO) or oxides containing aluminum and silicon (kaolinite, Al-Si-O)), and non-visible inclusions (NVI). Nevertheless, has been confirmed that fatigue damage initially occurs generally on carbon black agglomerates or oxides such as ZnO (between $2 \cdot 10^{-3}$ and $5 \cdot 10^{-3}$ mm). However, those two types of inclusions correspond to different crack initiation mechanisms, and most of the time, only the initiations on carbon black agglomerates are followed by crack propagation that leads to failure. Furthermore, the interrupted tests reveal that initiation of cracks starts very early in fatigue life and are followed by a relatively slow propagation.

A further analysis around carbon black agglomerates by the analysis of the SEM images, have shown that Carbon black agglomerates exhibit a spherical shape, and that fatigue crack initiation mechanism can be divided into three stages Figure 3.4: stage 1, debonding at the pole; stage 2: opening on the sides; stage 3: growth at the surface and in the volume, which can be also considered as the early stages of crack propagation. Actually, a flaw can be an activated site or a crack. At relatively small strains, the percentage of flaws in stage 1 decreases during the fatigue life, whereas the percentages of flaws in stages 2 and 3 increase. These evolutions, also observed at strains above 100%, tend to validate the proposed mechanism, in so far as it is progressive, and it confirms that the carbon black agglomerates are responsible for the critical cracks (stage 3).

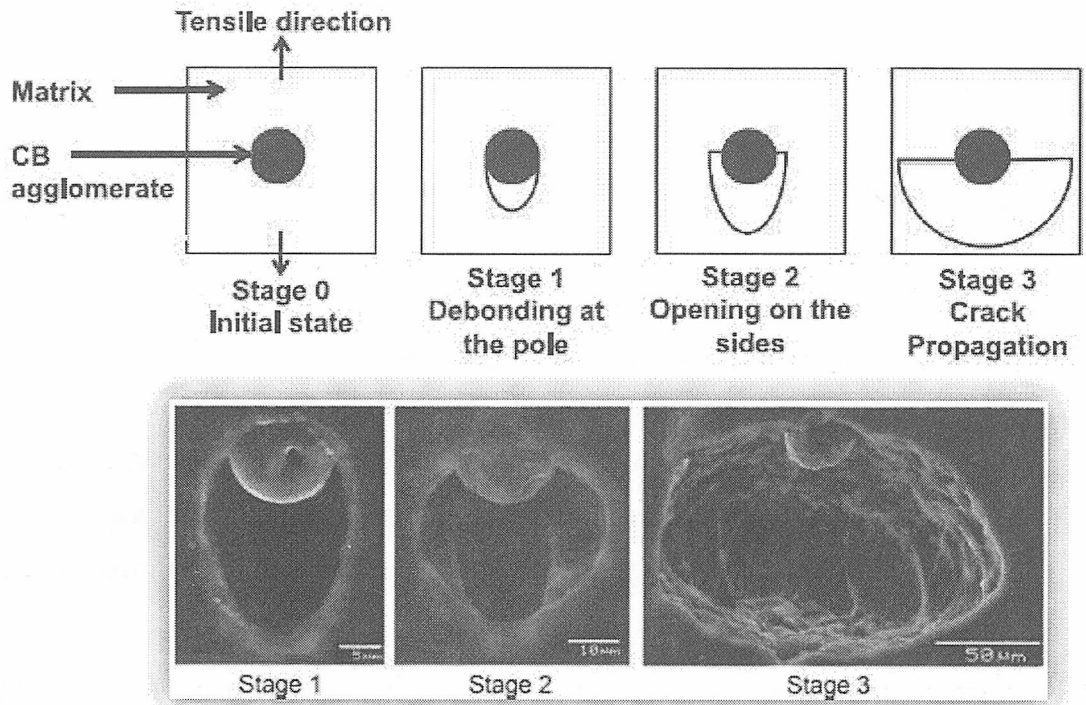


Figure 3.4 Schematic representation and real image capture of fatigue crack initiation mechanism around a carbon black agglomerate [150]

Table 3.1 Summary of reported initial flaw size values that have been taken from Lake and Lindley [89], Lake [158] and Choi and Roland [139] for different types of elastomers.

Elastomer type	$c_0 / \mu\text{m}$
Unfilled butyl rubber (IIR)	50
Unfilled poly-butadiene (BR)	25
Unfilled styrene butadiene rubber (SBR)	55
Unfilled acrylonitrile-butadiene rubber (NBR)	40
Unfilled natural rubber (NR)	25
Unfilled low purity natural rubber (SMR-10)	29
Unfilled medium purity natural rubber (SMR-L)	26
Unfilled deproteinised high purity natural rubber (DPNR)	16
Unfilled guayule rubber (GR)	29
HAF black filled natural rubber (NR)	50

Table 3.2 Geometric features of filled rubber [37].

Feature	Size
Large Carbon Black Agglomerate [154]	200×10^{-3} mm
Smallest flaw visible to naked eye	100×10^{-3} mm
Typical size of intrinsic defects [151]	40×10^{-3} mm
Small Carbon Black Agglomerate [154]	20×10^{-3} mm
Coarse Carbon Black Particle [159]	500×10^{-6} mm
Fine Carbon Black Particle [159]	10×10^{-6} mm
Distance along polymer chain between crosslinks (assuming 300% macro-stretch=100% chain extension, crosslink density of $5.8 \times 10^{19}/\text{cm}^3$) [152]	1×10^{-6} mm
Length of a single monomer unit (isoprene) [146,160]	500×10^{-9} mm
Spatial distance between crosslinks (based on crosslink density of $5.8 \times 10^{19}/\text{cm}^3$) [152]	300×10^{-9} mm
Length of a main-chain, polysulfidic bond [161]	100×10^{-9} mm

3.1.3.2. Integrated Power-Law Model

Fatigue life is determined by the number of cycles that a pre-existing flaw takes to grow to a critical size. The life calculation is done by integrating the growth rate of the fastest growing flaw, with the assumption that flaw growth is planar and all of them grow similarly. As mentioned in section 3.1.2.3 fatigue crack growth has four regimes of fracture, each with their own mathematical descriptive equation. Hence, if the prediction wants to be of major precision the piece level integration over the entire range of fatigue crack growth behaviour is performed, and yields the most accurate fatigue life predictions [162,163]. In practise, however, it is common to assume power-law behaviour over the entire range of life of the flaw, giving acceptable results [48,155,164].

The combination of the power-law that defines the crack growth rate in the third regime, Eq. 3-22, and equation for the energy release rate calculation of the specific specimen, in this case the simple tension specimen by Eq. 3-17, result in a closed-form relationship between the fatigue life, N , and the fatigue crack growth rate dc/dn :

$$\frac{dc}{dN} = f[T(c, W)] = BT^F = B(2kWc)^F \quad \text{Eq. 3-25}$$

Then integrating,

$$N_f = \int_0^N dN = \int_{c_0}^{c_f} \frac{1}{f[T(c, W)]} dc = \int_{c_0}^{c_f} \frac{1}{B(2kW)^F} c^{-F} dc \quad \text{Eq. 3-26}$$

$$N_f = \frac{1}{F-1} \frac{1}{B(2kW)^F} \left[\frac{1}{c_0^{F-1}} - \frac{1}{c_f^{F-1}} \right] \quad \text{Eq. 3-27}$$

We can see from Eq. 3-27, that if the initial flaw size c_0 is much smaller than the critical flaw size, c_f , then the life becomes independent of the critical flaw size.

$$N_f = \frac{1}{F-1} \frac{1}{B(2kW)^F} \frac{1}{c_0^{F-1}} \quad \text{Eq. 3-28}$$

Initial flaw size is regarded as a property intrinsic to a given virgin material, as will be explained on section 3.1.3.1. The parameter, k , is a proportionality constant that depends weakly on strain, therefore, if variation of k with strain is neglected; the constants of the equation may be combined into a single material property D .

$$N_f = DW^{-F} \quad \text{Eq. 3-29}$$

This derivation applies only to uniaxial loading, and small crack sizes, where the energy release rate can be factored into the strain energy density and the size of the crack. Note that while the energy release rate is defined for a specific crack, the strain energy density is defined for a material point. Therefore, for multiaxial situations many facts have to be taken into account, and the use of strain energy density presents some limitations. The factorization only applies in uniaxial loading, under multiaxial strain states not all of the strain energy density is available to be released due to crack growth. The amount of strain energy density released would be the same for a given increment of crack growth, not depending of crack orientation. In certain multiaxial strain conditions cycle can maintain a constant strain energy density, while simultaneously cycling the individual strain components.

In the aim of giving an answer to the exposed limitations several researchers proposed new parameters as a more generally applicable strain energy release rate factorization for small flaws in multiaxial loading. Mars et al. [54] and Saintier et al. [62,68] proposed two differentiated approaches involving the same critical plane concept, each one developed by their own. Both works were published

simultaneously in 2003. Mars [54] derived the cracking energy density, a continuum parameter aimed at a more general purpose accounting of available strain energy density for the growth of a crack in a given material plane. Saintier et al. [68] proposed a critical plane approach for fatigue crack initiation based on the micro-mechanics of crack initiation. They considered both damage and reinforcement mechanisms observed in elastomers. More precisely, the maximum normal stress acting on the critical plane, defined by the plane experiencing the maximum principal stress over a cycle, was considered to control the fatigue damage evolution. The reinforcement mechanism was related to the minimum crystallinity level on the critical plane during a cycle. Few years later Verron and Andriyana [70] adopted the Configurational Mechanics theory; more precisely, authors related the energy released during defects growth to the properties of the configurational stress tensor.

Currently, from the above mentioned fatigue life solutions, the only one that has been implemented in a commercially available code is the one developed by Mars [54]. He has implemented the fatigue analysis method in a code (Endurica) that has to be used together with a finite element analysis software. The above mentioned equations had been adapted for using with cracking energy density to compute nucleation life, and meet the needs to solve simple uniaxial loadings as well as complex variable amplitude multiaxial loadings. The fatigue analysis code has been used for calculations in the present project, thus the details of equations are presented in the section 3.2.

3.1.4. Summary and Applications of Analysis Approaches

There are two main approaches for analyzing fatigue life in rubber components, the crack nucleation approach, and the crack growth approach. In rubber, the crack growth approach has been studied and used extensively. There can be little doubt that the precursors to fatigue failure in rubber are flaws that exist in the virgin material. Additionally, it had been seen that the major part of life is consumed on the nucleation phase. Then, the approach that relates the crack growth and crack nucleation approaches for small cracks, by using an integrated power-law model of the fatigue crack growth rate, had been developed and is currently used as the main fatigue life prediction method.

The Crack Growth approach is used when cracks become large enough that a nucleation approach no longer applies. The biggest difficulties in this approach, are determining the energy release rate associated with the crack, and predicting the location and path of the fastest growing crack, especially when the geometry and loading are complex. When the crack of interest is small, an additional problem is the determination of the initial size and shape of the crack. Small flaws are of particular importance, since most of a component's life is spent on the growth of small flaws.

The nucleation approach is advantageous for analyzing fatigue life, with no explicit consideration of individual cracks. Crack initiation is normally related to the continuum mechanics quantities (e.g. stress or strain) which are macroscopic. The most widely used parameters for crack initiation are the maximum principal strain, maximum principal Cauchy stress and strain energy density. Approaches such as the cracking energy density or based on configurational mechanics (Eshelby stress tensor) are more complex and recent approaches, which deal with multiaxial fatigue analysis of elastomers.

For uniaxial situations in which failure initiates from a small flaw, the strain energy density can be used to estimate the energy release rate of the flaw, from which fatigue life can be computed, given the fatigue crack growth curve. Nevertheless, for multiaxial situations, the strain energy density is not generally appropriate because not all of the energy is available to be released by the growth of a flaw on a specified plane. The cracking energy density was developed for the analysis of fatigue crack nucleation under multiaxial loading. It was found especially important to account for the effect of material plane rotation, and crack closure. The observed growth rates of nucleated cracks under multiaxial loading were compared with estimates of the crack driving force based on cracking energy density, strain energy density, and maximum principal strain Will [37]. It is demonstrated that estimating the energy release rate based on cracking energy density provided the most consistent correlation with results from all loading paths that were tested for the axial/torsion specimen, and from uniaxial fatigue crack growth testing using the planar tension specimen.

Multiaxial fatigue life prediction results can be correlated based on equivalent strain approaches, energy approaches, equivalent stress approaches, and critical plane approaches. Critical plane models can be used for both proportional and non-proportional loading conditions, and are based on the physical process of the

damage. Critical plane approaches can be strain-based (such as the maximum normal strain), stress-based (such as the maximum principal Cauchy stress), or energy-based (such as, strain energy density or cracking energy density). Energy-based critical plane approaches can reflect the constitutive behaviour of the material, while stress or strain-based critical plane approaches do not. An important issue that should be considered in multiaxial fatigue is in-phase versus out-of-phase loading. When the different loading channels reach to their peak values at the same time, the loading is called in-phase, while when the time of reaching maximum or minimum value for different load channels are different, the loading is called out-of-phase.

In general, a good multiaxial fatigue model should be robust, sensitive to load phasing and mean stress, and applicable to variable amplitude loading. Another important characteristic is the ability to consider crack closure effects. Having considered all this mentioned aspects we have decided to use critical plane approach, by cracking energy density parameter, and using the plane of minimum life as criteria to select the failure plane for the following nucleation life computations.

In the literature, the first fatigue life prediction applications we find used strain energy density for fatigue life prediction. Many engineers and researchers have used strain energy density to correlate analysis results to experimental component life data. Most of the studies refer to the original work of Gent, Lindley, and Thomas [88], or to the follow-up studies of Lake and Lindley [122,165], reflecting the argument presented in the previous section, that the strain energy density is a measure of the energy release rate of naturally occurring flaws.

Building on Ro's results [74], DeEskinazi [166] used the Finite Element Method to compute the strain energy density in three tires with design differences. He correlated observed differences in fatigue life to computed strain energy density levels. The study also evaluated several strain-based criteria, and concluded that strain energy density was the most promising. Oh [167] and Yamashita [168] used strain energy density to predict the fatigue life of bushings and vibration damping devices.

Saintier et al. [68] proposed a critical plane approach for fatigue crack initiation based on the micro-mechanics of crack initiation. They used for the study a diabolo specimen, under non-proportional multiaxial loading, dependent on the material, fatigue crack growth orientation was found to be on the plane of maximum shear

stress amplitude, maximum normal stress plane, or even mixed mode shear and tensile cracking.

Mars and Fatemi [169] designed a novel specimen for investigating the mechanical behaviour of elastomers under multiaxial loading conditions. They used their designed ring specimen with axial, torsion, and both proportional and non-proportional axial-torsion loadings. Harbour et al. [170] used the same specimen and performed both constant and variable amplitude axial-torsion experiments. They used two rubber materials, one which strain crystallizes (Natural Rubber) and one which does not (SBR). Harbour et al. [97] suggested using cracking energy density which is the portion of the strain energy density that is available to cause crack growth on a particular plane. They used the maximum normal strain to find the critical plane and the cracking energy density on that plane to determine fatigue life. Their results showed that this criterion produced similar fatigue life results compared to other approaches such as cracking energy density, strain energy density and maximum principal strain. They [97] also studied the effect of variable amplitude multiaxial loading and concluded that Miner's linear damage rule gave reasonable predictions for their experimental results.

Initially Verron et al. [99] and later Verron and Andriyana [70] adopted the Configurational Mechanics based on Mars theoretical foundation. The approach is still under development, and require further work in order to fully establish a rigorous connection between energy release rate and this continuum parameter, the Eshelby second-order stress tensor [107]. On their publications, Verron and Andriyana [70,171] have correlated their fatigue crack nucleation predictions with formerly published results by Mars [37,69] and Saintier [62].

Aït-Bachir et al. [172], work together on an approach that addresses a continuum theory capable to provide, for every material point in a body, the driving force acting on a hypothetical idealized small crack. They used Configurational Mechanics to derive the energy release rate of a center-cracked region under arbitrary far-field homogeneous multiaxial loading conditions. For the sake of simplicity only the 2D problem is investigated. The method for the computation of the energy release rate consists in Rice's J-integral [112]. For two-dimensional problems, the J-integral is a contour integral that is evaluated on a path that starts on one of the crack faces and ends on the other.

Zarrin-Ghalami and Fatemi [173] evaluated the robustness of methodologies for fatigue life prediction of elastomeric components under complex loading conditions and performed a validation work by using an automobile cradle mount made of natural rubber. Applications to constant amplitude axial-torsion in-phase and out-of-phase loading, as well as variable amplitude loading, are demonstrated using experimental results from a vehicle cradle mount made of natural rubber.

Zine et al. [95] applied the cracking energy density criterion in a finite element code and found good agreement between numerical and analytical results for common strain states. Their experiments results over a diabolo and an axisymmetric specimen also showed the efficiency of this criterion to explain fatigue life of elastomers under multiaxial loading conditions.

Ayoub et al. [174] established a relationship between the fatigue life of styrene-butadiene rubber and the stretch amplitude. They conducted multiaxial constant and variable amplitude tests on cylindrical (axisymmetric) specimens. The specimen curvature radius was large enough to minimize the stress triaxiality effect. Their results showed a good agreement between predicted and experimental fatigue lives. The predictions were based on continuum damage mechanics improved by incorporating cracking energy density criterion. The developed model is both a fatigue damage criterion and an accumulative damage rule.

Wang et al. [175] evaluated fatigue life prediction approaches by using experimental results from proportional and non-proportional loading paths applied to small axisymmetric diabolo specimens made of vulcanized NR. They proposed a continuum damage mechanics model for fatigue damage behaviour of elastomers. They used the Ogden model to construct the constitutive relation for carbon-filled natural rubber. They introduced an equation for fatigue life as a function of applied nominal strain amplitude. They concluded that maximum principal strain and octahedral shear strain provides good predictions of the fatigue life. They also found that comparing to traditional criterion of strain energy density; the cracking energy density model gives better life predictions. They concluded their proposed relation could describe experimental data very well, though restricted to R ratio of zero and fixed frequency values.

Lacroix et al. used the dissipated energy density (DED) as a tension fatigue criterion to describe the uniaxial fatigue behaviour of polychloroprene rubber (CR) dumbbell specimens, and displayed interesting results. Poisson et al. [176] developed a uniaxial

Haigh diagram that suggested the possible crystallization of the polychloroprene under tension. Two methods were proposed to determine this parameter. The first approach, based on the experimental global results, defines the DED as the area contained on the stress-strain hysteresis loop resulting from the cyclic loading of rubber-like materials. And a local calculation uses the finite element method to compute the intrinsic dissipation. The latter parameter being unstable during a complete cycle, its average was then chosen as the fatigue criterion. Both criteria displayed encouraging results.

One of the first applications on real cases using, crack growth approach, based on fracture mechanics approach, came from Clapson and Lake [121]. They studied the crack mouth opening displacement using fatigue crack growth data generated in the laboratory. They developed an estimate of the energy release rate cycle, successfully predicting the rate of growth of cracks at the base of tread pattern grooves in tires.

Huang and Yeoh [177] developed a semi-empirical fatigue crack growth model to predict belt edge durability in tires. The model was based on an estimate of the maximum energy release rate per cycle in a tire, and fatigue testing of a cord-rubber composite model of the tire's belts. Choi, Roland, and Bissonette [178] analysed failure in a large, elastomeric torpedo launcher. Medri and Strozzi [98] analysed crack growth in elastomeric seals. Stevenson et al [179] developed a model to predict the puncture behaviour of thick rubber components penetrated by a sharp-cornered cylindrical indenter.

Numerical implementations of a direct fracture mechanics approach remain labour intensive and computationally expensive. Automated mesh adaptation is required to make these approaches suitable for general use. The lack of general purpose algorithms for crack growth analyses in rubber is known. Fatigue simulation software developers are working on solving it.

Muhr et al. [180] worked on one of first trials to adapt the finite element mesh in the region of the crack tip as the crack propagates, and calls up a finite element solver as a subroutine to calculate the strain energy release rate at each increment in crack length. They investigated the reliability of Software for simulating crack propagation, Zencrack, with Abaqus as the solver, for calculations of strain energy release rate for an edge crack in a strip of rubber in simple extension. The application

of Zencrack to failure of "O" rings by internal cracking is also presented to show how the approach could be applied to a rubber component. W. Mars developed Hyperfatigue during his PhD thesis, which later was improved and become in the first commercial code of fatigue life prediction, named Endurica – a patented system for analyzing the effects of multiaxial, variable amplitude duty cycles on elastomers [181]. During the development of the software number of fatigue life prediction studies had been performed by Mars and co-workers in several real part applications. Mars et al. [123] used at that time the own developed Hyperfatigue software to perform a fatigue life analysis of an exhausts mount. Nowadays Fe-Safe commercialized the Endurica CL solver for fatigue analysis code implemented on the software in the Fe-Safe/Rubber module, or can be purchased the Endurica analysis code by itself to predict the durability behaviour of real rubber components.

3.2. Fatigue Life Determination

The two stages of fatigue failure process are governed by the same physical crack growth mechanisms. The initial stage of crack nucleation occur when a natural flaw of size c_0 develops into a crack of critical size c_f . Crack nucleation life is the number of cycles N_f required a crack to grow to a size of c_f . The final stage of crack growth is that when nucleated cracks grow until structural failure. Due to the slow growing rate of microscopic flaws during the nucleation phase, in relation to the rapid growing rates that occur in propagation phase, the crack nucleation occupies the major part of the total fatigue life as it is illustrated in the graph of Figure 3.5.

In the nucleation stage every material point in the structure are considered potential failure locations, in order to identify the critical location for a crack to nucleate. The crack driving force is estimated for potential cracks under the load history which is dependent of crack position and orientation. This is realized by the equivalent parameter, cracking energy density, which considers any uniaxial or multiaxial loading conditions.

The crack growth stage focus attention on one particular crack. The crack driving force varies along the crack front, and depends strongly on details of the geometry of the structure and the crack. Figure 3.6 illustrate the typical evolution of crack driving force at a critical flaw. The feature that differentiates the crack growth from the crack

nucleation stage is that crack driving force is independent of other length scales of the specimen, and therefore varies linearly with the crack size [37,182]. Once the crack grows until a determined size, usually after nucleation, crack driving force comes to be governed by additional length scales, generally resulting in non-linear dependence of the crack driving force on crack size.

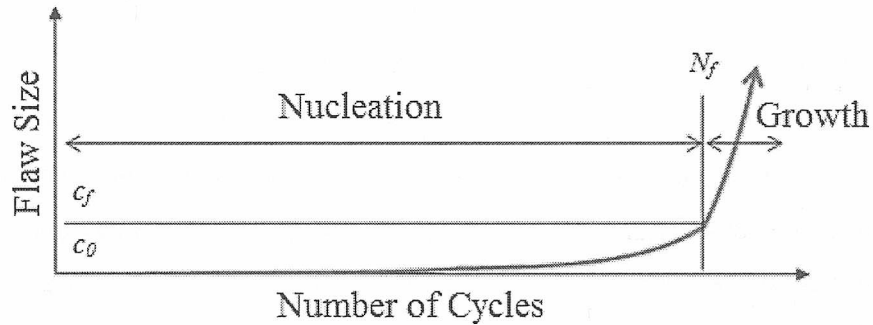


Figure 3.5. Crack nucleation and growth phases during a typical fatigue failure case.

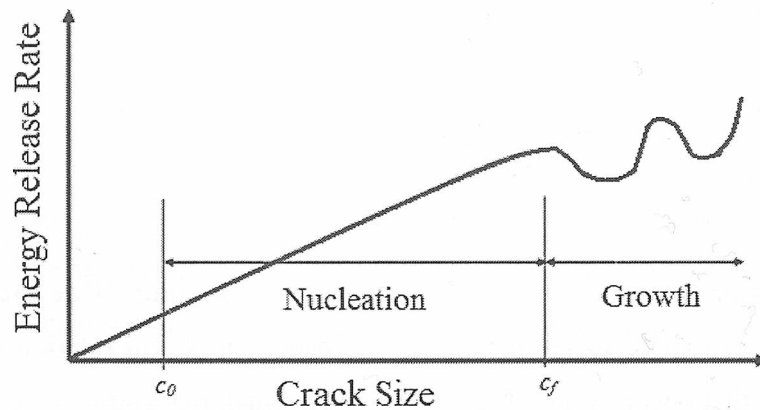


Figure 3.6 Energy release rate evolution during fatigue crack nucleation and growth as the crack is growing, represented by the crack size

For component life predictions a hybrid approach, fatigue crack initiation approach is used along with fatigue crack growth approach based on fracture mechanics. Fracture mechanics approach is used to characterize crack growth behaviour of the material, quantifying driving forces experienced by individual crack through by the energy release rate, T , which is used for total fatigue life prediction of the component, based on specimen crack growth rate data and finite element simulation results. The crack nucleation approach estimates the damage rate and critical locations in the component geometry from the strain history of each element. It predicts the development of small cracks, and considers the critical plane to estimate the

dependence of damage development on orientation of the material plane. To estimate the dependence in orientation the cracking energy density parameter is used, which is independent of size of the defect, depends on state of loading, and on orientation of crack plane. Therefore, fatigue nucleation life predictions for either simple uniaxial or complex multiaxial variable amplitude loading are computed using the critical plane approach determined by cracking energy density parameter, and using the plane of minimum life as criteria to select the failure plane. Actually, for simple strain histories ($R = 0$, constant amplitude, no crack closure except at fully unloaded state), the plane of crack initiation may be computed from the hypothesis that the critical plane is the one that maximizes the cracking energy density. For these histories, the plane that maximizes the peak cyclic cracking energy density will also maximize the amplitude of cracking energy density, and will minimize the computed life. For more complex strain histories, a critical plane algorithm is required to find the plane where is computed the shortest fatigue life.

The computation of life is done by integrating the growth rate of the fastest growing flaw, with the assumption that flaw growth is planar and self-similar. The fatigue nucleation life is obtained from the number of cycles required for the crack to grow from an initial size c_0 to a final size c_f in the integration presented in Eq. 3-26.

3.2.1. Energy Release Rate Computed by Cracking Energy Density

The cracking energy density parameter developed by Mars [37], identifies the portion of the total strain energy density that is available to be released as the crack grows. In the context of elasticity, it is postulated that the energy available to be released on a given surface is equal to the work performed by the tractions on the surface in deforming the surface. Thus, the increment in cracking energy density dW_c is given by the dot product of the traction vector $\vec{\sigma}$ with the corresponding strain vector increment $d\vec{\epsilon}$, as it is shown in Eq. 3-1. This definition accounts for both normal and shear loadings of the given surface. On Mars [37] is explained that traction vector $\vec{\sigma}$ is defined for a given stress state σ , and a given material plane defined by a unit normal vector, \vec{r} . Similarly, the strain vector $\vec{\epsilon}$ quantifies, for the given strain state ϵ , the normal and shear strains associated with a vector in the

direction of the same material plane unit normal vector, \vec{r} . As a result, it is achieved the basic definition of cracking energy density on Eq. 3-30:

$$dW_c = \vec{r}^T \cdot \sigma d\varepsilon \vec{r} \quad \text{Eq. 3-30}$$

For a given crack orientation, this expression may be integrated to determine the cracking energy density, W_c , as a function of the strain state, and is independent of the strain history. The cracking energy density depends additionally, on the material plane of interest, as specified through the unit normal vector, \vec{r} . Therefore, the cracking energy density, W_c , depends on both the state of loading and the orientation of the material plane on which it is evaluated.

The necessity of accounting for finite strains and nonlinear elasticity arises when rubber is subjected to deformations of sufficient severity to cause failure by fatigue or fracture. For accounting that, it is necessary to distinguish between deformed and undeformed configurations, and between references made to points embedded in the material, and references made to points fixed in space. Making these distinctions, results in two different approaches to the description and mathematical formulation of physical principles.

The definition for cracking energy density to state in terms of a material description is often used in finite strain elasticity, Eq. 3-31. The use of a material description is especially essential for the cracking energy density, since it refers to a particular material plane, not a fixed plane in space. For calculation, a material description of the cracking energy density is used which remains valid at finite strains, and for nonlinear elastic materials [37].

$$dW_c = \frac{\rho}{\rho_0} \frac{\vec{R}^T C \tilde{S} dE \vec{R}}{\vec{R}^T C \vec{R}} = \frac{\rho}{\rho_0} \frac{\vec{R}^T (2E + I) \tilde{S} dE \vec{R}}{\vec{R}^T (2E + I) \vec{R}} \quad \text{Eq. 3-31}$$

$C = 2E + I$, where C is the Green deformation tensor, E is the Green-Lagrange strain tensor, \tilde{S} is the 2nd Piola-Kirchhoff stress tensor, T is the Cauchy stress tensor, and ρ / ρ_0 is the ratio of the deformed mass density to the undeformed mass density (i.e. the ratio of undeformed volume to the deformed volume). \vec{R} is the unit vector in the current configuration \vec{r} in terms of the corresponding unit vector in the undeformed

configuration. The relationship between unit vectors in the current configuration \vec{r} and the unit vector in the undeformed configuration \vec{R} is then given by:

$$\vec{r} = \frac{F\vec{R}}{|F\vec{R}|} \quad \text{Eq. 3-32}$$

It is commonly assumed that the energy release rate, T , is the driving force for fatigue crack growth in rubber. For calculations the approach developed by Mars [37] is used, where energy release rate of a small and oriented crack, under uniaxial loads, can be computed via the cracking energy density for perfectly elastic situations.

$$T = -\frac{dU}{dA} = KW_c c \quad \text{Eq. 3-33}$$

As shown in, Eq. 3-33, the energy release rate can be factored into the cracking energy density W_c , the flaw size c , and a constant of proportionality, K . This factorization has been demonstrated to be adequate to be applied for arbitrary multiaxial loadings [170,183–185]. Then, knowing that cracking energy density is equal to the strain energy density in simple tension, Eq. 3-17 can be re-written to calculate the strain energy density in the following equation:

$$T = 2kW_c c \quad \text{Eq. 3-34}$$

The slowly changing strain constant of proportionality, $k(\lambda)$, is assumed to have the same magnitude of the theoretical value of π , which is close to the computed value for $\lambda=1$ from Eq. 3-19. Then, the dimensionless parameter, K , is assumed to have a value $K = 2\pi$, not taking into account the state of deformation. Strictly speaking, K , is known to depend weakly on details of constitutive behaviour, and on the mode and magnitude of deformation. This dependency is ignored to simplify the calculations.

3.2.2. Fatigue Life Computation

The number of cycles required to the crack to reach a specified size that defines the end of the analysis, is called the crack nucleation life. The Endurica fatigue analysis code is used for computing cracking energy density histories and the corresponding

fatigue lives for arbitrarily complex strain cycles. The energy release rate, T , is estimated, for an assumed crack, at the centroid of each element in the model by the Eq. 3-34. The strain history components are obtained from the finite element model by applying some loading history to the part, and recovering the resulting nominal strain components at each instant in time. The program takes as input the history of the strain tensor components, the elastic constitutive model, and the fatigue crack growth curve in terms of the energy release rate. The strain history is given at the centroid of each finite element in the model, and the history number is set to the element number. The Endurica code output includes the cracking plane, the history of the cracking energy density on that plane, and the number of cycles required for a given flaw in the cracking plane to grow to a critical size. Given the crack growth behaviour and the energy release rate history, the fatigue life is computed by the following integral Eq. 3-35

$$N_f = \int_{c_0}^{c_f} \frac{1}{f(T(c, W_c, R))} dc \quad \text{Eq. 3-35}$$

Evaluating the fatigue lives at all locations within the part, at the centroid of each element, and on a user defined number of distinct plane orientations, for each loading case. From the results, the location of failure is predicted as the point with the shortest fatigue life. Then, in the FEA post-processing software each element is simply coloured according to the fatigue life of the element centroid, and the point of failure can be located by locating the element number.

The function $f(T)$ in the denominator of the function to be integrated in Eq. 3-35 defines the rate of crack growth, Δc , per application of the block of load history as a function of the applied history of crack driving force, T . The crack driving force is thus a function of the crack size, c . For the purpose of predicting crack nucleation life, the initial crack size have to be many orders of magnitude smaller than part features, and so Eq. 3-34 may be expected to provide a reasonable prediction of the crack driving force. 1 mm has been used as the upper bound for the analysis, nearly when c approaches a size corresponding to full rupture of the specimen. This is justified by the fact that the fraction of life spent growing the crack from c_0 to c_f is expected to be much greater than the fraction of life spent growing the crack from c_f to complete rupture. It is compulsory to be the final crack size smaller on the relative

dimensions of the part, in at least 10% of c_f , to which Eq. 3-35 can be meaningfully applied.

As mentioned in section 3.1.2.3 fatigue crack growth has four regimes of fracture, each with their own mathematical descriptive equation. Hence, if the prediction wants to be of major precision the piece level integration over the entire range of fatigue crack growth behaviour [162,163]. In practise, however, it is common to assume power-law behaviour over the entire life of the flaw, giving acceptable results [48,155,164]. The combination of the power-law that defines the crack growth rate in the third regime, Eq. 3-22, and equation for the energy release rate calculation of the specific specimen, results in the closed-form relationship between the fatigue life. Then, the fatigue crack growth rate dc/dn presented in Eq. 3-25, and has been later integrated into Eq. 3-26. The energy release rate factorization shown in Eq. 3-33 has been demonstrated [37] to be adequate to be applied for arbitrary multiaxial loadings. Thus, Eq. 3-33 is introduced into the Eq. 3-26 obtaining the following expression:

$$N_f = \frac{1}{F-1} \frac{1}{B(KW_c)^F} \frac{1}{c_0^{F-1}} \quad \text{Eq. 3-36}$$

By the present equation cracking energy density is considered into the fatigue nucleation life calculations. The constants of the equation may be combined into a single material property D as shown in Eq. 3-29, and the equation is resumed in the following expression:

$$N_f = DW_c^{-F} \quad \text{Eq. 3-37}$$

Thus, a commonly used derivation is obtained, that applies not only to uniaxial loadings, also to multiaxial loadings.

3.2.3. Crack Closure Effect

The approach used in Endurica CL analysis code computes separately the independent contributions to cracking energy density due to the normal and shear components of the loading history. When the normal crack face traction is compressive, the normal contribution to cracking energy density is set to zero. The stored elastic energy is not available to be released by crack growth when loading is

in compression. In contrast, there are shear planes on which the cracking energy density is nonzero, and such planes used to be oriented at 45 degrees from the loading axis. Under pure hydrostatic compression cracks at all orientations experience closure, and there is not crack growth. In simple compression, no energy may be released on planes perpendicular to the loading axis, since the compressive stress on that plane causes closure.

3.2.4. Crack Orientation Effect

The rate of growth of an oriented flaw depends strongly on the orientation of the defect. When parameters such as strain energy density, octahedral shear strain, and maximum principal strain are applied as scalar equivalence criteria, they do not address this dependence, since they do not refer to a particular material plane. The cracking energy density is specifically defined with respect to a material plane, and thus considers the effects of flaw orientation. Remember that the plane that maximizes the peak cyclic cracking energy density will also maximize the amplitude of cracking energy density, and will minimize the computed life. For more complex strain histories, a critical plane algorithm is required to find the plane that result in the shortest computed life.

For proportional loading, the strain state does not rotate, and maximizing the increment of dW_c also maximizes W_c . For nonlinear elastic materials, W_c may be evaluated along any convenient path without loss of generality [37]. The increment dW_c may therefore be maximized by evaluating Eq. 3-38.

$$\frac{d}{d\vec{r}}(dW_c) = \frac{d}{d\vec{r}}(\vec{r}^T \sigma d\epsilon \vec{r}) = 0 \quad \text{Eq. 3-38}$$

The consideration of the crack orientation is based on the derivation based upon a cracking energy density, Eq. 3-30, that is only based on the absence of crack closure, i.e. when the normal component of the load on the cracking plane is tensile. This formulation predicts that crack initiate on a plane such that pure mode I loading is always achieved.

When the cracking plane experiences compressive normal loading, the work done by normal components of the load should be disregarded. In contrary, planes distinct to the direction of maximum principal strain may be favoured, shear planes for

example. In simple compression, shear planes maximize the cracking energy density, which experience combined mode II shear and mode I compression. For an isotropic material under proportional straining the principal directions of the stress tensor and the strain increment tensor coincide, therefore the cracking plane is perpendicular to the direction of the maximum principal tensile strain.

Small kinks that appeared at the crack tips, may result in an effective crack orientation at apparently compressive normal loadings. Nevertheless, the crack kinking phenomenon is not of great importance, due to the fact that cracks on favourable planes grow much more rapidly than cracks on unfavourable planes. In fact, over the long term, only the most favourable plane matters, since cracks in other planes will naturally become reoriented in the favourable growth direction.

3.3. Factors that Affect the Fatigue Life of Rubber

There are many factors that influence the fatigue life of rubber. Those factors may be classified as being related to: (i) mechanical load history, (ii) environmental conditions, (iii) formulation of the rubber compound, and (iv) dissipative aspects of the stress-strain constitutive behaviour.

Most of the factors do not affect the fatigue life individually, they are interdependent. Therefore, the quantitative understanding of each factor is necessary for giving robust and accurate predictions of fatigue life, while a qualitative understanding is required for efficient design of rubber components.

The influence of each of the factors on fatigue crack nucleation and growth has been discussed on a large number of publications. Nevertheless, is considered mandatory on a PhD related of fatigue life prediction to make an update of the literature review of factors affecting the fatigue life of rubber. The structure of the updated review presented below is based on Mars [55].

3.3.1. *Mechanical Loading*

Defining a fatigue cycling test, few parameters have to be fixed. The aim of laboratory testing use to be to reproduce and study the behaviour of real parts by simple mechanical histories applied. Fatigue involves crack growth and failure due to fluctuating loads, characterized by parameters such as maximum, alternating,

minimum and mean loading, and/or the R -ratio. Parameters are interdependent, so defining the value of any two the remaining parameters are determined. Those shall be divided in two groups depending on their influence on final results. The parameters traditionally presented against which crack growth rate or fatigue life data is plotted (i.e. alternating or maximum load), and the parameters that modify the influence of the aforementioned ones (minimum load, mean load, or R -ratio)

Other aspects of the mechanical load history that may influence the fatigue process include prior load history (sequence of high and low severity events, prolonged periods of rest), duty cycle, loading rate, sequence, and waveform shape. Each of these factors will be discussed below.

In the following discussions, to denote the mechanical severity the term “load” will be used in refer to any of various criteria associated with specific analysis approaches: strain, stress, strain energy density, energy release rate, etc.

3.3.1.1. Maximum Load and Fluctuating Loading

It is important to be familiar with fatigue testing specific terminology in order to avoid misunderstood and misinterpreted results. Maximum load refers to the maximum value of the fluctuating load. In the earliest rubber fatigue studies, fatigue life was tabulated against alternating strain. This tabulation is important to differ between a static load (which does not cause fatigue failure, even at high, sub-fracture levels), and a fluctuating load (which can cause fatigue failure, even at low levels). Although it does not quantify, by itself, the fluctuation that is inherent to the fatigue process, the maximum load is important for the following reasons. First, the stress-strain response of filled elastomers depends heavily on the maximum load. Second, the maximum load is defined instantaneously, and corresponds to a specific material configuration (the same may be said of the minimum loading).

In later development of the fracture mechanics approach for fatigue crack growth in rubber, the fatigue crack growth rate was tabulated against the maximum energy release rate attained during the cycle [81].

There are different ways to define and tabulate fatigue data, against alternating or maximum load, so long as the minimum (or mean or R ratio) loading is also stated.

Initially, both fatigue crack growth and fatigue crack nucleation studies have been conducted under conditions of fully relaxing cyclic loading ($R = 0$). Especially important in cases where material is a strain crystallizing rubber.

The plot of crack growth rate in function of maximum energy release rate represents the fatigue crack growth rate behaviour of rubber with the four regimes of growth, as shown in Figure 3.3, and discussed in section 3.1.2.3.

When the maximum load (for $R = 0$ conditions) remains below the mechanical threshold, in the sub-threshold regime, cracks or flaws do not grow, resulting in apparently infinite life [165]. Under such conditions, mechanical factors don't affect and other factors (usually environmental nature, like ozone) may eventually cause changes.

When the loading is above the threshold, but below the critical value that results in sudden fracture, a power law relationship is commonly observed. A power law relationship is often observed both in fatigue crack nucleation tests (load vs. life) and in fatigue crack growth tests (load vs. crack growth rate). The relationship between fatigue crack growth tests and crack nucleation tests in this regime was derived in section 3.1.3.2. Above a critical value of maximum load, the fatigue crack growth rate accelerates rapidly to unstable fracture.

3.3.1.2. *Minimum Load, Mean Load, and R-Ratio*

As mentioned in the previous section, there are different ways to define a fatigue fluctuating test. By two parameters of minimum load, mean load and R-ratio a fatigue test is defined. Depending on the polymer and filler types we are dealing with, the effect of minimum or mean loading influence greatly on fatigue life. Increasing the minimum strain has a beneficial effect in strain-crystallizing rubbers up to a maximum. This effect has great practical significance, since rubber components often support a large static load, upon which smaller dynamic loads are superimposed [66].

The benefit of increased minimum strain was studied first in natural rubber by Cadwell et al [66]. Several years later, Fielding [71] studied two newly developed synthetic rubbers, hoping to find a similar minimum strain effect. He found that Butyl-B exhibited the benefit, but that GR-S (SBR) rubber did not. In rubbers that do not exhibit strain-crystallization, increasing the minimum strain can have a

deleterious effect [71], but not necessarily [38]. Fielding identified strain crystallization as the mechanism responsible for the life improvement in Natural Rubber and in Butyl-B.

Comprehensive studies were reported by Lindley for fatigue crack growth in crystallizing [186] and in non-crystallizing [38] rubbers. An important difference between the crack growth behaviour of crystallizing and non-crystallizing rubbers is that under a static load, non-crystallizing rubbers exhibit steady crack growth, while crystallizing rubbers exhibit no crack growth. For non-crystallizing rubbers, the crack growth rate under static load is a function of the time-averaged energy release rate. Under cyclic load, in non-crystallizing rubbers the crack growth rate can be computed as the sum of steady growth due to static loading, and cyclic contributions [38].

Lindley's study [186] characterized the fatigue crack growth rate of gum Natural Rubber as a function of the R -ratio. The R -ratio is the ratio of the cycle minimum to the cycle maximum load. Lindley computed, apparently the first, R based on the history of the energy release rate, ie $R = T_{\min} / T_{\max}$. Lake and Lindley [89] observed a decrease in the crack growth per cycle under non relaxing loading conditions In the case of NR materials. Figure 3.7 illustrates the difference in crack growth rate per cycle when the minimum strain energy release rate in a loading cycle is about 6% of the maximum, the threshold strain energy release rate is effectively increased and the crack growth per cycle at higher strain energy release rates is reduced by a factor of 10. The reason behind this is usually attributed to crystallization in the highly strained region around the crack tip.

Busfield et al [187] studied the applicability of existing fracture mechanics approaches for predicting the direction of crack growth in an inclined pure shear test specimen under mixed mode, $R = 0$ (mode I and mode II) loading. The ability to predict direction of growth with existing techniques appears to be limited. The growth direction was successfully predicted for $R = 0$ conditions. Under $R > 0$ conditions, the observed crack path deviates significantly from the path associated with the maximum energy release rate. This result has been attributed to anisotropy in the fatigue crack growth properties, induced by the action of finite strains on rubber's molecular network. The tendency of the crack to deviate as described above also depends on polymer type, fillers, temperature, and strain state. More

deviation is favoured by polymers that exhibit strain crystallization, higher filler levels, lower temperature [188], and strain states that favour crystallization (for example, simple tension is more favourable to strain crystallization than equibiaxial tension) [73].

Mars [37] developed model to describe the effect of R ratio on the crack growth rate. The model is purely empirical and is based on the following observations. First, that at any given constant R ratio, the effect of maximum energy release rate on fatigue crack growth rate approximately obeys a power-law, at least above the fatigue threshold. Second, the power-law relationships for each individual R ratio appear to converge at a single point defined by the critical energy release rate and a maximum fatigue crack growth rate. The model developed embodied all this observations and has been used on this thesis.

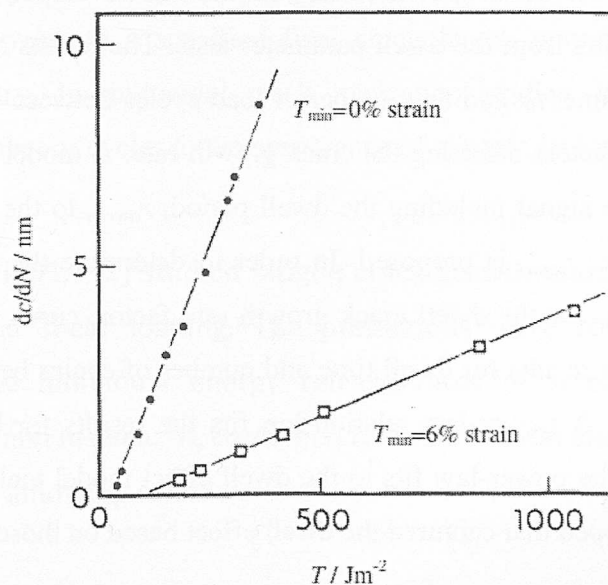


Figure 3.7 The crack growth per cycle, dc/dN , as a function of maximum strain energy release rate, T , for different minimum tearing energies, T_{\min} . T_{\min} equal to zero and T_{\min} equal to about 6% of the maximum (Lake and Lindley [89])

3.3.1.3. Annealing and Dwell Periods

Roland [189] studied the effect of prolonged static load periods (“annealing”) on the strength and fatigue life of polyisoprene-based elastomers (a crystallizing rubber). The annealing effect in both the fatigue life and ultimate tensile strength was analysed, finding that have a parallel effect on both. He have seen that annealing increased fatigue lifetime relative to the results for uninterrupted fatigue testing after

24 hours or more, and better at elevated strain (e.g., 124% elongation). Fatigue life was evaluated under $R = 0$ displacement control to a maximum strain of 124%. Annealing periods in the range from 0 to 3 days were investigated.

Harbour et al. [190] realized that current fatigue prediction methods do not account for the dwell effect. They performed a series of uniaxial fatigue crack growth experiments on filled SBR under variable amplitude loading conditions. Test signals alternate periods of cyclic loading with dwell periods ranging from 1 to 100 seconds at a near zero stress level. Signals that include the dwell produced higher crack growth rates than corresponding constant amplitude test signals without a dwell period. Using experimental crack growth rate as comparative dwell period tests produce up to 30 times greater rates than constant amplitude ones. Harbour et al. go further on the study and they solve an existing need until then and account for the dwell effect on crack growth rates, a model was developed for the dwell effect based on the results from the dwell parameter tests. The results of these tests indicate that the dwell time, t_d , and the number of load cycles between dwell periods, N_d , are the dominant factors affecting the crack growth rate. A model relating the crack growth rate for the signal including the dwell period, r_{dwell} , to the constant amplitude crack growth rate, r_{nom} , is proposed. In order to determine the appropriate mathematical relationship for the dwell crack growth rate factor, curve fits for the average crack growth rate results for dwell time and number of cycles between dwell periods were performed. A power-law relationship fits the results for both parameters the best. Applying the power-law fits to the dwell effect model yields on an empirical model was developed that captured the dwell effect based on those parameters.

$$r_{dwell} = r_{nom} (1 + c_d t_d^{c_1} N_d^{c_2}) \quad \text{Eq. 3-39}$$

Where the coefficient c_d and the exponent c_1 and c_2 are based on curve fits to the experimental data. The model accurately represents the dwell effects in terms of both parameters. It should be noted that the model differs from the experimental rate indicating a possible tendency for the model to slightly over predict the dwell effect at shorter dwell times.

Dwell periods also produced increased crack growth rates in natural rubber, but the effect was less significant. They proposed that “the effect is caused by the time-dependent recovery in the rubber microstructure at the crack tip producing a

localized and temporary elevated stress-state during loading events immediately following a dwell period”.

3.3.1.1. *Multiaxiality*

Rubber components in service rarely operate under the simple strain states evaluated in fatigue studies using lab specimens. Recent advances in simulation technology make possible to predict realistic multiaxial load histories. Since last decade the ability to predict fatigue life from computed load histories seems to be possible, lot of improvements are being achieved.

Fatigue crack growth under multiaxial conditions has been broadly investigated, in contrast to crack nucleation that less has been investigated till last decade. In multiaxial crack growth studies, the objective is to predict the growth rate and propagation direction of a given crack. Knowing the growth rate history of material, the number of cycles to a specified final crack length may be computed for a complex geometry. In multiaxial crack nucleation studies, the objective is to ascertain the number of cycles to the appearance of a crack, its location, and possibly its orientation.

Stevenson et al [191,192] studied fatigue crack growth under combinations of compression and shear loading. The predictions were based on analytical estimates of the individual energy release rates of small cracks in axial compression T_c , and in shear T_s , combined to obtain a total energy release rate T according to the following rule.

$$T = (\sqrt{T_c} + \sqrt{T_s})^2 \quad \text{Eq. 3-40}$$

Busfield et al [187] take advantage of recently developed finite element possibility to compute energy release rates to successfully predict both the rate and direction of crack growth in an inclined pure shear test specimen at $R = 0$ loading. Mixed mode crack growth rates for $R = 0$ loading were successfully predicted based on mode I, $R = 0$ fatigue crack growth data. Under multiaxial loading, the crack path tends to grow in such a way that mode I loading is approached. Taken together, the apparent successes reported in these studies suggest that, if direction of propagation is properly accounted for, the fatigue crack growth characteristic curve of rubber is independent of whether the loading is mode I, mode II, or mode III.

Mars and Fatemi [183,184] recognized the need of better understanding the multiaxial effects on rubber fatigue, especially in crack nucleation. Tough research work had performed reviewing theoretical aspects, observing experimental and developing a new methodology for multiaxial fatigue nucleation of defects or flaws [169,193]. The lack on multiaxial fatigue crack nucleation prediction was notable, and a number of initiation-based models for multiaxial fatigue of elastomer have been proposed since the first Mars [54] and Saintier [62,68], and later Verron and Andriyana [100]. The mentioned approaches and some newer have been detailed on chapter 3.1.1.4

3.3.1.2. *Loading Frequency and Waveform*

The different test frequency and waveform, both, alters the strain rate, and the time under deformation for each cycle. All of those programmable testing parameters effects are affecting each other, and their consequences are not easy to determine on their own, without taking into account their interrelation.

The effect of loading frequency depends on polymer type. For rubbers that exhibit strain crystallization, frequency is not observed to have much effect on fatigue life, under isothermal conditions, over a range of at least 10^{-3} to 50 Hz [50]. For non-crystallizing rubbers, frequency is observed to have a larger effect. The effect has been attributed to time-dependent constant crack growth, associated with viscoelasticity [38,87,89]. This steady component of crack growth is more important at frequencies below 0.2 Hz. Lake and Lindley showed that crack growth rates due to time-dependent (steady crack growth), and cycle-dependent (mechanical fatigue) contributions are additive. The time-dependent component of the crack growth rate depends on the mean value of the energy release rate.

Thick components can exhibit a large temperature rise in comparison to thin components. At sufficiently high frequencies, thermal runaway, an additional failure mechanism becomes important. Thermal runaway occurs when the rate of internal energy dissipation becomes greater than the rate of heat transfer to the surroundings [53]. When this occurs, the temperature increases rapidly, causing severe degradation of the rubber. The effects of temperature are greater in non-strain-crystallizing rubbers, whose strength derives from viscoelasticity [50].

Most studies of fatigue crack propagation have utilized the simple sinusoidal excitation. Instead of choose the signal that better reproduce the real loading case, simple sinusoidal is predominant in the literature. Shape has been found to influence fatigue behaviour, particularly for non-crystallizing polymers. A pulse waveform, considered more realistic to the strain history in a tire, has been compared to a sinusoidal waveform by several researchers [164]. The effect depends not only on polymer type, but also on other compound ingredients. Accounting for the effect of loading rate on the cyclic crack growth rate, note that the loading rate in the pulse waveform is much greater than the loading rate in the sinusoidal waveform.

Andreini et al. [194] support scientific discussion contributing with data generated comparing the sine mode versus pulse waveform at same strain rate on three different samples based on NR, SBR, and BR. Regarding the waveform influence on fatigue behaviour, effects were found to be different depending on the polymer present in compound and its ability to get oriented: high for natural rubber, intermediate for BR, and negligible for SBR. No differences were observed for polymers with weak or no strain-orientation capability, while significant differences in crack propagation resistance were observed in NR, which possesses an intrinsic tendency to permanent macromolecular chain orientation.

3.3.1.3. *Loading Sequence*

As should be extrapolated from stress relaxation studies (Mullin's effect), applying step-up and step-down load sequence don't have to have same consequences over rubber components fatigue life. Sun et al [195] studied the effects of applying step-up and step-down sequences of strains on residual ultimate tensile strengths in typical filled tire compounds. The study found that "in all cases, a series of increasing strains...", "... reduced the (residual ultimate) strength to a greater degree than the same strains applied in decreasing order." This effect is attributed to a strain-dependent Paris-law exponent, and to the effect of stress-softening or Mullins effect, which is discussed in Chapter 4.

3.3.1.4. *Duty Cycle*

Mars [196] investigated the duty cycle on each material plane along with its corresponding damage to transform the multiaxial loading into the potential localized flaws. After identifying the damaging events, the original duty cycle is simplified

and reconstituted to a new duty cycle, even the amount of the most damaging events. The new shortened duty cycle maintains those features of the original duty cycle corresponding to the original mode of failure and shortens the time scale of the test. For multiaxially loaded rubber parts, Flamm et al. [197] proposed discretizing the continuous signal by a level crossing cycle counting method for each loading channel. Then they constituted the stress amplitude history and performed Rainflow cycle counting on these alternating points.

3.3.2. *Environmental Conditions*

Environmental effects have a great importance on rubber fatigue life, in both crack nucleation and crack growth. Nevertheless due to its deleterious effect it is crucial particularly at long life. Both the stress-strain and fatigue properties of rubber evolve in a way that is highly dependent upon the temperature of the material, and upon the presence and concentration of various chemical reactants.

3.3.2.1. *Temperature*

Temperature has a deleterious effect on all fatigue life or crack growth of rubber made components. The effect is greatest in non-strain-crystallizing rubbers whose strength derive from viscoelasticity. For gum SBR in displacement controlled tests, an increment in temperature from 0°C to 100°C result in a fatigue life drop by a factor of 10^4 . For gum NR in displacement controlled tests, fatigue life drops by a factor of only 4, for the same temperature range [157]. The ability of natural rubber to crystallize at high strains changes relatively little at least over the temperature range 10-80°C. On the independent study of temperature effect in crystallizing materials, the improvement of the fatigue resistance due to the crystallization in highly strained zones in the vicinity of the crack tip. If the temperature rises in this zone, the crystals melt and the reinforcement effect is not visible anymore. The incorporation of fillers may reduce the temperature dependence slightly [51].

3.3.2.2. *Ozone*

Ozone concentrations on the atmosphere can cause cracking within a few weeks in unprotected rubber components. Minimum surface tensile strain is required for ozone to generate cracks to start growing in a direction perpendicular to the strain. Due to the stress concentration, elastomer network chains at a crack tip are energetically

favourable for reaction with ozone. Exposure to ozone during a long-term fatigue test significantly increases crack growth rate and shortens life [40,157,158,165,198–202]. Ozone reacts with carbon-carbon double bonds in the main polymer chain, causing scission of the chain.

Crack growth due to ozone attack occurs whenever the instantaneous energy release rate exceeds a small threshold; often denoted G_z . G_z is typically much smaller than the mechanical fatigue threshold T_0 [40,199,200]. The value of G_z depends strongly on compound formulation, particularly the presence of antioxidants/antiozonants. For a not protected rubber, $G_z \approx 0.1 \text{ J/m}^2$. The presence of antiozonants can increase G_z by a factor of 10 or more [1]. For comparison, the mechanical fatigue threshold is approximately $T_0 \approx 50 \text{ J/m}^2$. Ozone does not appear to affect the value of the mechanical fatigue threshold as mechanical fatigue is more severe [203]. Other chemical agents can attack rubber in a manner similar to ozone [204]. Above the threshold value G_z or T_z , the rate of crack growth $dc/dt=r_z$ due to ozone attack is independent of the crack driving force. The crack growth rate depends on the ozone concentration and on the temperature Θ . Two mechanisms control the crack growth rate. At temperatures near the glass transition T_g , the crack growth rate is proportional to the temperature, independent of ozone concentration. At sufficiently high temperatures, $\Theta - T_g > 100^\circ\text{C}$, the crack growth rate depends only on ozone concentration, and is independent of temperature. The total rate of crack growth can be estimated via the following model due to Gent and McGrath [204].

$$\frac{dc}{dN} = \left(\frac{1}{R_1} + \frac{1}{R_2} \right)^{-1} \quad \text{Eq. 3-41}$$

$$R_1 = K_z c_{O_3} \quad \text{Eq. 3-42}$$

$$R_2 = K_V e^{\frac{F_V(\Theta - T_g)}{G_V(\Theta - T_g)}} \quad \text{Eq. 3-43}$$

R_1 reflects the rate at which ozone molecules impact elastomer network chains at the crack tip. R_2 is related to viscoelastic behaviour, through the finite time required to redistribute crack tip strains, after scission of a network chain. Typical values for these parameters are: $K_z=0.8E-5 \text{ m/sec L/mg}$, $K_V=0.12E-14 \text{ m/sec}$, $F_V=40$,

$F_V=52^\circ C$. These constants were derived [204] for a series of butadiene-styrene copolymers with styrene content in the range 0-80%.

3.3.2.3. *Oxygen*

The presence of oxygen influences mechanical fatigue behaviour in at least two ways. First, exposure to oxygen decreases the mechanical fatigue crack growth threshold from its value in vacuum. Second, oxygen dissolved or diffused in the rubber may induce chemical changes over time to the bulk elastomer network structure; this process is commonly called oxidative aging. Oxidative aging cause embrittlement and reduce fatigue crack growth resistance [51].

Even for new rubber specimens with no prior exposure, the presence of oxygen increases the fatigue crack growth rate, at constant energy release rate. The effect is conveniently described in terms of the energy release rate required to maintain a constant crack growth rate. At low energy release rates, for unfilled natural rubber, the energy release rate in air is approximately half the energy release rate in vacuum, for the same fatigue crack growth rate [51]. The difference becomes less significant at higher energy release rates, but depends on test frequency. For lower frequencies, the difference persists to higher energy release rates. The magnitude of the effect depends also on polymer type. Gent and Hindi [144] compared crack growth rates under both static and cyclic loadings, in air and in vacuum, for NR, SBR, and BR. They observed only a factor of two change in fatigue crack growth rate for NR, due to the presence of oxygen. For SBR and BR, a factor of 8 difference between air and vacuum was observed. They demonstrated that the oxygen effect on fatigue crack growth rate is reversible, in an experiment in which oxygen atmosphere was applied, then removed, then applied again.

Beatty [205] reported an eight years study to comprehensive the oxidative hardening effect of SBR. It is shown that oxidation increase the hardness of rubber and several factors affecting on the hardening process are reported. Most synthetic rubbers harden in a manner qualitatively similar to the hardening of SBR. Thus, to predict service life of commercial products, it is important to bear in mind all above mentioned effects. Note that laboratory test specimens are thinner that real thick components, leading to slower rates of oxidation, and thus longer service life than predicted from laboratory specimens [53].

Oxidative aging irreversibly changes the mechanical properties of the rubber, including the fatigue and fracture properties. In general, aging causes embrittlement of the rubber, faster fatigue crack growth, reduced threshold and critical fracture energies, and shorter fatigue life [206]. The aging effect depends strongly on many formulation and processing variables. Some of these are discussed in section 3.3.3.

3.3.3. Rubber Formulation

Rubber has the peculiarity that a wide range of mechanical properties can be achieved by varying the compound formulation and manufacturing process. The factor in compounding that mostly influence the fatigue behaviour are the type and quantity of: polymer, filler, antiozonants, antioxidants, and curatives. Manufacturing processes also influence fatigue behaviour through their influence on factors such as ingredient dispersion, state of cure, and the presence and nature of precursor sites for crack initiation. There are many factors that affect the fatigue life of a rubber specimen in many different, complex and interacting ways. It may be said on the basis of fatigue theory, that compounding variations affect fatigue life through the effect of amount and stability of crosslinks upon the physical properties at any given point in the rubber specimen.

3.3.3.1. Polymer type

The polymer type or nature of rubber has influence on several aspects of the fatigue behaviour. Whether or not the polymer exhibits strain crystallization is a primary consideration [138]. Strain crystallization has been shown to have beneficial consequences on fatigue performance at moderate or high strain levels, and shows a small sensitivity to environmental effects [144]. The primary difference is that in non-strain-crystallizing rubbers, continuous crack growth under a static load occurs in contrast to the stick-slip growth of strain-crystallizing rubbers.

A review of elastomeric polymer types and their applications is given by Hamed [207]. Examples of polymers that exhibit strain crystallization include natural rubber (NR), and isoprene rubber (IR), and polychloroprene (CR). While Polymers exhibiting little or no crystallization include styrene-butadiene rubber (SBR), polybutadiene (BR), butyl rubber (IIR), acrylonitrile-butadiene rubber (NBR) and ethylene-propylene rubber (EPDM).

Due to the wide range of properties that are possible in engineered rubbers, it is difficult to give results representative of a given polymer type in specific applications, except for highly simplified or standardized formulations. Lake and Lindley's results for fatigue crack growth behaviour of eight polymer types [200], both filled and unfilled, are shown in Figure 3.8. Results shown have common reference on the literature, as presented polymers show the described fatigue crack growth behaviour. From these data, it can be seen that rubbers that exhibit strain crystallization (NR and CR - compounds A and D of Figure 3.8) have a lower slope on fatigue crack growth curve, and are superior at high energy release rates, relative to other elastomers. At high energy release rates, it can be seen that differences in elastomer type can account for as much as two orders of magnitude in crack growth rate. At low energy release rates, the differences appear to be smaller.

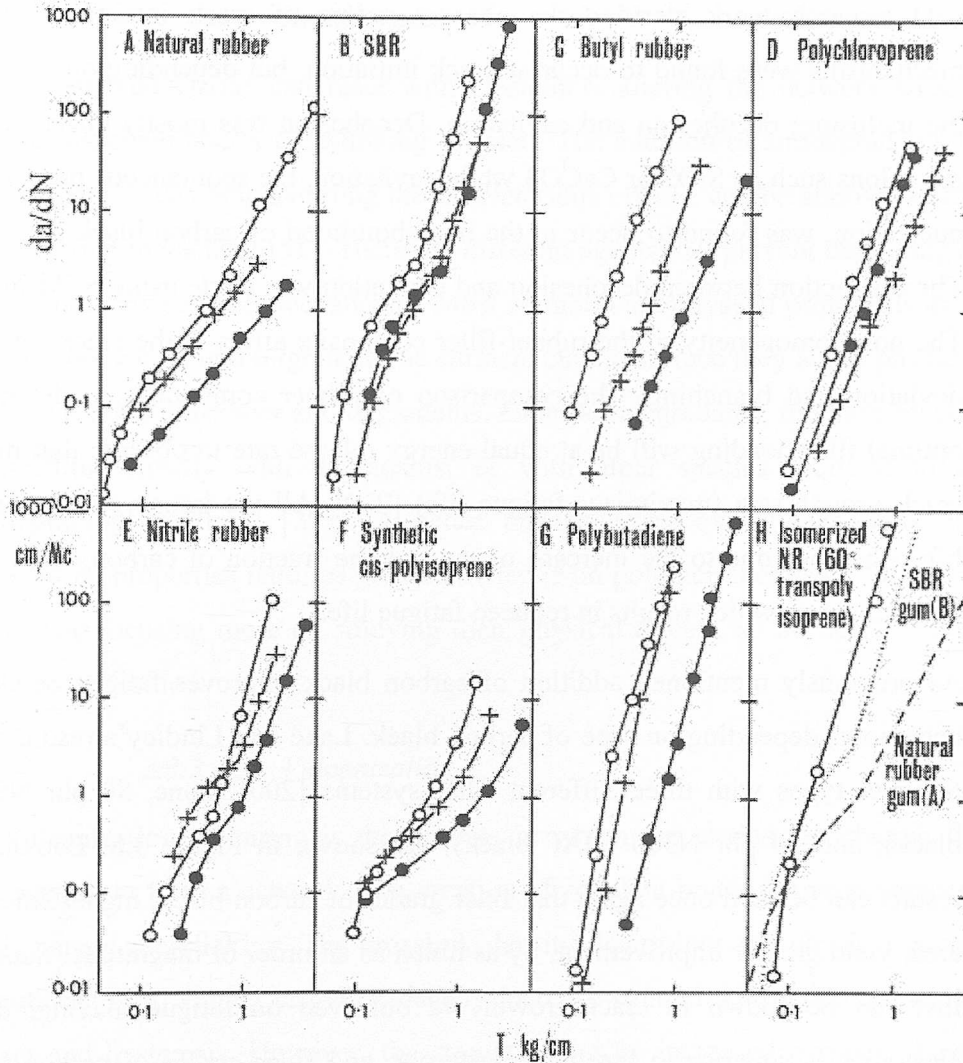


Figure 3.8 $R = 0$ fatigue crack growth behaviour for 8 elastomer types. Results for unfilled, and two filler types are shown [200]. \circ Gum; \bullet Filled with 50 phr N300 carbon black (fine) Filled with; $+$ Filled with 50 phr N900 carbon black (coarse)

3.3.3.2. Filler

To strength raw material in rubber compounds it is common to add carbon black fillers. The strengthening effect [208] depends on filler type, and the volume fraction used [170]. Taking into account just the strengthening effect on the material, at same volume fraction, low structure black are superior to high structure blacks, and higher filler surface area is beneficial [209]. The effect of filler on fatigue properties has been attributed to multiple mechanisms. The addition of carbon black induced pronounced changes on stiffness and hysteresis; this improvement will have to take into account at high frequency fatigue tests, due to the thermal runaway of material. The addition of filler particles during the mixing and fabrication is a critical process particles use to agglomerate resulting in increases effective initial flaw sizes. Le Cam

[61] research work clarified the obscure nature of crack initiation. Two main mechanisms were found to occur at crack initiation, but depending on the nature of the inclusion: decohesion and cavitation. Decohesion was mostly observed at rigid inclusions such as SiO₂ or CaCO₃ while cavitation, the spontaneous process of void nucleation, was found to occur in the neighbourhood of carbon black agglomerates. The distinction between decohesion and cavitation was made using SEM inspection. The non-homogeneity of the rubber-filler composite affect at the crack tip blunting, deviation and branching. The comparison of rubber compounds to determine the optimal filler loading will be at equal energy release rate to observe that minimizes crack growth rate (maximizes fatigue life) [210]. All the improvements on fatigue life behaviour due to the increase of the volume fraction of carbon black go to an optimal above which results in reduced fatigue life.

As previously mentioned addition of carbon black improves fatigue crack growth behaviour, depending on type of carbon black. Lake and Lindley's results for eight polymer types with three different filler systems [200] (none, 50 phr N900 (MT black), and 50 phr N300 (HAF black)) are shown in Figure 3.8. Looking to the results can be seen once again that finer grades of carbon black, higher filler surface area, yield greater improvement, by as much as an order of magnitude. Same effects that can be shown in crack-growth are observed on fatigue loading, the filled elastomer is superior to the gum elastomer, and finer grades of carbon black are superior to coarser grades [154].

Due to the stiffer effect of carbon black fillers, it is important to consider whether an application operates under displacement control, load control, or somewhere in-between. In displacement control, minimizing compound stiffness (by using less filler, for example) will minimize the energy release rate, resulting in maximum fatigue life. In load control, however, minimizing compound stiffness will lead to higher displacement, usually increasing the energy release rate, and resulting in poor fatigue life. Effective comparisons of compound differences must therefore account not only for differences in the fatigue properties (at constant energy release rate), but also for differences in the operating energy release rate, due to differences in compound stiffness. Similar conclusions but arguing the selection of coarse or fine carbons, both in same volume fraction, is published on [154].

3.3.3.3. *Antidegradants*

Oxygen and Ozone can react with elastomers altering the network structure, and causing chain and/or crosslinking scission. The addition of antidegradants to rubber compounds can help avoiding those deleterious effects, can be almost as effective as operating in vacuum [51]. There are different agents that prevent degrading chemical reactions by several mechanisms. Most common are physical protectants as waxes in a rubber compound migrate to the surface. On the surface they act as physical barrier between the elastomer and degradants. Other antidegradants, function by chemically reacting directly with degradants, or with other species required to complete degrading reactions. [207]. A better understanding of antidegradants effects on material properties requires great knowledge on polymer chemistry. On this exercise we are focusing more on studying their physical effects, so no deeper research has been performed.

3.3.3.4. *Vulcanization*

Vulcanization or curing is the process in which the chains are chemically linked together to form a network. The creation of covalent bonds between adjacent chains is named crosslinking. The crosslink density determines the physical properties of rubber [153]. Higher crosslink density increase strength and modulus, while reduce set and hysteresis. However, the strengthening by increased number of crosslinks, has in consequence a decreasing ability of the elastomer to dissipate energy through hysteresis. Therefore the improvement effect is until an optimum crosslink density, which results in the longest fatigue life [211].

The type of crosslink formed during vulcanization is of great importance for fatigue properties [50,122,161]. Polysulfidic crosslinks appear to be better than monosulfidic or direct carbon-carbon (peroxide cure) crosslinks. The superiority of polysulfidic crosslinks is attributed to the ability of the crosslink to break before primary elastomer network chain carbon-carbon bonds. In addition polysulfidic crosslink has the advantage to subsequently reform. This mechanism leads to increased crack tip blunting, and to increased dissipation due to hysteresis.

As discussed in section 3.3.3.2, to compare effectively improvements due to vulcanization must account not only for differences in fatigue properties, also for energy release rate. Compound stiffness has a direct effect on energy release rate, but

improving effect depends on whether the application is subject to load control or displacement control.

Santangelo and Roland [26] verified that double network of natural rubber (NR) has a higher modulus than single network of equal crosslink density. Fatigue life of double networks NR was also found to be as much as a factor of 10 higher than conventionally crosslinked NR, although tensile strength was slightly lower.

3.3.4. *Dissipative Effects*

An energy criterion for crack growth for linear elastic materials was proposed by Griffith [94]. It was assumed that mechanical energy lost from the system was balanced by corresponding increases in the surface free energy of the fracture surfaces. This concept was first applied successfully to the tearing of rubber which exhibit highly nonlinear, elastic constitutive behaviour by Rivlin and Thomas [77]. It was recognized that the decrease in mechanical energy of the system was balanced, not only by increased surface free energy, but also by work done through dissipative mechanisms associated with the crack tip. For strain crystallizing elastomers, crystallization is another source of dissipation.

Filled rubbers exhibit dissipative mechanical responses, not only at high strains (network chain breakage, strain crystallization), also at small and moderate strains, particularly under cyclic loading. The precise effect of these dissipative processes on crack tip fields is not well understand, because multiple mechanisms are involved, and because constitutive models capable of describing all the mechanisms are not available. As discussed in section 3.1.2.4, dissipative processes near the crack tip result in crack tip blunting, and in reduced crack tip stress/strain levels. Also, that dissipation in the bulk of a rubber specimen reduces the energy available to be released by crack growth. Experience suggests however, that despite the uncertainties, a fracture mechanics approach may be usefully applied to fatigue crack growth in filled rubbers [212].

Relationships between hysteresis and fatigue properties have been observed by many researchers [39,117,139]. Hysteresis seems like controls the sensitivity of the crack growth rate with respect to tear energy: the higher the hysteresis, the lower the slope (power-law exponent) of the energy release rate-crack growth relationship.

3.3.4.1. *The Mullins Effect*

The Mullins effect [3,138,143] is an initial transient softening of the stress-strain curve in rubber. The first loading of the virgin rubber gives a much stiffer response than subsequent loadings. The degree to which rubber is softened depends on the maximum value of the strain experienced during the loading history. The larger the maximum strain experienced, the softer the stabilized response. Subsequent loadings of equal or lesser magnitude tend to stabilize after few cycles. The Mullins effect is exhibited primarily by filled rubbers. It is widely believed that this transient dissipative mechanism is beneficial to the strength and fatigue properties of filled rubbers [50]. It has to be considered on simulations that each material point in a non-uniformly strained body achieves a distinct stabilized stress-strain response, depending on the maximum strain experienced at each point [2].

3.3.4.2. *Strain-Crystallization*

Strain-crystallization is a high-strain hysteresis mechanism that certain elastomers exhibit due to an applied strain [138,139]. At large strains, the polymer network chains become sufficiently aligned such that a highly ordered state exists [4]. This causes a time-dependent phase change in the elastomer from an amorphous rubbery state to a crystalline state. When the strain is reduced sufficiently to allow polymer network break the alignment, the crystallized elastomer returns to the rubbery state [213]. Strain crystallization added stiffness and hysteresis to the material, and crystalline state exhibits increased resistance to crack growth in the crack front. This causes a significant improvement on fatigue properties with increasing minimum strain, as discussed in section 3.3.1.2. SBR material is non-crystallizing and the phenomenon less evident. However, non-fully relaxing cycles may have a small effect similar to strain crystallization because of the occurrence of static, time dependent crack growth [213].

Ellul [50], as discussed in section 3.3.1.2, reported on the significant effect of frequency for non-crystallising rubbers due to viscoelastic behaviour of material. This reflects the time dependent element of the cyclic crack growth, and is superimposed on the cyclic crack growth measurement. This component is especially important at low frequencies (below 0.2Hz). For strain crystallising rubbers crack growth does not occur in a time dependent manner and cracks can only propagate

above a given critical applied tearing energy. Hence, the time dependent component does not dominate, and cyclic frequency has very little effect on the crack growth per cycle [89]. However, if the frequency is high, especially for thick specimens, excessive heat can be generated [214]. The degradation due to the temperature is then the predominant cause of failure, instead of the mechanical cyclic crack.

3.3.4.3. *Rate Independent Hysteresis*

The phenomenon of hysteresis results from the loss of energy on stretching and relaxing rubber during a load-unloading cycle. The energy dissipated (hysteresis) is seen on the force deformation plot, by the area between the loading and unloading curves. The dissipation of energy causes softening on rubber during the unloading phase. The magnitude of the energy loss is greater in filled elastomers than in unfilled, and the hysteresis increases with the amount of particulate filler. In typical filled rubbers, at low and moderate strains, the observed hysteresis loop is approximately rate independent. The rate-independent behaviour is not captured accurately by linear viscoelasticity. Triboelastic models have recently been used to model this behaviour [140–142]. Even if the energy loss mechanism is still active at high strains, its magnitude is small compared to losses associated with Mullins effect and strain crystallization.

3.3.4.4. *Viscoelasticity*

Unfilled elastomer shows a stress-strain behaviour that can be reasonably modelled as linear viscoelastic. In addition, due to this viscoelastic behaviour unfilled rubber exhibit a negligible dissipation [215].

Associated with viscoelasticity, non-crystallizing rubber shown a steady crack growth under static load. In strain crystallizing rubbers, crack propagates in a steak (crack arrest) –slip (relative rapid crack growth) manner [66,71,88,89]. As noted in section 3.3.1.2, in amorphous rubbers, the total fatigue crack growth rate can be computed as the sum of steady growth due to static loading, and cyclic contributions. At higher frequencies, and higher filler levels, the cyclic contribution can dominate the fatigue behaviour [38]. Inversely, at low frequencies or low filler levels, crack growth under static loading must be carefully considered.

4. Material Fatigue Behaviour Characterization

Mechanical fatigue behaviour of rubber depends on a number of factors that affect on life, as is detailed in section 3.3. Likewise, the approaches to analyse and characterize fatigue crack nucleation, and fatigue crack propagation behaviours are summarized in section 3.1. The main characteristic of the nucleation approach is that cracks are not introduced artificially into the test specimen, only intrinsic flaws or defects are present. Then, the component failure can be defined by at least three different criteria: (i) as the number of cycles required for cracks of a given size to appear, (ii) as the stiffness of the specimen to decrease by a specific amount, and (iii) as specimen rupture. To characterize the crack nucleation we have used the last criteria, the rupture of the test sample. In contrast, crack propagation approach requires an external crack to be induced by a razor blade, and the rate of the crack to grow is measured.

In both approaches, uniaxial, constant-amplitude, sinusoidal cyclic loading over simple geometry specimens provides a baseline against to compare the results of more complex geometry and loading tests. In order to predict the failure of a body subjecting complex loading, based on measurements made on a simple geometry specimens subjected to uniaxial loadings, there must be an equivalence principle on which to base comparisons. In general, the equivalence principles associated with the nucleation and propagation approaches involve a parameter that characterizes mechanical severity [37], and must be related to both, fatigue failure and crack growth. Thus, a unique value of the parameter has to define a unique value of fatigue life or crack growth rate, for any specimen geometry and loading case. As discussed in section 3.1.1.4, the energy release rate quantified by the cracking energy density or strain energy density appears to be the only two parameters that satisfy the requirements.

This chapter presents the experimental program for characterizing material properties and fatigue behaviour using simple geometry specimens under constant amplitude loading. The different test procedures for obtaining fatigue nucleation life and crack growth properties are explained in detail. Crack growth experiments have been conducted first at fully relaxing conditions, or zero R-ratio. Then, have been

conducted at non-fully relaxing conditions of several levels of minimum strain, thus positive R-ratios. It has been selected two materials to work with in the project, one filled Natural Rubber (MCN) that strain crystallizes, and one filled SBR + BR (MBS) compound that does not strain crystallizes. It has to be taken into consideration, that as mentioned in section 3.3.1.2, positive minimum strain arrests the growth of cracks, and this beneficial effect is more pronounced in strain crystallizing rubbers, as has been explained in section 3.3.4.2.

The characterization method has been defined after a large literature review, two internships on prestigious rubber research centres, and advises of a fatigue life prediction expert, Dr. Will Mars. I had been for five weeks in the Rubber Research Group of Dr. James Busfield in Queen Mary University of London. Then, I had been for five months in the group of Dr. Zoltan Major, in the Polymer Competence Centre Leoben, in Austria. Finally, the guidance of Dr. William Mars has been key to define and implement a feasible process. During the collaboration with him in an industrial project he convinced us of the importance of process automation, and he advised us in the process. In the project, the specific material characterization to fatigue had been done at Leartiker lab. Thus, the testing procedure and data processing had been automated, and scope of characterization tests had been adequately defined.

The intrinsic flaw size of the material is determined by the observation and comparison of crack nucleation life results with a set of strain life curves, computed from hypothetical initial flaw sizes. The material intrinsic flaw size is the principal data to predict the nucleation and fatigue life. Additionally, in the simple tension cycling to break test has been installed a system for automatically take pictures of the situation of the crack during the testing. Thus, the volume density of crack precursors can be measured and classified by size. In the approach is assumed that cracks propagate from these initial flaws at varying rates, depending on the particular size, shape, and orientation of each flaw.

4.1. Fatigue Crack Growth Testing

The objective of the crack growth tests is to characterize the rate at which a crack grows due to a loading history. The characterization of crack growth behaviour is defined by the curve of crack growth rate versus a parameter independent of

specimen geometry and loading history. The preferred equivalence parameter in rubber fatigue and fracture analysis is the energy release rate. The arguments explaining the reason why is selected a test procedure, test sample, and other preferred parameters has been done in section 3.1.2.

Crack growth fatigue cycling tests at non-relaxing ($R_\epsilon > 0$) and fully relaxing ($R_\epsilon = 0$) conditions have been run to measure the arrest of the growth due to strain crystallizing effect. It has been used multiple R ratio fatigue crack growth characterization data for the computation of parameters that feed the constitutive model defining the influence of R ratio in fatigue life of rubber. R ratio in strain is defined by the following equation,

$$R_\epsilon = \frac{\epsilon_{min}}{\epsilon_{max}} \quad \text{Eq. 4-1}$$

4.1.1. Fatigue Crack Growth Characterization Tests

Fatigue crack growth behaviour of a rubber material is defined by variables computed from the fitting of crack growth rate versus tearing energy curve. There is not any test standard for measuring the fatigue crack growth behaviour in rubber. Nevertheless, the procedures and analysis are reasonably well-documented in the literature, and are in widespread use, at least for the case of $R = 0$ cyclic loading.

The planar tension test specimen was chosen to run the crack growth measurements. Is the preferred specimen due to the advantage of, under displacement control, being the energy release rate independent of crack size [1,48–52,77,162]. Since the energy release rate is independent of crack size, the fatigue crack growth rate is also constant, on average, and the crack length varies linearly with applied cycles [88,161]. The planar tension test specimen used has nominally a width of $w = 188$ mm, height of $h = 35$ mm and thickness of $t = 2$ mm. For all tests an initial crack is produced by cutting the specimen along the mid-plane, with a razor blade. The crack is introduced at one edge to a depth of approximately $c_0 = 50$ mm, to avoid specimen edge effects.

The design details and gripping arrangement is similar for all fatigue crack growth tests and is shown in Figure 2.8.A. Test were performed at the lab temperature of

nominally 20°C on the MTS Bionix 370.02 Servohydraulic Testing Machine with 15 KN load cell.

The equation to compute the energy release rate, T , for pure shear test specimen, as mentioned in section 3.1.2.2, is:

$$T = Wh \quad \text{Eq. 4-2}$$

Specimen strain energy density W was computed via integration of the unloading path of the engineering stress-strain curve.

$$W_{\text{Unloading}} = \int_{\varepsilon_{\text{max}}}^0 \sigma d\varepsilon \quad \text{Eq. 4-3}$$

The stress-strain loop was computed from displacement x and force F measurements made on the cracked specimen. Image processing method has been used for measuring crack; therefore displacement-force data of previous cycle to taking the picture are registered.

The undeformed cross-sectional area for the stress σ calculation was computed based on the measured specimen thickness t , and the difference between the initial specimen width w , and the instantaneous crack length c ,

$$\sigma = \frac{F}{t - (w - c)} \quad \text{Eq. 4-4}$$

Strain ε is computed from measured displacement, by an empirical strain-displacement relationship. The special configuration of planar tensile specimen used for testing, by two ears for better clamping, as shown in Figure 2.8. A, gives perfect agreement between: strains computed from grip to grip distance, x , divided by initial gage length, h , and strains measured by video-extensometer. This perfect agreement is lost at high strain levels, but up to 100% strain can be considered linear as shown in Figure 4.1. For strain computations both strain measurements are assumed perfectly linear. The peak strain for fatigue cyclic test is usually below 100%, hence strain measurement will be directly computed from the LVDT displacement measurement. Hence, the equation used to compute engineering strain is,

$$\varepsilon = \frac{x}{h}$$

Eq. 4-5

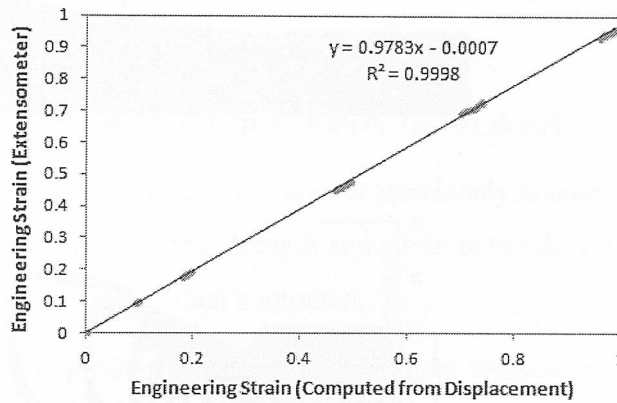
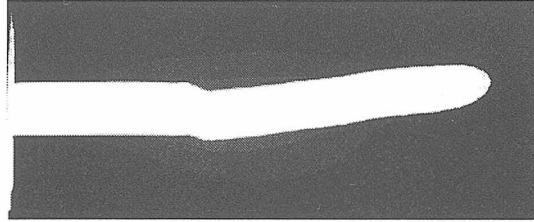


Figure 4.1 Strain – Displacement relationship for Planter Tension sample up to 100% strain

The shape and length of the crack is measured from digital images. The capture of images is realized by digital cameras, triggered by a pulse voltage outputted from the controller of the test machine. The camera is positioned at a distance enough far, such that the field of view covers approximately half of the width of the specimen surface, from the cracked side to the centre. The position of the camera is fixed during the full test. An initial calibration picture is taken with a ruler fixed in the rubber surface. From this first picture with the ruler on it we calibrate the crack measurement system by the *pixel/known distance* relationship. Subsequent pictures of the cracked specimen are then automatically measured by the image processing system named *Image J*. Crack measurement automation is important to be competitive in price, and reduce deadlines of data delivery. Images are post-processed by a sequence of operations shown in Figure 4.2. Operations are automated by a customized script on python for *Image J*, and it is run in a batch mode to process all pictures together. Last script operation outputs the (x,y) coordinates of the crack edge. Finally, opening the output file in a spreadsheet program the crack length is computed from the maximum value of the x coordinate.

A)



B)

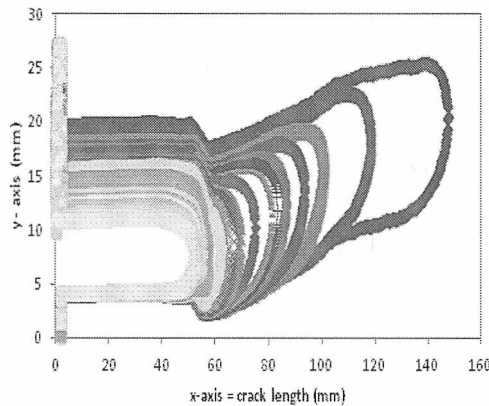


Figure 4.2 Sequence of pictures to explain the Image J image processing system work process. A) Uploaded raw picture, then the model is converted in binary, and at last step a Line Graph operation is executed to obtain (x,y) coordinates of the crack edge, and B) finally crack edge coordinates are plotted in a spreadsheet program like Excel.

The script that is run in batch mode for each of every picture has the following command lines.

```
//run("Threshold...");  
setThreshold(0, 80);  
run("Convert to Mask");  
run("Make Binary");  
makeRectangle(6, 430, 1616, 504);  
run("Analyse Line Graph");
```

The selection of an appropriate crack measurement interval can be difficult when the fatigue crack growth properties of a material are unknown. Too small strains result in wasted time making measurements that resolve no change in the crack length. Too large strain levels wastes test time, and unnecessarily consume the un-cracked amount of sample that will be needed for additional measurements. Hence, to limit the test we use a procedure that requires two preliminary tests to be run: the critical

tearing energy test explained in section 4.1.1.1, and the short fatigue crack growth test detailed in section 4.1.1.2. From the data obtained from those preliminary tests we define the principal characterization tests, fully relaxing and non-relaxing fatigue crack growth behaviour tests.

4.1.1.1. Monotonic Crack Growth Test to Break

The monotonic tensile to break test is run over previously cracked planar tension test sample. From the test the limiting strength and strain at break (ϵ_b) is determined, and the critical tearing energy T_c is then computed.

The initial crack was produced by cutting the planar tension specimen at one edge with a razor blade along the mid-plane. Initial crack length has been cut of a length of approximately $c_0 = 50 \text{ mm}$ to avoid specimen edge effects. Monotonic tensile test is run at 1% / sec., until the crack grows catastrophically to break. The stress-strain curve was computed from displacement and force measurements. Strains were calculated using an empirical strain-displacement relationship, described in section 4.1.1. The undeformed cross-sectional area for the stress calculation was computed based on the measured specimen thickness, and the difference between the initial specimen width and crack length. Crack length is not measured during the test and is considered of same length, c_0 , as in initial stage length for computations

$$\sigma = \frac{F}{t - (L - c_0)} \quad \text{Eq. 4-6}$$

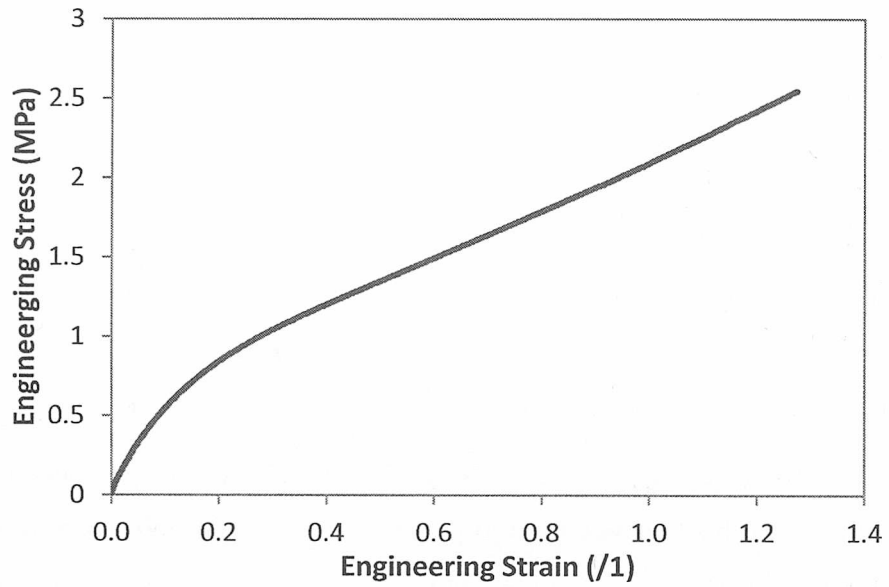
Strain energy density at break $W_{(\epsilon_b)}$ was computed via integration of the loading path of the engineering stress-strain curve, from the initial zero strain until the strain at break value, ϵ_b , as shown in Figure 4.3.

$$W(\epsilon_b) = \int_0^{\epsilon_b} \sigma d\epsilon \quad \text{Eq. 4-7}$$

And finally the critical tearing energy is computed by the critical tearing energy equation, and using the strain energy density at break value,

$$T_c = W(\epsilon_b)h \quad \text{Eq. 4-8}$$

A)



B)

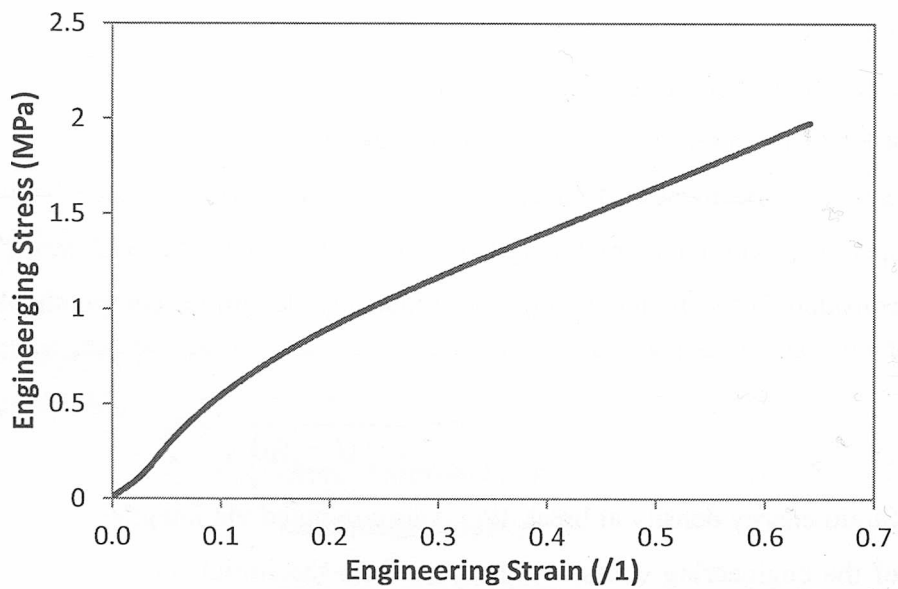


Figure 4.3 Engineering stress-strain curve of monotonic tensile to break test of pre-cracked planar tension test sample. A) MSB (Specimen P3 was selected). B) MCN (Specimen P2 was selected.)

Table 4.1 Strength parameters derived from edge cracked planar tension tests

Material	Engineering Stress at break, MPa	Engineering Strain at break	Strain Energy Density at break, mJ / mm ³	Critical Tearing Energy, kJ/m ²
MSB	2.546	1.274	1.93	65.686
MCN	1.976	0.641	0.74	25.456

4.1.1.2. Short Fatigue Crack Growth Test

Short fatigue crack growth test is an accelerated fatigue crack growth test of a pre-cracked planar tension test specimen to estimate the crack growth power-law slope. The test is an incremental peak strain cycling test designed to run in two hours. The incremental strain goes from zero to the previously determined strain at break ϵ_b , performing one cycle at every strain.

The test set-up and general conditions are same for all the fatigue crack growth tests as has been explained in section 4.1.1. The specific conditions for the particular case of short fatigue crack growth test are explained next. The cycling frequency is $\omega=5$ Hz, cycle waveform is sine, test duration of $P=7200$ seconds, and number of images that are collected during the whole test, $M=50$. Image capture will be realized at a strain of 90% of previous peak strain. The images are collected at every number of test cycles (N_{test}) divided by the number of pictures we desire to acquire (M). The test is finished when the specimen breaks or at $N=N_{test}$

$$N_{test} = \omega P \quad \text{Eq. 4-9}$$

Figure 4.4 show the test scheme with history of peak strain (top), and history of crack length (bottom). Test is designed to start at minimum strain and finish in two hours (N_{test}) at a defined maximum strain, or if specimen breaks before, when it has broken. The engineering strain and crack size, are plotted in a graph of two parallel abscissa scales, against time t , and number of cycles N . The cycling strain ramp and the instants for acquisition of pictures are detailed on the same plot, shown in Figure 4.4. Peak strain value ϵ_{max} , at every cycle number N can be computed from,

$$\epsilon_{max}(N) = \dot{\epsilon}_{max} N \quad \text{Eq. 4-10}$$

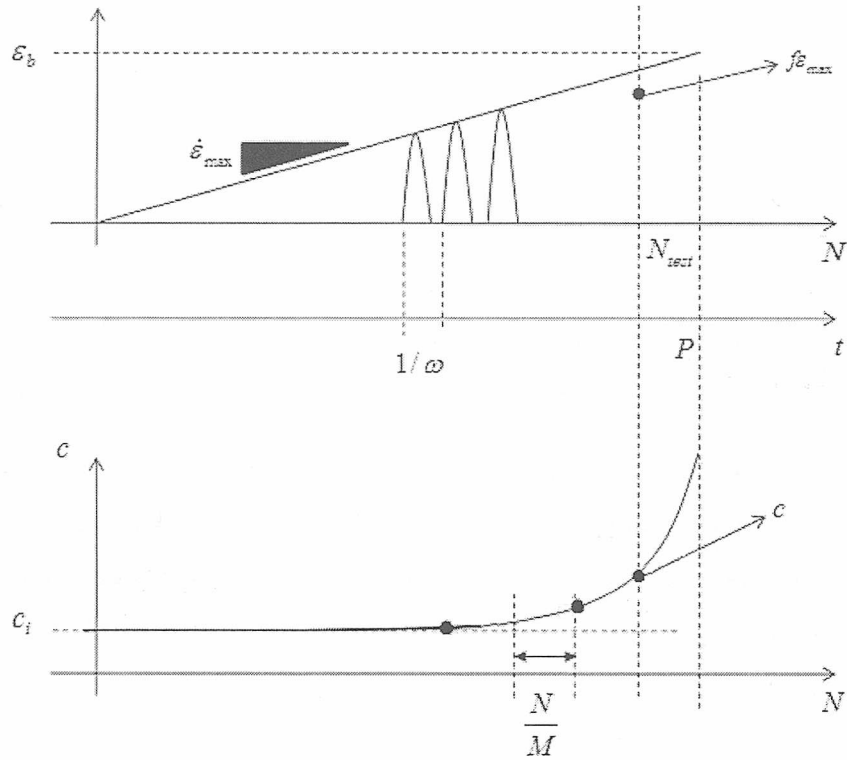


Figure 4.4 Test scheme showing history of peak strain (top), and history of crack length (bottom)

Hence, at every incremental N/M number of cycles, a picture of the sample is captured to measure the crack by *Image J* software [216]. The image processing method is detailed in section 4.1.1. Then, Stress-strain loop of the previous cycle to pause the test to take the pictures for crack measurements is registered. To be precise, stress-strain loop is computed from measured displacement-force data. Strains are computed, using an empirical strain-displacement relationship, detailed in section 4.1.1. The un-deformed cross-sectional area for the stress calculation was computed based on the measured specimen thickness, and the difference between the initial specimen width and crack length. Crack length increase with the number of cycles, and is updated for every stress computation with the crack length measurement of previous cycle picture. The stress is calculated from,

$$\sigma = \frac{F}{t - (L - c)} \quad \text{Eq. 4-11}$$

Specimen strain energy density W was computed via integration of the unloading path of the engineering stress-strain curve by Eq. 4-3. Then, tearing energy is computed replacing the strain energy density value previously computed by Eq. 4-2.

The aim of this short test as has been mentioned initially is to determine the crack growth law, which is used to limit the subsequent long crack growth test. In the Figure 4.5 can be seen the fitting of crack length increment versus engineering strain. The potential equation that fits the curve is known as crack growth power-law is,

$$\Delta c = \alpha(\dot{\epsilon}_{max}N)^\beta \quad \text{Eq. 4-12}$$

α and β parameters are computed from equation Eq. 4-12.

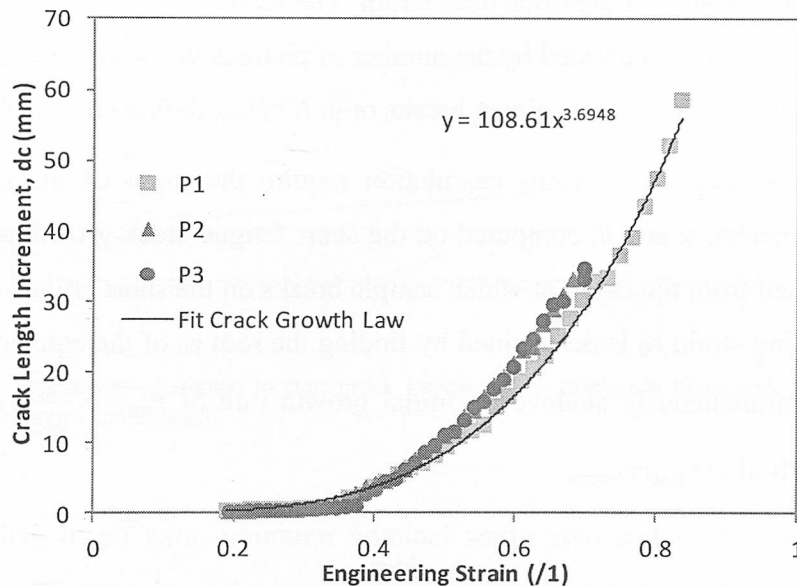


Figure 4.5 Graph of crack growth as a function engineering strain. Power regression fitting curve is plotted, which defines the crack growth law. MCN Material results are shown.

4.1.1.3. Fully Relaxing Fatigue Crack Growth Test Experiments

Long fatigue crack growth test is run to compute the parameters B and F that define the crack growth law. The law defines, as has been explained in section 3.1.2.3, the crack growth behaviour in the Regime 3, where the flaw grows at constant rate. Crack growth law, Eq. 3-22, is the equation that fits the materials behaviour curve on logarithmic scale plot of crack growth rate versus energy release rate.

The test set-up and general conditions are same for all the fatigue crack growth tests as has been explained in section 4.1.1. The testing conditions for the particular case of long fatigue crack growth test are explained next. The long fatigue crack growth test is a cycling test with incremental peak strain. The applied loading waveform is sinusoidal, and at a frequency of $\omega=5 \text{ Hz}$. Tests are run in displacement control at a

fixed minimum strain of 0 mm, and the maximum strain increments the magnitude step by step. Nominal peak strains vary in a range defined by a previous short fatigue crack growth test. Minimum strain is set to zero to characterize the $R = 0$, fully relaxing, fatigue condition. At the same time, that avoids crack growth arrest due to any strain crystallization effect.

This is the long fatigue crack growth test, the duration is of $P=86400$ seconds and number of images to collect during the test is of $M=100$. Image capture is realized at a strain of 90% of previous peak strain. The images are collected at every number of test cycles (N_{test}) divided by the number of pictures we desire to acquire (M). The test is finished when the specimen breaks or at $N=N_{test}$, defined by Eq. 4-9.

Starting and final strains calculation require the input of the crack growth law parameters, α and β , computed on the short fatigue crack growth test. Final strain is defined from the strain at which sample breaks on the short fatigue crack growth test. Starting strain ε_0 is determined by finding the root ε_0 of the equation, with the target to simultaneously achieve an initial growth rate of $r_{min} = \frac{c_{min}}{N_{test}}$ and a final crack length of $c(N_{test})=c_{max}$.

$$\frac{\frac{c_{max}}{\alpha \varepsilon_0^\beta} + 1}{\frac{N_{test} r_{min}}{\alpha \beta \varepsilon_0^\beta} + 1} - 1 = 0 \quad \text{Eq. 4-13}$$

Peak strain ramp rate is determined by

$$\dot{\varepsilon}_{max} = \frac{r_{min}}{\alpha \beta \varepsilon_0^{\beta-1}} \quad \text{Eq. 4-14}$$

Figure 4.6 show the test scheme designed to start crack growth at the minimum observable rate and end ate targeted maximum crack length. In a parallel scale time t and number of cycles N , versus respectively crack size c and engineering strain. The cycling strain ramp at and picture acquisition moments are detailed on it.

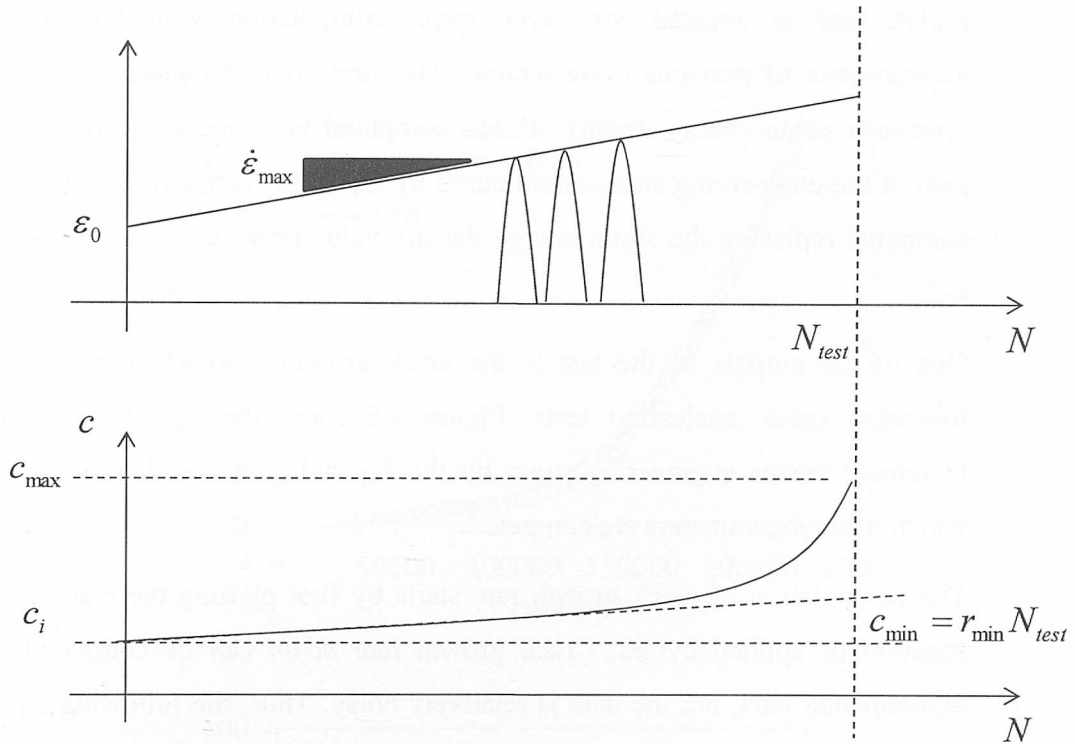


Figure 4.6 Test scheme designed to start crack growth at the minimum observable rate and end at targeted maximum crack length

Test cycling begin with minimum nominal strain zero and peak strain calculated from

$$\varepsilon_{max}(N) = \dot{\varepsilon}_{max}N + \varepsilon_0 \quad \text{Eq. 4-15}$$

During the cycle, the peak strain is incremented an amount after every N_{test}/M increment of number of cycles. The test is defined to end at the sooner of specimen break or $N=N_{test}$. Peak strains ε_{max} remain constant during the cycling from one picture to the next. The taken pictures are processed by *Image J* software [216] to measure crack lengths. This processing method is detailed in section 4.1.1. Then, Stress-strain loop of the previous cycle to pause the test to take the pictures for crack measurements is saved. To be precise, the displacement and force are measured and from there stress-strain loop is computed. Strains were computed from measured displacements, using an empirical strain-displacement relationship, detailed in section 4.1.1. The un-deformed cross-sectional area for the stress calculation was computed based on the measured specimen thickness, and the difference between the initial specimen width and crack length. Crack length increase with the number of

cycles, and is updated for every stress computation with the crack length measurement of previous cycle picture. The stress σ is calculated from, Eq. 4-11. Specimen strain energy density W was computed via integration of the unloading path of the engineering stress-strain curve by Eq. 4-3. Then, energy release rate T is computed replacing the strain energy density value previously computed in the Eq. 4-2.

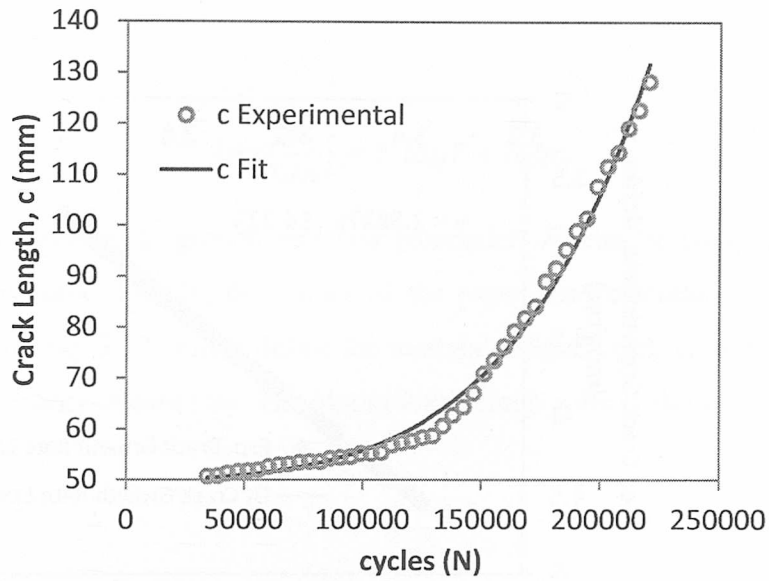
One of the outputs of the test is the crack growth law, which is used to limit following crack nucleation tests. Figure 4.5 show the fitting of crack length increment versus engineering strain by the Eq. 4-12, the crack growth law, from which α and β parameters are computed.

The computation of crack growth rate starts by first plotting the crack length as a function of applied cycles. Crack growth rate dc/dn can be computed from the experimental data, but the data is relatively noisy. Thus, the following equation for fitting of data has been used to compute c values, and obtain a smoother data for later computations.

$$c = c_0 + A \int W^F dN \quad \text{Eq. 4-16}$$

Hence, A and F parameters define the crack length versus cycle relationship, and crack growth rate dc/dn can be computed by Eq. 3-22.

A)



B)

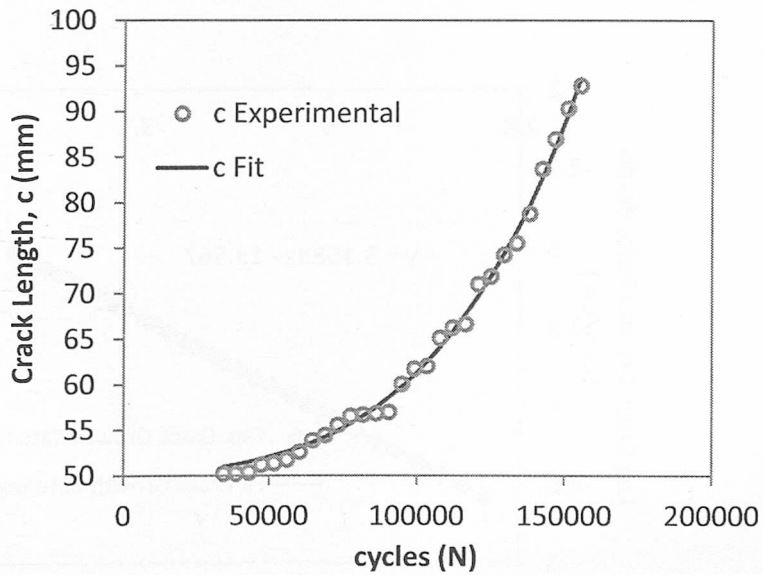
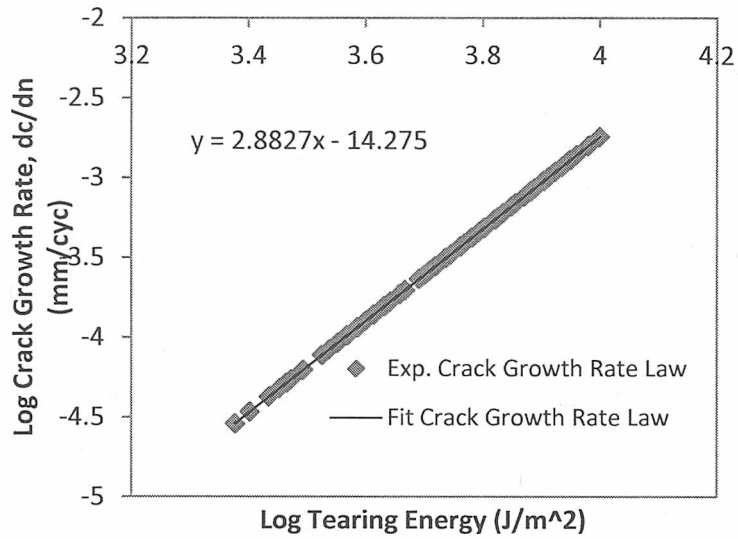


Figure 4.7 Plot of experimentally determined and fitted crack lengths as function of performed cycles. A) is the plot of the MCN material behaviour and B) is the plot of the MSB material behaviour.

To calculate the F parameter value of Eq. 3-22, it has to be transformed the values of crack growth rate and energy release rate into logarithmic. The plot of crack growth behaviour in logarithmic values is shown in Figure 4.8.

A)



B)

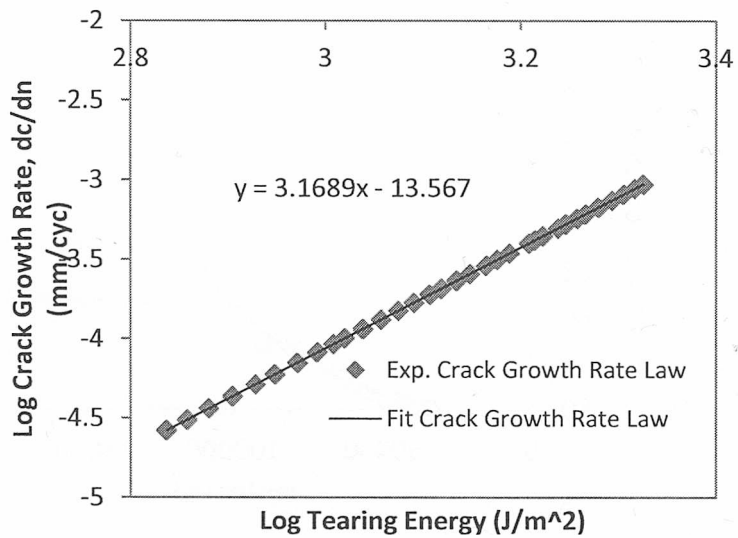


Figure 4.8 Plot in logarithmic values of crack growth rate versus energy release rate. The linear regression equation is also shown. A) is the plot of the MCN material behaviour and B) is the plot of the MSB material behaviour.

The linear regression of logarithmic crack growth rate versus logarithmic energy release has the form of:

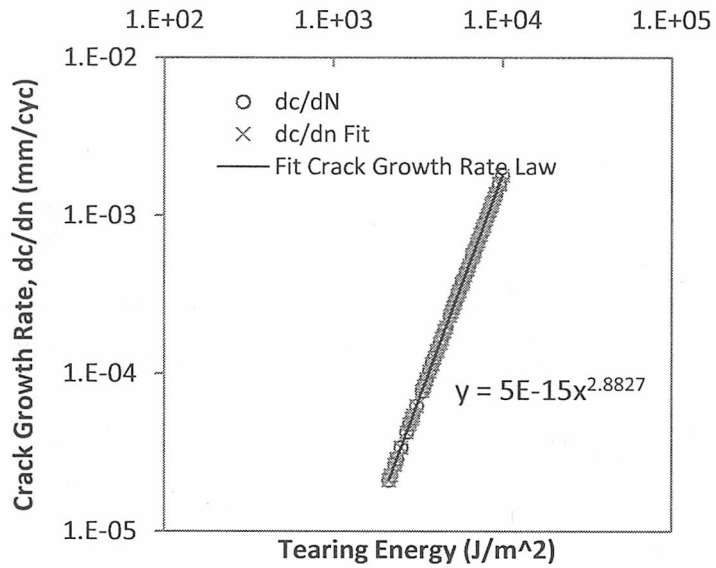
$$\log\left(\frac{dc}{dn}\right) = F \log T + b \quad \text{Eq. 4-17}$$

Changing in the equation the assumption, $b = \log r_c$, we can write the equation as follows,

$$\log \left(\frac{dc}{dn} \right) = F \log T + \log r_c \quad \text{Eq. 4-18}$$

Thus, the fatigue crack growth rate law parameter, F , can be computed from the slope of the curve. Finally, the values of the parameters calculated previously are substituted on Eq. 3-22, which define the material fatigue crack growth behaviour in function of energy release rate. The plot in logarithmic scale is shown in Figure 4.9.

A)



B)

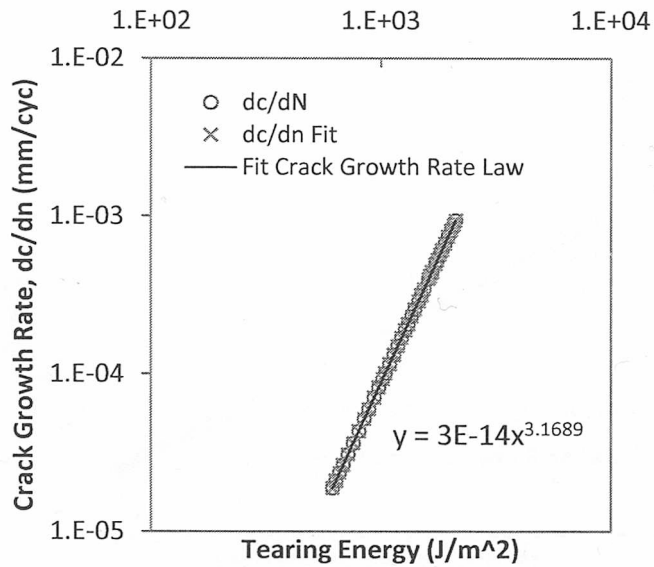


Figure 4.9 Plot in logarithmic scale of crack growth rate versus energy release rate. The linear regression equation is also shown. A) is the plot of the MCN material behaviour and B) is the plot of the MSB material behaviour.

The fully relaxing ($R=0$) fatigue crack growth tests have been explained on the present section, the monotonic crack growth tensile test to break in section 4.1.1.1, short fatigue crack growth test in section 4.1.1.2, and long fatigue crack growth test in the present section. Therefore, most of parameters that define the material fatigue crack growth behaviour have been already computed, but there are additional

parameters that contribute for better characteriza the fatigue crack growth behaviour in all of four refimes of growth. .

As mentioned in section 3.1.2.3, the fatigue crack growth behaviour of material present four regimes of growth before to fracture. The fatigue crack growth test set provides the parameters to determine the crack growth behaviour on the entire range of regimes. The equations, previously detailed from Eq. 3-20 through Eq. 3-23, and a representative material behaviour curve are summarized on Figure 4.10.

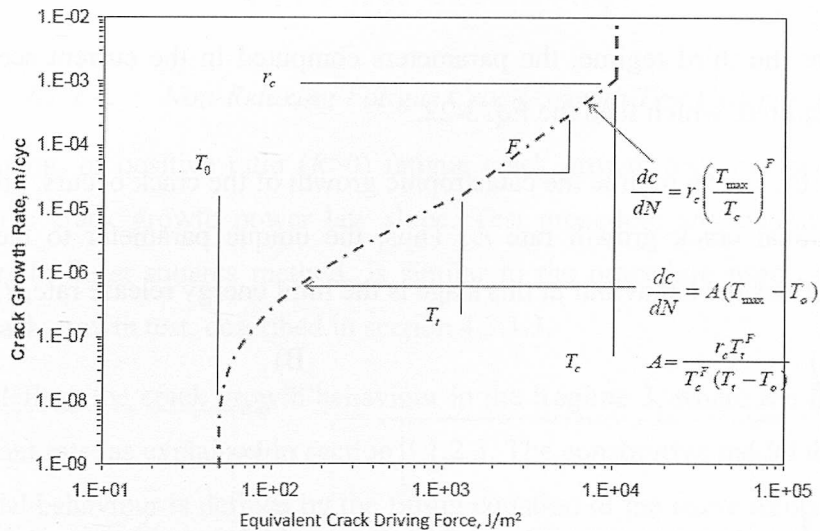


Figure 4.10 Plot of the Lake and Lindley [122] model, with four regimes of fatigue crack growth behaviour and their correspondent descriptive equations. The plot have been taken from Endurica user manual [217]

The first regime requires the determination of initial energy release rate T_0 value, but there is not yet any experimental method to compute this magnitude in a reasonable time. So long as the peak energy release rate T remains below a threshold T_0 , crack growth proceeds at a constant rate r , due solely to environmental attack. Therefore, in cases where the rubber part is not expected to last more than $1e6$ cycles, the value of T_0 does not alter that much the final fatigue crack growth prediction. Thus, the parameter value is taken from already published material data. One representative value taken for any natural rubber is $T_0 = 50 J^2$.

The second regime requires the computation of the parameter A by the following equation,

$$A = \frac{r_c T_t^F}{T_c^F (T_t - T_0)} \quad \text{Eq. 4-19}$$

Critical energy release rate parameter T_c is computed by the monotonic crack growth test to break, section 4.1.1.1. Critical crack growth rate r_c is computed replacing the T_c value on Eq. 3-22. The exponential parameter F is calculated by the long fatigue crack growth test, in the current section. The threshold energy release rate T_t is determined by the following equation,

$$T_t = \frac{T_0}{1 - \frac{1}{F}} \quad \text{Eq. 4-20}$$

For the third regime, the parameters computed in the current section B and F , are required, which feed the Eq. 3-22.

In the fourth regime the catastrophic growth of the crack occurs, growing the crack at critical crack growth rate r_c . Thus, the unique parameter to feed the model that defines the behaviour at this stage is the limit energy release rate, T_c .

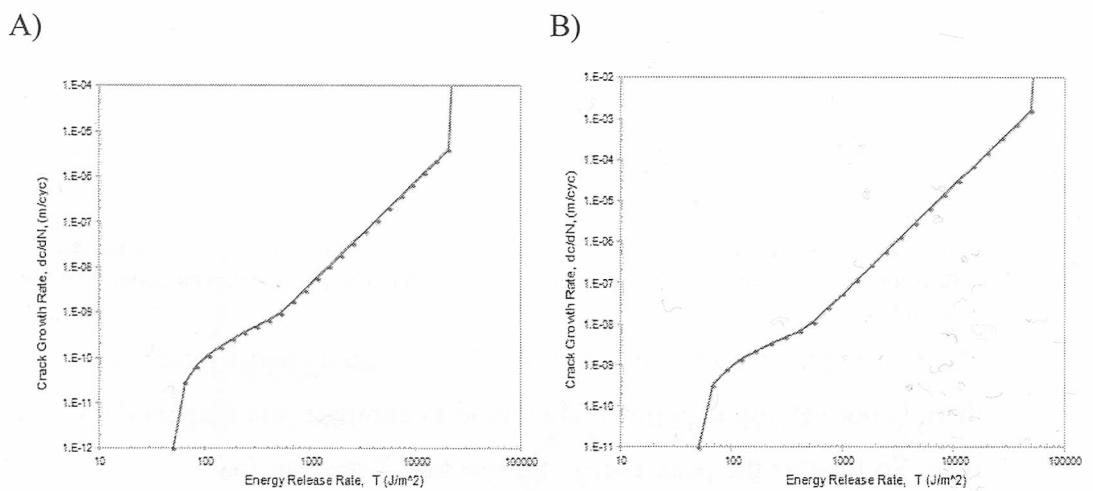


Figure 4.11 Plot of the fatigue crack growth behaviour based on Lake and Lindley model [122]. A) is the plot of the MSB material behaviour and B) is the plot of the MCN material behaviour.

Table 4.2 Parameter values which define the fatigue crack growth behaviour by Lake and Lindley [122] model.

	MSB	MCN
T_c (KJ/m ²)	54.302	21.053
r_c (mm/cyc)	2.05	0.0041
F	2.64	2.27
T_0 (J/m ²)	50	50
T_t (J/m ²)	500	500

4.1.1.4. Non-Relaxing Fatigue Crack Growth Test Experiments

Non-Relaxing, or positive ratio ($R > 0$) fatigue crack growth tests are performed to estimate the crack growth power law slope. Test procedure and determination of parameters by least squares method, is similar to the procedure used on the long fatigue crack growth test, described in section 4.1.1.3.

The law defines the crack growth behaviour in the Regime 3, where the flaw grows at a constant rate, as explained in section 3.1.2.3. The constitutive model that defines the material behaviour is defined by the fitting equation of the curve of crack growth rate versus energy release rate in the plot at logarithmic scale. The crack growth law has been already defined in Eq. 3-22. Experimental testing of one edge cut pure shear test sample are required to compute the parameter F of the crack growth law.

The test set-up and general conditions are similar to previously detailed fatigue crack growth tests in section 4.1.1. Particular conditions of the non-relaxing fatigue crack growth test are detailed next. The test is run on sinusoidal waveform, at a frequency of $\omega = 5$ Hz, in displacement control. The peak strain value is kept fixed at a constant value, and minimum strain value is programmed to go increasing after a defined number of cycles. This increment of R ratio to positive values, usually generates an arrest in the crack growth rate, particularly on rubbers that strain crystallize. The material characterization then, keep test conditions at $R = 0$ until the rate of grow of the crack get stable, and then the minimum starts to increase ($R > 0$), executing a set of cycles at every several minimum strain values, therefore R ratio values.

Test duration is of $P = 86400$ seconds (24 hours), and the number of pictures to be collected during the whole test have been limited to $M = 100$. Image capture is realized at a strain of 90% of previous peak strain. The images are collected at every

set of test cycles (N_{test}), that is calculated dividing total cycles between the number of pictures we desire to acquire (M). The test is finished when the specimen breaks or at $N=N_{test}$, as it is defined by Eq. 4-9. Actually, to save time and increase efficiency it have been defined for the same test sample three peak strain levels (Z), and obtain results for three different conditions in 24 hours.

Figure 4.12 and Figure 4.13, show the schemes that defines the non-relaxing crack growth rate test. Commanded strains and expected crack measurements are plotted respectively as a function of applied cycles. The most important parameters to program test procedures are highlighted in the schemes.

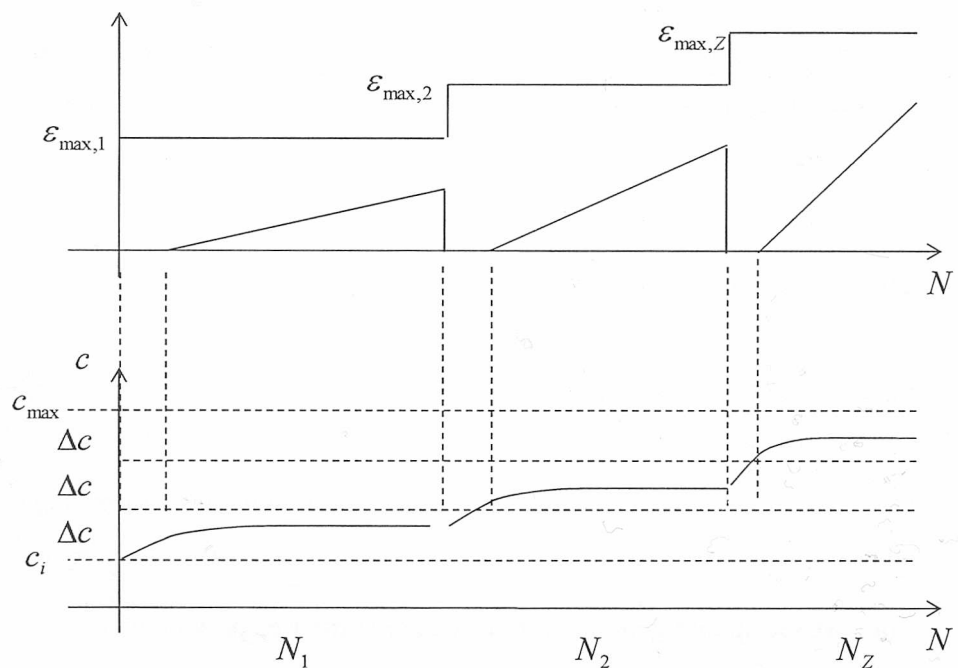


Figure 4.12 Overall test scheme for characterizing crack retardation with nonrelaxing cycles

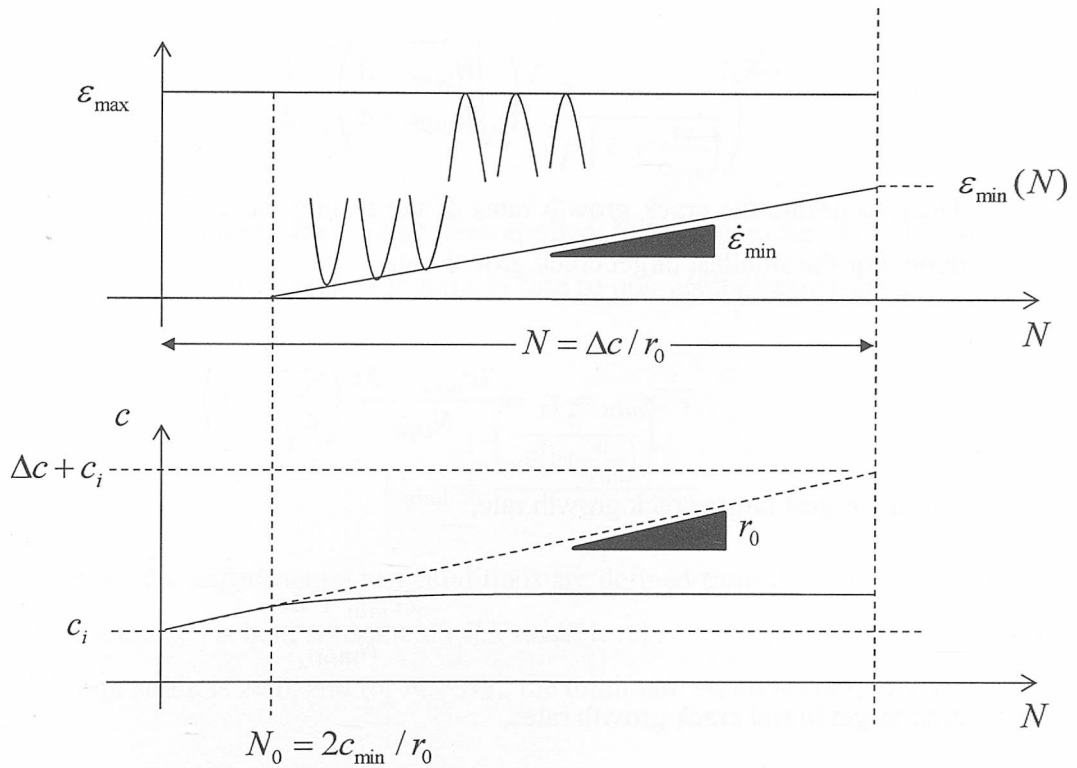


Figure 4.13 Representative scheme of a hypothetical test conditions for a single peak strain level.

Testing procedure requires computing the magnitude of some parameters that defined the test conditions. Test is divided in three peak strain levels Z . Total specimen gauge width available per strain level is estimated from the following set of computations.

$$\Delta c = \frac{c_{max}}{Z} \quad \text{Eq. 4-21}$$

The logarithmic spacing factor f between pictures is given by the root of

$$c = \sum_{i=1}^Z f^{Z-1} - \frac{N_{test}}{N_{min}} \quad \text{Eq. 4-22}$$

For the case where $Z=3$,

$$f = \left(\sqrt{\frac{N_{test}}{N_{min}}} - \frac{3}{4} \right) - \frac{1}{2} \quad \text{Eq. 4-23}$$

Then, to define the crack growth rates of the testing, next computations have to be done. For the smallest target crack growth rate

$$r_{min} = r_1 = \frac{2c_{min} + \Delta c}{N_{test}} \left(\sum_{i=1}^Z f^{1-i} \right) \quad \text{Eq. 4-24}$$

For the largest target crack growth rate,

$$r_{max} = r_z = \frac{2c_{min} + \Delta c}{N_{min}} \quad \text{Eq. 4-25}$$

And target initial crack growth rates,

$$r_i = f^{1-i} r_{min\epsilon}, \quad i=1, 2, \dots, Z \quad \text{Eq. 4-26}$$

To determine the cycle at which the ramp of minimum strain starts to increase is defined for level i by the equation

$$N_{0,i} = 2 \frac{c_{min}}{r_i} \quad \text{Eq. 4-27}$$

The number of cycles to be applied during strain level i ,

$$N_i = \frac{\Delta c}{r_i} \quad \text{Eq. 4-28}$$

The three peak strains are defined by the data collected from the long fatigue crack growth tests, the parameters α and β . For the strain level i the maximum strain level computation equation have the form detailed next,

$$\epsilon_{max,i} = \left(\frac{r_i}{\alpha\beta} \right)^{\frac{1}{\beta-1}} \quad \text{Eq. 4-29}$$

Then, the minimum strain level computation at the end of strain level i is done by the following equation,

$$\varepsilon_{min,i} = \varepsilon_{max,i} - \left(\frac{r_i}{\alpha\beta \left(2 + \frac{\Delta c}{c_{min}} \right)} \right)^{\frac{1}{\beta-1}} \quad \text{Eq. 4-30}$$

Then, the minimum strain ramp rate applied following cycle $N_{0,i}$, (based on not dropping r below the observable limit in case of non-crystallizing rubbers)

$$\dot{\varepsilon}_{min,i} = \frac{\left(\frac{r_i}{\alpha\beta \left(2 + \frac{\Delta c}{c_{min}} \right)} \right)^{\frac{1}{\beta-1}}}{N_i} \quad \text{Eq. 4-31}$$

Therefore, the experimental test conditions are defined from this computed data. The peak strain $\varepsilon_{max,i}$ is held constant at each strain level $i=1, 2, \dots, Z$. For $N \leq N_{0,i}$ case the minimum strain is zero, and for $N > N_{0,i}$, the minimum strain is computed from,

$$\varepsilon_{min,i} = \dot{\varepsilon}_{min,i} (N - N_{0,i}) \quad \text{Eq. 4-32}$$

Once $N=N_i$ the test level is ended, but not the complete testing. Next strain level repeats same test cycling by new peak strain levels and conditions.

The computations required to determine fatigue crack growth rate in terms of strain energy release rate are very similar to those detailed for fully relaxing fatigue crack growth test. The main difference resides on the strain energy density calculation. Figure 4.14 show the plot of strain energy loops, where the area under the unloading curve is drawn to show the strain energy density that has to be computed. The peculiarity of $R > 0$ cycling conditions is shown in the Figure 4.14, where the unloading curve is not going to the zero stress position, and therefore the strain energy density is computed from the sum of following two equations,

$$W = \Delta W + W_{min} \quad \text{Eq. 4-33}$$

Strain energy density on unloading from minimum strain W_{min} ,

$$W_{min} = \int_0^1 \tilde{\sigma} d\varepsilon \quad \text{Eq. 4-34}$$

Where, $\tilde{\sigma}(\varepsilon)$ is the last unloading stress-strain curve obtained during the fully relaxing range of the measurement. The strain on $\tilde{\sigma}(\varepsilon)$ at point 0 is defined as the set

value, and the stress magnitude thereis of zero MPa. The strain and stress at point 1 are identical to the minimum of the dynamic cycle.

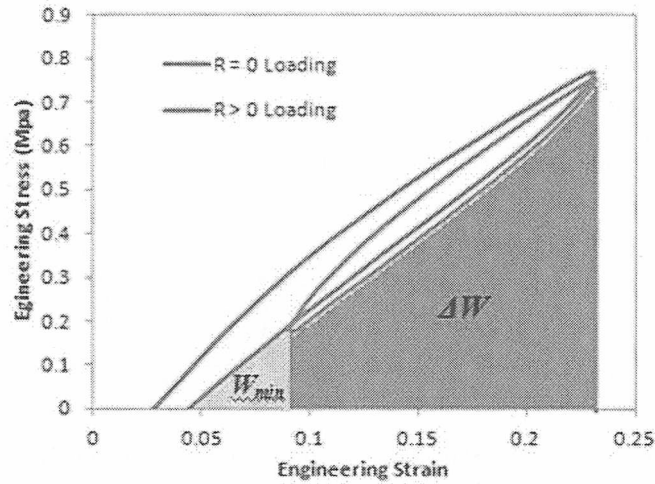


Figure 4.14 Plot of stress-strain loop for a fully relaxing test cycle and a non fully relaxing cycle. Area under the curve is drawn to show the strain energy density that has to be computed.

Once the strain energy density is calculated, strain energy release rate is computed by Eq. 3-22.

4.1.1.5. Effect of R-ratio on Fatigue Crack Growth

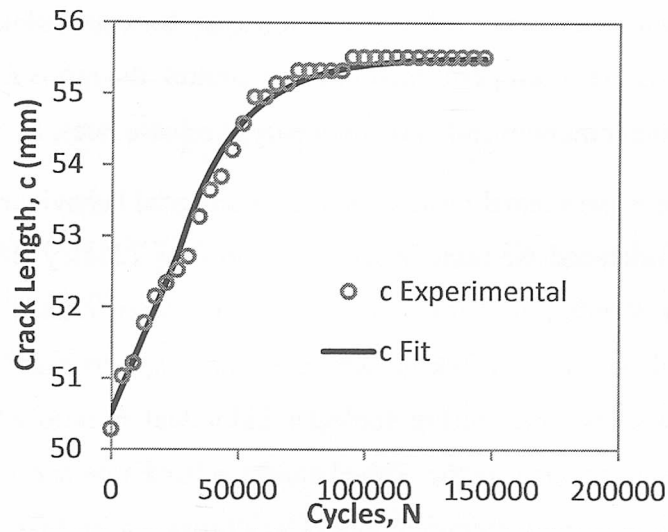
The objective of the crack growth experiments presented in this section is to characterize the dependence of the crack growth rate on the loading history, and especially for non-relaxing conditions. The phenomenological Mars-Fatemi model [218] is used to consider the effect of R ratio on fatigue crack growth rate. Then observed effects of R ratio are assessed, and compared with predictions.

At this point, the obtained data from tests have to be analysed. Firstly experimental data have to be smoothed to compute the value of crack size c by the following model,

$$c = c_1 + \Delta c \left(1 - e^{-\frac{N-N_1}{\tau}} \right) \quad \text{Eq. 4-35}$$

The curve fitting, results on a crack length versus applied cycles plot, that is shown in the Figure 4.15. Minimization of the sum of square errors between experimental crack length c and calculated crack size values is done to determine the parameter τ .

A)



B)

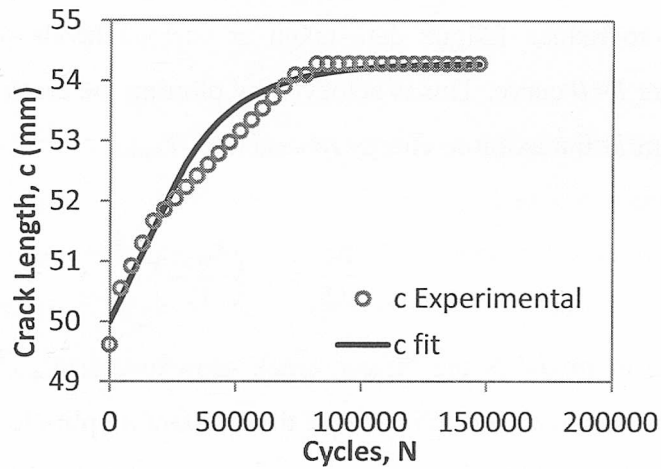


Figure 4.15 Crack length measurement in function of performed cycles. The fitted crack length is superimposed over experimental results, which shows an appropriate fitting. A) is the plot of the MCN material behaviour and B) is the plot of the MSB material behaviour.

Hence, crack growth rate r is computed by the following equation,

$$r = \frac{\Delta c}{\tau} e^{-\frac{N-N_1}{\tau}} \quad \text{Eq. 4-36}$$

Fatigue crack growth behaviour on the third regime is defined by the parameters B and F . The parameter F represents the slope of the curve, therefore the rate of growth of the crack. Then, controlling the decrease of F parameter value, the arrest of growth is measured, and thus the influence of R ratio due to crystallization is determined. The computation of parameter F requires the knowing of parameters T_c

ad r_c values, which are computed from the previously performed long crack growth rate characterization. Additionally, have to be clarified that although the crack growth test has been performed in strain control, the ratios R_T are computed from the ratio of the minimum and maximum energy release rates, $R_T = T_{min}/T_{max}$.

From the experimental results obtained at material behaviour characterization tests, it can be concluded the same observations done by Lindley [186]. First, that at a given constant R ratio, the effect of maximum energy release rate above the fatigue threshold on fatigue crack growth rate, obeys approximately a power-law. Second, that power-law relationship for each individual R ratio appears to converge at a single point defined by the critical energy release rate and a maximum fatigue crack growth rate. A new empirical model was proposed by Mars [218] that embodied all this observation in the Mars-Fatemi model Eq. 4-37. By using this model it is possible to reduce fatigue data taken at various levels of R ratio into a single equivalent $R=0$ curve. This is achieved by plotting the crack growth rates against the equivalent $R=0$ maximum energy release rate, $T_{max,0}$.

$$\frac{dc}{dN} = r_c \left(\frac{T_{max}}{T_c} \right)^{F(R)} \quad \text{Eq. 4-37}$$

The ratio of dc/dN is the fatigue crack growth rate. T_{max} is the maximum energy release rate attained in each cycle of the constant amplitude loading history. T_c is the critical energy release rate, and r_c is a maximum fatigue crack growth rate corresponding to T_c , at which fatigue crack growth curves from all R ratios are assumed to converge. The crack retardation effect manifests itself as a decrease in the rate of crack growth as the R ratio is increased at constant peak energy release rate (peak strain). For reference, the fully relaxing curve is plotted along with the crack arrest measurements, along with curves drawn for a series of increasing R ratios.

Critical crack growth rate, r_c , is estimated from the previously performed fully relaxing test, from the value of F when $R = 0$, and the value of T_c , by the following equation obtained from Eq. 3-22.

$$r_c = r_0 \left(\frac{T_0}{T_c} \right)^{-F} \quad \text{Eq. 4-38}$$

The values of F_i of the function $F(R)$ were directly determined from results shown in Figure 4.16, via the following equation,

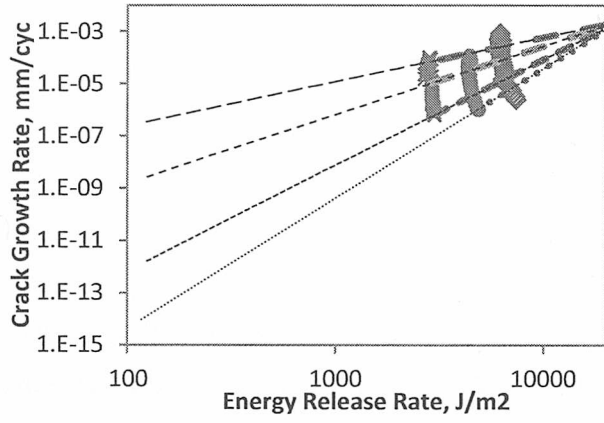
$$F(R) = \frac{\log(r) - \log(r_c)}{\log(T) - \log(T_c)} \quad \text{Eq. 4-39}$$

Fatigue crack growth rate exponent, $F(R)$, for several R ratio testing conditions is calculated by the above Eq. 4-39. Dependence of the fatigue crack growth rate on the R ratio is introduced entirely in the power-law exponent, $F(R)$, of Eq. 4-37. As a result, the effect of R ratio on fatigue crack growth exponent $F(R)$ can be plot as shown in Figure 4.17. Therefore, $F(R)$ can be computed by a single material constant exponential function Eq. 4-40, which characterize the material's dependence on R , to those required to capture the $R = 0$ behaviour.

$$F(R) = F_0 e^{F_1 R} \quad \text{Eq. 4-40}$$

The fitting to experimental results done by the Eq. 4-40 is shown in Figure 4.17. The model sacrifices accuracy particularly for small, but nonzero, values of R . For the design process, where limited fatigue behaviour material data is available, it may be worthwhile to decrease slightly the accuracy for the simplicity of quantifying the R ratio effects with a single material parameter, F_1 . F_0 is retained in the curve-fits, as it is the F value determined for the material at $R = 0$ conditions. Actually, the computed values for the $R = 0$ condition, and retained for the present curve-fits are T_c and F_0 . A nonlinear least-squares technique have been used to compute F_1 parameter and have been summarized in Table 4.3.

A)



B)

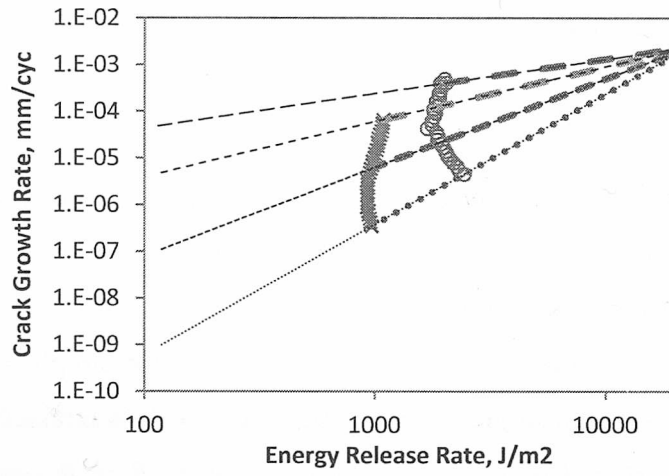
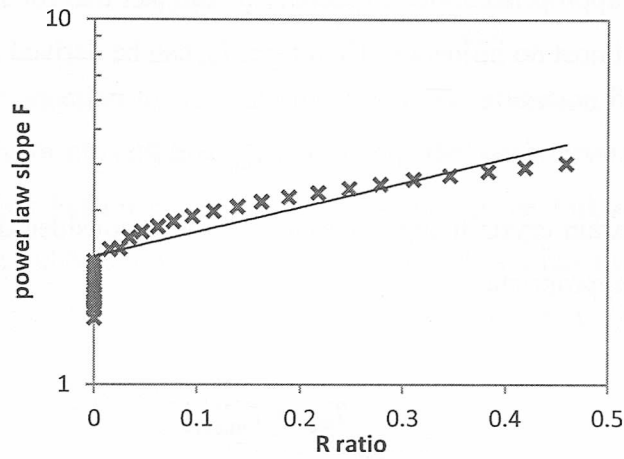


Figure 4.16 A plot of the crack arrest effect. Fitting of crack growth law tendency lines (solid line), and experimental results or observations (dots) are plotted. Observations and fitted curves are marked according to the R ratio. The graph shown in A) is from the MCN material, and the B) is from the MSB material.

A)



B)

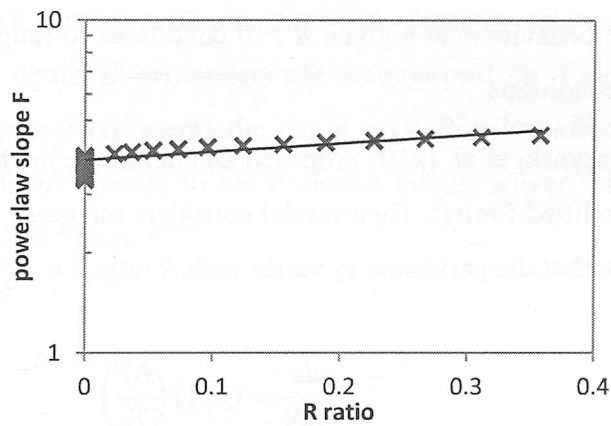


Figure 4.17 A Plot of the effect of R_T ratio on fatigue crack growth exponent $F(R)$. The graph shown in A) is from the MCN material, and the B) is from the MSB material.

Table 4.3 Value of F_0 and F_I parameters that define the exponential function Eq. 4-40, which define the dependence of materials on the R ratio in non-relaxing strain conditions.

	MCN	MSB
F_0	2.25	3.8
F_I	1.53	0.57

The amount of data to collect at a number of R ratio levels is reduced to a single equivalent $R = 0$ fatigue crack growth curve by using the presented model in Eq. 4-40. This is accomplished by plotting the crack growth rate or fatigue life against the equivalent fully relaxing energy release rate, T_{eq} .

For non-strain crystallizing rubbers the well-known Paris law [115] is the simplest and most appropriate model, specially by the fact that for small R ratios, these model predicts almost no influence. Therefore, T_{eq} can be derived as,

$$T_{eq} = \Delta T \quad \text{Eq. 4-41}$$

And for strain crystallizing materials, has been considered that Mars [218] model is the most appropriate

$$T_{eq} = T_{max,R}^{\frac{F(R)}{F(0)}} T_c^{\left(1 - \frac{F(R)}{F(0)}\right)} \quad \text{Eq. 4-42}$$

Where $T_{max,R}$ is the maximum energy release rate at a given R ratio, $F(R)$ is the power-law exponent, and T_c is the critical energy release rate. The model relates fatigue life behaviours at a given $R > 0$ conditions to fatigue failure at the same life for $R = 0$ conditions.

Ostojka-Kuczynski et al. [219] proposed an alternative model, summarized below in a slightly modified format. Their model considers the range of crack driving force ΔT , and regards that the parameter r_c varies with R ratio, i.e. $r_c = r_c(R)$.

$$\frac{dc}{dN} = r_c(R) \left(\frac{\Delta T}{T_c}\right)^F \quad \text{Eq. 4-43}$$

For $0 < R < 1$, the function $r_c(R)$ is given by,

$$r_c(R) = r_c 10^{-(b_1 R^2 + b_2 R)} \quad \text{Eq. 4-44}$$

where b_1 and b_2 are material parameters. This is an interesting approach to be considered for future research works.

The ability to obtain a single characteristic curve using Eq. 4-42 is highly sensitive to the choice of $F(R)$. This is not surprising, given the strong dependence of crack growth rate on R . The material behaviour plotted in Figure 4.17 shows clearly the influence of R ratio on the crack growth rate. This influence is expressed mathematically through the parameter T_{eq} , and can be computed by following strain-crystallization function $X(R)$.

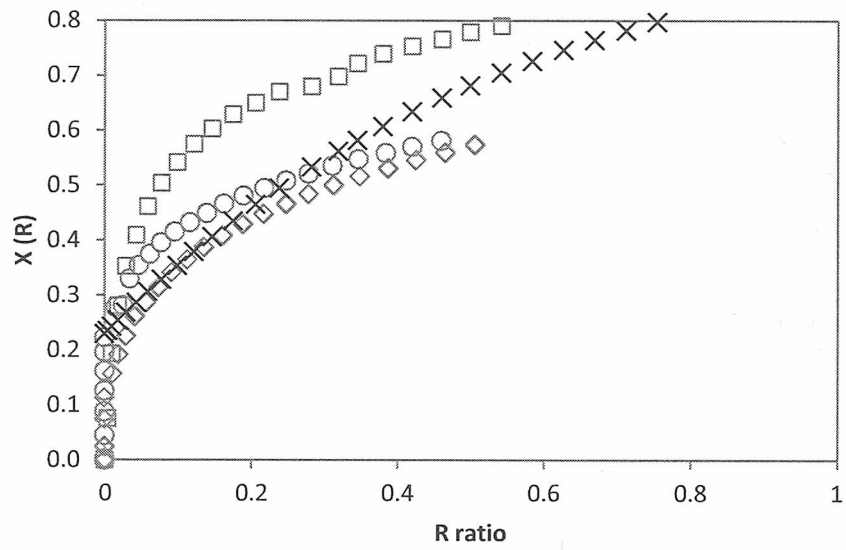
$$X(R) = \frac{\log(T) - \log(T_{eq})}{\log(T_c) - \log(T_{eq})} \quad \text{Eq. 4-45}$$

There is a second equation to calculate the strain crystallization function depending on the data we have already analyzed. Relating the strain-crystallization function $X(R)$ with the Mars Fatemi model for $F(R)$, results in the following function. For strain crystallizing rubbers, once F_i has been tabulated as a function of R_i for all test conditions by the Eq. 4-40, the strain-crystallization function $X(R)$ can be computed as follows:

$$X(R) = 1 - \frac{F(0)}{F(R)} \quad \text{Eq. 4-46}$$

The resultant crack growth rates as a function of energy release rate are shown in Figure 4.18, and obtained parameters are summarized on Table 4.4. The tabular function $x(R)$ obtained represents the strain crystallization effect on crack growth rate, and can be input directly to the Endurica fatigue solver. The tabular function obtained is plotted on Figure 4.18.

A)



B)

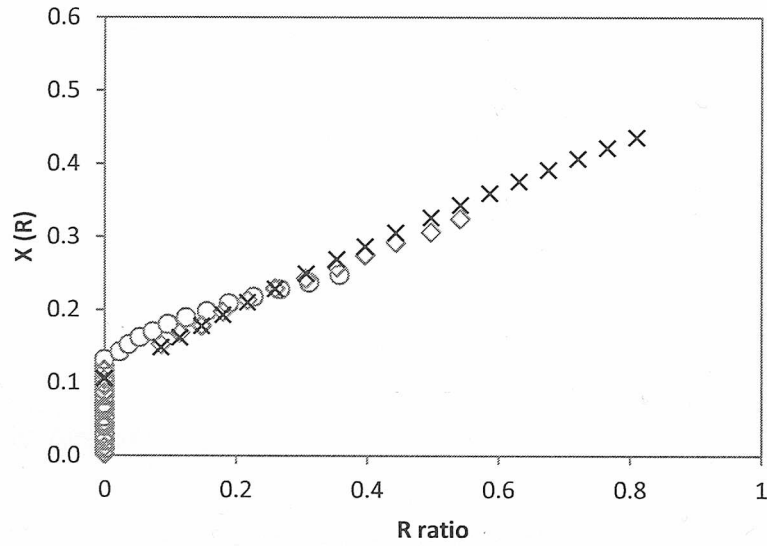


Figure 4.18 Observations of strain crystallization function $x(R)$ for crack growth under nonzero minimum strain. The obtained results for first replicate of test conditions with first sample are in hollow circle, for second replicate are in hollow diamond, for the third replicate are in hollow rectangle, and all of them are compared with tabulated crystallization function, marked with 'x'. The graph shown in A) is of the MCN material, and the B) is of the MSB material.

Table 4.4 Tabular data of crystallization law of both MSB and MCN material

R, X(R) MSB		R, X(R) MCN	
0.000	0.105	0.000	0.230
0.086	0.148	0.004	0.235
0.115	0.162	0.010	0.243
0.148	0.178	0.018	0.254
0.180	0.193	0.029	0.269
0.218	0.210	0.043	0.287
0.260	0.229	0.059	0.306
0.307	0.249	0.078	0.329
0.354	0.269	0.099	0.354
0.397	0.287	0.122	0.379
0.444	0.305	0.147	0.406
0.497	0.326	0.175	0.435
0.542	0.343	0.206	0.465
0.587	0.360	0.239	0.495
0.631	0.376	0.283	0.533
0.676	0.392	0.319	0.562
0.721	0.407	0.345	0.582
0.765	0.422	0.380	0.607
0.810	0.436	0.420	0.634
		0.461	0.659
		0.499	0.682
		0.542	0.705
		0.584	0.726
		0.627	0.746
		0.669	0.764
		0.712	0.781
		0.754	0.797
		0.797	0.812

The tabular data have been constructed from the previously computed parameters that define the material behaviour, and substituted in Eq. 4-46. It has been computed until a value of R ratio of 0.8. At higher values of R ratio the curve of $X(R)$ is computed in the region of the crack growth behaviour curve dc/dn vs T , where the slope is nearly vertical. This means, that a small change in R ratio, or small variation of test amplitude, results in a prediction of a very small crack growth, or in a catastrophic crack growth.

Analyzing obtained results on the effect of R ratio for each of both materials, it can be appreciate strain crystallizing material MCN, and the non strain crystallizing material MSB have a differentiated behaviour. The effect of $R > 0$ cycles to decrease the fatigue crack growth rate it is more accentuated in the MCN material, in the

strain crystallizing material. The improvement is very significant at low strain ranges, whereas becomes less significant at large energy release rate ranges. This is consistent with the fact that, at constant ε_{min} , the R ratio decreases as the energy release rate range increases.

4.2. Fatigue Crack Nucleation Testing

The objective of fatigue crack nucleation test is to tabulate the number of cycles to failure of a specimen as a function of a selected equivalence parameter. The obtained material data results are adequate to compare the behaviour of each rubber blend at crack nucleation. Nevertheless, the equivalence parameters used do not uniquely relate to crack nucleation life, and therefore obtained crack nucleation data from geometrically simple lab specimens can't be used to confidently assess crack nucleation life in geometrically complex real components.

4.2.1. Fatigue Crack Nucleation Characterization Tests

Fatigue crack nucleation experiments are performed over simple tension test specimen. First, a preliminary monotonic strain to break test is run to determine the strain at break point, and then cycling to break tests are run at leastwise two peak strains, defined by the data obtained from the strain at break test. The resultant data of the fatigue crack nucleation test, at each strain cycling test, is the number of cycles at break.

The selection of equivalence parameter for crack nucleation has been already done in section 3.1.1.4. The energy release rate and the cracking energy density appear to be the only two that satisfies the requirements. In practice, energy release rate is the most used, based on the argument of being directly related to the strain energy density of a small crack embedded in a material subjected to simple tension condition. Therefore, strain energy density is used as equivalence parameter on the following crack nucleation tests.

4.2.1.1. Monotonic Strain to Break of Simple Tension

The simple tension monotonic strain to break test is the preliminary test of fatigue crack nucleation test. The obtained strain at break value is a starting point to define crack nucleation experiments, and it is widely used as a parameter for specifying

rubber compounds. The test is a simple tension monotonic strain to break test of the ASTM D412, type C dumbbell standard rubber fatigue specimen. It is performed at a strain rate of 1%/sec, at a room temperature of nominally 23°C.

From the test, the entire strain-stress loop and strain at break value are saved. Results are useful to compare different materials behaviour, for specifying them. In addition, monotonic simple tension to break test is a necessary preliminary test to configure the cyclic fatigue crack nucleation test. Strain at break value is an input parameter on the nucleation test definition procedure.

Figure 4.19 show the stress-strain curve of monotonic strain to break test, while Table 4.5 summarizes the obtained strain at break values. The low repeatability of MSB material has to be highlighted from the observed results.

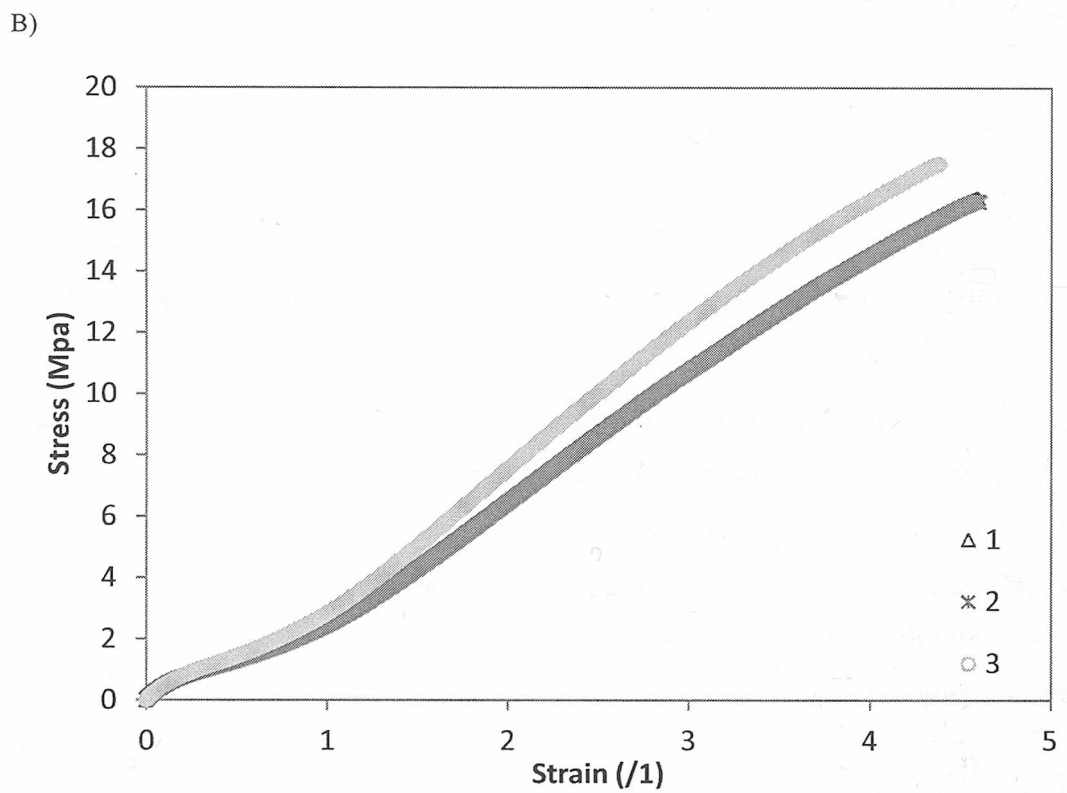
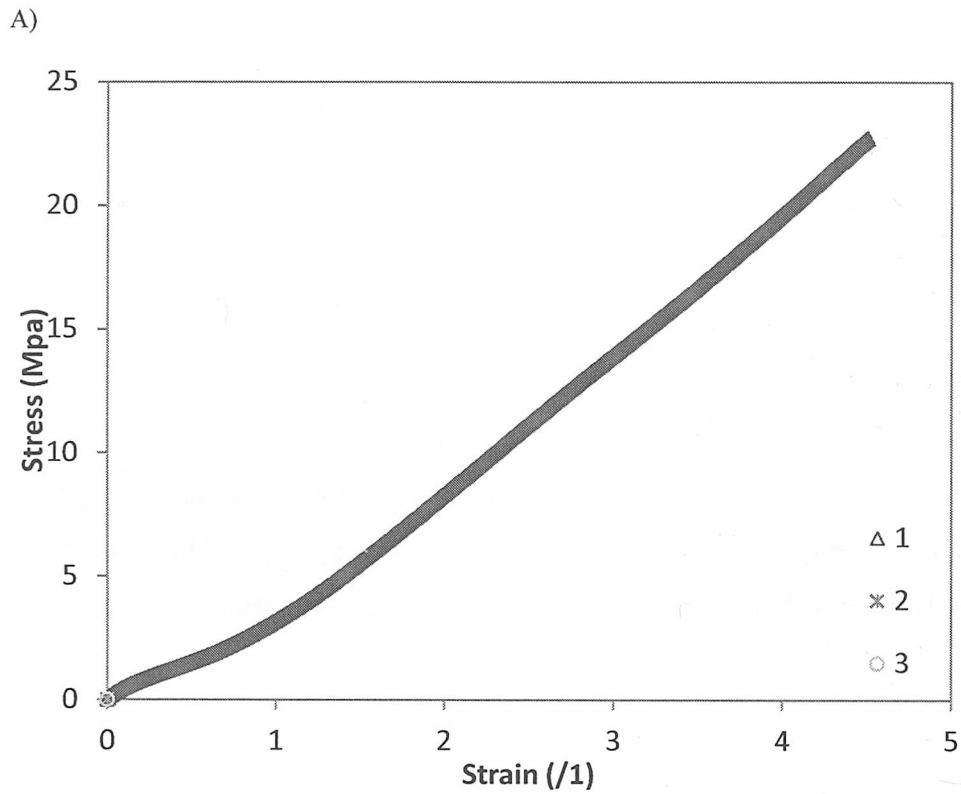


Figure 4.19 Simple tension stress-strain curves to break for MSB and MCN materials. A) is the plot of the MCN material behaviour and B) is the plot of the MSB material behaviour.

Table 4.5 Simple tension strain at break results ($\epsilon_{ST,b}$) for MSB and MCN materials

	$\epsilon_{ST,b}$	
	MCN	MSB
Replicate 1	4.51	4.59
Replicate 2	4.50	4.59
Replicate 3	4.65	4.38
Average $\epsilon_{ST,b}$ value	4.55	4.52

4.2.1.2. Cycling to Break of Simple Tension

Fatigue cyclic strain to break test is a crack nucleation measurement to use in determination of flaw sizes. Test ASTM D412, type C dumbbell standard rubber fatigue specimens were used in this research, as shown in Figure 4.20.

ASTM D412, type C dumbbell standard rubber fatigue specimens are used in this investigation, as shown in Figure 4.20. Test set-up and measurement methods are similar to monotonic simple tension test described in Section 0. Testing is performed on MTS Bionix 370.02 Servohydraulic Test Machine with 500 N loadcell, shown in Figure 4.20. The machine applies a displacement controlled, sinusoidal waveform. The frequency is of 2 Hz, and tests are run at lab temperature, nominally 20C. The test has to be run at least at two strain levels $Z=2$, to have enough data to feed the flaw size determination procedure. Minimum strain value is zero, $R=0$ ratio, to avoid any possible influence due the strain crystallization of material (Section 3.3.1.2 and 3.3.4.2). The cycling test amplitudes for MCN and MSB material are summarized in Table 4.6.

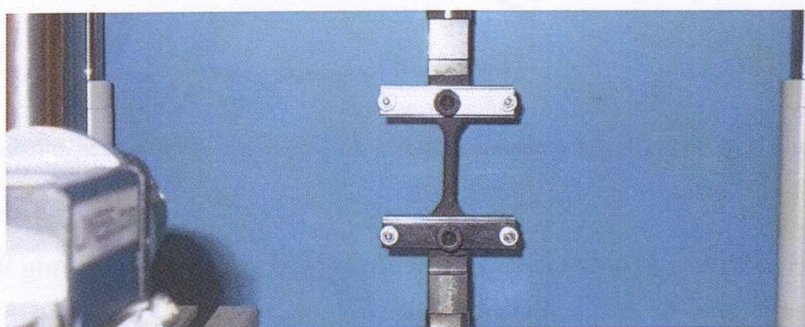


Figure 4.20 Simple tension test sample and gripping configuration for the cycling test. The camera is use to capture the crack growth.

There is not any strain measurement system, or extensometer, capable to measure properly the strain of a rubber test sample during cycling tests. Therefore, the test is

commanded and controlled in displacement. Then, strain is computed from a strain-displacement relationship, obtained from the monotonic tensile to break test data. The strain is measured by observing ink marks drawn on the homogeneous portion of the dumbbell by video-extensometer. Strain measurement correspondent to several grip to grip displacements can be determined. The polynomial regression gives the best fitting for the strain in function of displacement relationship, as it is plot in

. The equation is used to compute the peak strains of the commanded displacement cycling tests. Table 4.6 summarizes the test conditions, commanded peak displacements and resulting strain values.

Table 4.6 Fatigue cycling test conditions in displacement and strain values.

Grip to Grip Displacement mm	Strain Calculated by Fitting Curve %
81	150
99	180

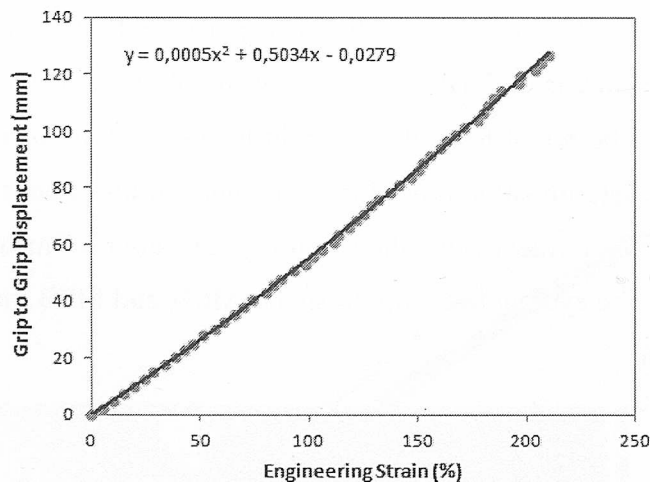


Figure 4.21 Strain-displacement relationship for simple tension specimen at uniaxial tensile test.

Periodically pictures of the specimen surface are captured during the test, like shown in Figure 4.26. From these images, the number of growing crack precursors can be counted by *Image J* software [216]. The additional information of number of cycles obtained is helpful for the prediction of stiffness loss.

In all durability tests that are run until the rupture or failure of material, is interesting to adjust or limit the duration of tests. Nevertheless, cycling to failure tests depend on

the commanded loading to limit the testing time. Hence, a peak value definition procedure is used to determine two peak strain values. The procedure requires the following input parameters from preliminary tests: (i) crack growth parameters α , β from fatigue crack growth test; and (ii) strain at break $\varepsilon_{st,b}$ from monotonic simple tension strain to break test. Other limited conditions are, that the time budget is of $P= 28800$ seconds (8 hours), cycle frequency $\omega = 2 \text{ Hz}$, and number of strain levels Z have to take into account. Substituting the above mentioned parameters values in Eq. 4-47 to Eq. 4-52, target life for each of the strain levels to run is calculated.

$$N_{test} = \omega P \quad \text{Eq. 4-47}$$

For the first strain level $i=1$, the target life is defined as,

$$N_{target,i} = (N_{test})^{i/z} \quad \text{Eq. 4-48}$$

And from defined target life, first target strain is defined as,

$$\varepsilon_1 = \varepsilon_{ST,b} (N_{target,1})^{-1/\beta-1} \quad \text{Eq. 4-49}$$

To calculate the second strain ($i=i+1$) level has to wait until first strain level have been completed. Update the remaining test time budget to,

$$N_{test} = N_{test} - N_i \quad \text{Eq. 4-50}$$

Compute next target life as,

$$N_{target,i} = (N_{test})^{i/z} \quad \text{Eq. 4-51}$$

And, then compute next target strain as,

$$\varepsilon_1 = \varepsilon_{i-1} \left(\frac{N_{target,i}}{N_{i-1}} \right)^{-1/\beta-1} \quad \text{Eq. 4-52}$$

Described procedure is of great interest whenever the material to characterize is unknown, and is of great importance to use it when testing time budget is strictly limited. The materials we are working on the thesis are known for us, since we have worked with them during the implementation of procedures. Therefore, the two peak strains had been defined without the above mentioned procedure, but as a shown,

Table 4.7 summarize material parameters required to feed above described procedure.

Table 4.7 Fatigue nucleation experiment conditions defined for material intrinsic flaw size determination tests

	α	β	$\varepsilon_{st,b}$	ε_1	ε_2
MCN	12,301	6.07	4.55	1.5	1.8
MSB	1.0 e ⁶	7.59	4.52	1.5	1.8

The data acquisition programmed save the displacement and force at the peak of every cycle. From the data acquired peak strain, peak stress and material stiffness are computed. The stiffness loss of the material is also appreciable plotting the engineering stress in function of applied number of cycles, like shown in Figure 4.22. Fatigue life test results from experimental are summarized in Table 4.8.

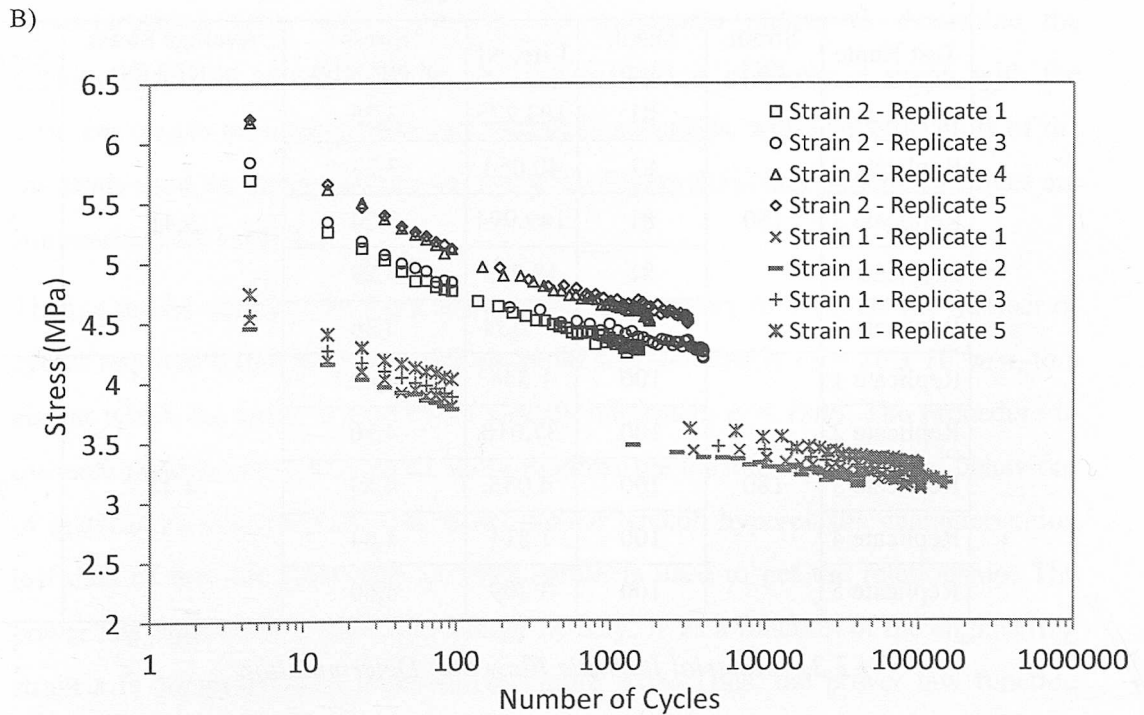
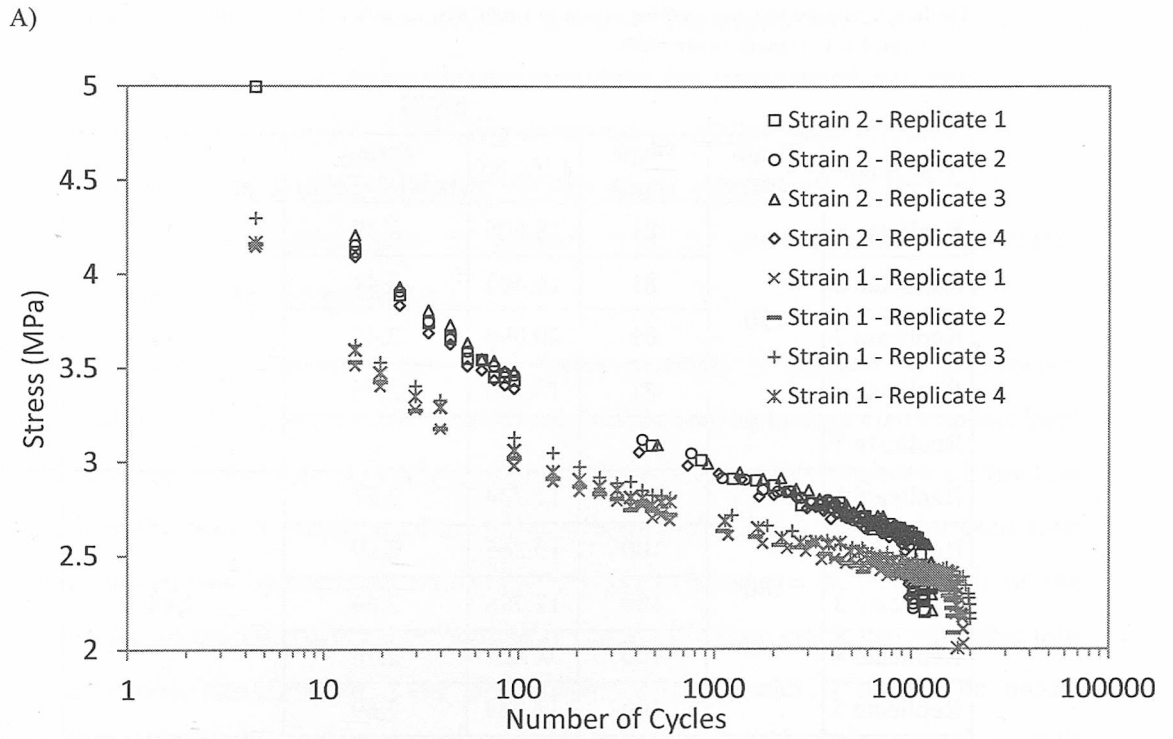


Figure 4.22 Typical stiffness loss behaviour until break at two strain levels is represented. Stress is plotted against the number of cycles in logarithmic scale. A) is the plot of the MCN material, and B) is the plot of the MSB material.

Table 4.8 Simple tension cycling strain to break test results for two materials, MSB and MCN; Results are given for two peak strain tests.

MCN						
Test Name	Strain (%)	Displ. (mm)	Life, Nf	Stress at Nf/2 (MPa)	Average Stress at Nf/2 (MPa)	Average Life
Replicate 1	150	81	18.605	2,39	2,42	18.108
Replicate 2		81	16.495	2,41		
Replicate 3		81	20.095	2,45		
Replicate 4		81	17.239	2,45		
Replicate 5		-	-	-		
Replicate 1	180	100	11.734	2,71	2,68	11.165
Replicate 2		100	10.265	2,69		
Replicate 3		100	12.795	2,64		
Replicate 4		100	9.789	2,70		
Replicate 5		100	11.244	2,69		
MSB						
Test Name	Strain (%)	Displ. (mm)	Life, Nf	Stress at Nf/2 (N)	Average Stress at Nf/2 (N)	Average Life
Replicate 1	150	81	103.225	3,26	3,41	81.762
Replicate 2		81	40.054	3,27		
Replicate 3		81	149.994	3,24		
Replicate 4		81	18.205	3,89		
Replicate 5		81	97.334	3,36		
Replicate 1	180	100	1.544	4,42	4,44	9.524
Replicate 2		100	37.018	4,10		
Replicate 3		100	4.035	4,33		
Replicate 4		100	1.814	4,64		
Replicate 5		100	3.209	4,69		

4.2.2. Material Intrinsic Flaw Size Determination

Intrinsic flaw size determination is the procedure to calibrate the flaw size of the rubber compound. This is determined by the comparison of crack nucleation life results with a set of strain life curves, computed from hypothetical initial flaw sizes. Fatigue life is determined by the number of cycles that a pre-existing flaw takes to grow to a critical size. The life calculation is done by integrating the growth rate of the fastest growing flaw. It is assumed that all cracks start growing at the same time,

but the rate of growth is not the same for all flaws. The natural variability inherent in fatigue crack nucleation measurements can then be rationalized in terms of the associated variations in flaw size. The computation of flaw size requires the input data from a set of preliminary tests: fatigue crack growth test in section 4.1.1.3, fatigue crack nucleation test in section 4.2.1.2, and material hyperelastic characterization test in section 2.6.1.

Fatigue crack growth behaviour of a rubber material is defined by parameters obtained from the fitting of crack growth rate versus tearing energy curve as has been explained in Section 4.1.1. Fatigue crack growth shows four regimes of fracture based on the rate of propagation as detailed in section 3.1.2.3, each with their own mathematical descriptive equation. It is interesting to be as precise as possible on the prediction, so the integration over the entire range of fatigue crack growth behaviour is performed, therefore the Lake and Lindley [122] model is used. The model requires to be feed by a number of parameters provided from fatigue crack growth characterization tests, which provides the parameter values to determine the behaviour on the entire range. In the Figure 4.10 it is shown a graph with the different ranges of crack growth rate and their equations, while specific plots of the materials used on the project are shown in the Figure 4.11, and parameter values are summarized on Table 4.2.

Then, a model defining the crack growth rate is necessary to compute the number of cycles required a flaw to grow from an initial size, nominally $c_0 = 10 \times 10^{-3} \text{mm}$, to a size at which the crack is considered already nucleated, $c_f = 1 \text{mm}$. The procedure to estimate material flaw size additionally requires the elastic strain density behaviour of material as a function of peak strain. Planar tension hyperelastic characterization test data of the stabilized state at 100% strain is used to get the relationship. The power law regression of the strain energy density, W as a function of the engineering strain ε is computed as it is shown in Figure 4.23. Thus, the power law function defined by Eq. 4-53 is used to compute strain energy density at defined peak strain values.

$$W = a\varepsilon^b \quad \text{Eq. 4-53}$$

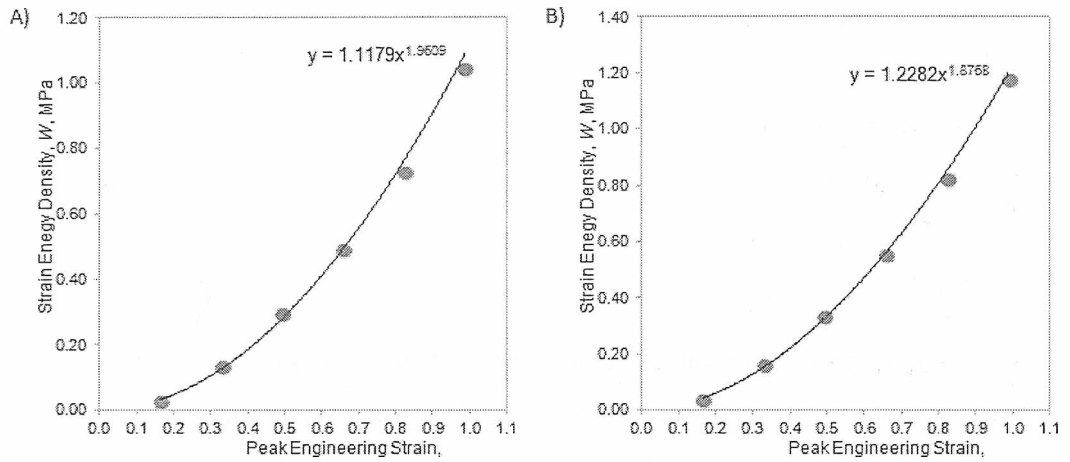


Figure 4.23 Elastic behaviour of material as a function of strain obtained from Planar Tension test sample. A) is the plot of the MSB material behaviour and B) is the plot of the MCN material behaviour.

Table 4.9. Parameter values of the power law function shown in Eq. 4-53

	a	b
MSB	1.118	1.96
MCN	1.228	1.88

The inherent elastic material behaviour defined by Eq. 4-53 is the input for further tests of one edge cracked planar tension. Calculation of energy release rate T depends on the gauge section strain energy density, W , the crack length, a , and a slowly changing strain constant of proportionality, $k(\lambda)$. The relationship has been explained in section 3.1.2.2, and defined by the equation Eq. 3-17. The constant of proportionality is computed by Eq. 3-19. Therefore, the fatigue crack growth rate r at various cycling peak strains is computed substituting the known parameter values in the Eq. 3-22.

In the section 3.1.3.2 is explained how the combination of the power-law that defines the crack growth rate in third regime Eq. 3-22 and equation for the energy release rate calculation of the simple tension specimen Eq. 3-17 show a relationship between the fatigue crack growth rate dc/dn and energy release rate. Integrating over crack size the both sides of Eq. 3-25, we obtain the relationship between the fatigue life, N , and the crack size by Eq. 3-26. Therefore, the fatigue life can be computed, as the number of cycles required a flaw to grow from the material intrinsic flaw size c_0 to a final size of 1mm. The intrinsic flaw size of material is unknown, but it is possible to

consider a number of different intrinsic flaw sizes, and compute the amount of cycles required the crack to grow until a crack size c_f of 1 mm. In simple tension test sample at a crack size of 1 mm the part can be considered has been broken. This crack size is considered generically a critical size, due to the way of growing catastrophically in few cycles.

The graph presented in Figure 4.24 is constructed from flaw size calibration data, plotting initial flaw size versus fatigue life values for several peak strains. On the other hand, based on the relationship defined by Eq. 3-27 fatigue life is computed in function of applied peak strain levels for several flaw sizes, this is graphically shown in Figure 4.25. Simple tension fatigue cyclic experimental test results for two peak strain levels are superimposed into graphs, and thus are correlated with theoretical fatigue life curves, constructed to estimate the initial flaw size of the material. Fatigue life results and flaw size estimations are summarized on Table 4.10.

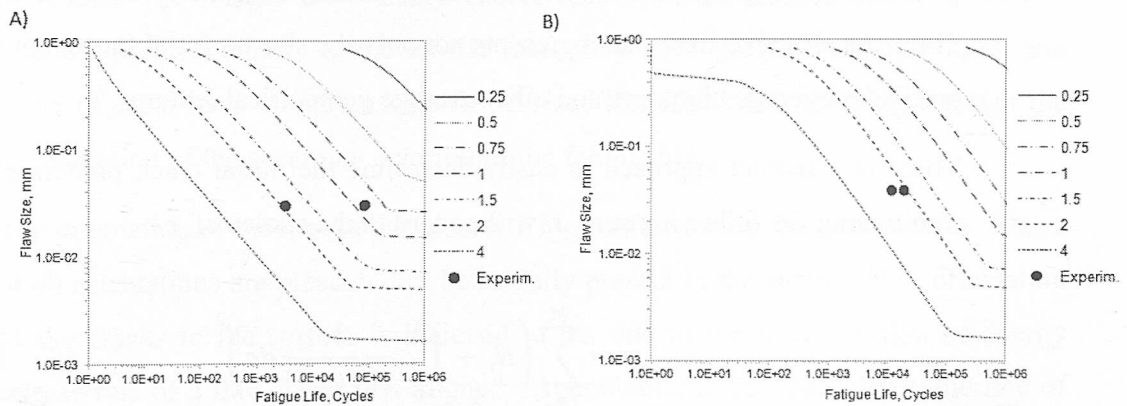


Figure 4.24. Graphical representation of flaw size versus Fatigue life for several strain levels (ranging from 25% to 400% peak strain). A) is the plot of MSB material with an estimation of a flaw size of 0.03 mm; and B) is the plot of MSB material with an estimation of a flaw size of 0.04 mm.

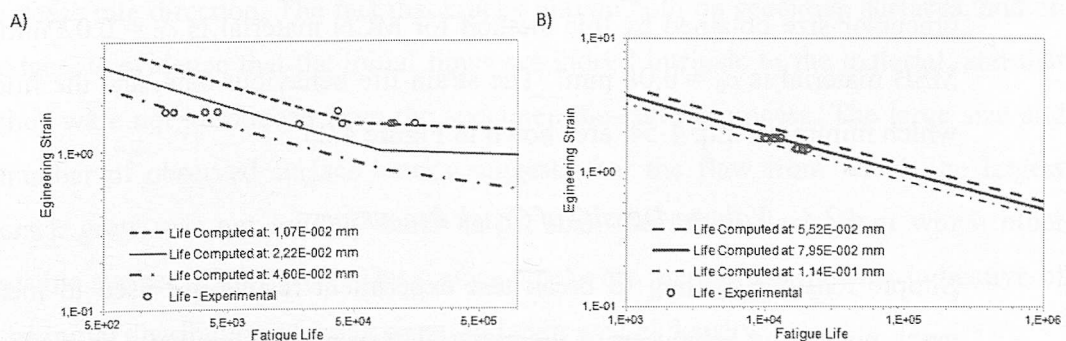


Figure 4.25 Strain-life calibration curve with experimentally obtained fatigue life and computed strain-life curves. A) is the plot of the MSB material (continuous line is for flaw size of 0.022 mm); and B) is the plot of the MCN material. (continuous line is for flaw size of 0.08 mm)

Table 4.10 Fatigue crack nucleation life experimental results, and computed initial flaw size.

	Engineering Strain	Life, N	Computed Initial Flaw Size (mm)	Average initial Flaw Size (mm)
MSB	1.5	81,762	0.01	0.022
	1.8	3,019	0.046	
MCN	1.5	18,108	0.052	0.08
	1.8	11,165	0.114	

The described method is used to determine initial flaw size. Nevertheless, the computed flaw sizes show a high dispersion due to the low repeatability of fatigue life results at every tested peak strain levels, and average value is taken. The flaw size resulting from this approach must be viewed as an effective flaw size. The effective flaw size therefore represents the size of an idealized initial flaw required to give the same growth history observed for actual, irregularly shape initial flaws. Thus, the effective flaw size represents not only the size of initial flaws, but also their particular average bluntness and other average geometrical features.

There is a second approach to easily determine the initial crack precursor size by minimizing the following sum, s , with regard to the choice of, c_0 :

$$s = \sum_{i=1}^m \left(N_i - \int_{c_0}^{c_f} \frac{1}{r(T(\varepsilon_i))} dc \right)^2 \quad \text{Eq. 4-54}$$

ε_i and N_i are observed points on the strain-life curve, obtained via fatigue-to-rupture experiments on an amount of m simple tension strips, Table 4.10. The crack precursor size obtained by this method for MCN material is $c_0 = 0.02$ mm, and for MSB material is $c_0 = 0.08$ mm. The strain-life behaviour data, and the fitted curve, which minimizes Eq. 4-54, are shown in Figure 4.25.

4.2.3. Volume Density of Crack Precursors

Simple tensions cycling to break test experiment results are used to measure the crack nucleation behaviour of the material. Several pictures have been taken during the testing to better understand the surface effects that are happening during the nucleation and propagation of microscopic cracks presumably present in the virgin material. Figure 4.26 show the observed distribution of flaws throughout the surface

of the MCN material specimen. In the approach is assumed that cracks propagate from these initial flaws at varying rates, depending on the particular size, shape, and orientation of each flaw.

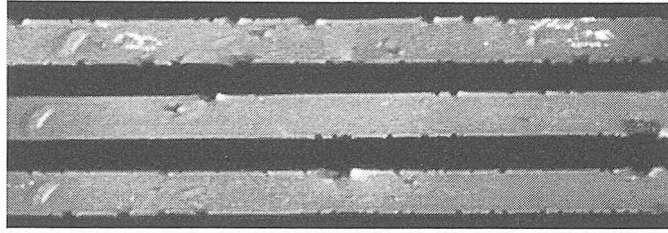


Figure 4.26. Images of cracks developing in the surface of each specimen are shown. The pictured specimen is almost failed, and is shown as slightly strained to permit observation of the cracks. Images are in order from first to third replicate.

Specimens that are shown on Figure 4.26 are in the previous state to completely break. The pictures are taken in a slightly strained position to permit the observation of cracks. The images show many visible cracks on the surface of the specimen, oriented perpendicularly to the tensile load, they have grown from the edges, and some of them have already a significant size. The first crack growing through the cross-section of the specimen determines the fatigue life.

The orientation of the cracks has clearly a high influence on the rate of grow. Flaws of all orientations are presumed to be initially present in the surface. The orientation of the cracks in the surface is believed to be, due to the maximization of energy release rate of a flaw when it is aligned perpendicular to the load. Then, the rate of growth of favourably oriented flaws is more rapid, and accelerates quicker than other flaws. Also, other flaws are going to be oriented into this maximum strain energy release rate direction. The fact that cracks initiate both on specimen surfaces, and on edges, is evidence that the initial flaws are indeed intrinsic to the material, and that they were not introduced from the specimen die-cutting process. The large size and number of observed surface cracks suggests that the flaw from which the largest crack grew was not initially much larger than the initial flaws from which other visible surface cracks grew. The surface cracks are therefore somewhat indicative of the initial distribution of crack sizes, and their spatial density.

From the images it is possible to count cracks and with the software *Image J* even the size can be measured (the process is similar to that described on section 4.2.2, for crack size measurements). Then, the density should be counted per unit specimen

surface area. May be density per material volume should be more appropriate as the initial flaws are intrinsic to the material itself (large filler agglomerates, voids, or other unintended inclusions). Jago [220] reviewed techniques useful for imaging and surveying crack pre-cursors, not only on the surface of a specimen, but also in the bulk. The imaging techniques available in this research work are not adequate for showing internal cracks, thus only surface flaws are counted.

In the present characterization method the ultimate specimen failure is determined by fracture. The flaw density is not needed to predict the evolution of a single critical flaw. Nevertheless, the flaw density data is used later on section 6.1, as an input parameter on the model for stiffness loss prediction.

The MCN material, natural rubber compound, with the recipe shown in Table 2.2, has been used in the development of the approach presented in chapter 4. The carried out test experiment is a small variation of simple tension cycling to break experiment, detailed in section 4.2.1.2. Testing is carried out at a frequency of 2 Hz, at fully relaxing conditions, in displacement control and sinusoidal shape cycling. Three replicates were done at the unique peak deformation of 150 %. Strain was determined from the relationship of strain - displacement, calculated from previous monotonic tensile to break tests, procedure is detailed in section 4.2.1.2. During each fatigue test, peak load was monitored and recorded periodically. The test was stopped after complete specimen rupture. The difference from the standard simple tension cycling to break test reside on the periodically taken photographs of the specimen surface during the test. The last picture prior to specimen rupture is used to count the number of growing crack precursors. The resultant pictures are shown on Figure 4.26. *Image J* software was used to count the number of cracks in the surface of the specimen. The number of counted cracks is summarized in Table 4.11.

Table 4.11 Fatigue test results with peak strain of 150% for MCN material.

Replicate	Fatigue Life	Counted Cracks
1	20876	41
2	15082	26
3	19064	49

4.3. Summary of Material Characterization

The ability to understand and predict the stress-strain response of rubber influences the ability of modeling fatigue life. The initial cyclic stress-strain response of filled rubbers exhibits significant softening due to the stress relaxation known as the Mullins effect. Hyperelastic models do not capture the Mullins effect. When developing hyperelastic curve fits to cyclic stress-strain curves from laboratory test specimens, have to be considered the maximum strain experienced in the specimen of being representative of the maximum strain experienced in the component to be modeled. For considering the Mullins effect, Ogden and Roxburgh model has been used, which produced an isotropic model based upon a strain energy density function. On the approach, the virgin monotonic stress-strain behaviour is modelled using a conventional hyperelastic strain energy density function. Several existing hyperelastic constitutive models were reviewed. Although many options exist for accurately modeling nonlinear elastic behavior the Reduced Polynomial or Yeoh third order model was used in this work. Monotonic and initial cyclic stress-strain experiments were conducted for three main stress states: simple tension, simple compression, and planar tension.

Entire material characterization to fatigue has been carried out satisfactorily at Leartiker facilities, including: fatigue crack growth rate, strain energy release rate threshold, material intrinsic flaw size determination, volume density of crack precursors, R-ratio effect on fatigue crack growth, stiffness loss behavior. The material data computed have been used to feed the fatigue life, nucleation life and stiffness loss life simulations. Test procedures for obtaining all of required parameters are complex and laborious. On the first stage have been designed and implemented. Then the procedures have been optimized with high automation of test execution, data collection, and data processing. As a result, would be concluded that costs and data delivery time limits are not currently a drawback to run rubber fatigue predictions and analysis.

5. Component Fatigue Life Predictions

This chapter presents the fatigue life prediction, and experimental procedures and results of uniaxial experiments of an automotive component made by two different filled rubber compounds, MSB and MCN. The component selected for the study is a rubber mount to hang the exhaust system of a car. In the normal service, the exhaust mount is attached to the car body and the exhaust system by means of two metallic pins. One pin is coming from the car body and the other pin from the exhaust system, passing each one through each of the two circular holes of the mount. The rubber part is isolated from the assembly, and mounted in a tool for testing it in the servo-hydraulic MTS Bionix test machine. Uniaxial fatigue cyclic loadings have been defined for the testing. Constant amplitude cyclic loadings have been defined at three peak levels, commanded in sinusoidal waveform and at fully relaxing (R ratio=0) conditions. Initially, experimental testing have been carried out in displacement control mode, and measured peak force values at cycles 10th to 20th have been used to define the subsequent tests in force control mode.. For both modes of control experimental cyclic tests have been carried out at same initial cyclic peak displacement levels, as summarized on Table 5.1 and Table 5.2.

On the other hand, crack nucleation life simulations have been performed at same test conditions as component real experiments. The life prediction is a laborious work with preliminary tasks to be overcome with satisfactory results. The main task has been the static finite element analysis of component stress strain behaviour, to make the correlation of material constitutive models, and finite element geometry model. Then, the component crack critical location has been identified, and crack nucleation life computed for correlation with experimentally obtained results.

5.1. Prediction of Component Stress Strain Behaviour

The calculation of stress-strain behaviour of complex geometries require of numerical methods, such as finite element methods, to carry out advanced engineering analyses. Finite element analysis is used to simulate the actual service performance of components at their design and development stage. Abaqus and

Anslys finite element softwares have been used to simulate the nonlinear and large deformation behaviour of the component.

5.1.1. Material Characterization

Material strain characterization is fundamental in the simulation process. There are specific material models implemented in finite element analysis software to deal with hyperelastic materials like rubber. Rubberlike materials show highly nonlinear elastic, isotropic and incompressible behaviour. Thus, specific and complex experimental testing procedures have been designed focused on getting the appropriate material data to feed and be fitted by the appropriate material models for finite element analysis. Material strain characterization process has been explained in section 2.5.2, while the material curve fitting has been detailed in section 2.6.

During the first cycles of the material characterization, and at all of three deformation modes a loss of stiffness is observed during the first stretch cycles. The initial softening phenomenon, also called the pre-stretch or preconditioning effect, is widely referred to as the Mullin's effect [3]. Subsequent loadings of equal or lesser magnitude rapidly tend to a steady state. This effect is considered to be a consequence of the breakage of links inside the material, and both filler-matrix and chain interaction links are involved in the phenomenon. Therefore, is a transient effect and is exhibited primarily by filled rubbers. Mullin's effect can be considered for cyclic material properties determination in two different ways. One method consists on using a stabilized cyclic stress-strain response. By the application of stable deformation curve, initial softening or Mullin's effect is inherently considered. Nevertheless, in the present project a second methodology has been selected to consider the material softening. Several researchers have modelled it in a suitable way for using it in continuum mechanics for finite element analysis [32,34,47]. The model selected on this research work has been the proposed by Ogden and Roxburgh [32,36], which is the most accepted, and is already implemented in the most popular finite element codes (Abaqus, Ansys, LS-Dyna, Nastran). It is required the experimental unloading-reloading data several strain levels for at least three of different deformation modes. We have worked with stress state data of simple tension, simple compression and planar tension. Additionally, biaxial tension data would be added if it is available. The procedure used for the fitting has been detailed by the specific equations in section 2.6.2. The material parameters obtained from the

fitting by the hyperelastic model are detailed in Table 2.9, and Mullins parameters for the consideration of the damage of material in Table 2.10.

5.1.2. Finite Element Model Construction

A survey of geometric designs of exhaust mounts resulted in the existence of a wide variety of shapes and sizes. The mount under study on the current research work is geometrically simple as shown in Figure 5.1. It has two circular holes for inserting two 10 mm diameter support pins, one to be attached to the automobile body, and the other one to be attached to the exhausts system. The overall dimensions of the mount are 84 x 50 x 41 mm.

The FE model consist on quarter part of component model due to the symmetries of the geometry and uniaxial loading applied in the two symmetry planes. The model has a fine mesh with an element global size of three. Displacement is applied to the reference point which is coupled with inner FE nodes of the mount at the interface with metallic part by utilizing the rigid body constraint capability of the software.

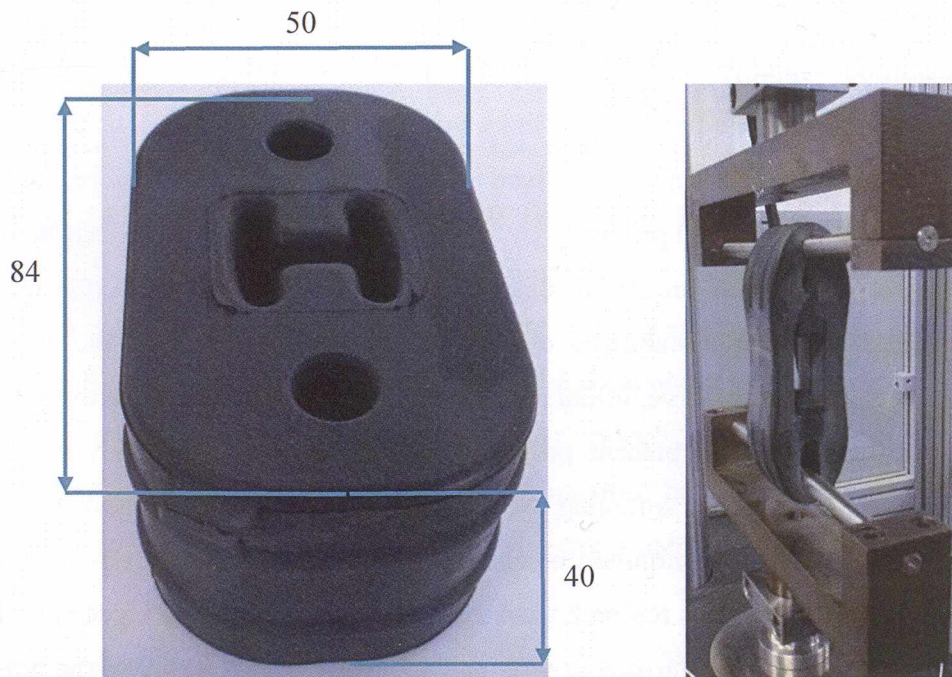


Figure 5.1. Exhausts mount component dimensions in mm, and gripping system for fatigue and stiffness loss experimental tests

In the analysis of an exhausts hanger there may be several types of nonlinearities: geometric nonlinearities, material nonlinearities, and contact nonlinearities. Due to them, even a small model can require substantial computation cost, and therefore, it

is important to keep the number of unknowns as small as possible. It has been followed the recommendation to use a graded mesh, concentrating the greatest mesh density in zones with the highest stress gradients, and take advantage of symmetries. In addition, there is the nonlinear behaviour of material, and large displacements that endure in service.

The simulations to convert the loading history into a strain history for each element which will be used to feed the Endurica CL were carried out in two finite element analysis softwares. The strain history of each element is required for fatigue life and stiffness loss computations. The strain history from any of the finite element analysis software, have to have a specific structure. Currently, Endurica CL has available in the code a python script to output the data from Abaqus in the proper format. By contrast, up to date, there is not any script developed in the Ansys parametric design language (APDL) to output the data for Endurica. Therefore, the simulations have been done in Abaqus. In fact, in the project have been working on a script in APDL for getting the output data in the correct format from Ansys for Endurica CL, and some static simulations have been carried out. The details of performed simulations with each software are explained on following sections 5.1.2.1 and 5.1.2.2.

The coefficient of friction is a parameter that strongly influences the resultant stiffness magnitude in the simulation of components. The exhaust hanger is a rubber made component, which is stretched by two cylindrical metallic pins and without any lubrication. The finite element analyses have to repeat virtually the tests at same conditions, therefore, proper friction coefficients that represent a non-lubricated situation have to be modelled. Slippage between support pins and the circular holes in the hangers is allowed, and this effect is handled in the finite element analysis (FEA) software, by the use of special interface or contact elements. It has been decided not to consider the influence of friction on fatigue life and stiffness loss simulations. Thus, in the Abaqus simulations it has not been considered any friction. Nevertheless it have been carried out, independently to the simulations for the fatigue nucleation and stiffness loss analysis, several simulations to acquire conscience of how much influence. This independent study has been carried out in Ansys software. The special interface elements have been fed by the adequate value of coefficient of friction. A similar fatigue life analysis had been carried out by Mars et. al. [123], and they concluded that “fatigue life turns out to be extremely sensitive to details of

friction and interference fit at the mounting hole". The same paper has been used to define the following coefficients of friction for the simulations: a static / Dynamic Friction of 1.2, and a coefficient of friction for non lubricated interface of 1.04. These details have been taken into consideration in the simulation procedure as explained in section 5.1.2.2 for the analysis done in the Ansys software.

5.1.2.1. *Abaqus Model*

One-quarter of the full component shown on Figure 5.1 was modelled by the use of symmetries on both, loading and boundary conditions, and geometry. The finite element mesh has been built by 8525 eight node linear brick elements with hybrid formulation. The mount is supported by a steel pin, modelled as a rigid, frictionless cylinder in contact with the hole, as is shown of Figure 5.2 where the finite element model is observable. The material parameters obtained in section 2.5.2 has been used to feed the finite element quasi-static analysis as detailed in section 5.1.1. The treatment of effect of friction has been explained previously in the general explanation of finite element analysis procedures. Thus, the default frictionless contact interaction model from Abaqus has been programmed.

The quasi-static simulation carried out using Abaqus software was for constant amplitude loading conditions. For hyper-elastic materials fully hybrid formulation elements with full integration were used for large deformations due to lower distortion. Proper element type, integration scheme and reasonable meshing strategy are all important factors to consider for appropriate modelling and simulation of large deformation rubber components. Hybrid element locking is a key issue in the large deformation simulation computations of 3-D models, which is caused by large element distortion. Element locking can be lessened by proper meshing and element selections. A too fine mesh exhibits more sensitivity to element volumetric locking, especially in large strain areas [221].

Finite element analysis of model is done to transform the global loading history on a strain history for each element. This strain history on every element is the required input data, for subsequent fatigue analyses by the Endurica code. Nevertheless, the strain history has to be outputted at a specific format, and the finite element model is recommendable to meet two conditions to better quality of results. The bulk modulus has to be used in the analysis, instead of true incompressibility, rubbers near

incompressibility means that tiny variations in the volume strain will produce large variations of the hydrostatic pressure. Request to output nominal strains (NE) in local element coordinates for strain cycle recovery, the fatigue calculations have to be made in a coordinate system that translates and rotates with the material.

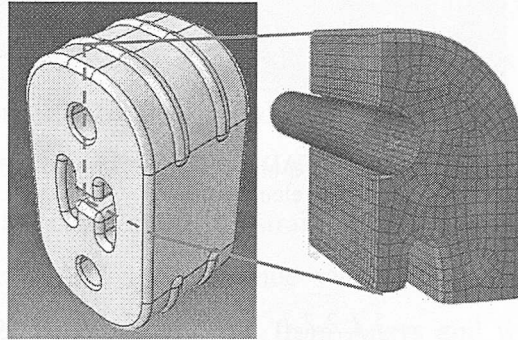


Figure 5.2. Left side image show the CAD model of the exhausts mount component. Right side image is a quarter-symmetric of Abaqus finite element model.

5.1.2.2. *Ansys Model*

Element type used for the 3-D modelling is a brick eight node element. The mesh consists of 2230 elements. It uses the selective reduced integration method or B-bar method, using two different integration orders for volumetric and deviatoric components. Reduce integration for volumetric components and full integration for deviatoric components.

In order to simulate constant amplitude uniaxial loading cyclic test, a simple loading quasi-static finite element analysis have been performed. Ansys parametric design language (APDL) has been used to easily run the set of simulations. The APDL script automates the test, having the option to alter loading conditions and the designed model easily.

As mentioned previously slippage must be allowed between the support pins and the circular holes in the hangers. This effect is handled in Ansys by the use of special interface elements or contact elements as TARGE170 and CONTA174.

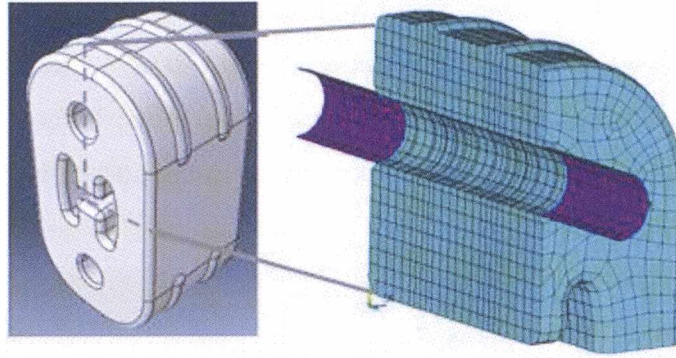


Figure 5.3 Left side image show the CAD model of the exhausts mount component. Right side image is a quarter-symmetric of Ansys finite element model.

5.1.2.2.1. APDL of Ansys to output the strain history

Fatigue life computations require a preliminary finite element analysis to convert the loading history that is repeated in the cycling into a strain history at each element.. During the present project, it has been worked on the APDL scripts for outputting the strain histories from Ansys in the proper structure to feed the Endurica code. This development requires the knowledge of the APDL language to program the output and input of required files for and from the fatigue analysis code. Even The developers of Endurica are interested on the development, and they are collaborating replying any query.

Currently the scripts have been written in APDL for Ansys and implemented in Endurica. The code for outputting results from Ansys to Endurica, has the correct format, Endurica understands the data inside the file, and can work with it correctly giving a fatigue life prediction. The next aim in this section have been to input back the obtained fatigue life results per element into the Ansys finite element analysis software to graph results back into the 3D mesh model. This aim has been also achieved positively, and it has been possible to see the results in Ansys. Unfortunately, the obtained fatigue life result is not in perfectly agreement with that obtained from Abaqus output file for the simple tension test specimen.

The source of the difference in fatigue life, and is the strain histories of each elements outputted from Ansys. The strain history is outputted in specific conditions, and having asked to Ansys to output the strain results in the same way to Abaqus, the results are similar, but not equals. It is ordered to Ansys model to report nominal strain in a local coordinate system, but it does not capture the same history as in

Abaqus. This difficulty has not been solved, and after having invest a long period even contacting Ansys assistance service have been decided to leave it in this phase of implementation to solve it on future works.

For the correlation work the model of a simple tension specimen have been selected, first a stretch have been applied, and then a translation of the upper surface. This loading has been applied to verify in Ansys if strain history is accounting the rotation of element, being rotated also local coordinate system in the element, and reporting nominal strains in local coordinate systems properly. From the beg inning differences were observed in the comparison of strain histories from Ansys and Abaqus.. Anyway, it has been decided to continue with the implementation, to verify if Endurica CL accepts the outputted files from Ansys and was able to perform the fatigue life predictions. The correlation of both prediction results is presented in Figure 5.4 in a fatigue life vs. element number plot. The fatigue life prediction for most of elements show a good correlation, nevertheless, these few elements that are far from the results obtained from Abaqus, are enough to alter the prediction of the fatigue life behaviour of the full model. Therefore, currently, the developed scripts and methodology to work with Ansys for Endurica fatigue life predictions is not useful.

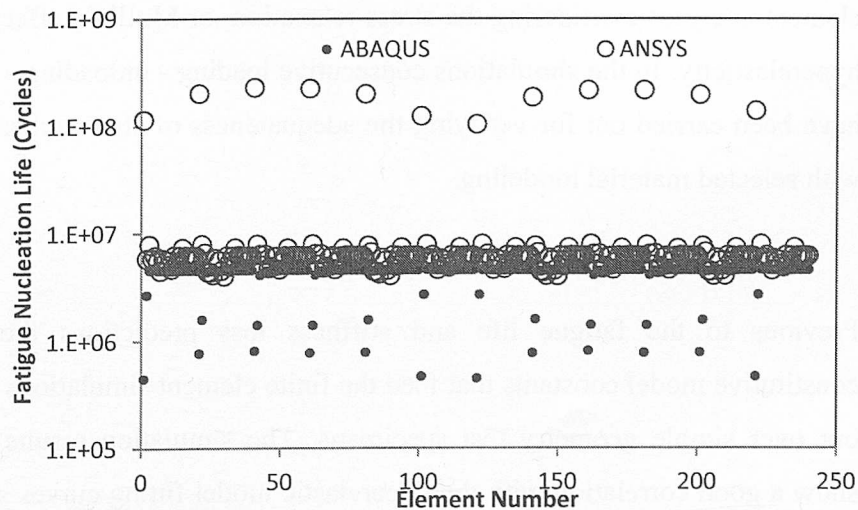


Figure 5.4. Fatigue nucleation life vs. element number are plotted for the simple tension specimen in MCN material. Fatigue life is computed in Endurica from Strain history results obtained from Ansys (hollow circle) and Abaqus (filled circle), modelled in both Ansys and Abaqus for the MCN material.

The details of the APDL scripts are presented on Appendix I.

5.1.3. Finite Element Model and Material Verification

To verify the finite element model and material constitutive model, it has been correlated the reaction force to applied displacement result measured on simulations, with the load cell measurements in experiments. The simulations for the correlation work have been carried out in Ansys. The reaction forces have been computed by the sum of each reaction force at each node, which is connected to the embedded surface, and are registered by a pilot node. Then, from the reaction force result in function of the commanded displacement has been built a graph of force vs. displacement, where are plotted for correlation simulation and experimental testing results.

Previously to the correlation work over the complex geometry component, a similar correlation work has been carried out over simple geometry test specimens. The experimental test results used for the material characterization and fitting the models have been used for doing the correlation with simulation results. During the material characterization procedure, four relaxation cycles at eight different peak strain levels have been performed per test sample. The Yeoh of 3rd order and Ogden Roxburgh constitutive models have been used to define the material behaviour for finite element analyses considering the stress relaxation, or Mullin's effect, along with the hyperelasticity. In the simulations consecutive loading - unloading - reloading cycles have been carried out for verifying the adequateness of stress relaxation predictions with selected material modeling.

5.1.3.1. Correlation of Material Model

Previous to the fatigue life and stiffness loss predictions the verification of constitutive model constants that feed the finite element simulations has to be carried out over simple geometry test specimens. The simulation results are expected to show a good correlation with the hyperelastic model fitting curves shown on section 2.6.1. Actually, the verification is run over same specimen geometries and strain conditions used for the material characterization. Correlation work has been carried out at three strain states, thus specimen geometries, simple tension, planar tension, and simple compression. The verification has been carried out for both project

materials, MCN and MSB. The constitutive models used for finite element simulations have been the Reduced Polynomial, or Yeoh 3rd order, along with the Ogden Roxburgh model, considering the stress relaxation, or Mullin's effect, along with the hyperelasticity. The simulations have been performed in the finite element analysis software Ansys, by using the parametric design language (APDL) to reduce the pre-process and post-process time.

Figure 5.5.A)

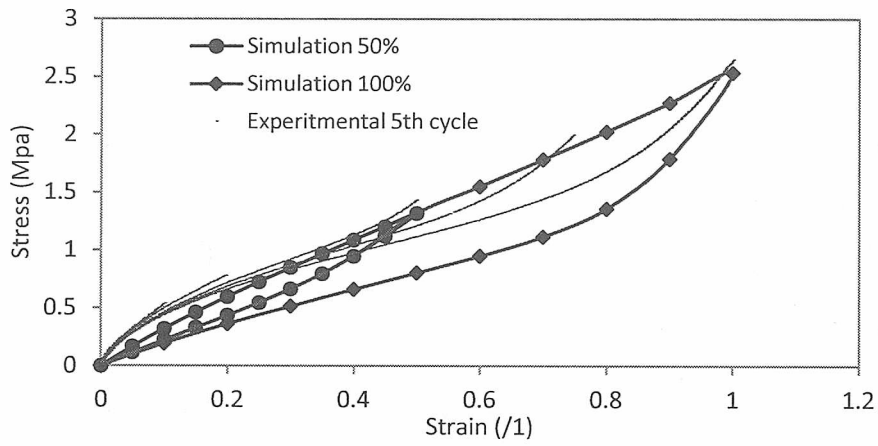


Figure 5.5.B)

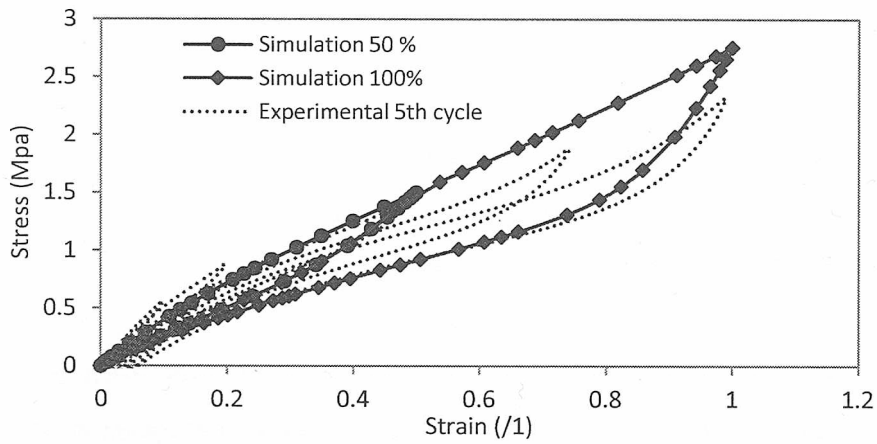


Figure 5.5.C)

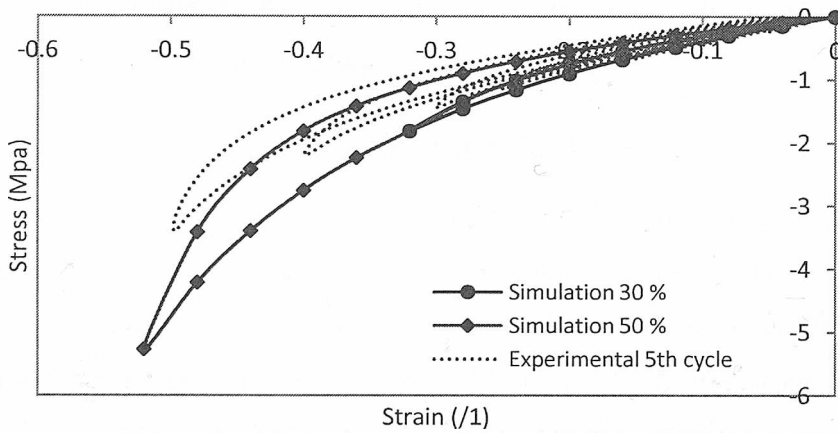


Figure 5.5 Stress vs. strain plot of three specimen geometries, and for MCN material. The graphs show the experimentally obtained results in dot line, and the simulation results at 50 and 100 % strain in solid circle and solid diamond respectively. In the Figure 5.5.A) is for the simple tension, Figure 5.5.B) is for the planar tension, Figure 5.5.C) is for the simple compression.

Figure 5.6.A)

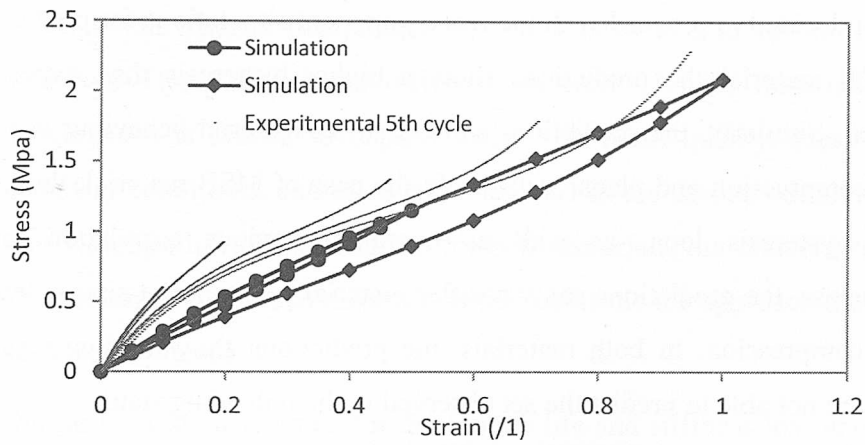


Figure 5.6.B)

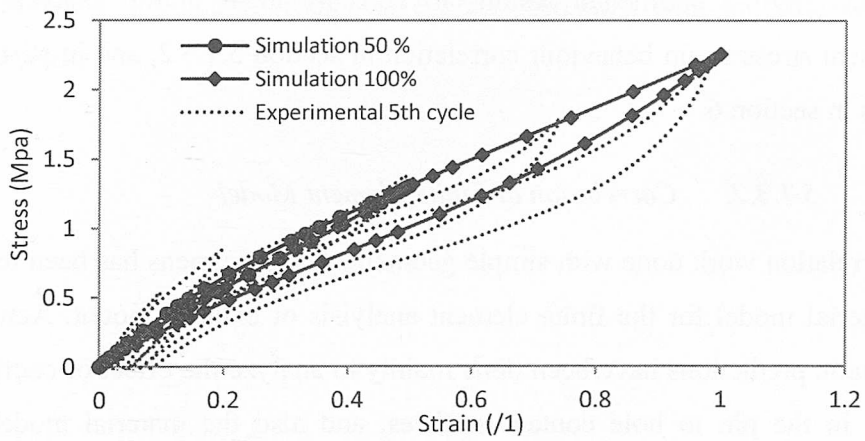


Figure 5.6.C)

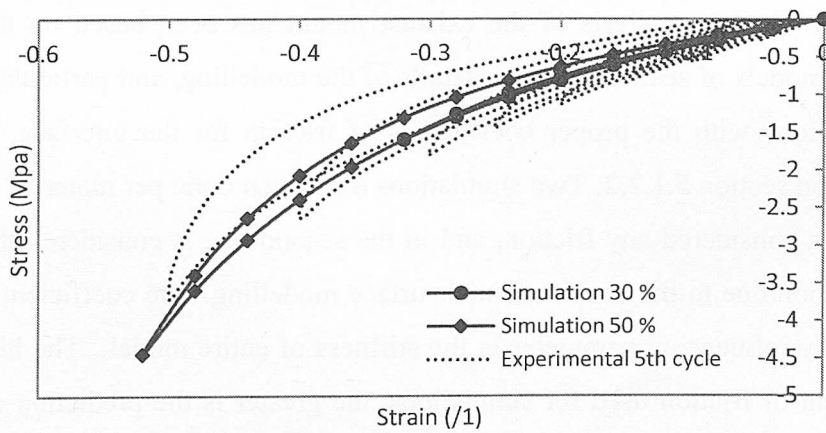


Figure 5.6. Stress vs. strain plot of three specimen geometries, and for MCN material. The graphs show the experimentally obtained results in dot line, and the simulation results at 50 and 100 % strain in solid circle and solid diamond respectively. In the Figure 5.6.A) is for the simple tension, Figure 5.6.B) is for the planar tension, Figure 5.6.C) is for the simple compression.

The observed correlations are considered adequate in general for both materials, thus has been decided to proceed with the real component simulations for predictions. For the MCN material the predictions show a higher hysteresis than experimentally measured. Similarly, the predictions show a stiffer material behaviour especially at simple compression and planar tension. In the case of MSB material, the prediction of the hysteresis loop, as well as overall behaviour correlation are good. Nevertheless, the predictions show a softer material behaviour at simple tension and simple compression. In both materials, the predictions show that current material models are not able to predict the set observed in the unloading states

Being aware that there is room for improvement, we take note of the error of deviations from experimental results, to consider them in the analysis of later component stress strain behaviour correlation in section 5.1.3.2, and in stiffness loss analysis in section 6.

5.1.3.2. Correlation of Finite Element Model

The correlation work done with simple geometry test specimens has been to validate the material model for the finite element analysis of exhaust mount. Actually, the quasi-static predictions have been done mainly to analyze the effect of coefficient of friction in the pin to hole contact surfaces, and also the material models which considers the Mullins effect.

The finite element analysis of the exhaust mount has been based on the verified material models of section 5.1.3.1. Details of the modelling, and particularly contact specifications with the proper coefficients of friction for the interface, have been detailed on section 5.1.2.2. Two simulations have been done per material, in the first one is not considered any friction, and in the second one is considered that there is high friction due to the non-lubricated surface modelling. The coefficient of friction is a highly influencing parameter in the stiffness of entire model . The higher is the coefficient of friction used for simulations, the greater is the prediction of stiffness obtained. The stiffness is computed from the force reaction result registered as the opposition of rubber component to the commanded pins uniaxial displacement. The mode in which the force is measured is by the pilot node, which is collecting all the reactions from the surface of the pin that is in the side of non-movement.

The peak displacements defined for simulations, which represent the cyclic loading levels in the fatigue life predictions, have been tied to the limited convergence achieved. Those have been different on each of both materials. The achieved convergence is known to depend mainly on mesh quality, mesh size, geometry, boundary conditions, and material behaviour. In the carried out simulations the first four variables have been identical for both materials, but convergence displacement level obtained have been different, which confirms the approach that material model has great influence.

During the tests performed for the fatigue life and stiffness loss analysis for section 5.2, the peak force and displacement values have been collected at specific cycle numbers. Prediction results have been correlated with the data collected at these cycles.

Figure 5.7 A)

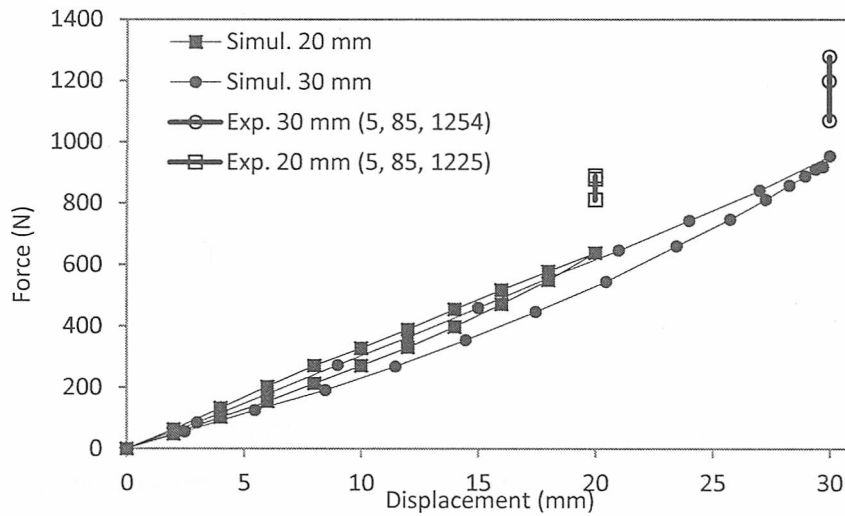


Figure 5.7 B)

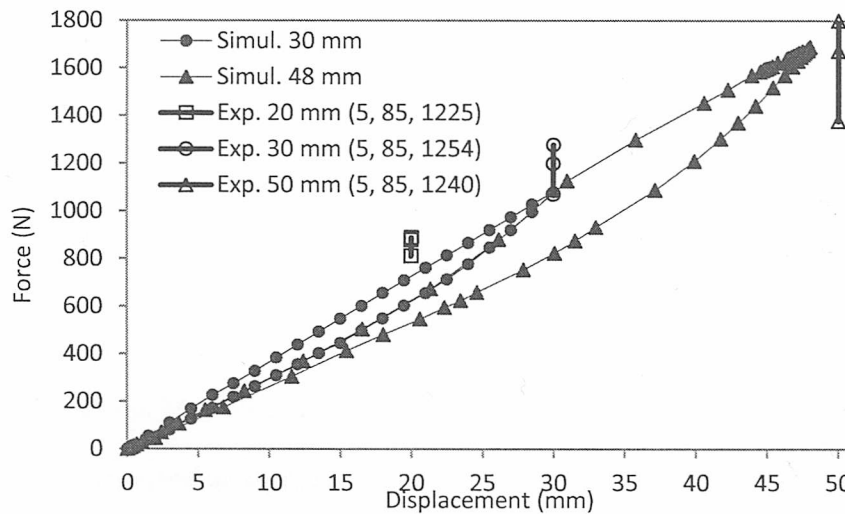


Figure 5.7. Force vs. displacement (F-D) plot of an exhaust mount made of MCN material. The graph represents the simulation results by F-D plot for two peak displacements 20mm in solid square, 30 mm in solid circle; and three experimental results at 20, 30 and 50 mm in hollow square, circle and triangle respectively, for three cycling peak displacements: 5, 85, 1200. In the Figure 5.7 A) is represented the case considering no friction, and in the Figure 5.7 B) is represented the case considering rubber to metal friction.

Figure 5.8 A)

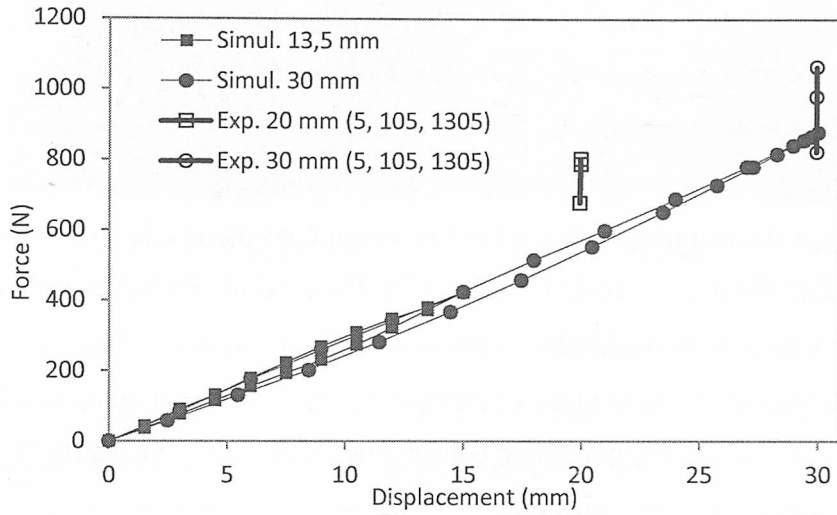


Figure 5.8 B)

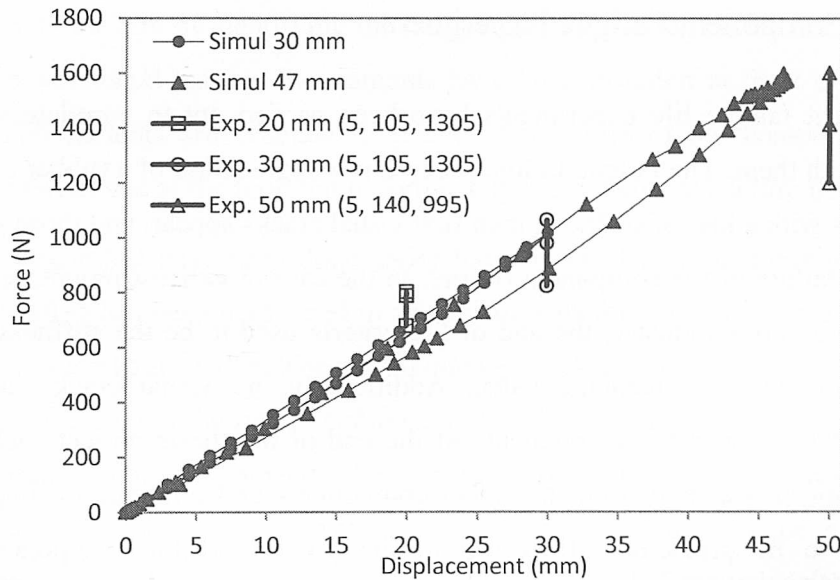


Figure 5.8. Force vs. displacement (F-D) plot of an exhaust mount made of MCN material. The graph represents the simulation results by F-D plot for two peak displacements 20mm in solid square, and 30 mm in solid circle; three experimental results at 20, 30 and 50 mm in hollow square, circle and triangle respectively, for three cycling peak displacements: 5, 85, 1200. In the Figure 5.8 A) is represented the case considering there is no friction, and in the Figure 5.8 B) is represented the case considering rubber to metal friction.

In the correlations of both materials it is noteworthy the stiffening effect of friction coefficients in the finite element prediction results. The simulation results obtained with friction coefficient included in the model show a stiffer behaviour than without friction one. As a result, the prediction considering rubber to metal friction is closer to experimentally observed behaviour.

MCN material component predictions with no friction considered on it have shown a softer behaviour than experimentally observed (Figure 5.7 A). Nevertheless, once the appropriate coefficient of friction has been considered in the simulation, the stiffness of the overall model has been increased and better correlate, as it is shown in Figure 5.7 B. At low displacement levels, 20 and 30 mm, it is still predicted a softer behaviour of the component, but at the maximum convergence level achieved, nearly 50 mm, it is obtained a similar stiffness. In the case of MSB material component predictions, have to be highlighted similar conclusions to those mentioned for MCN. The predicted behaviour is close to experimentally obtained at small displacements, 20 and 30 mm, and at the maximum convergence level achieved, nearly 50 mm, have predicted a slightly higher stiffness.

5.2.Component Fatigue Experiments

Component fatigue life experiments have been carried out to correlate simulation results with them. The fatigue failure process is a degradation of a rubber component that starts with a loss of stiffness, then first visual cracks appear, and those grow until the total failure of the component occurs. In the case of exhaust mount, and usually in the automotive industry, the end of life criteria used to be the stiffness loss of a certain amount in percentage value. Additionally, no visual cracks used to be permitted to exist in the component. At the end of the thesis project each of three degradation phases that occur in rubber components under fatigue loadings will be possible to be predicted. However, on the present section component fatigue experimental work conditions and obtained results are presented. The exhaust mounts have been tested to uniaxial constant amplitude fully relaxing cycling tests. Two cameras have been installed in front of the test machine to take pictures at determined number of cycles. The set up can be observed on Figure 5.9. Thus, from taken pictures the nucleation life can be measured, and at same time there is a visual confirmation of nucleation zones.

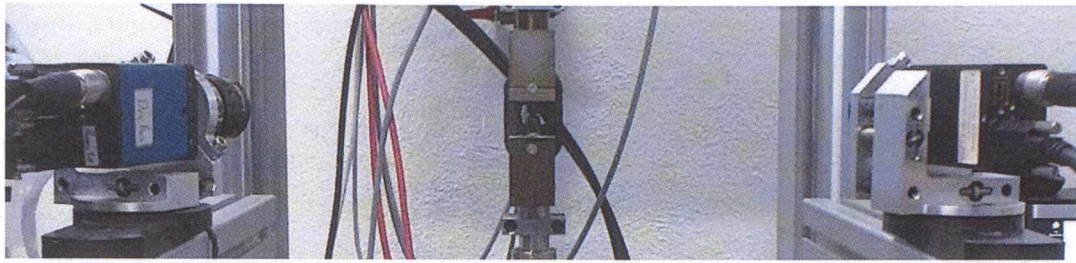


Figure 5.9 Component fatigue life test set-up with two cameras installed in front of the MTS Bionix Servo-hydraulic test machine to acquire images of the first visual crack during the testing.

5.2.1. Fatigue Test Experiment Conditions and Results

The rubber exhaust mount is isolated and mounted in a tool specifically designed for testing it in a servo-hydraulic MTS Bionix machine. Fatigue test set-up is shown on Figure 5.1 and Figure 5.9. The union of the component to the testing tool by metallic pins is not lubricated, and therefore there is a high influence of friction on results. With the aim of identifying the fatigue critical location on the component during the experimental testing, two cameras have been installed in front of the test machine. The cameras are oriented to see the both sides of the component, avoiding the interference of the tool, but unfortunately are not able to capture the back face.

Fatigue test have been done under the control of both, displacement and force, the loading has been performed in sinusoidal waveform at several peak values and the R ratio is of zero value. The test frequency in all cases has been of 2 Hz, to avoid any self-heating of the rubber component. For the testing at different control modes it has been sought to command initially same magnitude strain and stress peak values, for that, first displacement values were defined and the fatigue cycling tests were realized. From these experimental results, the peak force values at 10th to 20th cycle were annotated to define the magnitudes for the force control tests.

The carried out test conditions, and obtained average of fatigue crack nucleation results are summarized for MCN material on Table 5.1, and for the MSB material on Table 5.2. The experimental values of the number of cycles to nucleation life inherently have a lack of accuracy, due to the fact that cracks have been nucleated in the period between pictures. The measurement of the crack length, performed in a visual manner from pictures, has also a lack of accuracy due to the human factor in the evaluation process, even being carried out with the help of Image J software. Therefore, there is a scattering in the nucleation life results. In the Figure 5.10 is

shown the graphical representation of fatigue life results in logarithmic scale in function of carried out replicates at each initial peak displacement.

From results can be concluded that loading control mode has a great influence on fatigue life. Fatigue test controlled in force show a shorter life than commanded in displacement. It is also appreciable the high scatter of these kind of measurements, principally due to the measurement method, but additionally due to the low repeatability of rubber to fatigue cycling. The scattering is more pronounced at short life, at high displacement cycling levels.

Table 5.1. Fatigue testing operating conditions and obtained fatigue life average results for exhaust mount made by MCN material.

MCN				
Test Control Type	Disp. Mín. (mm)	Disp. Max. (mm)	Frequency (Hz)	Nucleation Life
Disp. 1	0	+20	2	76,667
Disp. 2	0	+30	2	16,333
Disp. 3	0	+50	2	1,500
Disp. 3	0	+ 60	2	900
Test Control Type	Force Mín. (N)	Force Max. (N)	Frequency (Hz)	Nucleation Life
Force. 1	0	+750	2	109,000
Force. 2	0	+885	2	41,333
Force. 3	0	+1280	2	8,500

Table 5.2. Fatigue testing operating conditions and obtained fatigue life average results for exhaust mount made by MSB material.

MSB				
Test Control Type	Disp. Mín. (mm)	Disp. Max. (mm)	Frequency (Hz)	Nucleation Life
Disp. 1	0	+20	2	-(*)
Disp. 2	0	+30	2	218,000
Disp. 3	0	+50	2	5,500
Disp. 4	0	+60	2	1,300
Test Control Type	Force Mín. (N)	Force Max. (N)	Frequency (Hz)	Nucleation Life
Force. 1	0	+850	2	166,100
Force. 2	0	+1000	2	91,000
Force. 3	0	+1300	2	5,667

(*) The installed cameras to capture the first visual crack were not able to see any crack at none replicates.

Figure 5.10. A)

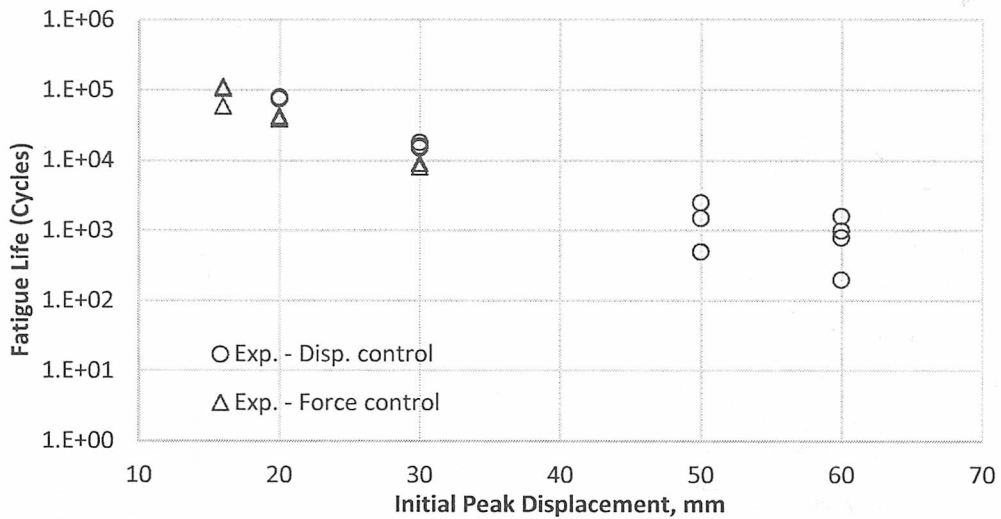


Figure 5.10. B)

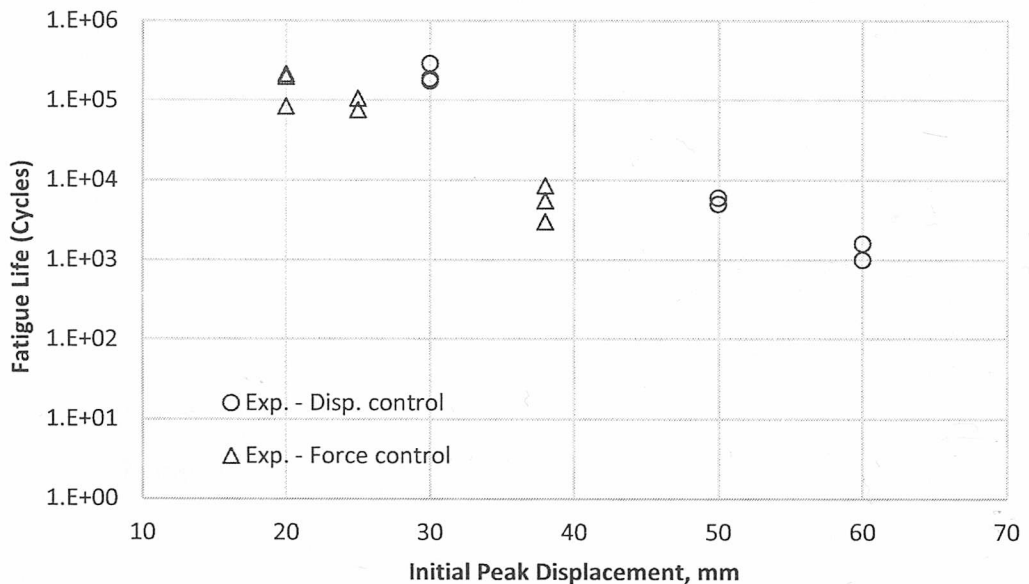


Figure 5.10. Entire fatigue nucleation life results at all replicates of each initial peak displacement conditions, commanded at both, force and displacement. Figure 5.10. A) Results for exhaust mount made by MCN material. Figure 5.10. B) Results for exhaust mount made by MSB material.

5.2.2. Localization of First Nucleated Cracks

In order to predict the damage due to fatigue the identification of critical location is essential. The identification of fatigue critical location on real component experiments have been done assisted by two cameras installed in front of the testing machine. The test set up is shown in the Figure 5.9. The two cameras take pictures of front faces and corners identified as potential to failure in the simulations. Actually, the implemented system has limitations, and back side is not visible for cameras.

This makes difficult to determine precisely when first crack in the component has nucleated, thus obtained results have shown high scatter. Occasionally, crack started on the back side, and was not possible to determine when nucleated, and test had been considered invalid. Nevertheless, implemented method has been approved for being functional. From there, first nucleated crack zones have been identified as it is shown in the representative picture of one of replicates in Figure 5.11. The cracks are nucleated in the inner surface of the rubber component holes, where cylindrical metallic pins are inserted. The pictures have been taken in a stretched position of the component to be easier to distinguish where exactly the crack has been nucleated. This is located at an angle of 30 to 45 degrees relative to the horizontal plane. The same behaviour, and therefore same nucleation zones, has been observed in both materials, MSB and MCN, made exhaust mounts. In the Table 5.3 pictures at fatigue crack nucleation instant for MCN and MSB material made exhaust mounts are presented. The images have been cut, showing only the nucleation zones. Pictures have been presented for each control type, loading level and replicate. Analyzing the table can be concluded that for both material made components, in all loading cases the crack nucleation is in the same zone.

The crack nucleation zones are those where maximum strains are measured due to the mechanical loading, and are magnified by the rubber to metal friction on contact surfaces due to lack of lubrication. The high friction between surfaces produces an increment of temperature in the contact zones, and degrades the rubber in these critical zones of the component. Consequently the crack nucleation rate has been increased. Unfortunately this effect has not been considered in the simulations done for fatigue crack nucleation predictions. Nevertheless, this has been taken into consideration in the analysis of obtained prediction results.

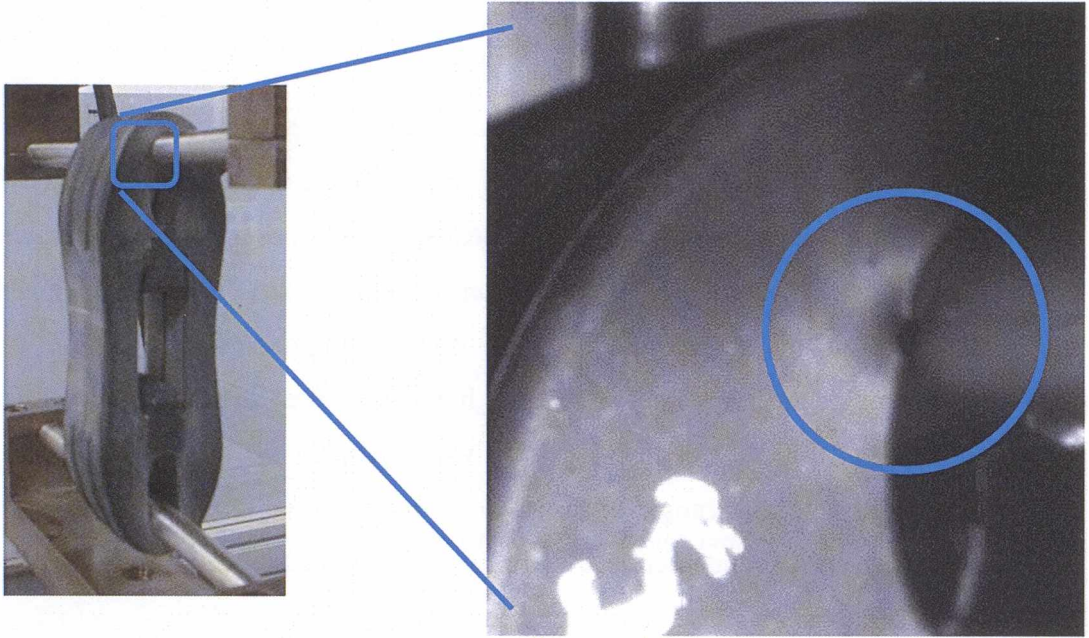


Figure 5.11. Representative image of the cycling fatigue test of MCN material made exhaust mount, which is amplified in the typical fatigue crack nucleation zone to better see the crack.

Table 5.3.A Table of pictures at fatigue crack nucleation instant for MCN material made exhaust mounts. The images are cut in the nucleation zone. Pictures have been presented for each control type, loading level and replicate.

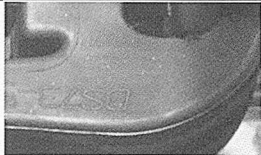
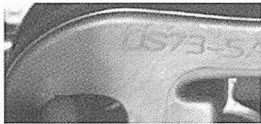
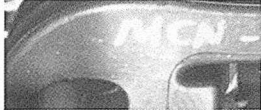
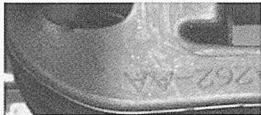
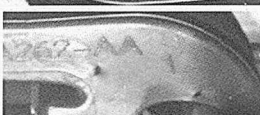
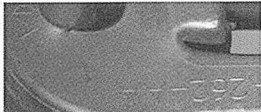
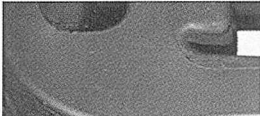
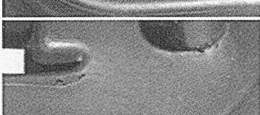
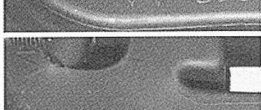
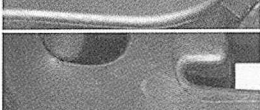
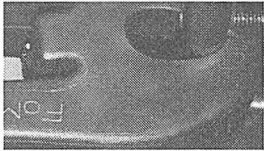
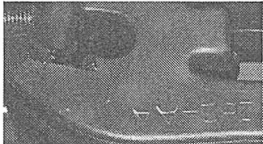
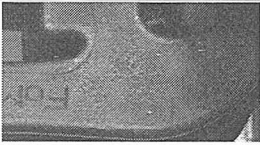
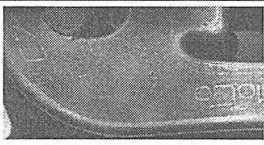
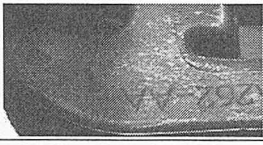
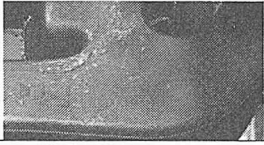
MCN				
Test Control l Disp. (mm)	1 st	2 nd	3 rd	Nucleation Life (Mean)
20				76,667
30				16,333
50				1,500
60				900
Test Control l Force (N)	1 st	2 nd	3 rd	Nucleation Life (Mean)
750				166,100
885				91,000
1280	-			5,667

Table 5.4.B Table of pictures at fatigue crack nucleation instant for MSB material made exhaust mounts. The images are cut in the nucleation zone. Pictures have been presented for each control type, loading level and replicate.

MSB				
Test Control	1 st	2 nd	3 rd	Nucleation Life (Mean)
Disp. (mm)				
30	-	-		-(*)
50	-		-	218,000
Test Control	1 st	2 nd	3 rd	Nucleation Life (Mean)
Force (N)				
850				166,100
1000	-			91,000
1300				5,667

(*) The installed cameras to capture the first visual crack were not able to see any crack at none replicates.

5.3.Component Crack Nucleation Life Prediction

There are some essential steps in order to predict the fatigue damage of rubber components. The first one is to identify the fatigue critical location and map the load history to study the elements in that zone. In the project all elements of the component have been analyzed, and most affecting instant is clear as have been simulated uniaxial constant amplitude fully relaxing cyclic loadings in displacement control. The energy release rate quantified by the cracking energy density has been the parameter used for identifying and measure the fatigue damage. The cracking

energy density [54] represents the portion of the total strain energy density that is available on a particular plane to be released through crack growth, and also introduces the critical plane concept in the context of elasticity, based on the assumption that available energy is greater on given material planes. The cracking energy density on the critical plane was calculated from the strain history via the fatigue life prediction software Endurica CL using the Yeoh third order model. Then, again using Endurica CL, from integration of the power law fatigue crack growth rate relationship to energy release rate based on cracking energy density, fatigue life is calculated for the critical location in the component.

Therefore, for complex geometry components a numerical method such as the finite element analysis is required. The component life prediction procedure used is based on both crack initiation and crack growth approaches. Constant amplitude specimen test data are used as the basis of fatigue life curve for crack nucleation. Whereas specimen crack growth data and the initial natural flaw size in the material are used for crack growth or total fatigue life of the component. The load levels used for component testing in section 5.2 are higher than those applied in the component in actual service condition. This was necessary in order to induce fatigue failure in a reasonable time period.

The objective is to validate the simulation procedure for complex geometry rubber components under constant amplitude uniaxial fatigue loading. Nevertheless the damage parameter and procedure used are adequate also to deal with variable amplitude multiaxial loadings. The applicability of the procedure has been tested by the analysis of an automotive exhaust mount component. The obtained predictions are correlated with real component experimental results.

The material characterization to fatigue crack growth have been detailed in section 4.1.1. The intrinsic flaw size of the material has been experimentally determined in section 4.2.2. Then, the quasi-static strain history of the real component to feed the Endurica CL solver has been computed by Abaqus finite element analysis software in section 5.1.2.1.

The strain history has been computed in section 5.1.3 in Ansys software, but the Endurica CL requires the strain history data to be in a particular format. Unfortunately, I had no success on writing the correct script to output strain history

during the project. The work done to obtain the strain life data in the proper configuration from Ansys and in an automated manner by using the APDL scripts as detailed in section 5.1.2.2.1. Thus, it will be one of the future works, to find the missing line in the APDL script.

5.3.1. Fatigue Crack Nucleation Life Prediction

The Endurica CL solver for elastomer fatigue analysis takes as input the history of the strain tensor components per element, the hyperelastic constitutive model data, flaw size of material and the crack growth rate in function of the strain energy release rate data. Actually, the hyperelastic constitutive model data have been used already in the quasi-static simulations in Abaqus, to convert the loading histories into the history of the strain tensor components of each element. The strain history on the centroid of elements is the required input data for subsequent fatigue analyses by Endurica CL solver. The details of the Abaqus finite element analysis are given in section 5.1.2. The fatigue crack growth behaviour data of material is required for fatigue nucleation life predictions. Then, Endurica will compute the fatigue nucleation life, which is defined as the number of cycles required to grow the crack from its initial intrinsic flaw size to a critical size determined in 1 mm [54,62,63]. In a conservative approach the fatigue life should be considered to happen at nucleation life, Saintier et al. [64] estimated that an 80 % of the life is spent in propagating the fatigue crack from the initial flaw size, from 100 - 200 μm to a critical size usually defined in 1 mm. From the computations, Endurica CL sorts in a list the predicted number of cycles to nucleation life for each element.

Nucleation life of component is therefore concluded from the result of shortest life element, which is considered will be the first growing crack until break. The prediction method and defined criteria are very conservative, and short life has been predicted from simulations in comparison to experimentally observed. From one side, elements of high distortion and strain concentrations alter the prediction with strain history results computed from the finite element analysis. From the other side we have deeper analyze pictures taken during the experiments have shown that first observed cracks were previously nucleated and have coming growing from inner side of the hole to the outer surface. Thus, it has been decided that to correlation with what has been observed in the experiments, is more appropriate to consider as fatigue nucleation life the number of cycles at which 2% of elements have been nucleated.

This fatigue life result is computed using the percentile Parameter. Test conditions and results for a percentile of 0.02 are summarized in Table 5.5 and Table 5.6. In the tables nucleation life predictions at force and displacement control types are shown. Actually for both control types the finite element analysis are done in displacement control, and then the damage effect due to the control type is taken into account in the Endurica CL solver for rubber fatigue. The approach developed for the Endurica CL solve for considering the control type effect on the fatigue cycling is detailed in the section 6.2.1

Table 5.5. Fatigue life prediction conditions and obtained results for the exhaust mount made by MCN material.

SIMULATION – MCN				
Test Control Type	Disp. Mín. (mm)	Disp. Max. (mm)	Nucleation Life	Nucleation Life at a Percentile of 0.02
Disp. 1	0	+20	256	356,000
Disp. 2	0	+30	36	24,351
Disp. 3	0	+50	7	792
Test Control Type	Disp. Mín. (mm)	Disp. Max. (mm)	Nucleation Life	Nucleation Life at a Percentile of 0.02
Force. 1	0	+20	53	67,985
Force. 2	0	+30	0	4,620
Force. 3	0	+50	0	151

Table 5.6. Fatigue life prediction conditions and obtained results for the exhaust mount made by MSB material.

SIMULATION – MSB				
Test Control Type	Disp. Mín. (mm)	Disp. Max. (mm)	Nucleation Life	Nucleation Life at a Percentile of 0.02
Disp. 1	0	+20	41	293,000
Disp. 2	0	+30	1	16,252
Disp. 3	0	+50	0	238
Test Control Type	Disp. Mín. (mm)	Disp. Max. (mm)	Nucleation Life	Nucleation Life at a Percentile of 0.02
Force. 1	0	+20	13	94,507
Force. 2	0	+30	0	5,170
Force. 3	0	+50	0	76

To correlate fatigue crack nucleation life prediction results with experimentally obtained, the graphs shown in Figure 5.12 and Figure 5.13 have been constructed. Experimentally carried out test conditions, and obtained average of fatigue crack nucleation results are summarized for MCN material on Table 5.1, and for the MSB material on Table 5.2. From the plots of the correlations have to be highlighted the perfect agreement obtained at low amplitude cycling conditions, for both materials. Similarly, it should be noted the adequateness of predictions following the life decrease tendency when peak loadings have been increased. In the case of control mode effect, this has been also properly predicted, computing a shorter life when the fatigue cycling is controlled in force. Nevertheless, generally the fatigue life predictions are far from experimentally observed behaviour. The computer aided simulations predict a considerably less long-lived component than measured on experimental tests. This effect has been more pronounced for MSB material made mounts, in contrast to MCN material made mounts.

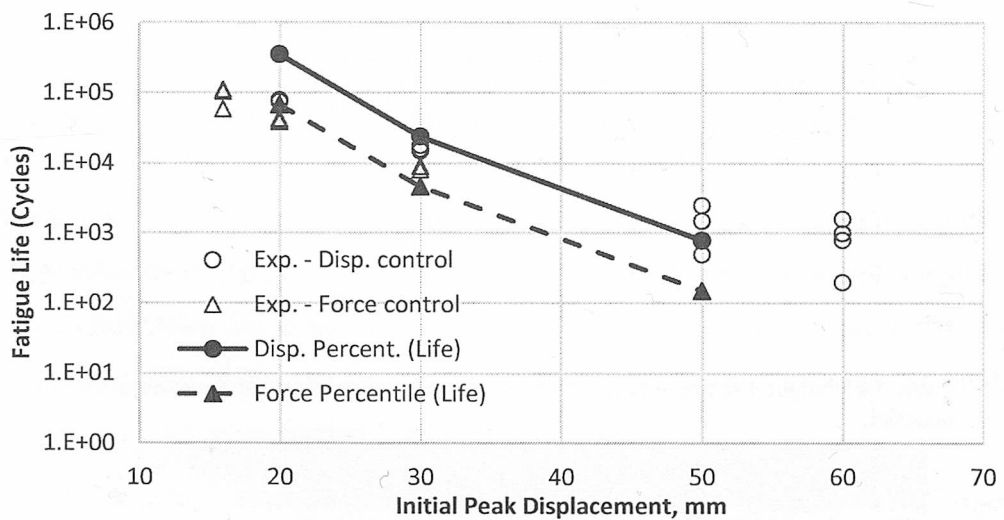


Figure 5.12. The fatigue life in logarithmic scale vs. The initial peak displacement are shown in the following graph. Fatigue life predictions (hollowed symbols) are correlated with carried out experimental results (full symbols) for the exhaust mount made by MCN material. Circles are for displacement control loadings, while triangles are for force control loadings.

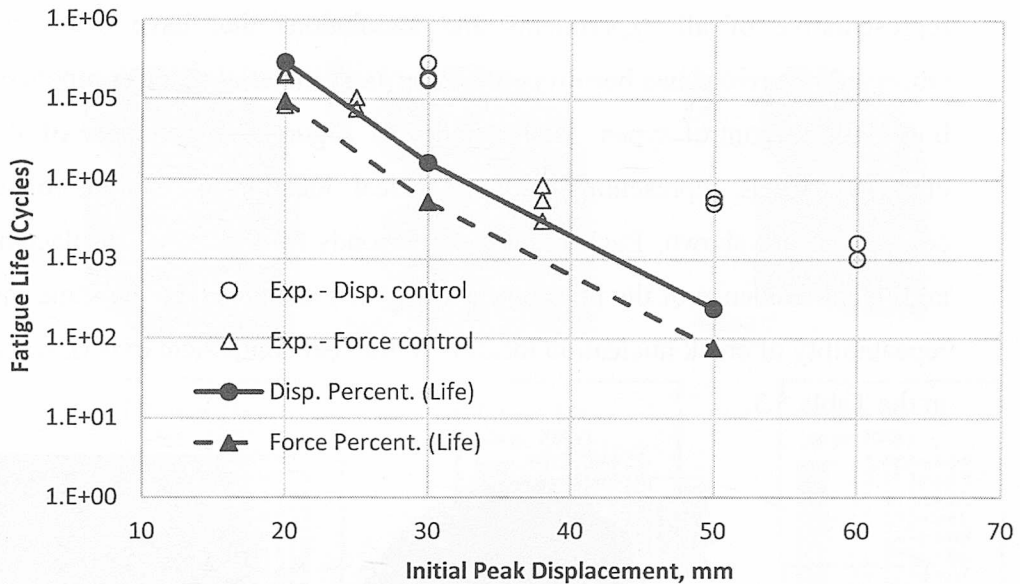


Figure 5.13. The fatigue life in logarithmic scale vs. The initial peak displacement are shown in the following graph. Fatigue life predictions (hollowed symbols) are correlated with carried out experimental results (full symbols) for the exhaust mount made by MSB material. The circles are for displacement control loadings, while the triangles are for force control loadings.

5.3.2. Identify the Fatigue Critical Location

The fatigue critical location is identified by the shortest fatigue life prediction element measured in the Endurica CL solver for rubber fatigue analysis. The solver has been fed by strain history of each element obtained from the finite element analysis of the component model in Abaqus. The strain history is required to be of the centroid of each element. Thus, the fatigue life predictions are computed per element, and therefore the critical zones in the component can be identified. Actually, the life result is a sorted list of two columns with the element number on first, and the corresponding life prediction in the second column. Then, with script from Endurica CL it is possible to plot back this fatigue life prediction per element into the Abaqus mesh model of the component. Having the component geometry in the finite element analysis software is easy to identify there the crack nucleation zones.

The fatigue life simulations have been carried out for two of project materials. Test conditions and results have been summarized in Table 5.5 and Table 5.6. On the other hand, fatigue experiments have been summarized on Table 5.1 and Table 5.2. The correlation of predictions with experimental results has been done by the pictures of results faced like there are shown on Figure 5.14. The shown images are

representative of all experiments and simulations that have been carried out. Observed behaviour has been repetitive, for both material made components and for both fatigue control types. Additionally, in Figure 5.15 pictures of three finite element models representing fatigue critical location predictions of the MCN component are shown. Each picture corresponds to one cyclic displacement level, and is the evidence of the high repeatability of predictions. In the same manner, the repeatability of crack nucleation location in the real component experiments is shown in the Table 5.3.

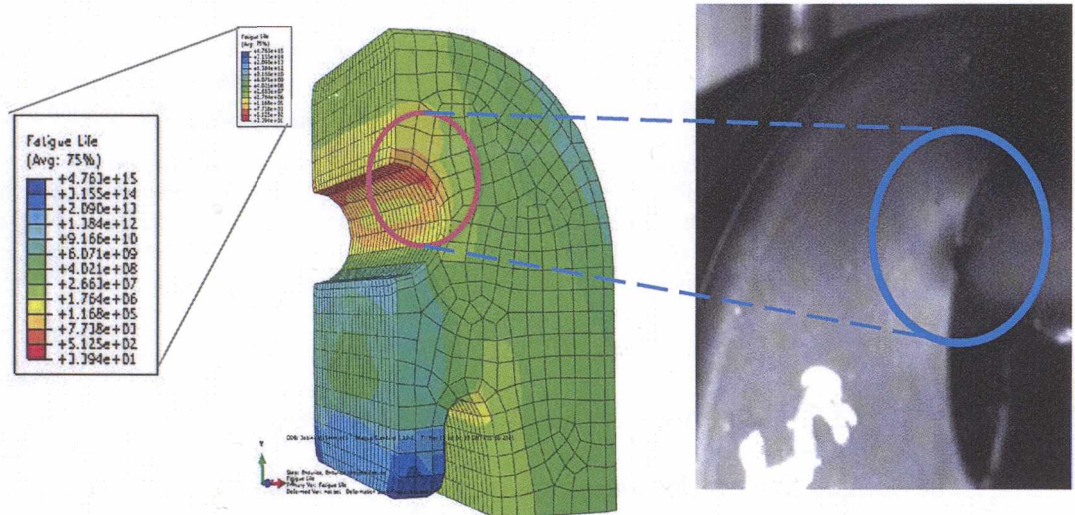


Figure 5.14. Comparative image of simulation results in a quarter part of entire model (left side) and a capture of the component during the fatigue test in the instant that a crack is nucleated. Prediction and experimental components shown in the pictures are both made of MCN material.

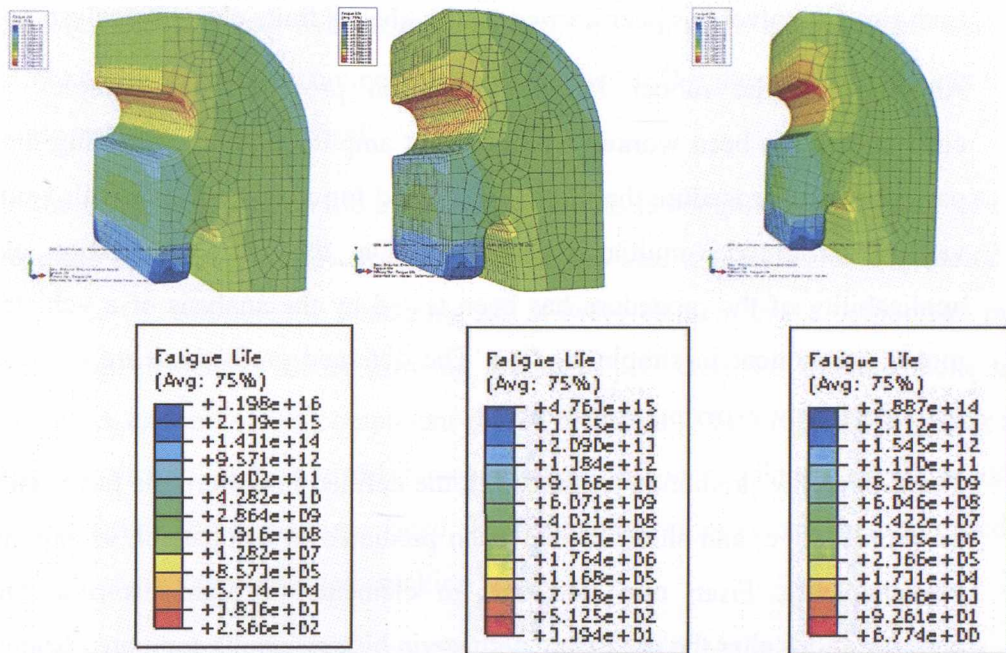


Figure 5.15. The finite element models of fatigue life prediction results at three different peak displacement levels simulated for the MCN material made exhaust mount component. Fatigue Life distribution (in log10 scale) for a displacement of 20 mm between pins.

5.4. Summary of Component Fatigue Life Predictions

In the crack nucleation life predictions all elements of the component model are analyzed as potential to failure. The cracking energy density based energy release rate has been used to identify and measure the fatigue damage, and critical plane. The critical locations are identified in the component from the minimum life element, computed from the integration of the damage function. For complex geometry components a numerical method such as the finite element analysis is required. The component life prediction procedure considers both crack initiation and crack growth approaches. Constant amplitude fatigue cycling simple tension specimen test data is used as the basis to construct the fatigue life curve for crack nucleation. Whereas specimen crack growth data and the initial natural flaw size of material are used for crack growth or total fatigue life computations of the component. The load levels defined for component testing are of higher magnitude than usually applied in service conditions in the component, in order to induce fatigue failure within a

reasonable time.. The quasi-static strain history of the real component to feed the Endurica CL solver has been carried out in Abaqus finite element analysis software.

Although, in the rubber fatigue simulation procedure for complex geometry components has been worked with constant amplitude uniaxial loading the damage parameter and procedure that has been defined for computations are also suitable for variable amplitude multiaxial loadings. On this first correlation work the applicability of the procedure has been tested by the analysis of a vehicle exhaust mount component in simple loading. The obtained predictions are correlated with real component experimental results.

The fatigue life prediction method with the defined initial criteria has been found to be conservative, and short life has been predicted in comparison to experimentally measured life. From one side, due to elements of high distortion and strain concentrations alter the prediction with strain history results computed from the finite element analysis. Additionally, a deeper analysis of during the experiments taken pictures has shown that first observed cracks were previously nucleated and have coming growing from inner side of the hole to the outer surface. Thus, it has been decided that for correlation with experimentally observed behaviour, is more appropriate to consider as fatigue nucleation the number of cycles at which a determine percent of elements have already been nucleated. This fatigue life result is computed using the percentile function. Test results for a percentile of 0.02, which means that a 2% of elements have been nucleated, for force and displacement control types have been computed to be correlated. Actually, for both control type simulations the finite element analyses have been run in displacement control. Then the damage effect due to the control type is taken into account in the Endurica CL solver for life predictions with the damage functions detailed in section 6.2. To correlate fatigue crack nucleation life prediction results with experimentally obtained, the graphs shown in Figure 5.12 and Figure 5.13 have been constructed. From the plots of the correlations have to be highlighted the perfect agreement obtained at low amplitude cycling conditions, for both materials. Similarly, it should be noted the adequateness of predictions following the life decrease tendency when peak loadings have been increased. The control mode effect has been also properly predicted, computing a shorter life when the fatigue cycling is controlled in force. On the other hand, analyzing entire curve the fatigue life predictions are far from

experimentally observed behaviour. The computer aided simulations predict a considerably less long-lived component than measured on experimental tests. This effect has been more pronounced in the case for MSB material made mounts than in those made by MCN material

In the analysis of fatigue life by the Endurica CL is computed the number of cycles required by a crack to grow from the initial flaw size to a nucleated considered size. Endurica CL compute the nucleation life at every element in the component model, and from element of faster growing cracks is predicted the cracking zone in the model. A capture of the component model identifying the predicted cracking zone, and the picture of first visible crack in the component taken during the exhaust mount fatigue experiment are faced. There is a perfect agreement between predicted and experimentally observed cracking zones.

Additionally have to be analyzed the initial decision of not consider some factors on fatigue life computations, even knowing that they would influence on fatigue nucleation life prediction of components. Those have been the self heating of the component and rubber to metal friction. The fatigue predictions is known that would be affected due to increment of temperature in the component or self heating due to hysteresis of material, as well as due to the friction of rubber to metal in the pin holes. Similarly predictions depend on the overall stiffness of component that would increase if friction coefficient would be considered in simulations. Therefore, can be concluded that implemented procedure is operational and working satisfactorily, but in the project has not been considered all the influencing factors, and will have to be done in future works.

6. Component Stiffness Loss Prediction

In rubber fatigue the strain energy density may depend not only on the instantaneous strain or stress, but also on damage state of material, and on the mode of control imposed in the fatigue test. The stiffness loss approach relates the differentiated particular damage developments of different loading modes in a function. The parameter that quantifies the damage is the normalized stiffness, and a function has been defined that contemplates the effect of stiffness loss and crack size on the strain energy density. The approach has been implemented in Endurica CL solver for rubber fatigue analysis. The fatigue-to-rupture experiments for material characterization on simple tension strips have been run in fully relaxing displacement control. The peak force during each cycle has been recorded for determining the damage. The resultant stiffness loss data is normalized by its initial stiffness E/E_0 , and the damage is plotted as function of the normalized fatigue life N/N_f . It has been assumed that all strain amplitudes produce the same identical stiffness loss characteristic curve. Thus, the obtained relationship is given as a tabular definition of the damage function, as a lookup table, to feed the fatigue solver; and then compute the stiffness loss on entire component by the finite element analysis with damaged material model by the Uhyper.

Additionally to the consideration of stiffness loss and crack size on the strain energy density, a constitutive model has been tested to consider the contribution of cracks in the softening effect. For this aim, the softening function is defined with a constitutive model instead of the tabular data. The model is considering the contribution of cracks in the softening effect. It is known that the size and volume density of the very largest crack precursors directly governs the accelerating stiffness loss effect that immediately precedes specimen rupture. It is also known that at earlier times, the effects of smaller precursors also contribute significantly to loss of stiffness. The tendency to grow and abundant presence of crack precursors to cyclic softening effects has been considered in the constitutive model. The first few loading cycles applied in a cycling fatigue test are known to cause a rapid transient decrease in stiffness, as originally demonstrated by Mullins [3]. Then, cyclic loading beyond the first few cycles, stiffness loss follow a semi-logarithmic trend. Once crack development starts to accelerate, the stiffness loss rate increase until the test is

stopped, or until specimen rupture. The calculations are based on the crack growth kinetics of individual flaws in terms of flaw size. The theory behind the constitutive model is detailed in the section 6.1.

6.1. Loss of Stiffness and Development of Crack Precursors during Fatigue

At the microscopic scale, rubber materials naturally contain defects that under the action of repeated loading grow to finally produce cracks [1]. Consider, for example, the microscopic material features or defects shown in Figure 6.1. To the extent that the defects are becoming larger, it is simultaneously observed that stiffness decreases as cycles are applied [2]. Simple tension specimens are cycling to fatigue tested under displacement control, from the stiffness loss behaviour obtained has been considered the relationship to the growth of crack precursors in the material. The size and volume density of the largest crack precursors directly governs the accelerating stiffness loss effect that immediately precedes specimen rupture. Additionally, at earlier times, the effects of smaller precursors also contribute significantly to loss of stiffness.

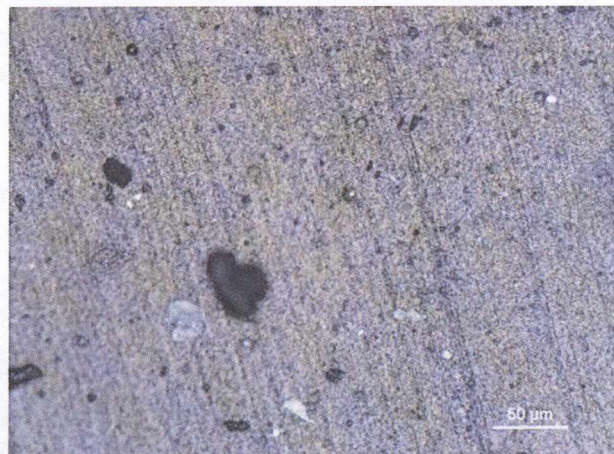


Figure 6.1 Microscope image showing typical microstructure or subject material

6.1.1. Crack Precursors

The presence, character, and development of crack precursors in rubber have been widely demonstrated in the literature. Gent et al. [88] first demonstrated the strong dependence of crack nucleation life on the size of crack pre-cursors, and the relationship between crack nucleation and crack growth behaviours in rubber. Jago

[220] recently used X-Ray computed microtomography technique, useful for imaging and surveying crack pre-cursors, not only on the surface of a specimen, but also in the bulk. Crack precursors have been seen to occur in a range of sizes, with smaller precursors occurring more frequently, and larger precursors occurring less frequently. Additionally concluded that during more than 80% of the fatigue life, micro cracks propagated independently, following the shielding process described by Mars [185]. The coalescence mechanism is observed only in the final life stage. For example, Mars & Fatemi [185] reported observations in which precursors of size 20 microns occurred at a volume density of $5000 / \text{mm}^3$, and precursors of size 100 microns occurred at a volume density of $3 / \text{mm}^3$.

The fatigue life is governed by the very largest crack precursors in a given material. These cracks are reported to range in size, from 20 to 200 microns, as has been discussed in Section 3.1.3.1 [88,122,151,152,154,222,223], and to be originated from both intrinsic and extrinsic sources. The precise nature of such flaws remains obscure because it appears that there are multiple sources for flaws of the observed effective size. These sources may include naturally occurring contaminants or voids in the base polymer, imperfectly dispersed compounding ingredients, filler agglomerates, mould lubricants, and imperfections in mould surfaces.

During the loading that components suffer in normal life, a microscopic inhomogeneity existing in the material experiences forces that tend to drive growth. Significant progress has been made in recent years to establish procedures for calculating these crack driving forces. Ait Bachir et al [172] developed an alternative continuum theory based approach capable to provide, for every material point in a body, the driving force acting on a hypothetical idealized small crack. Computing the energy release rate of an idealized crack per unit of crack length (so that this parameter has unit of energy per unit of volume and quantifies the energy density available at each point for driving crack growth) in terms of stress and strain at each material point, and of the given orientation of the idealized crack. Nait Abdelaziz et al [224] extended de fracture mechanics framework to no-cracked specimens. They developed a fracture criterion based upon the intrinsic defect concept. The fracture criterion required the input data of fracture toughness of the material in terms of critical value of a new developed generalized analytical formulation of J integral, the

constitutive law of the material and the breaking stretch of a smooth specimen under uniaxial tension.

6.1.2. Cyclic Stiffness Loss

Cyclic stiffness loss is inherent in rubber material compounds. The first few loading cycles applied in a rubber component or specimen test are known to cause a rapid transient decrease in stiffness, as famously demonstrated by Mullins [3,225]. The Mullins effect is believed to originate when a new peak load causes the destruction of internal bonds in the rubber. The internal bonds are thought to be associated with individual chains in the elastomer molecular network, or with the functional surfaces of individual filler particles. Stiffness loss has been treated extensively, from both experimental and computational perspectives. The importance of the Mullins Effect in the rubber's mechanical response, cause several researchers to model it in a way suitable for use in continuum mechanics or Finite Element Analysis [32,34,47]. The model proposed by Ogden and Roxburgh [32] is the preferred, and is implemented in the principal finite element codes (Abaqus, Ansys, LS-Dyna, Nastran). It is a phenomenological model of the effect that represents the stiffness loss as occurring entirely during the first loading cycles, and that captures the dependence of the stiffness loss on the material's memory of a previous highest load.

Beyond first few cycles, stiffness loss follow a semi-logarithmic trend [2]. The rate of this trend is smaller than the initial Mullins effect, at least until the crack nucleation life is approached. Once crack development starts to accelerate, the stiffness loss rate increase until the test is stopped, or until stiffness loss is completed at specimen rupture.

In many design scenarios, it is the loss of stiffness of a rubber component which limits the life. There are rubber parts where the existence of cracks is permitted, provided that stiffness losses do not exceed a magnitude, quantified in percentage values. There is an interest to incorporate the stiffness loss effect into numerical models, and to understand how mode of cycling control influences in the life, Mars [226]. Several attempts have been made in the direction of constitutive modelling. Some approaches were focused on the structure and evolution of the material at the scale of polymer chains and individual filler particles. Boyce et al [227] investigated the subjacent microscopic mechanisms which govern the strain history effects, using

micromechanical modelling of the composite structure and its deformation. Micromechanical models of the load–unload–reload behaviour of a representative TPV have been presented, and have shown a good agreement with experimental. Marckmann et al [228] developed a new network alteration theory, which has been implemented by modifying the eight-chains constitutive equation of Arruda and Boyce [25]. Cantournet et al [229] modelled Mullins effect with by dissipative friction phenomena due to internal sliding of the macromolecular chains and to sliding of the connecting chains on the reinforcing filler particles. Lorenz et al [230] developed a microstructure based model of rubber reinforcement describing the stress softening and hysteresis by the breakdown and re-aggregation of strained filler clusters. The model named dynamic flocculation describes the physical origin of the stress/strain behaviour of filled elastomers. Rickaby & Scott [231] presented a model combining the inelastic features of stress relaxation, hysteresis and residual strain with the Arruda–Boyce eight-chain model of elasticity.

The abundant presence of microstructures in rubber parts induces to think on their possible contribution on the stiffness loss of compounds. The following constitutive model considers the contribution on cyclic softening of crack precursors, their tendency to grow, and their volume density.

6.1.3. Theory

To incorporate the influence of crack precursors in the fatigue life determination process has been needed to incorporate it into a constitutive model. On the following section the development of the model is explained. It has been stated reviewing the relations that govern the development of an individual defect, and then considering how each defect contribute on the loss of stiffness.

6.1.3.1. Crack Precursor Development

The driving force T acting on a small crack precursor of size c in a simple tension test specimen strained to strain energy density W may be written as in Eq. 3-17 of section 3.1.2.2, for the edge cracked tensile crack growth test piece. The non-dimensional factor k may be estimated as a function of the stretch ratio λ . The equation used is a simplification of Greensmith's [86] equation Eq. 3-19 for one edge cracked simple tension specimen.

$$k = 3/\lambda^{1/2} \quad \text{Eq. 6-1}$$

Under cyclic straining, the crack precursor will grow at a rate r , governed by the fatigue crack growth rate law Eq. 3-22. r_c , T_c , and F are material parameters for crack growth rate definition, obtained from section 4.1.1.3, Table 4.2, and T_{max} is computed by Eq. 3-17.

The number of cycles required for the crack precursor to grow from its initial size c_0 to a final size c_f , in simple tension test specimens, is given by,

$$N_f = \int_{c_0}^{c_f} \frac{1}{r(T(c))} dc = \frac{T_c^F}{r_c(2kW)^F} \frac{1}{F-1} [c_0^{1-F} - c_f^{1-F}] \quad \text{Eq. 6-2}$$

At some number of cycles $N < N_f$, can also be written,

$$N = \frac{T_c^F}{r_c(2kW)^F} \frac{1}{F-1} [c_0^{1-F} - c^{1-F}] \quad \text{Eq. 6-3}$$

So long as $c \gg c_0$, this implies that the consumed life fraction N/N_f is related to the normalized flaw growth c/c_0 as

$$\frac{N}{N_f} = 1 - \left(\frac{c}{c_0}\right)^{1-F} \quad \text{Eq. 6-4}$$

6.1.3.2. Stiffness Loss Theory

The presence of a high number of crack precursors in rubber material induces to think on the importance of quantifying their contribution on the overall component stiffness loss. Each crack precursor reduces the strain energy in the material by an amount depending on its current size. If the strain energy density of material containing no crack precursors is W_0 , then the strain energy density W of material containing defects may be calculated as follows

$$W = W_0 - \Delta U \rho_c \quad \text{Eq. 6-5}$$

ρ_c is the volume density of such defects. ΔU is the amount by which a single defect reduces the total strain energy. It may be estimated by using the energy release rate definition as presented in Eq. 3-12 to evaluate

$$\Delta U = - \int_{c_0}^c 2k W_0 c dA \quad \text{Eq. 6-6}$$

The area increment dA , for a penny-shaped crack growing self-similarly, is $dA=2\pi cdc$, leading to

$$\Delta U = -4\pi k W_0 \int_{c_0}^c c^2 dc = -\frac{4\pi k W_0}{3} [c^3 - c_0^3] \quad \text{Eq. 6-7}$$

Taking $C=4\pi k/3$, we may rewrite Eq. 6-5 as

$$W = W_0 \left(1 - C \rho_c c_0^3 \left[\left(\frac{c}{c_0} \right)^3 - 1 \right] \right) \quad \text{Eq. 6-8}$$

Or, remembering Eq. 6-4,

$$W = W_0 \left(1 - C \rho_c c_0^3 \left[\left(1 - \frac{N}{N_f} \right)^{\frac{3}{1-F}} - 1 \right] \right) \quad \text{Eq. 6-9}$$

Eq. 6-9 shows that the strain energy density is reduced by a factor depending on the initial size of the crack precursor c_0 , and on the life fraction consumed N/N_f . However, considers only the effects on stiffness loss of the very largest crack precursors in the material. In practice, precursors will start growing all of them at same time, but at different rates depending on the location, and therefore strain level they endure. The rate of growth depends on the initial size of the flaw as is determined by the fatigue crack growth rate law. Therefore, the rates of growth of small flaws will necessarily be smaller than that of the largest precursors. Although, in contrast, because of their abundance, the amount of flaws increase with decreasing size, thus, it's hypothesized that the cumulative effect of their growth will generate an additional decrement of stiffness [232]. The idea is reflected on the following model,

$$\Delta W_{c < c_0} = \int_0^{c_0} \rho_c(c) \Delta U(c) \zeta(c) dc \quad \text{Eq. 6-10}$$

$\rho_c(c)$ is a function describing the volume density of crack precursors as a function of their initial size c . The flaws of higher size will be few in comparison with those of minor size, which will increase without limits as initial size approaches zero. $\zeta(c)$ is a participation function, which accounts for the fact that not all defects present in the material will contribute to stiffness loss. Only those defects surrounded by strained material may contribute. Defects surrounded by material that has been relieved by the growth of larger cracks (i.e. crack shielding effects) do not contribute.

Instead of trying to evaluate Eq. 6-10, which depends on information required from new test and characterization methods not currently developed and therefore not readily available to an analyst. The following empirical form has been studied as a representation of the additional contributions of distributed crack precursor growth.

$$\Delta W_{c < c_0} = (W_1 - W_0) \frac{\log(N/N_0)}{\log(N_1/N_0)} \quad \text{Eq. 6-11}$$

N_0 and N_1 are two convenient times, chosen such that $1 < N_0 < N_1 < N_f$. W_0 and W_1 are the observed strain energy density at times N_0 and N_1 , respectively. This choice reflects semi-logarithmic stiffness decay, and can be combined with Eq. 6-9 to give the total stiffness loss as

$$W = W_0 \left(1 - C \rho_c c_0^3 \left[\left(1 - \frac{N}{N_f} \right)^{\frac{3}{1-F}} - 1 \right] - \left(1 - \frac{W_1}{W_0} \right) \frac{\log(N/N_0)}{\log(N_1/N_0)} \right) \quad \text{Eq. 6-12}$$

Basically, the hypothesis adopted defends that the softening mechanism is governed on a per cycle basis in association with the growth of crack precursors. The conceptual motivation had been adopted from the experimental works by Derham & Thomas [233] and McKenna & Zapas [234]. Derham & Thomas hypothesized the enhancement of creep produced by cyclic rather than static loading is related to the stress softening. Admitting that the mechanism of stress softening itself is not established, and a number of factors are involved, they concluded that the enhancement is reminiscent to the crack growth behaviour of natural rubber.

McKenna & Zapas further studied the phenomenon observed by Derham & Thomas. They conducted stress relaxation and creep experiments under static and cyclic loading. They found that softening effect in cyclic loading, where the load was applied continuously, was quite pronounced, whereas under repeated loading, the amount of softening was small. They concluded that this failure behaviour can be related to stress softening through a failure envelope. Therefore, should be noted that both of these studies considered the effects of cyclic loading, and found that material evolution on a per-cycle basis was much greater than could be accounted for by considering solely the known time-dependent behaviour under steady loading.

6.1.4. Experimental

The experimental test procedure used for material stiffness loss characterization is a small variation of simple tension cycling to break test detailed in section 4.2.1.2. The MCN material has been selected for the development work, with the recipe shown in Table 2.2. Testing was carried out at fully relaxing conditions in a sinusoidal waveform, with the cycling controlled in displacement. The test frequency has been limited at 2Hz. Three replicates were done at a unique strain level of 150%. The test was commanded in displacement control, and strain magnitude was previously computed from a strain - displacement relationship, detailed in section 4.2.1.2, and shown on Figure 4.21. During cycling to break test peak force was monitored and recorded periodically. The procedure of measurements has been detailed in section 4.2.3 along with the volume density of cracks precursors counting, and results are summarized in Table 4.11.

6.1.5. Results and Discussion

The simple tension cycling to break test experiment individual results are given in Table 4.11. The geometric mean of all fatigue life (number of cycles to rupture) observations was 18,174 cycles. Heat built up was negligible in these tests, while 2 Hz frequency of the test and 2 mm thickness of specimen doesn't heat up the material as a result of the hysteretic effects.

Figure 6.2 shows the measured peak stress as a function of cycles during each test replicate, and it is also plotted the Eq. 6-12 fitting curve for comparison.

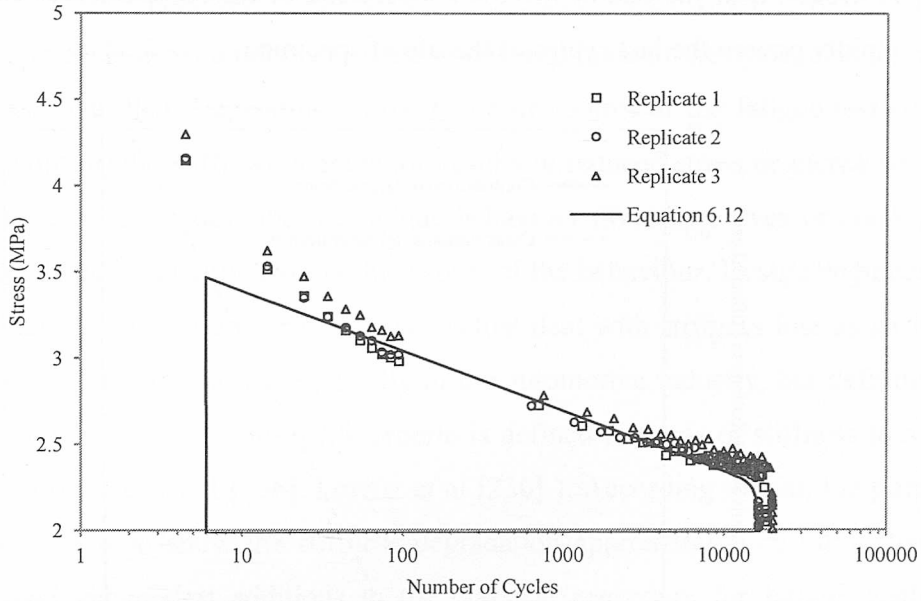


Figure 6.2. Stress drop history during a fatigue test with a cycling peak strain of 150%.

The determination of the parameters of Eq. 6-12 starts computing the areal crack density, by dividing the average number of counted cracks (38.7) by the visible surface area, which in the undeformed configuration was 134 mm². The volume crack density ρ_c was then computed as the 3/2 power of the areal crack density, giving $\rho_c = 0.155/\text{mm}^3$. The parameter C was obtained using $C=4\pi k/3$, for a strain of 150 % as $C = 7.95$. The initial flaw size was selected, based on the microscope image of Figure 6.1, as 40×10^{-3} mm. It has been assumed that the power-law slope F of the fatigue crack growth rate law is equal to two, a value typical of natural rubber based compounds Gent & Mars [1]. It has been taken advantage of the fact that under strain control can be written:

$$\frac{\sigma_1}{\sigma_0} = \frac{W_1}{W_0} = 0.74 \quad \text{Eq. 6-13}$$

Where σ_0 is the stress at the reference cycle, here taken as $N_0 = 100$, and $N_1 = N_f = 18,174$.

The relative contributions of the ‘largest defect’ and the ‘all other defects’ terms to the total stiffness loss are plotted separately in the graph shown in Figure 6.3. It can be seen that for most of the history of the test, the smaller defects, presumably because of their abundance relative to the largest defects, govern the stiffness loss.

However, near the end of life the contribution of the largest defect that grows very rapidly govern the last cycles of the life of specimen.

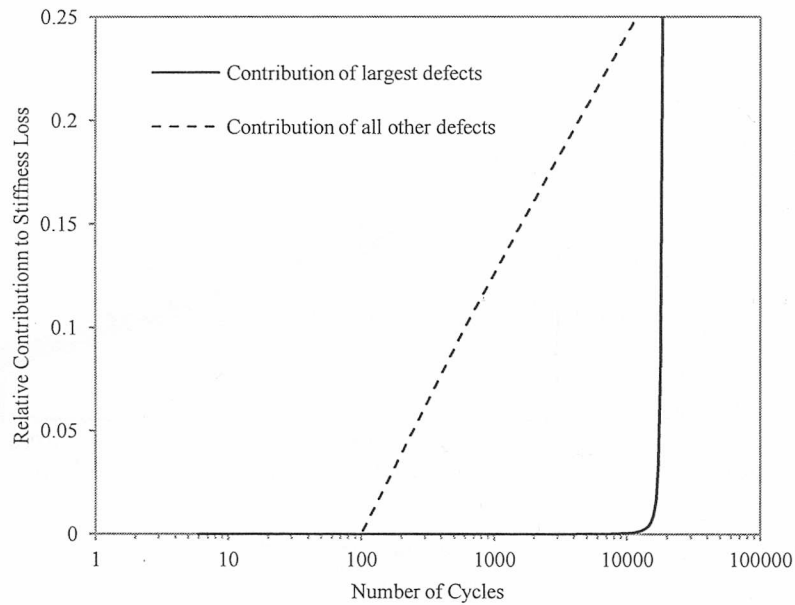


Figure 6.3. Relative contribution of the “large” defect and “all other” defect terms in Eq. 6-12.

6.1.6. Summary of Development of Crack Precursors Influence

Simple tension fatigue crack nucleation test presents a loss of stiffness when cyclic loads are applied. The stiffness loss can be rationalized in terms of growth of crack precursors distributed throughout the material. The proposed model presents a good fit using physically reasonable parameters values. From the observed behaviour can be presumed that the size and volume density of the largest flaws are the parameters which govern the accelerating stiffness loss that precedes the specimen rupture.

The loss of stiffness that is observed at initial transient cycles, associated with Mullins effect has not been fitted by the proposed model. Furthermore, the gradual semi-logarithmic loss observed after has been here presumed to arise in association with the large number of crack precursors with sizes smaller than the characteristic largest precursor.

6.2. Cycling Control Type Influence on Stiffness Loss

Fatigue damage in elastomer causes usually degradation of the stiffness prior to rupture. The mechanisms of this degradation seems to have origins in both molecular

and mesoscopic processes in the material [220,222,232,234]. The effects of a given operating cycle depend not only on the initial amplitude of the cycle, also on how the cycle is controlled. Depending on the mode of control of the fatigue test (stress or strain control) the stiffness degradation results in reduced stress or increased strains. The usual forms to describe the fatigue behaviour (Wohler curves or crack growth curves) do not explicitly address this aspect of the behaviour. Design engineers have identified the lack of analysis approaches that deal with stiffness loss as an integral part of the fatigue process, especially in the automotive industry, but definitively in any rubber part where end-of-life criteria is defined in terms of stiffness loss (Brieu et al [235], Diani et al [236], Lorenz et al [230]). According to that, the purpose of this section is to show the stiffness degradation approach, which rationalized and computed via modest additions to the classical procedure for fatigue analysis in rubber.

The fatigue damage have shown, that at a given initial starting level, cycling the parts in force control lead to shorter the life more than in displacement control [226]. Therefore, the stiffness loss approach has to consider the effect of control mode on fatigue life, and evolution of stiffness with number of performed cycles. The stiffness loss approach relates the differentiated particular damage developments of different loading modes in a function. It is assumed that all strain amplitudes produce the same identical stiffness loss characteristic curve. The approach has been implemented in Endurica CL solver for rubber fatigue analysis.

6.2.1. Theory

The crack nucleation life N_f of an elastomer can be computed from knowledge of how the rate of crack growth dc/dN depends on the energy release rate T of typical small crack precursors [1,88]. To demonstrate the calculation, it is used the simple power-law form for the fatigue crack growth rate curve $r(T)=dc/dN$ given originally by Thomas [81], which is written in terms of the r_c , T_c , and F , material parameters in Eq. 3-22.

For sufficiently small cracks, the energy release rate is proportional to the size of the crack precursor c [172,237], and to the portion of strain energy density that is available to be released due to the growth of cracks on a given material plane (named by Mars [37] as cracking energy density, W_c). In the particular case of simple

tension, where all of the strain energy density is available, can be written as presented on Eq. 3-17. The non-dimensional factor k may be estimated as a function of the stretch ratio λ as shown in Eq. 6-1, a simplification of Greensmith's [86] equation.

In rubber fatigue the strain energy density may depend not only on the instantaneous strain or stress, but also on damage state of material, and on the mode of control imposed in the fatigue test. The state of damage has been related with the fatigue loading control mode in one function. The equation considers the differentiated damage development of particular loading modes. The parameter that quantifies the damage is the normalized stiffness, and the equation contemplates the effect of stiffness loss and crack size on the strain energy density. The mode of control of cycling is considered in the function by the deformation index X , based on that Mars [226] approach. In general, a mechanical process involves the change in state of a material. If the material is linearly elastic, in fact, the stress and strain will be related as follows:

$$\sigma = \varepsilon E \quad \text{Eq. 6-14}$$

A class of processes that is of special interest is the one for which the following relation is maintained:

$$Q = \varepsilon E^{\frac{1-X}{2}} = \sigma E^{-\frac{1+X}{2}} \quad \text{Eq. 6-15}$$

Here Q represents generally a factor of the linear elastic law, whose specific type is determined by choice of parameter X . Eq. 6-15 shows a partition of the stiffness E into conjugate factor that relate stress and strain. Depending on the choice of deformation index, various equivalent forms of the linear stress-strain form can be recovered. For strain controlled experiments is $X=1$, and for stress controlled experiments $X=-1$. Intermediate values are also contemplated in the model for special loading cases. In the case of energy controlled loading tests is $X=0$, because the energy is kept constant during the testing and until failure. On this cases where the parameter X is known, the general relations permit estimates to be made of the changes in strain, energy, or stress history which are associated with changes in stiffness dE .

Therefore, in the stiffness loss approach have been defined a function h that relates the stiffness loss to crack growth. Strain energy density may be expressed in terms of its initial value W_0 , and the ratio of the current stiffness E to the original stiffness E_0 , as it is expressed in Eq. 6-16.

$$\frac{W}{W_0} = \left(\frac{E}{E_0}\right)^X = \left(h\left(\frac{c - c_0}{c_f - c_0}\right)\right)^X \quad \text{Eq. 6-16}$$

The parameter h is a function of the ratio of instantaneous crack precursor size growth $c - c_0$ to end of life growth $c_f - c_0$. For example, may be chosen $h(0)=1$ to reflect that the reference stiffness is associated with the initial condition, and $h(1)=0.85$ to reflect that at the time when cracks have reached their end-of-life size c_f , when the material has lost 15% of its stiffness. Depending on the material, component and application the end of live size and stiffness loss percentage can be specified as desired or required by standards.

The combination of the power-law that defines the crack growth rate in the third regime, Eq. 3-22, and equation for the energy release rate calculation of the specific specimen, in this case the simple tension specimen by Eq. 3-17, result in a closed-form relationship between the fatigue life, N , and the fatigue crack growth rate dc/dn . From the integral of this combination, the number of cycles required for the crack precursor to grow from its initial size c_0 to a final size c_f , in simple tension test specimens is obtained. Finally, by the consideration of damage development and loading control mode by Eq. 6-16, the following Eq. 6-17 is obtained. Eq. 6-17 may be solved numerically to compute the number of cycles N_f required to grow a crack from initial size c_0 to final size c_f , with initial strain energy density W_0 under a particular control mode specified by the deformation index X .

$$N_f = \frac{1}{r_c} \left(\frac{T_c}{CW_0}\right)^F \int_{c_0}^{c_f} (h^X c)^{-F} dc \quad \text{Eq. 6-17}$$

Therefore, the softening can be accounted during the integration for crack growth rate law. In the case of energy control, with $X=0$, can be evaluated analytically giving the result of,

$$N_{f,x=0} = \frac{1}{r_c} \left(\frac{T_c}{CW_0} \right)^F \frac{[c_0^{1-F} - c_f^{1-F}]}{F - 1} \quad \text{Eq. 6-18}$$

It may be rewritten the Eq. 6-17 with reference to the energy controlled crack nucleation life $N_{f,x=0}$ as

$$N_f = N_{f,x=0} (F - 1) \frac{\int_{c_0}^{c_f} (h^x c)^{-F} dc}{c_0^{1-F} - c_f^{1-F}} \quad \text{Eq. 6-19}$$

The Eq. 6-19 has been implemented in the Endurica CL solver for rubber fatigue analysis. The graphical representation of the tabular data used to feed the solver is shown in Figure 6.4, which relates the function h with the normalized fatigue life. For the approach has been decided to compute the material softening function from a simple tension cycling until failure test, at a peak level of 100% in strain control and 2 Hz frequency. The approach assumes that all strain amplitudes produce the same characteristic stiffness loss curve. From the obtained results the stiffness response, E , is normalized with the initial stiffness value, E_0 , and is plotted as a function of the normalized fatigue life N/N_f (so that energy control gives at final life $N/N_f=1$). In the approach the function $h=E/E_0$ relates the stiffness loss to crack growth.

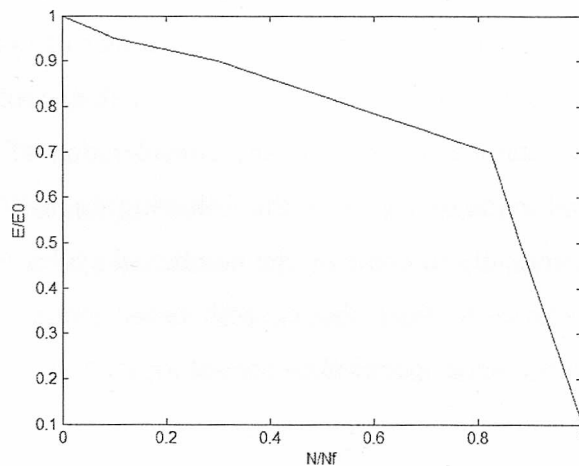


Figure 6.4 Graphical representation of the softening function $h=E/E_0$ versus the normalized fatigue life N/N_f

For a simple tension strip made by a natural rubber with a slope of $F=2$, that defines de fatigue crack growth behaviour, fatigue life has been computed numerically using Eq. 6-19. The mode of control is considered in the function, defined by the parameter

X and the function h . The evolutions of each reaction variable have been computed and results plotted in a graphical representation for several different values of initial amplitude in Figure 6.5.

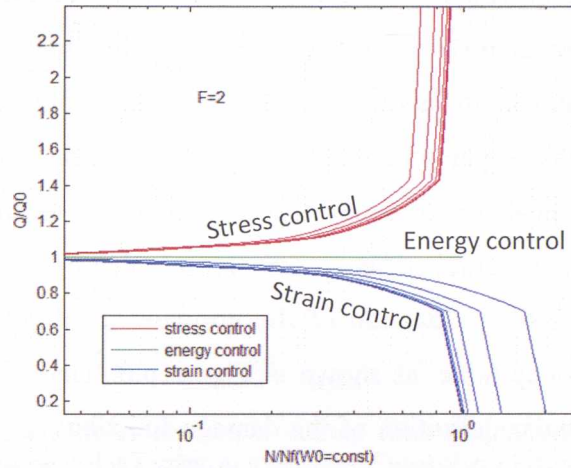


Figure 6.5. Evolution of reaction variables strain, energy, and stress for control under strain, energy, and stress. Each plot corresponds to a different value of initial amplitude.

The variable Q represents any of response variables strain, energy, or stress, that is conjugate to the stress, energy, and strain controlled input. This variable Q is plotted as a function of the normalized fatigue life N/N_f . For the energy controlled test $Q/Q_0 = W/W_0 = h^X$ is used for predicting failure. For a stress controlled test, the calculation predicts failure prior to the corresponding energy controlled test, and strain $Q/Q_0 = \varepsilon/\varepsilon_0 = h^{(X-1)/2}$ that increases with cycles. For a strain controlled test, the calculation predicts failure after the corresponding energy controlled test, and stress $Q/Q_0 = \sigma/\sigma_0 = h^{(X+1)/2}$ that decreases with cycles.

6.2.2. Stiffness Loss Characterization of Material

The characterization protocol described on section 4 has been used for material fatigue behaviour data collection. The simple tension cycling to break test results, detailed in section 4.2.1.2, have been used to construct the softening function h for the method described in section 6.2.1. The filled natural rubber compound, MCN, which ingredients have been detailed in Table 2.2, is the material selected for this work.

The specific fatigue properties required for the stiffness loss calculations are obtained from fatigue crack growth characterization, and crack precursor size determination. The material parameters r_c , T_c , and F , for crack growth rate definition have been

presented on section 4.1.1.3 in Table 4.2. The initial crack precursor size, c_0 , has been determined in section 4.2.2. for MCN material and the flaw size is of 0.08 mm. Then, for softening function to feed the Endurica CL fatigue solver has been selected the simplest option of the lookup table. From the cycling to break test results over the simple tension sample the stiffness loss of the material as a function of the normalized fatigue life is obtained. The test conditions and procedure used for the cycling to break test are detailed in section 4.2.1.2, but one additional data has been recorded, the peak force value at every cycle. The resultant stiffness loss data is normalized by its initial stiffness E/E_0 , represented by the peak force value, and the damage is plotted as function of the normalized fatigue life N/N_f to produce the mentioned lookup table, as shown in Figure 6.6. Thus, the obtained relationship is given as a tabular definition of the damage function, as a lookup table, to feed the fatigue solver; and then compute the stiffness loss in each element of the finite element model, like will be explained later on section 6.2.4.

Additionally, cyclic stress-strain behaviour is required to be characterized by three stress states data: simple tension, planar tension, and simple compression. The topmost point from each of a series of cyclic stress-strain curves has been selected, along with the strain and stress at rupture. These points have been then used to fit a 3rd order reduced polynomial Yeoh [22] constitutive model, to obtain the hyperelastic strain energy density function described in Eq. 2-33. The complete procedure is detailed in section 2.6, and material parameters are summarized in Table 2.9.

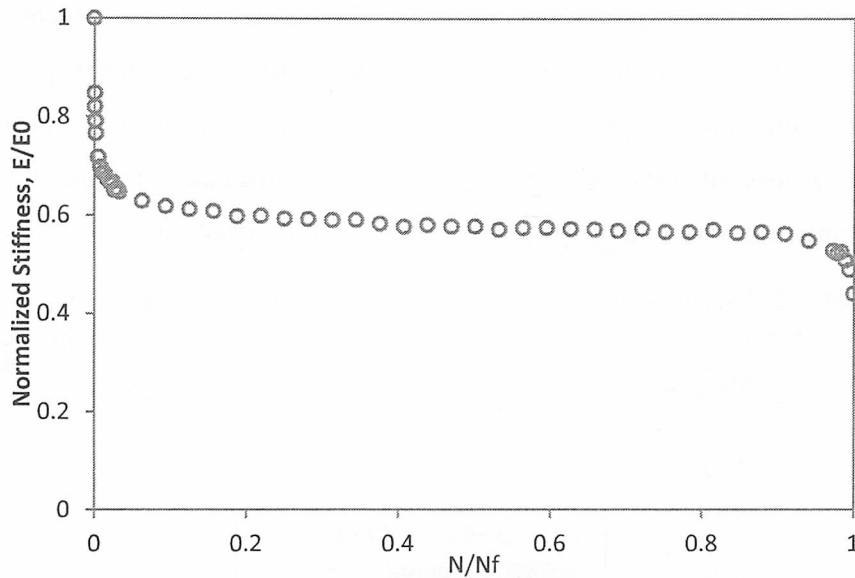


Figure 6.6. Normalized stiffness loss curve derived from simple tension strip experiment in displacement control, presented in a graph as a function of normalized life, N/N_f .

6.2.3. Component Fatigue Experiments

The component is a rubber mount used to link the exhaust system to the car body like it is shown in Figure 5.1. In service, the mount is attached to the car body and the exhaust system by metallic pins that pass through each of the two circular holes. The component was isolated and mounted in a specifically designed tool for testing in a servo-hydraulic MTS Bionix machine.

Fatigue cycling tests have been carried out under both displacement and force control, the loading has been commanded in sinusoidal waveform, and several peak values have been defined at fully relaxing conditions, R ratio of zero. For the testing at both control modes it has been sought to command same peak strain values for both strain controlled and stress controlled cycling tests at least for initial cycles. For this aim, the fatigue cycling tests in strain control mode were carried out first at defined peak displacement levels. During the cycling test it has been registered the peak force measured from 10th to 20th cycles, from there have been defined the force control test levels. It has been seen of major importance not to consider first cycles to avoid or overcome the Mullins softening effect. All the test conditions have been summarized on Table 6.1. In parallel work, registered force and displacement data during the cycling to break tests have been used to correlate with finite element quasi-static analysis carried out in section 5.1.3.2.

Figure 6.7 and Figure 6.8 show fatigue life results by the graphical representation of the evolution of normalized stiffness with regard to cycles for displacement and force controlled tests respectively. The end of life criterion for the tests had been defined on a loss of 15% of the initial stiffness. Displacement and force values were monitored during the test, and stiffness was computed via the secant method.

Table 6.1. Experimental operating conditions for exhaust mount fatigue testing.

Analysis	Disp. Mín. (mm)	Disp. Max. (mm)	Force Mín. (N)	Force Max. (N)
Exp. 1	0	+20	-	-
Exp. 2	0	+30	-	-
Exp. 3	-	-	0	885
Exp. 4	-	-	0	1280

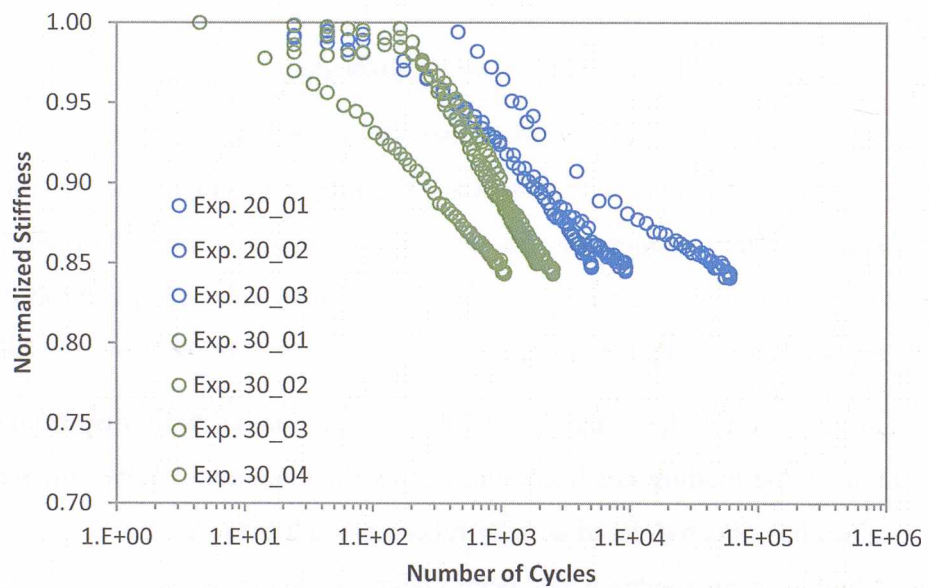


Figure 6.7. Evolution of normalized stiffness with regard to cycles, for displacement controlled mode tests. Two peak displacement value results are shown: Blue hollow circle is for 20 mm, and green hollow circle is for 30 mm.

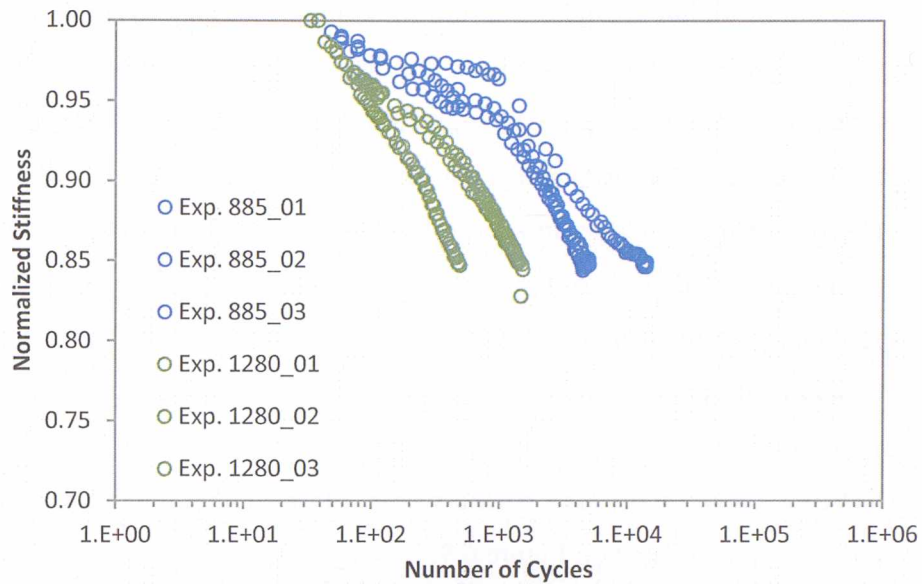


Figure 6.8. Evolution of normalized stiffness with regard to cycles, for force controlled tests. Two peak force value results are shown: Blue hollow circle is for 885 N, equivalent to 20 mm peak displacement, and green hollow circle is for 1280 N, equivalent to 30 mm peak displacement.

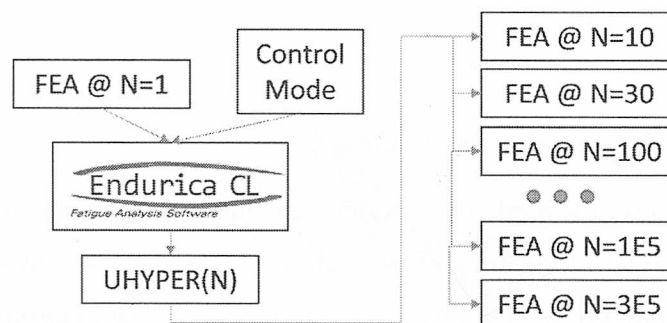
6.2.4. Analysis Procedure

The stiffness loss prediction requires an initial finite element analysis of the exhaust mount model at undamaged conditions (i.e. at $N = 1$), thus, it is fed with material data obtained from first characterization cycles. The material data has been fitted by a hyperelastic constitutive model, as detailed in section 2.6. The carried out finite element analysis are similar to those explained in section 5 for fatigue life prediction, performed with the software Abaqus and detailed in section 5.1.2.1. These simulations are carried out in displacement loading, even for predictions of fatigue life at force loading conditions. The strain history obtained from these simulations is the same for both type of loadings, and the major damage that generates force loading condition, and therefore the shorter life, is considered in the computations at Endurica. Therefore, the aim of this first finite element analysis is double, first to convert the displacement loading history, in a strain history of each element, and second to compute the initial stiffness of component with raw material data.

In addition to geometry data the fatigue simulation code Endurica CL have to be fed by the material damage function, computed in the section 6.2.2. Then, in the computations by EnduricaCL it is created a user-defined subroutine UHYPER for each instant in the lifetime of component model. Actually, by the UHYPER is

defined a new state of material from the initially defined hyperelastic model by the damage function, which considers the damage level of material depending on the number of cycles that has been applied and loading control mode. Nevertheless, the predictions depend principally on the material data that is a cycle-dependent property. In the Endurica input file has to be defined the cycling control mode for strain control with $X=1$, or for stress control with $X=-1$. Then, the UHYPER defined the damage state of material at defined number of cycles. Thus, a series of finite element analyses have to be carried out, one per each desired instant in the lifetime of component, with the corresponding damaged material data defined by the UHYPER, and finally the stiffness loss of the entire model is computed. The workflow is illustrated on Figure 6.9.

Figure 6.9. Schematic representation of analysis workflow to predict the rubber components stiffness loss.



One finite element analysis for each desired fatigue lifetime, N , have been carried out. Each simulation is performed up to a certain peak displacement, and reaction force result of the entire component are outputted to plot in a graph as a function of fatigue cycle number, N . Dividing obtained reaction force by commanded displacement the stiffness of the mount has been computed. The evolution of the stiffness with the number of cycles is then plotted in both, Figure 6.12 and Figure 6.13.

The fatigue life software Endurica CL on its original configuration computes the fatigue life until first growing crack grow from its initial flaw size and achieves the nucleation size usually of one millimetre. Thus, for the stiffness loss computation it has been enabled the coexistence of several nucleated cracks at predicted critical locations on model. The amount of cracks enabled to coexist will be defined by the percentile. Percentile is a measure used in statistics indicating the value below which a given percentage of observations in a group of observations fall. For example, the

20th percentile is the value (or score) below which 20 percent of the observations may be found. Therefore, by allowing the coexistence of cracks by the percentile, a major fatigue life will be predicted. In the same manner, a larger stiffness loss will be predicted.

The parameter percentile has been defined in the current study independently to the component material behaviour. On the other hand, the component geometry and size have been considered on its definition, due to the larger number of cracks that would be permitted to coexist. Therefore, the experience gained by the use of the stiffness loss prediction capability will be of great importance for the correct definition of the percentile value on future case studies. In the Figure 6.10 is shown a graphical representation of predicted number of cycles depending on percentile values. It can be seen in the graph, that a small percentile results in a prediction of a short life, and this can be considerably increased with small increments of percentile magnitude.

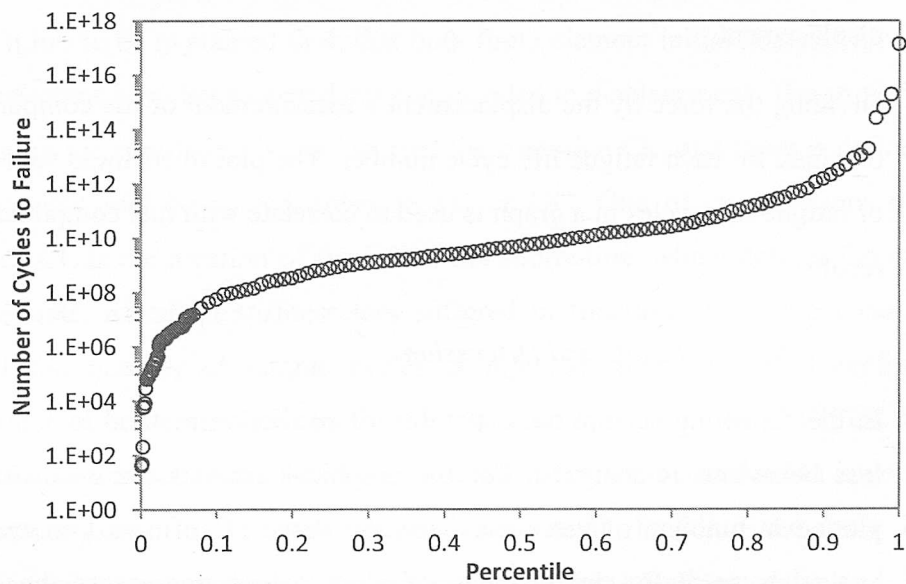


Figure 6.10. Graphical representation of predicted number of cycles in function of programmed percentile values for the exhaust mount made by MCN material.

It is assumed same stiffness loss magnitude at low strain levels and higher strain levels. In this way, convergence difficulties that happen at highly non-linear finite element simulations are not a limitation for stiffness loss predictions. Thus, the procedure extrapolates the simulation results obtained at lower loading levels, and carried out at fatigue life cycles. Differences are found between the stiffness loss measured at small strain levels and at higher strain levels, but often for industrial

components this is the only practical solution. The finite element simulations with the softened material state defined by the UHYPER for each specified cycle number may result in an unstable model. The MCN material has shown a high stiffness loss, and this made impossible to get convergence at same strain levels as defined on the experimental work. Therefore, the above mentioned practical solution has been used. The experimental fatigue test over the real component had been carried out at a cycling peak displacement of 20 mm between exhaust mount pin holes. Nevertheless, in the finite element simulations the maximum convergence obtained have been of a peak displacement of 1.4mm. Thus, with MCN material has been found the above mentioned limitation in the finite element simulations, and has been solved assuming that same damage happens at low and high peak strain levels. Thus the set of simulations have been carried out stretching component up to 1.4 mm displacement between holes, and obtained stiffness loss prediction is assumed to be the same as for 20 mm. From the simulations is computed the reaction force to the commanded displacement.

Dividing the force by the displacement a measurement of the component stiffness is obtained for each fatigue life cycle number. The plot of stiffness values as a function of fatigue life cycles in a graph is used to correlate with real component experimental results.

6.2.5. Results and Discussion

In the following section the capability of prediction method to follow the stiffness loss behaviour is analyzed. For the graphical analysis the normalized stiffness is plotted in function of life cycles, and the shape of stiffness loss curve is observed analyzing specially the changes of slope which represents the loss rate. The magnitude of predicted cycles to loss stiffness is correlated with experimentally obtained results over the exhaust mount made of MCN material.

On the other hand, from the predictions from Endurica of nucleation life per element, it has been identified the cracking zone in the model. The analysis has been presented on section 5.3.2. In the Figure 5.14 has been faced the finite element model with the prediction results. Periodically have been take pictures of the component during the fatigue experiments, and images of first observable crack are used to correlate with

simulation results. In the pictures can be identified clearly the cracking zone, and as concluded previously, there is a perfect agreement in the cracking zones.

Finally, it has been carried out a study of most influencing parameters in the stiffness loss predictions. The magnitudes of these parameters on the stiffness loss prediction procedure have been changed for better understanding the manner and proportion that prediction result is altered. This study will be of great importance for future predictions, and will have a great value for taking correct decisions on following simulations. The study have been carried out with the same exhaust mount component model, but in this case made of MSB material data.

6.2.5.1. Stiffness Loss Tendency on Graphical Representation

The graphical representation of stiffness loss curves computed for displacement and force control are shown in Figure 6.11. The force controlled simulations (FC) exhibit shorter life than displacement controlled simulations (DC) in both of tested loading levels. It has to be explained first, that both finite element initial analysis for FC and DC predictions have been carried out commanded in displacement. The strain history obtained in the simulation is used to feed the Endurica CL, and there is defined also if component will be cycled either in FC or DC. One of computations done in Endurica CL is the creation of the UHYPER subroutine, which defines the material damage state, based on stiffness loss suffered in function of loading control type defined and number of fatigue cycles at inputted strain history. Therefore, the component model is simulated by finite element analysis, with the UHYPER defined material data and for each of desired life cycles. From the simulations is computed the reaction force to the commanded displacement. Dividing the force by the displacement a measurement of the component stiffness is obtained for each fatigue life cycle number. The plot of stiffness values as a function of fatigue life cycles in a graph is used to correlate with real component experimental results. The correlation work has been done independently for those commanded in displacement, and those commanded in force. The mentioned correlation work results are shown on Figure 6.11 for both studied materials on the present project. Analysing the shown graphs can be concluded that simulation done for strain or displacement control test gives a prediction of one half of decade longer life than done for stress or force control test.

Figure 6.11.A)

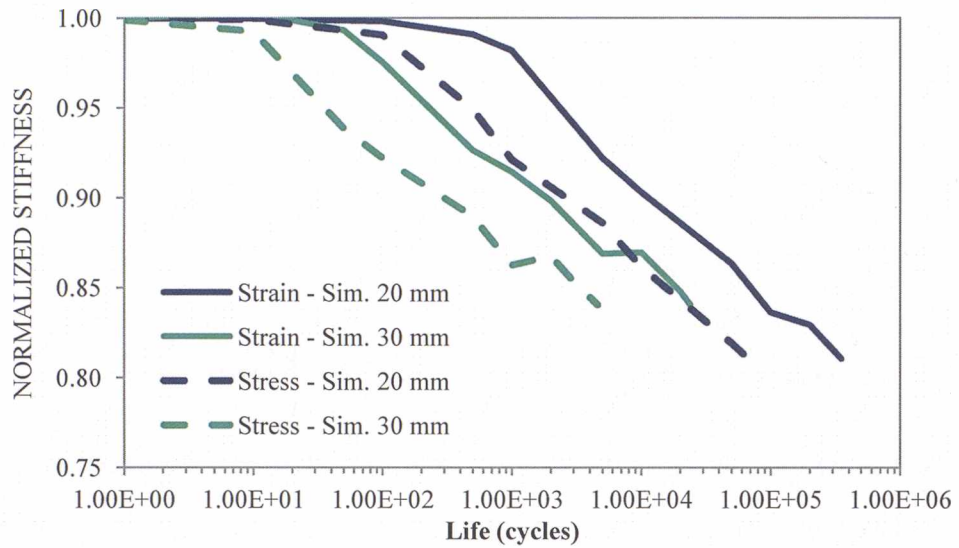


Figure 6.11.B)

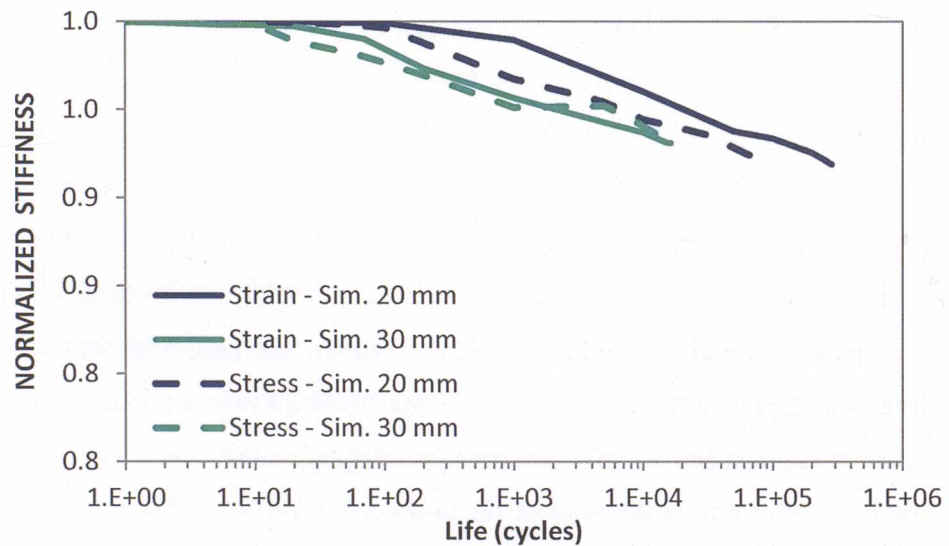


Figure 6.11. Computed graphical evolution of stiffness loss, for strain and stress controlled conditions. Normalized stiffness is plotted against life cycles. Solid lines are for strain control cases and dashed lines for stress control cases. Figure 6.11.A) is for exhaust mount made by MCN material and Figure 6.11.B) for the one made by MSB.

The simulation results shown on Figure 6.11 are correlated with experimentally obtained data in section 6.2.3. The analysis of results from correlation has been separated in two, one for each loading control mode. Unfortunately, in the case of experimentally obtained results with MSB material, they have shown low

repeatability, and have been decided to discard the whole batch of tested components. It has been assumed that bad repeatability found has been due to high differences in the vulcanization of components. Therefore, the MSB material component results have been discarded and thus correlation work has been focused on MCN material component.

From the comparison of stiffness loss curves performed at strain control, presented on Figure 6.12, is concluded that the trend of curve of stiffness loss is predicted well. Quantitatively there is a difference of a decade in the amount of cycles until failure. The simulation predicts a decrease of stiffness in the second third of component life smaller than the decrease measured in the real component experimental test. Additionally, the rate of stiffness loss during the second third of the life has been increased. In consequence, the predicted fatigue life is longer than experimentally measured.

In the case of the stiffness loss curves obtained at stress control, results are presented on Figure 6.13. In this case, it is appreciated that the simulation predicts an early initiation of stiffness loss. Likewise, the slope of the curve presents a similar drop in the first half of life for both, the simulations and the experiments. On the other hand, on second half of the life, the experimental curves are steeper than simulated. On experimental test results can be observed that rate of stiffness loss has increased, whereas on simulation results has not changed. Therefore, it can be concluded that fatigue life predictions are of almost one decade longer than measured on experimental tests.

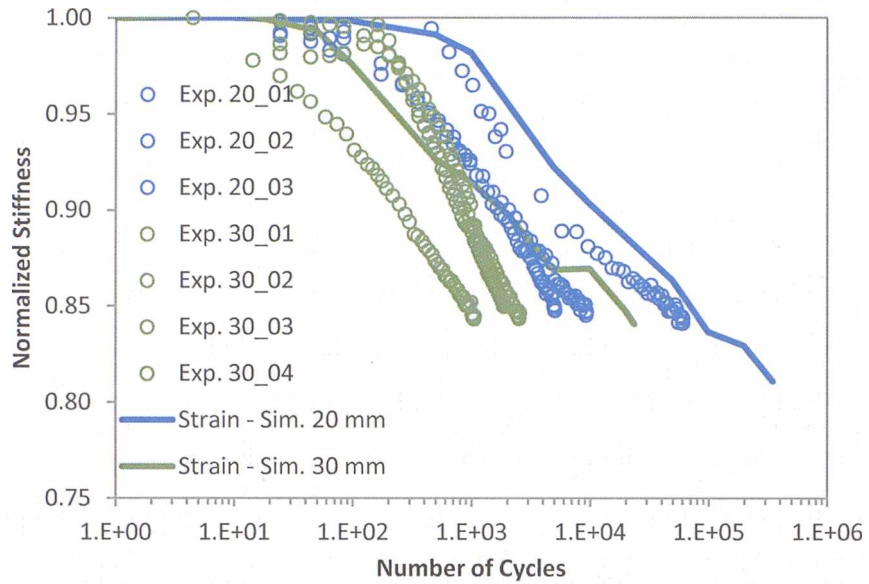


Figure 6.12. Computed and experimentally obtained evolution of stiffness loss at strain control conditions. Normalized stiffness is plotted against life cycles. Solid lines are for simulations of strain control, and symbols for experimental strain control tests. The Blue coloured are for 20 mm peak displacements and green coloured one for 30 mm peak displacements. Shown results are of MCN material.

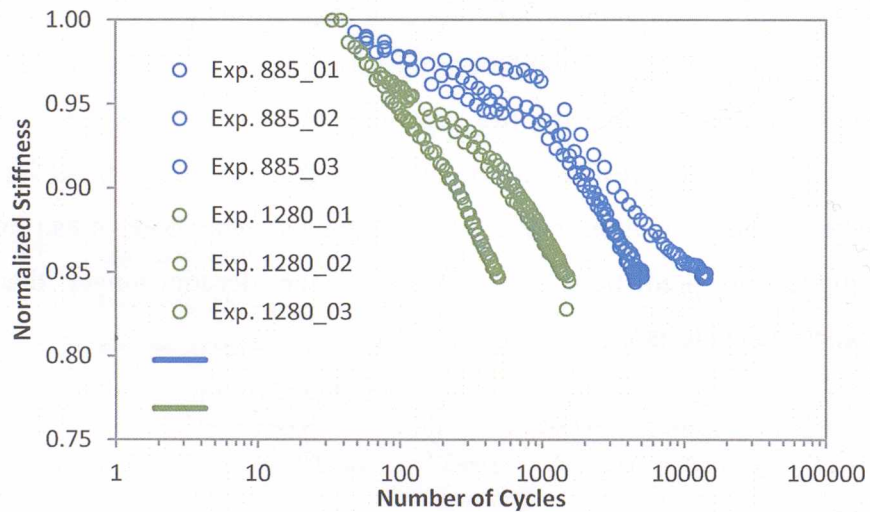


Figure 6.13. Predicted and experimentally obtained stiffness loss curves commanded at stress. Simulation has been carried out to a peak displacement, but cycling conditioning has been considered at stress control. Normalized stiffness is plotted against life cycles. Solid lines are for simulations of stress control, and symbols for experimental stress control tests. The Blue coloured are for first small force and green coloured for a second higher force. Figure 6.13.A) is for exhaust mount made by MCN material.

6.2.5.2. Stiffness Loss Quantitative Results

The life to stiffness loss is computed from the number of cycles at which a loss of stiffness in a range of 15 to 20 % is measured. In the simulations of MCN material,

the initial flaw size of 0.04 mm computed on section 4.2.2 is used. The percentile value has been defined in 0.02 for allowing a small amount of cracks to coexist, and expecting that this would result in a prediction of a loss of 15-20% in stiffness. The numerical results of predictions and experiments are shown respectively on Table 6.2 and Table 6.3. The results of force and displacement modes of control are included on these tables. The numerical results obtained for MCN material show that prediction is optimistic in contrast to measured experimentally.

Table 6.2. Numerical results of computed stiffness loss and fatigue life at that stiffness drop, for strain and stress controlled conditions.

Predicted from Simulations – Strain Control				
Displacement	Flaw Size	Percentile	Life	Stiff. Loss
20 mm	0.04	0.02	356,757	19%
30 mm	0.04	0.02	24,249	16%

Predicted from Simulations – Stress Control				
Displacement	Flaw Size	Percentile	Life	Stiff. Loss
20 mm	0.04	0.02	67,985	19%
30 mm	0.04	0.02	4,620	16%

Table 6.3. Numerical mean value results of experimental stiffness loss and fatigue life at that stiffness drop, for strain and stress controlled conditions.

Experimental Results – Strain Control		
Displacement	Life	Stiff. Loss
20 mm	9,459	15%
30 mm	2,585	15%

Experimental Results – Stress Control		
Force	Life	Stiff. Loss
885 N	5,140	15%
1280 N	1,570	15%

6.2.5.1. Cracking Zone Identification

In the complete analysis of fatigue life by the Endurica CL it is computed the number of cycles required by a crack to grow from the initial flaw size to a nucleated

considered size. Endurica CL compute the nucleation life at every element in the component model, and from the identified first growing cracks is predicted the cracking zone in the model. In Figure 6.14 are faced the component model identifying the predicted cracking zone, and the picture of first visible crack in the component taken during the exhaust mount fatigue experiment. There is a perfect agreement between predicted and experimentally observed cracking zones.

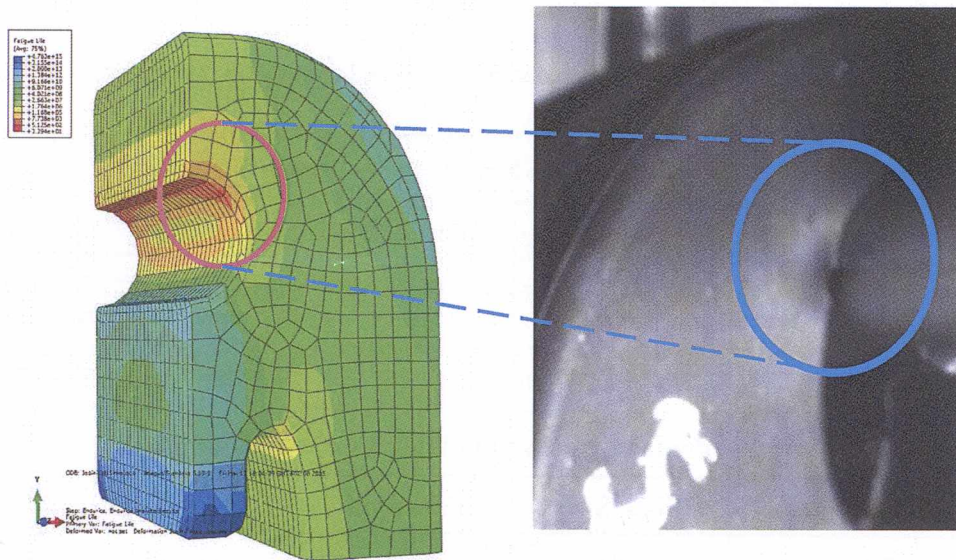


Figure 6.14. Comparison of fatigue crack nucleation point observed experimentally and obtained analytically

6.2.5.2. Study of Parameters that Influence on Stiffness Loss Predictions

The study of a group of parameters affecting the stiffness loss predictions require a series of simulations and analysis to be carried out. It has been defined three parameters to be analysed and several values at each of them. The finite element simulations pre-simulation have been decided to run up to a displacement of 20 mm. The MSB material has been selected because is the material due to the full convergence achieved in final simulations, with final damaged material state defined by the UHYPER subroutine. The simulations carried out with initially defined parameter values have predicted slower stiffness loss rate in comparison to experimentally observed. Thus, the aim varying parameter values has been to increment the rate of stiffness loss, and at the same time better understand their influence on: resultant stiffness loss rate, stiffness loss initiation instant, and number

of cycles to achieve the maximum loss of stiffness. The amount of stiffness loss predicted has been additional result to be analyzed. The three parameters with which have been decided to work have been: the initial flaw size, the percentile value, and the lookup table.

6.2.5.2.1. *The Flaw Size*

The initial flaw size is an intrinsic material parameter which is of great importance on crack nucleation phase, and in consequence for stiffness loss. The crack nucleation phase or life is the number of cycles that a crack needs to grow from its initial flaw size to a critical crack size of 1mm length. On his behalf, in the stiffness loss is assumed that a number of nucleated cracks coexist, and these will influence on components fatigue behaviour. The initial flaw size along with the crack growth rate is the main material parameter on which the crack nucleation life depends. The number of cycles required for first growing crack in a component to nucleate is valuable information for computing the stiffness loss. Internally the Endurica CL is considering the influence of the flaw size by the damage function detailed above in the analysis procedure section 6.2.4. For the study has been decided to vary initial flaw size values, without considering the material intrinsic flaw size, and measure the influence of each variation in the stiffness loss predictions. In the Figure 6.15 the results of simulations carried out at different flaw size values are summarized. The normalized stiffness versus the life to stiffness loss is plotted for four different flaw sizes: 0.009, 0.015, 0.05, 0.08 (mm). The smaller is the flaw size, is predicted a longer stiffness loss life. Nevertheless, the percentage of stiffness that is lost is not increased, and in the particular case of MSB material has been stuck in 8% loss.

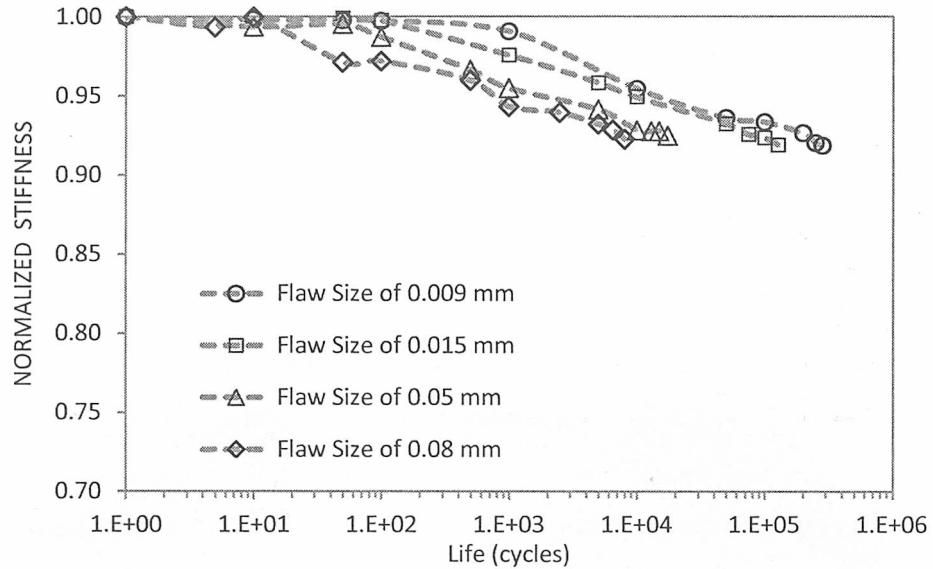


Figure 6.15. Normalized stiffness vs. stiffness loss life prediction results for four different initial flaw sizes for MSB material made exhaust mount simulation are plotted. The percentile value is kept constant at a value of 0.02. The four flaw sizes defined for simulations are: 0.009 (circle), 0.015 (square), 0.05 (triangle), and 0.08 (diamond), all of them in mm.

6.2.5.2.2. The Percentile

The percentile parameter is a mathematical trick for allowing the coexistence of several nucleated cracks, as has been mentioned in the analysis procedure in section 6.2.4. Therefore, by allowing the coexistence of cracks, a larger fatigue life will be predicted, and similarly, a larger stiffness loss. In the future its magnitude will be defined based on experience, attending to the component geometry and material fatigue properties. Nevertheless, in the current study the values have been defined with the aim of allowing to an adequate amount of cracks to coexist in the component model, and therefore for making a prediction close to experimentally obtained stiffness loss results.

The parameter percentile has been defined in the current study independently to the component material behaviour. Although, geometry and size of component have been in consideration for allowing a larger number of cracks to coexist due to the large size of exhaust mount. Therefore, the experience gained by the use of the stiffness loss prediction capability will be of great importance for the correct definition of the percentile value on future case studies. In the Figure 6.10 is shown a graphical representation of predicted number of cycles depending on percentile values. It can be seen in the graph, that a small percentile value results in a short life

prediction. Nevertheless, due to the nonlinear relationship of the function, with small increments of percentile the stiffness loss life prediction can increase considerably. The influence of different percentile values is summarized in a graphical representation of normalized stiffness versus the life to stiffness loss, plotted for four different percentile values (0.01, 0.02, 0.05 and 0.1) in Figure 6.16. Defining a high percentile value a high number of cracks is permitted to coexist on the component, and therefore the stiffness loss prediction will be higher. In the graph can be observed that the percentile value influence on the instant at which stiffness loss begins, and additionally has effects in the stiffness loss rate. Thus, at a major percentile value the instant of initiation of stiffness loss is retarded. But then, the rate of stiffness loss is also increased, and at the end the increase of stiffness loss life is not remarkable. The amount of stiffness loss measured at lowest percentile value used for the simulations has been of 6%, and has been increased to 8% at 0.02 percentile, and to 14% at 0.05 and 0.1 highest percentile values. From the analysis has been concluded that percentile value is to define in the range of 0.02 to roughly 0.07, whereas a value of 0.1 is already excessive.

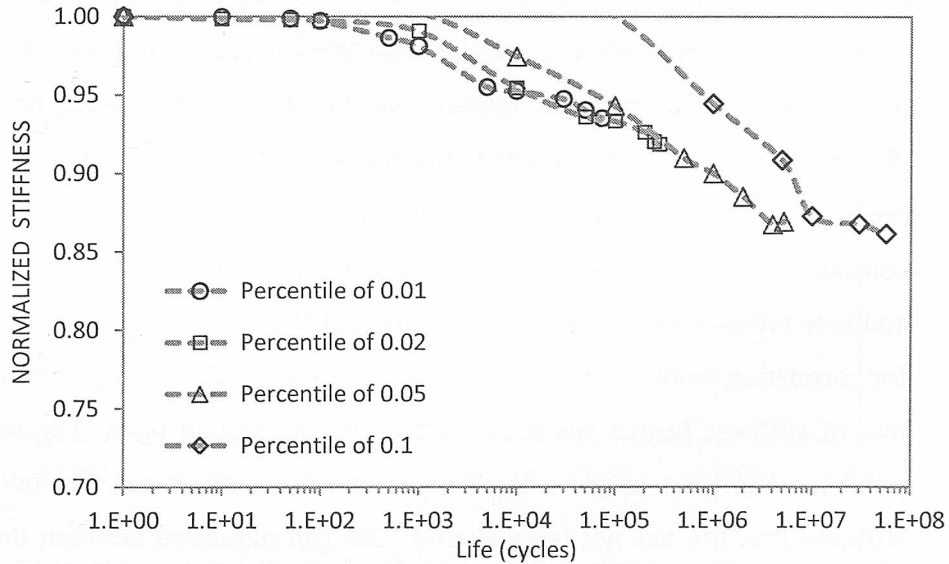


Figure 6.16. Normalized stiffness vs. stiffness loss life prediction results for four different percentile values for MSB material made exhaust mount simulation are plotted. The four different percentile values have been defined for simulations are: 0.01 (circle), 0.02 (square), 0.05 (triangle), 0.1 (diamond).

6.2.5.2.3. *The Lookup Table*

The lookup table is the main parameter influencing the stiffness loss predictions. In the section 6.1 has been presented the stiffness loss simulation approach, where it is postulated that each crack precursor reduces the strain energy in the material in function on its current size. Assuming that strain energy density of material containing no crack precursors is W_0 , then the strain energy density W of material containing defects may be calculated. It is not computed how much reduces the strain energy density each crack, but is considered by the lookup table in a phenomenological manner. The lookup table is the function that defines the material stiffness loss behaviour, the fraction of life consumed on each phase and amount that will be lost. The characterization test procedure detailed in section 6.2.2 has been designed expressly to quantify the damage and has been tested for first time on this project.

For analysing the influence of lookup table in the stiffness loss prediction, a second table of similar behaviour but with larger lost has been used to make a second prediction. The aim has been to observe on exhaust mount stiffness loss prediction the effect of the lookup table. In Figure 6.17 the two lookup tables have been presented in a graph, where normalized stiffness is plotted in function of the ratio of life divided by the final life, for showing the difference between both tables. The difference between them is small, but has a great influence on final stiffness loss predictions. For the analysis, the flaw size and percentile values have been kept constant at 0.08 mm and 0.01 respectively. In the Figure 6.18 are presented previous and new predictions in a plot of normalized stiffness in function of stiffness loss life for correlation work. From there, is firstly concluded that the cycle number at which loss of stiffness begins has been affected by the lookup table. The amount of loss predicted has been larger with the second table. In contrast, the rate of loss and stiffness loss life has not been altered. The gap measured between the two lookup tables used for simulations and stiffness loss predictions is of same magnitude, thus is considered to be proven that the amount of loss of stiffness predicted is proportional to the loss quantified on lookup tables.

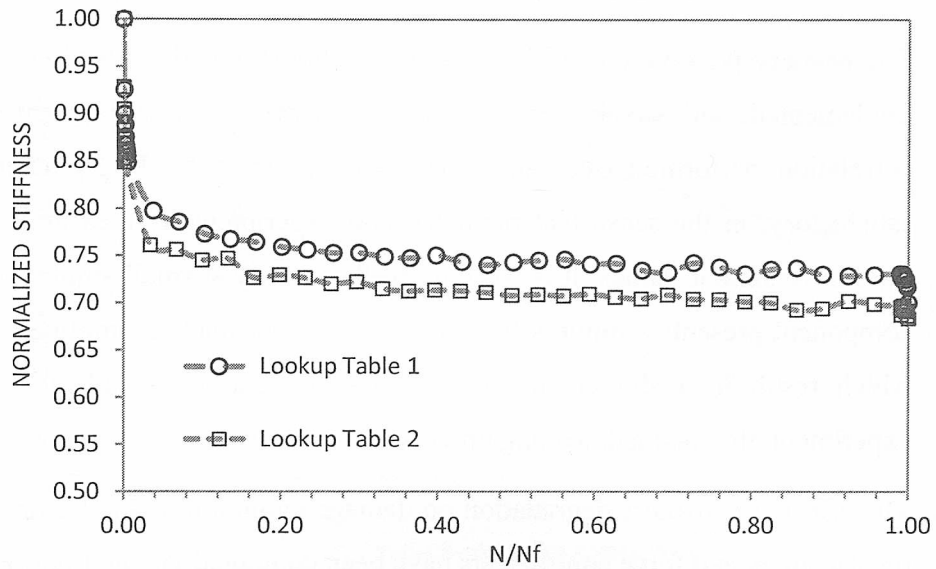


Figure 6.17. Normalized stiffness versus the ratio of life divided by the final life, N/N_f is plotted by the data of the lookup table, and thus the stiffness loss behaviour for the MSB material is represented. Two look up tables are shown: The number one (circle) is obtained from the mean values of all experimental test replicates, and the number two (square) from the replicate that showed the greatest stiffness loss.

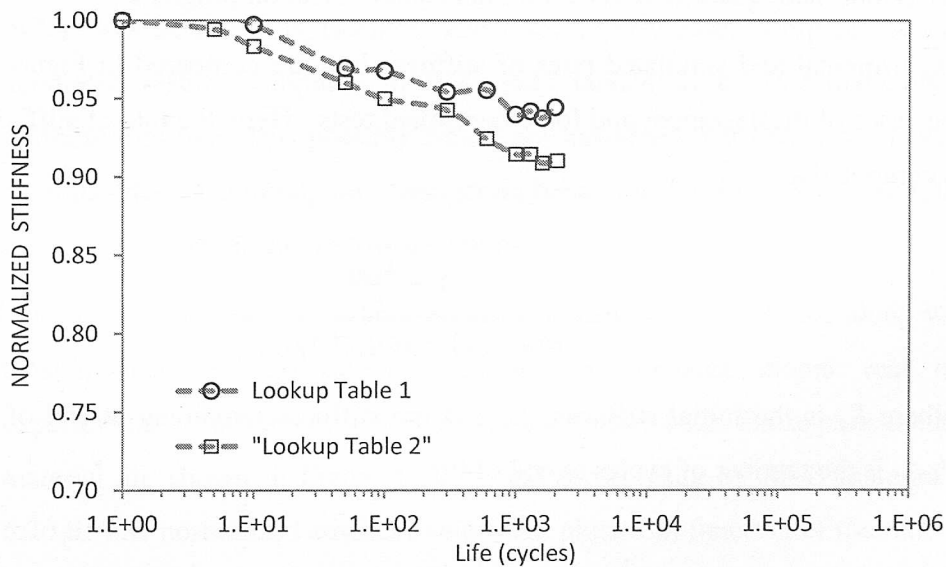


Figure 6.18. Normalized stiffness vs. stiffness loss life prediction results for two different lookup tables of MSB material made exhaust mount are plotted. Lookup Table 1 (circle) is related with experimentally obtained material data. Lookup Table 2 (square) obtained from the same MSB material experimental tests, but from the replicate that presented the greatest.

6.2.6. Summary of Cycling Control Type Influence

The primary positive conclusion is that developed equations, and code are already implemented and capable to give a reasonable stiffness loss prediction. First correlation performed over an exhaust mount made by MCN natural rubber is satisfactory, in the sense that predicted and experimentally measured stiffness loss rates have similar values. It is working well specially at small amplitudes, where the component presents a minimally long life. At larger loading amplitude fatigue tests, which result in a shorter life, the prediction made is considerably shorter than experimentally obtained, leading on very conservative design decisions.

The effects of stiffness degradation on damage evolution in an elastomer under both displacement and force control tests have been computed via the Endurica CL fatigue solver on the basis of characterizations of the material's stress-strain law, its fatigue crack growth rate curve, its stiffness loss curve in simple tension, and the crack precursor size computed from crack nucleation experiments. The exercise confirms that mode of control effects in fatigue reflect the same underlying material behaviour, here quantified via a minimal characterization program.

Experimental and simulated rates of stiffness loss are compared in Figure 6.19 for the cases of displacement and force controlled tests. Here, the rate of stiffness loss $\dot{\kappa}$ is computed as:

$$\dot{\kappa} = \frac{1 - \frac{K_{0.85}}{K_1}}{\log_{10}(1) - \log_{10}(N_{f,0.85})} \quad \text{Eq. 6-20}$$

Where K_1 is the initial stiffness, $K_{0.85}$ is the stiffness remaining at end of life, and $N_{f,0.85}$ is the number of cycles to end of life.

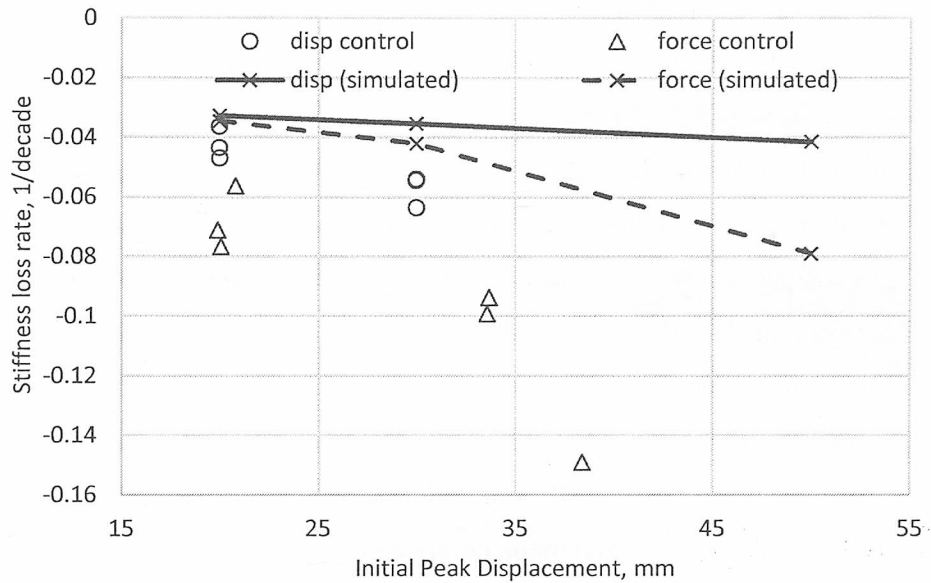


Figure 6.19. Comparison of stiffness loss rates experimentally obtained and computed by Endurica code, under displacement and force control tests over MCN material exhaust mount component. Experimental test results are shown in hollow symbols, while prediction results are shown by dashed and continuous lines.

The observed and simulated trends show strong similarities. The predicted differences between displacement and force control cases compare favourably. The simulated results computed in this study tended to be systematically lower in stiffness loss rate. This possibly would not have happened if it hadn't been neglected the Mullins effect in defining the stress strain behaviour for the analysis. But, this will be left to be clarified in future investigations.

Additionally, the exhaust mount model stiffness loss predictions, along with simple tension specimen experimental results, and exhaust mount real component experimental results are plotted in a graph in Figure 6.20. Those parts made by MCN material are shown in Figure 6.20.A, and those made by MSB material in Figure 6.20.B. The normalized stiffness values are plotted in function of the ratio of current life divided by the final life N/N_f , and thus is compared the amount of stiffness that is lost on each case. The aim of these plots is to correlate exhaust mount component prediction results with the experimentally obtained results, focusing on the amount of stiffness loss. The predictions are of the exhaust mount component at different peak levels. The plotted experimental results are simple tension specimen cyclic tests to failure at two displacement peak levels, and the exhaust mount component cyclic test to measure stiffness loss in both, strain and stress control. It must be remembered

that in the group of specimen results, those obtained at cycling displacement control are used to feed the lookup tables for Endurica CL computations. The correlation of prediction results with this simple tension experimental results, show that predicted amount of lost is less than a quarter of experimentally measured in case of both materials. Thus, can be concluded that lookup table is not the only parameter governing the stiffness loss prediction. The other correlation shown in these plots is between predicted and experimentally obtained results on real component. Actually, this is the result to be analysed in evaluating the adequacy of prediction method. It is shown that damage predicted in the component is less than half of the experimentally measured in the case of MCN material made component, and is less than a quarter in the case of MSB material made component.

Figure 6.20. A)

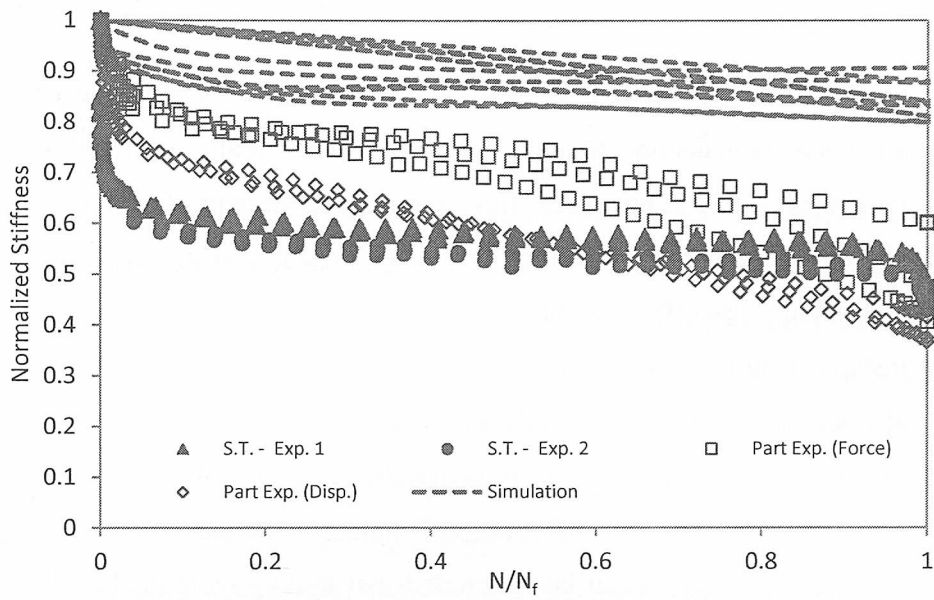


Figure 6.20. B)

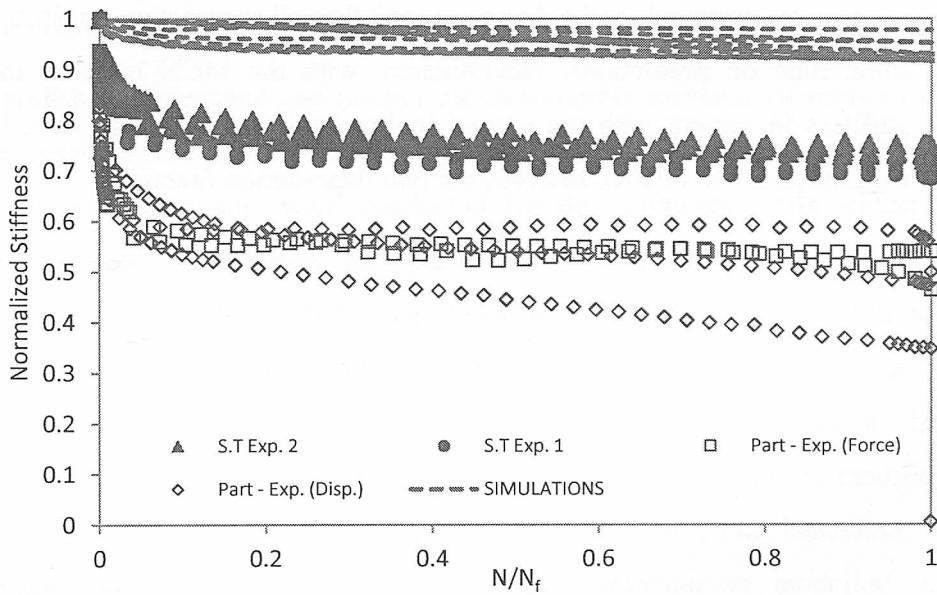


Figure 6.20. The normalized stiffness values are plotted in function of the ratio of current life divided by the final life N/N_f . The following stiffness loss results are plotted in a single graph: predictions on the exhaust mount model (dashed lines), experimental cycle to failure test on simple tension specimen at two peak levels (full symbols), and experimental cycle to stiffness loss test on real exhaust mount component (hollow symbol). Results for both materials are plotted: Figure 6.20. A) is for MCN material and Figure 6.20. B) is for MSB material.

Taken together, the results presented here illustrate that a relatively simple theory based upon classical fracture mechanical arguments, and augmented with information about the stiffness loss function and mode of control, is sufficient and

capable of producing realistic estimates of stiffness degradation for an engineering component.

In relation to the study of input parameters influencing stiffness loss predictions there are some conclusions to be summarized. The smaller is the flaw size a longer stiffness loss life is predicted. Nevertheless, the amount of stiffness that is lost is not bigger. The percentile value influences the instant at which stiffness loss begins, and additionally has effects in the stiffness loss rate. Thus, at a major percentile value the instant of initiation of stiffness loss is retarded. But then, the rate of stiffness loss is also increased, but at the end the increase in the amount of stiffness loss life is not so big. From the analysis done is concluded that percentile value is a parameter to define in the range of 0.01 to 0.07 values, whereas a value of 0.1 is already excessive. Finally, it can be concluded that lookup table data is the input data that most affecting related to amount of loss in the predictions. The relationship is not linearly proportional, and this has proved that all parameters are influencing at the same time on predictions. Nevertheless, with the MCN material the amount of stiffness increment with the second lookup table material data have been of same magnitude as the relative between the two degradation functions.

7. Conclusions and Future Works

7.1. Conclusions

A number of aspects related to the fatigue failure process in rubber have been studied in the research work. These include the stress-strain behavior under monotonic and initial cyclic conditions, the size and density of pre-existing flaw nucleation sites, the rate of growth of cracks, and stiffness loss due to fatigue damage. Commonly used theories for predicting crack growth and fatigue life under multiaxial and variable amplitude loading have been investigated, and have seen that the most suitable equivalent parameter is the cracking energy density. In addition to common material characterization tests additional one have been designed to feed newly developed models, including: a model relating the amount and density of cracks with the stiffness loss, a model relating the cycling control mode in the stiffness loss life.

The ability to understand and predict the stress-strain response of rubber often has direct consequences on the ability to model fatigue life. Monotonic and initial cyclic stress-strain experiments were conducted for the following strain states: simple tension, simple compression, and planar tension. The initial cyclic stress-strain response of filled rubbers exhibits significant softening known as the Mullins effect. Hyperelastic models do not capture the Mullins effect. For considering the Mullins effect, Ogden and Roxburgh model has been used, which produced an isotropic model based upon a strain energy density function. The function is modified by a term that contains a damage parameter to model the softening behaviour. On the approach, the virgin monotonic stress-strain behaviour is modelled using a conventional hyperelastic strain energy density function. Several existing hyperelastic constitutive models were reviewed. Although many options exist for accurately modeling nonlinear elastic behavior the Reduced Polynomial or Yeoh third order model was employed in this work. Finally, the fitting to experimental results obtained with the pseudo-elastic model address the dominant influence of the Mullins effect.

Entire material characterization to fatigue has been carried out satisfactorily for first time at Leartiker facilities, including: fatigue crack growth rate, strain energy release rate threshold, material intrinsic flaw size determination, volume density of crack

precursors, R-ratio effect on fatigue crack growth, stiffness loss behavior. The material data computed have been used to feed the fatigue life, nucleation life and stiffness loss life simulations. Test procedures for obtaining all of required parameters are complex and laborious. Thus, first have been designed and implemented, but then the procedures have been optimized with high automation of test execution, data collection, and data processing. Therefore, costs and data delivery time limits are not currently a drawback to run rubber fatigue simulations.

In the crack nucleation life predictions all elements of the component model are analyzed as potential to failure. The cracking energy density has been used to identify and measure the fatigue damage, and critical plane. The critical locations are identified in the component from the minimum life elements, computed from the integration of the damage function. For complex geometry components a numerical method such as the finite element analysis is required to get the strain history from the commanded loading history. The material characterization to fatigue crack growth and intrinsic flaw size has been experimentally calculated. The quasi-static strain history of the real component to feed the Endurica CL solver has been carried out in Abaqus finite element analysis software. The applicability of the procedure has been tested by the analysis of vehicle exhaust mount component. The obtained predictions are correlated with real component experimental results. Finally, the rubber fatigue simulation procedure for complex geometry components under constant amplitude uniaxial loading has been validated and with satisfactory results.

The prediction method and defined criteria are very conservative, and short life has been initially predicted from simulations in comparison to experimentally observed. It has been decided to consider as fatigue nucleation the number of cycles at which a determine percent of elements have already been nucleated. To correlate fatigue crack nucleation life prediction results with experimentally obtained the graphs shown in Figure 5.12 and Figure 5.13 have been constructed. From the plots of the correlations have to be highlighted the adequateness of predictions following the life decrease when peak loadings have been increased. The control mode effect has been also properly predicted, computing a shorter life when the fatigue cycling is controlled in force. On the other hand, in general the fatigue life prediction is far from experimentally observed behaviour. The computer aided simulations predict a considerably less long-lived component than measured on tests. This effect is more

pronounced in the case of MSB material made systems than in those made by MCN material

Additionally have to be analyzed the initial decision of not consider some factors for computations, even knowing that has influence on the fatigue nucleation life of components. Those have been the self heating of the component and rubber to metal friction. The fatigue predictions are altered due to increment of temperature in the component due to hysteresis of material, as well as due to the friction of rubber to metal in the pin holes. Similarly predictions depend on the overall stiffness of component that will increase if friction coefficient is considered in simulations. Therefore, can be concluded that implemented procedure is operating and working satisfactorily, but is not considering all factors and will have to be corrected in future works.

In the complete analysis of fatigue life by the Endurica CL it is computed the number of cycles required by a crack to grow from the initial flaw size to a nucleated considered size. A capture of the component model identifying the predicted cracking zone, and the picture of first visible crack in the component taken during the exhaust mount fatigue experiment are faced on Figure 5.14. There is a perfect agreement between predicted and experimentally observed cracking zones.

In rubber fatigue the strain energy density may depend not only on the instantaneous strain or stress, but also on damage state of material, and on the mode of control imposed in the fatigue test. The stiffness loss approach relates the differentiated particular damage developments of different loading modes in a function. The parameter that quantifies the damage is the normalized stiffness, and a function has been defined that contemplates the effect of stiffness loss and crack size on the strain energy density. The primary positive conclusion is that developed equations, and code are already implemented and capable to give a reasonable stiffness loss prediction.

The correlation performed over an exhaust mount made by MCN natural rubber is satisfactory, in the sense that predicted stiffness loss rates and experimentally measured have similar values. The results are fulfilling expectations especially at small amplitudes cycling tests, where the component presents longest life. At larger

loading amplitudes, resulting in a shorter life, the predictions are considerably shorter than experimentally observed, leading to very conservative design decisions.

The effects of stiffness degradation on damage evolution in an elastomer under both displacement and force control tests have been computed. The results confirm that mode of control effects in fatigue reflect the same essential material behaviour, here quantified via a minimal characterization program.

The rates of loss of component stiffness measured experimentally and predicted from simulations are correlated by facing them in a plot for displacement and force cycling control types. Both stiffness loss behaviours have strong similarities. The differentiated displacement and force control loading behaviour are compared favourably between predictions and experimental. It is predicted an acceleration resulting in a shorter life at force control cases, which is not observed at displacement control. The predictions tended to be in all cases of lower rate stiffness loss. It is concluded that this possibly would not have happened if Mullins effect would be considered in defining the stress strain behaviour for the analysis.

It has been presented a constitutive model for considering the stiffness loss that a simple tension specimen shows when cyclic loads are applied, without considering cycling control mode. The stiffness loss can be rationalized in terms of growth of crack precursors distributed throughout the material. Softening mechanism is governed on a per cycle basis. The proposed model presents an adequate fitting using physically reasonable parameters values. From the observed behaviour is presumed that the size and volume density of the largest flaws are the parameters which govern the accelerating stiffness loss that precedes the specimen rupture. Thus, constitutive model can be used instead of using the simple tension cycling test for considering material stiffness loss behaviour data. The gradual semi-logarithmic loss observed after the Mullins effect, has been here presumed to arise in association with the large number of crack precursors with sizes smaller than the characteristic largest precursor. The loss of stiffness that is observed at initial transient cycles, associated with Mullins effect has not been fitted by the proposed model. The work procedure designed is ready to work with it, and the constitutive model is implemented in Endurica CL, but unfortunately has been out of the scope of project to make the predictions and correlate them with experimental results.

7.2.Directions for Future Works

In the research work the efforts have been focused on developing and implementing the rubber components stiffness loss prediction capability in our own facilities. But, since the beginning the goal had to be achievable, and has been scoped in stiffness loss prediction of rubber components under uniaxial constant amplitude loadings. At the end of the work, directions for future investigations have been proposed to verify that developed capabilities are able to properly predict stiffness loss of rubber components at variable amplitude multiaxial loadings. At the same time, there are several details that have been seen that should be improved for optimizing the overall fatigue life and stiffness loss prediction methodology.

The implemented stiffness loss capability has been designed and used for uniaxial loadings, but also for using in short-term in multiaxial and variable amplitude loading cases. The cracking energy density equivalence parameter is used for fatigue life computations, and the material characterization for measuring the influence of R-ratio on fatigue crack growth is already implemented. Thus, everything has been designed for working with mentioned fatigue loading conditions in complex geometries. The simulation and later correlation experimental works remains to be done.

In relation to the provided complete rubber fatigue prediction model, there are several aspects potentials to be improved and to be done in future investigations:

One source of scattering of observed overall results could be due to self-heating observed when dealing with fatigue of rubbers, and which was completely neglected in the proposed developments.

The crack nucleation zones are those where maximum strains are measured due to the mechanical loading, and those are magnified by the rubber to metal friction due to lack of lubrication on contact surfaces. The high friction between surfaces produces an increment of temperature in the contact zones, degrades the rubber in these critical zones of the component, and consequently the crack nucleation rate has been increased. This is also a source of scattering of observed overall results, and which has been neglected in the developments. Related with the pin contact, considering rubber to metal friction in the simulations, the component reaction force to commanded displacement is considerably higher.. The effect has not been

considered in the simulations for fatigue crack nucleation predictions, even though have been taken into consideration in the analysis of obtained prediction results.

The cracking energy density calculations of this study assume Reduced Polynomial or Yeoh of third order hyperelastic behavior. The consequences of selecting other hyperelastic constitutive laws need to be investigated.

For the component stiffness loss prediction process it has been left to be improved by its own, through the experience that the technicians will acquire with the use of the code. There is still remaining work on the adjustment of most influencing parameter values depending on the component geometry, loading history and rubber material, which will be overcome with the use and getting experience.

Additionally for the stiffness loss computations, have remain to be done a complete prediction work with the constitutive model developed in the section 6.1. The model have fitted well the stiffness loss that a simple tension specimen presents, but rationalizing damage in terms of growth of crack precursors distributed throughout the material. The model has presented a good fit using physically reasonable parameter values. Unfortunately, it was outside the scope of the project to carry out the simulations using the developed constitutive model, and remains to be done in future works.

8. Publications and Communications

In the following section a list of publications is shown in Table 8.1 and a list of communications in Table 8.2. Besides, the publications have been attached on Appendix.

Table 8.1 List of publications

PUBLICATIONS				
TITLE	AUTHORS	EDITORIAL	BOOK, CHAPTER, JOURNAL	DATE
Relationship between displacement and force controlled fatigue tests	W. V. Mars, M.Isasi, A. Arriaga, J. Plaza	CRC Press / Balkema	Constitutive Models For Rubber IX, 417	2015
Loss of Stiffness During Fatigue and the Development of Crack Precursors	W. V. Mars, M.Isasi, A. Arriaga,	CRC Press / Balkema	Constitutive Models for Rubber VIII	2013

Table 8.2 List of communications

COMMUNICATIONS				
TITLE	AUTHORS	TYPE OF PARTICIPATION	CONGRESS	PLACE
Predicción de la vida a fatiga y pérdida de rigidez de un componente de caucho	M. Isasi, W. V. Mars, A. Arriaga, J. Plaza	Ponente	Spanish Conference on Fracture and Structural Integrity (International edition)	Zamora (Spain)
Relationship between displacement and force controlled fatigue tests	W. V. Mars, M.Isasi, A. Arriaga, J. Plaza	Co-Autor	European Conference on Constitutive Models for Rubbers IX	Prague (Czech Republic)
Loss of Stiffness During Fatigue and the Development of Crack Precursors	W. V. Mars, M.Isasi, A. Arriaga,	Co-Autor	European Conference on Constitutive Models for Rubbers VIII	San Sebastian (Spain)

9. References

- [1] A.N. Gent, Strength of Elastomers, in: J.E. Mark, B. Erman, M. Roland (Eds.), *Sci. Technol. Rubber*, Academic Press, 2013: pp. 419–454.
- [2] A.F. W V Mars, Observations of the Constitutive Response and Characterization of Filled Natural Rubber Under Monotonic and Cyclic Multiaxial Stress States, *J. Eng. Mater. Technol.-Trans. Asme - J ENG MATER TECHNOL.* 126 (2004). doi:10.1115/1.1631432.
- [3] L. Mullins, Softening of Rubber by Deformation, *Rubber Chem. Technol.* 42 (1969) 339–362. doi:10.5254/1.3539210.
- [4] L.R.G. Treloar, *The Physics of Rubber Elasticity*, Oxford University Press, 1975.
- [5] G.H. Ryder, Elastic Constants, in: *Strength Mater.*, International student edition edition, Palgrave, Basingstoke, Hampshire, 1969.
- [6] H.M. James, E. Guth, Theory of the elastic properties of rubber, *J. Chem. Phys.* 11 (2004) 455–481.
- [7] R.S. Rivlin, Large elastic deformations of isotropic materials. II. Some uniqueness theorems for pure, homogeneous deformation, *Philos. Trans. R. Soc. Lond. Ser. Math. Phys. Sci.* 240 (1948) 491–508.
- [8] P.J. Flory, Network Structure and the Elastic Properties of Vulcanized Rubber., *Chem. Rev.* 35 (1944) 51–75.
- [9] A.N. Gent, A New Constitutive Relation for Rubber, *Rubber Chem. Technol.* 69 (1996) 59–61. doi:10.5254/1.3538357.
- [10] M. Mooney, A theory of large elastic deformation, *J. Appl. Phys.* 11 (2004) 582–592.
- [11] R.S. Rivlin, Large Elastic Deformations of Isotropic Materials. I. Fundamental Concepts, *Philos. Trans. R. Soc. Math. Phys. Eng. Sci.* 240 (1948) 459–490. doi:10.1098/rsta.1948.0002.
- [12] R.S. Rivlin, Large elastic deformations, in: *Collect. Pap. RS Rivlin*, Springer, 1997: pp. 318–351.
- [13] R.W. Ogden, Recent Advances in the Phenomenological Theory of Rubber Elasticity, *Rubber Chem. Technol.* 59 (1986) 361–383. doi:10.5254/1.3538206.
- [14] J.J.. Busfield, *The Prediction of the Mechanical Performance of Elastomeric Components using Finite Element Analysis*, Ph.D. Dissertation, Queen Mary, University of London, 2000.

- [15] A.G. James, A. Green, Strain energy functions of rubber. II. The characterization of filled vulcanizates, *J. Appl. Polym. Sci.* 19 (1975) 2319–2330.
- [16] Y. Fukahori, W. Seki, Molecular behaviour of elastomeric materials under large deformation: 1. Re-evaluation of the Mooney-Rivlin plot, *Polymer*. 33 (1992) 502–508.
- [17] M.J. Gregory, The stress / strain behaviour of filled rubbers at moderate strains, *Plast. Rubber Mater. Appl.* 4 (1979) 184.
- [18] C.K.L. Davies, D.K. De, A.G. Thomas, Characterization of the Behavior of Rubber for Engineering Design Purposes. 1. Stress-Strain Relations, *Rubber Chem. Technol.* 67 (1994) 716–728. doi:10.5254/1.3538706.
- [19] Y. Obata, S. Kawabata, H. Kawai, Mechanical properties of natural rubber vulcanizates in finite deformation, *J. Polym. Sci. Part -2 Polym. Phys.* 8 (1970) 903–919.
- [20] D.F. Jones, L.R.G. Treloar, The properties of rubber in pure homogeneous strain, *J. Phys. Appl. Phys.* 8 (1975) 1285.
- [21] J. Gough, A.H. Muhr, A.G. Thomas, Material characterisation for finite element analysis of rubber components, (1998).
- [22] O.H. Yeoh, P.D. Fleming, A new attempt to reconcile the statistical and phenomenological theories of rubber elasticity, *J. Polym. Sci.-B-Polym. Phys.* Ed. 35 (1997) 1919–1932.
- [23] O.H. Yeoh, Characterization of Elastic Properties of Carbon-Black-Filled Rubber Vulcanizates, *Rubber Chem. Technol.* 63 (1990) 792–805. doi:10.5254/1.3538289.
- [24] R.W. Ogden, Large Deformation Isotropic Elasticity—On the Correlation of Theory and Experiment for Incompressible Rubberlike Solids, *Rubber Chem. Technol.* 46 (1973) 398–416. doi:10.5254/1.3542910.
- [25] E.M. Arruda, M.C. Boyce, A three-dimensional constitutive model for the large stretch behavior of rubber elastic materials, *J. Mech. Phys. Solids.* 41 (1993) 389–412.
- [26] O.H. Yeoh, Some Forms of the Strain Energy Function for Rubber, *Rubber Chem. Technol.* 66 (1993) 754–771. doi:10.5254/1.3538343.
- [27] D. Boast, V.A. Coveney, Finite element analysis of elastomers, Professional Engineering Pub., 1999.
- [28] H.R. ahmadi, J. Gough, A. Muhr, A.G. Thomas, Bi-axial experimental techniques highlighting the limitations of a strain-energy description of rubber, in: A. Dorfmann, A. Muhr (Eds.), *Const. Models Rubber*, CRC Press, 1999.

- [29] D11 Committee, Test Method for Rubber Property--Vulcanization Using Oscillating Disk Cure Meter, ASTM International, 2011.
- [30] F. Bueche, Mullins effect and rubber–filler interaction, *J. Appl. Polym. Sci.* 5 (1961) 271–281.
- [31] J. a. C. Harwood, A.R. Payne, Stress softening in natural rubber vulcanizates. Part IV. Unfilled vulcanizates, *J. Appl. Polym. Sci.* 10 (1966) 1203–1211. doi:10.1002/app.1966.070100811.
- [32] R.W. Ogden, D.G. Roxburgh, A pseudo–elastic model for the Mullins effect in filled rubber, *Proc. R. Soc. Lond. Ser. Math. Phys. Eng. Sci.* 455 (1999) 2861–2877.
- [33] S. Govindjee, J. Simo, A micro-mechanically based continuum damage model for carbon black-filled rubbers incorporating Mullins’ effect, *J. Mech. Phys. Solids.* 39 (1991) 87–112.
- [34] J.C. Simo, On a fully three-dimensional finite-strain viscoelastic damage model: formulation and computational aspects, *Comput. Methods Appl. Mech. Eng.* 60 (1987) 153–173.
- [35] C. Miehe, Discontinuous and continuous damage evolution in Ogden-type large-strain elastic materials, *Eur. J. Mech. Solids.* 14 (1995) 697–720.
- [36] A. Muhr, J. Gough, I.H. Gregory, Experimental determination of model for liquid silicone rubber: hyperelasticity and Mullins’ effect, in: A. Dorfmann, A. Muhr (Eds.), *Const. Models Rubber*, CRC Press, 1999.
- [37] W.V. Mars, *Multiaxial fatigue of rubber*, The university of Toledo, 2001.
- [38] P.B. Lindley, Non-Relaxing Crack Growth and Fatigue in a Non-Crystallizing Rubber, *Rubber Chem. Technol.* 47 (1974) 1253–1264. doi:10.5254/1.3540497.
- [39] A.R. Payne, R.E. Whittaker, Influence of Hysteresis on Tensile and Fatigue Failure in Rubbers, *Rubber Chem. Technol.* 45 (1972) 1043–1050. doi:10.5254/1.3542885.
- [40] M. Braden, A.N. Gent, The attack of ozone on stretched rubber vulcanizates. III. Action of antiozonants, *J. Appl. Polym. Sci.* 6 (1962) 449–455.
- [41] O. kramer, J.D. Ferry, Dynamic Mechanical Properties, in: F.R. Eirich (Ed.), *Sci. Technol. Rubber*, Elsevier, 1978: pp. 180–223.
- [42] C. Deeprasertkul, Dynamic mechanical properties of carbon black filled elastomer containing liquids., Queen Mary, University of London, 2000.
- [43] F.R. Eirich, *Science and Technology of Rubber*, Elsevier, 1978.
- [44] P.J. Flory, J. Rehner Jr, Statistical Mechanics of Cross-Linked Polymer Networks I. Rubberlike Elasticity, *J. Chem. Phys.* 11 (2004) 512–520.

- [45] A. Arrillaga, Z. Kareaga, E. Retolaza, A.M. Zaldua, Bestimmung des Vulkanisationsgrades von Gummi durch Quellung, *Gummi Fasern Kunststoffe*. 64 (2011) 669.
- [46] G.R. Bhashyam, *ANSYS Mechanical—A Powerful Nonlinear Simulation Tool*, Ansys Inc. (2002).
- [47] J.S. Bergström, M.C. Boyce, Large strain time-dependent behavior of filled elastomers, *Mech. Mater.* 32 (2000) 627–644.
- [48] G.J. Lake, Fatigue and Fracture of Elastomers, *Rubber Chem. Technol.* 68 (1995) 435–460. doi:10.5254/1.3538750.
- [49] A.G. Thomas, The Development of Fracture Mechanics for Elastomers, *Rubber Chem. Technol.* 67 (1994) 50–67. doi:10.5254/1.3538688.
- [50] M.D. Ellul, Mechanical Fatigue, in: *Eng. Rubber Des. Rubber Compon.*, Gent A., Carl Hanser Verlag, Munich, 1992: p. Chapter 6.
- [51] G.J. Lake, A.G. Thomas, Strength, in: *Eng. Rubber Des. Rubber Compon.*, Gent A., Carl Hanser Verlag, Munich, 1992: p. Chapter 6.
- [52] G.J. Lake, Mechanical Fatigue of Rubber, *Rubber Chem. Technol.* 45 (1972) 309–328. doi:10.5254/1.3544709.
- [53] J.R. Beatty, Fatigue of Rubber, *Rubber Chem. Technol.* 37 (1964) 1341–1364. doi:10.5254/1.3540402.
- [54] W.V. Mars, A. Fatemi, A literature survey on fatigue analysis approaches for rubber, *Int. J. Fatigue.* 24 (2002) 949–961. doi:10.1016/S0142-1123(02)00008-7.
- [55] W.V. Mars, A. Fatemi, Factors that Affect the Fatigue Life of Rubber: A Literature Survey, *Rubber Chem. Technol.* 77 (2004) 391–412. doi:10.5254/1.3547831.
- [56] M.S.C. Marc, Nonlinear finite element analysis of elastomers, *Tech. Pap.* (2005).
- [57] K.N. Morman, T.Y. Pan, Application of Finite-Element Analysis in the Design of Automotive Elastomeric Components, *Rubber Chem. Technol.* 61 (1988) 503–533. doi:10.5254/1.3536198.
- [58] D.W. Nicholson, N.W. Nelson, Finite-Element Analysis in Design with Rubber, *Rubber Chem. Technol.* 63 (1990) 368–406. doi:10.5254/1.3538262.
- [59] R.I. Stephens, A. Fatemi, R.R. Stephens, H.O. Fuchs, *Metal Fatigue in Engineering*, John Wiley & Sons, 2000.
- [60] T.L. Anderson, *Fracture Mechanics: Fundamentals and Applications*, Third Edition, CRC Press, 2005.

- [61] J.-B. Le Cam, Endommagement en fatigue des élastomères, Ph.D. Dissertation, Nantes, 2005.
- [62] N. Saintier, Fatigue multiaxiale dans un élastomère de type NR chargé: mécanismes d'endommagement et critère local d'amorçage de fissure, Ph.D. Dissertation, École Nationale Supérieure des Mines de Paris, 2001.
- [63] É. Ostoja-Kuczynski, Comportement en fatigue des élastomères: application aux structures antivibratoires pour l'automobile, Nantes, 2005.
- [64] N. Saintier, G. Cailletaud, R. Piques, Crack initiation and propagation under multiaxial fatigue in a natural rubber, *Int. J. Fatigue*. 28 (2006) 61–72. doi:10.1016/j.ijfatigue.2005.03.006.
- [65] A. Wöhler, Wöhler's experiments on the strength of metals, *Engineering*. 4 (1867) 160–161.
- [66] S.M. Cadwell, R.A. Merrill, C.M. Sloman, F.L. Yost, Dynamic Fatigue Life of Rubber, *Rubber Chem. Technol.* 13 (1940) 304–315. doi:10.5254/1.3539515.
- [67] D11 Committee, Test Method for Rubber Property--Extension Cycling Fatigue, ASTM International, 2011.
- [68] N. Saintier, G. Cailletaud, R. Piques, Multiaxial fatigue life prediction for a natural rubber, *Int. J. Fatigue*. 28 (2006) 530–539. doi:10.1016/j.ijfatigue.2005.05.011.
- [69] W.V. Mars, Cracking Energy Density as a Predictor of Fatigue Life under Multiaxial Conditions, *Rubber Chem. Technol.* 75 (2002) 1–17. doi:10.5254/1.3547670.
- [70] E. Verron, A. Andriyana, Definition of a new predictor for multiaxial fatigue crack nucleation in rubber, *J. Mech. Phys. Solids*. 56 (2008) 417–443. doi:10.1016/j.jmps.2007.05.019.
- [71] J.H. Fielding, Flex Life and Crystallization of Synthetic Rubber, *Ind. Eng. Chem.* 35 (1943) 1259–1261. doi:10.1021/ie50408a008.
- [72] B.J. Roberts, J.B. Benzies, The relationship between uniaxial and equibiaxial fatigue in gum and carbon black filled vulcanizates, *Proc. Rubbercon.* 77 (1977) 2–1.
- [73] J.R. Roach, Crack Growth in Elastomers under Biaxial Stresses, Ph.D. Dissertation, University of Akron, 1982.
- [74] H.S. Ro, Modeling and Interpretation of Fatigue Failure Initiation in Rubber Related to Pneumatic Tires, Purdue University, 1989.
- [75] N. André, G. Cailletaud, R. Piques, Haigh diagram for fatigue crack initiation prediction of natural rubber components, *Kautsch. Gummi Kunststoffe*. 52 (1999) 120–123.

- [76] F. Abraham, T. Alshuth, S. Jerrams, The effect of minimum stress and stress amplitude on the fatigue life of non strain crystallising elastomers, *Mater. Des.* 26 (2005) 239–245.
- [77] R.S. Rivlin, A.G. Thomas, Rupture of rubber. I. Characteristic energy for tearing, *J. Polym. Sci.* 10 (1953) 291–318.
- [78] A.G. Thomas, Rupture of rubber. II. The strain concentration at an incision, *J. Polym. Sci.* 18 (1955) 177–188.
- [79] H.W. Greensmith, A.G. Thomas, Rupture of rubber. III. Determination of tear properties, *J. Polym. Sci.* 18 (1955) 189–200.
- [80] H.W. Greensmith, Rupture of rubber. IV. Tear properties of vulcanizates containing carbon black, *J. Polym. Sci.* 21 (1956) 175–187.
- [81] A.G. Thomas, Rupture of Rubber. V. Cut Growth in Natural Rubber Vulcanizates, *Rubber Chem. Technol.* 32 (1959) 477–489. doi:10.5254/1.3542412.
- [82] A.G. Thomas, Rupture of Rubber. VI. Further Experiments of the Tear Criterion, *Rubber Chem. Technol.* 34 (1961) 66–75. doi:10.5254/1.3540210.
- [83] H.W. Greensmith, Rupture of rubber. VII. Effect of rate of extension in tensile tests, *J. Appl. Polym. Sci.* 3 (1960) 175–182.
- [84] H.W. Greensmith, Rupture of rubber. VIII. Comparisons of tear and tensile rupture measurements, *J. Appl. Polym. Sci.* 3 (1960) 183–193.
- [85] L. Mullins, Rupture of rubber. IX. Role of hysteresis in the tearing of rubber, *Trans. Inst. Rubber Ind.* 35 (1959) 213–22.
- [86] H.W. Greensmith, Rupture of rubber. X. The change in stored energy on making a small cut in a test piece held in simple extension, *J. Appl. Polym. Sci.* 7 (1963) 993–1002.
- [87] H.W. Greensmith, Rupture of rubber. XI. Tensile rupture and crack growth in a noncrystallizing rubber, *J. Appl. Polym. Sci.* 8 (1964) 1113–1128.
- [88] A.N. Gent, P.B. Lindley, A.G. Thomas, Cut growth and fatigue of rubbers. I. The relationship between cut growth and fatigue, *J. Appl. Polym. Sci.* 8 (1964) 455–466.
- [89] G.J. Lake, P.B. Lindley, Cut Growth and Fatigue of Rubbers. II. Experiments on A Noncrystallizing Rubber, *Rubber Chem. Technol.* 38 (1965) 301–313. doi:10.5254/1.3535649.
- [90] M.-P. Lee, A. Moet, Analysis of Fatigue Crack Propagation in NR/BR Rubber Blend, *Rubber Chem. Technol.* 66 (1993) 304–316. doi:10.5254/1.3538314.

- [91] N.A. Hocine, M.N. Abdelaziz, G. Mesmacque, Experimental and numerical investigation on single specimen methods of determination of J in rubber materials, *Int. J. Fract.* 94 (1998) 321–338. doi:10.1023/A:1007520003294.
- [92] P.B. Lindley, Energy for crack growth in model rubber components, *J. Strain Anal. Eng. Des.* 7 (1972) 132–140.
- [93] D.G. Young, Application of Fatigue Methods Based on Fracture Mechanics for Tire Compound Development, *Rubber Chem. Technol.* 63 (1990) 567–581. doi:10.5254/1.3538274.
- [94] A. Griffith, *The phenomena of rupture and flow in solids*, (1997).
- [95] A. Zine, N. Benseddiq, M.N. Abdelaziz, N.A. Hocine, D. Bouami, Prediction of rubber fatigue life under multiaxial loading, *Fatigue Fract. Eng. Mater. Struct.* 29 (2006) 267–278. doi:10.1111/j.1460-2695.2005.00989.x.
- [96] A. Martinovs, V. Gonca, Method of forecasting of mechanical properties and durations of service life of details from rubber, in: *5th Int. DAAAM Balt. Conf. Ind. Eng. Adding Innov. Capacity Labour Force Entrep.*, 2006.
- [97] R.J. Harbour, A. Fatemi, W.V. Mars, Fatigue life analysis and predictions for NR and SBR under variable amplitude and multiaxial loading conditions, *Int. J. Fatigue.* 30 (2008) 1231–1247.
- [98] G. Medri, A. Strozzi, Stress—Strain Fields in Compressed Elastomeric Seals and Their Extension to Fracture Mechanics, *Rubber Chem. Technol.* 59 (1986) 709–721. doi:10.5254/1.3538229.
- [99] E. Verron, J.-B. Le Cam, L. Gornet, A multiaxial criterion for crack nucleation in rubber, *Mech. Res. Commun.* 33 (2006) 493–498. doi:10.1016/j.mechrescom.2005.06.001.
- [100] A. Andriyana, E. Verron, Prediction of fatigue life improvement in natural rubber using configurational stress, *Int. J. Solids Struct.* 44 (2007) 2079–2092. doi:10.1016/j.ijsolstr.2006.06.046.
- [101] J.D. Eshelby, The force on an elastic singularity, *Philos. Trans. R. Soc. Lond. Ser. Math. Phys. Sci.* 244 (1951) 87–112.
- [102] J.D. Eshelby, The elastic energy-momentum tensor, *J. Elast.* 5 (1975) 321–335.
- [103] G.A. Maugin, *Material Inhomogeneities in Elasticity*, CRC Press, 1993.
- [104] P. Steinmann, D. Ackermann, F.J. Barth, Application of material forces to hyperelastostatic fracture mechanics. II. Computational setting, *Int. J. Solids Struct.* 38 (2001) 5509–5526. doi:10.1016/S0020-7683(00)00381-4.
- [105] G.A. Maugin, Material forces: concepts and applications, *Appl. Mech. Rev.* 48 (1995) 213–245.

- [106] E. Verron, Study of the simple extension tear test sample for rubber with Configurational Mechanics, *Int. J. Fract.* 147 (2007) 219–225. doi:10.1007/s10704-007-9165-3.
- [107] M. Ait-Bachir, E. Verron, W.V. Mars, Energy release rate of small cracks under Finite multiaxial straining, in: G. Heinrich, M. Kaliske, A. Lion, S. Reese (Eds.), *Const. Models Rubber VI*, CRC Press, 2009: p. 261.
- [108] C.E. Inglis, Stresses in a plate due to the presence of cracks and sharp corners, *SPIE Milest. Ser. MS.* 137 (1997) 3–17.
- [109] G.R. Irwin, Fracture dynamics, *Fract. Met.* 147 (1948) 166.
- [110] G.R. Irwin, Onset of fast crack propagation in high strength steel and aluminum alloys, *Sagamore Res. Conf. Proc.* 2 (1956) 289–305.
- [111] G.R. Irwin, Analysis of stresses and strains near the end of a crack traversing a plate, *J Appl Mech.* (1957).
- [112] J.R. Rice, A path independent integral and the approximate analysis of strain concentration by notches and cracks, *J. Appl. Mech.* 35 (1968) 379–386.
- [113] J.A.C. Harwood, A.R. Payne, Hysteresis and strength of rubbers, *J. Appl. Polym. Sci.* 12 (1968) 889–901.
- [114] M. Stommel, E. Haberstroh, R. Reter, The Finite Element Analysis-An Efficient Tool for Failure Prediction in Technical Rubber Parts, in: *Tech. Pap. Annu. Tech. Conf.-Soc. Plast. Eng. Inc., SOCIETY OF PLASTICS ENGINEERS INC*, 1997: pp. 3351–3357.
- [115] P.C. Paris, M.P. Gomez, W.E. Anderson, A rational analytic theory of fatigue, (1997).
- [116] L. Neumeister, J.L. Koenig, Crack Analysis of Unfilled Natural Rubber Using Infrared Microspectroscopy, *Rubber Chem. Technol.* 70 (1997) 271–282. doi:10.5254/1.3538432.
- [117] G.R. Hamed, Energy Dissipation and the Fracture of Rubber Vulcanizates, *Rubber Chem. Technol.* 64 (1991) 493–500. doi:10.5254/1.3538566.
- [118] G.R. Hamed, Molecular Aspects of the Fatigue and Fracture of Rubber, *Rubber Chem. Technol.* 67 (1994) 529–536. doi:10.5254/1.3538689.
- [119] A. Radir, A.G. Thomas, Tear Behavior of Rubbers Over a Wide Range of Rates, *Rubber Chem. Technol.* 54 (1981) 15–23. doi:10.5254/1.3535791.
- [120] K.A. Mazich, K.N. Morman, F.G. Oblinger, T.Y. Fan, P.C. Killgoar, The Effect of Specimen Thickness on the Tearing Energy of a Gum Vulcanizate, *Rubber Chem. Technol.* 62 (1989) 850–862. doi:10.5254/1.3536279.
- [121] B.E. Clapson, G.J. Lake, Truck Tire Groove Cracking Theory and Practice, *Rubber Chem. Technol.* 44 (1971) 1186–1202. doi:10.5254/1.3544800.

- [122] G.J. Lake, P.B. Lindley, Mechanical Fatigue Limit for Rubber, *Rubber Chem. Technol.* 39 (1966) 348–364. doi:10.5254/1.3544847.
- [123] W.V. Mars, J. Kingston, A. Muhr, S. Martin, K.W. Wong, Fatigue Life Analysis of an Exhaust Mount, in: P.-E. Austrell, L. Kari (Eds.), *Const. Models Rubber IV Proc. Fourth Eur. Conf. Const. Models Rubber ECCMR 2005 Stockh. Swed. 27-29 June 2005*, CRC Press, 2005: pp. 23–30.
- [124] A. Chudnovsky, A. Moet, Thermodynamics of translational crack layer propagation, *J. Mater. Sci.* 20 (1985) 630–635.
- [125] A. Chudnovsky, A. Moet, A theory for crack layer propagation in polymers, *J. Elastomers Plast.* 18 (1986) 50–55.
- [126] D.S. Dugdale, Yielding of steel sheets containing slits, *J. Mech. Phys. Solids.* 8 (1960) 100–104.
- [127] G.I. BARENBLATT, F.T.D.W.-P.A. OHIO, *The Mathematical Theory of Equilibrium Cracks Formed in Brittle Fracture*, Defense Technical Information Center, 1962.
- [128] C.L. Chow, T.J. Lu, Fatigue crack propagation in metals and polymers with a unified formulation, *Tire Sci. Technol.* 20 (1992) 106–129.
- [129] C.L. Chow, T.J. Lu, On the cyclic J-integral applied to fatigue cracking, *Int. J. Fract.* 40 (1989) R53–R59.
- [130] R.G. Forman, V.E. Kearney, R.M. Engle, Numerical analysis of crack propagation in cyclic-loaded structures, *J. Basic Eng.* 89 (1967) 459–463.
- [131] J. Weertman, Rate of growth of fatigue cracks calculated from the theory of infinitesimal dislocations distributed on a plane, *Int. J. Fract. Mech.* 2 (1966) 460–467.
- [132] G.J. Lake, O.H. Yeoh, Effect of crack tip sharpness on the strength of vulcanized rubbers, *J. Polym. Sci. Part B Polym. Phys.* 25 (1987) 1157–1190.
- [133] E.H. Andrews, Stresses at a Crack in an Elastomer, *Proc. Phys. Soc.* 77 (1961) 483.
- [134] E.H. Andrews, Rupture propagation in hysterical materials: stress at a notch, *J. Mech. Phys. Solids.* 11 (1963) 231–242.
- [135] W.G. Knauss, Stresses near a crack in a rubber sheet, *Exp. Mech.* 8 (1968) 177–181.
- [136] R.F. Lee, J.A. Donovan, J-Integral and Crack Opening Displacement as Crack Initiation Criteria in Rubber, *Rubber Chem. Technol.* 59 (1986) 787–799. doi:10.5254/1.3538234.
- [137] S.-J. Chang, Path-independent integral for rupture of perfectly elastic materials, *Z. Für Angew. Math. Phys. ZAMP.* 23 (1972) 149–152.

- [138] C.M. Roland, Network Recovery from Uniaxial Extension: I. Elastic Equilibrium, *Rubber Chem. Technol.* 62 (1989) 863–879. doi:10.5254/1.3536280.
- [139] I.S. Choi, C.M. Roland, Strain-Crystallization of Guayule and Hevea Rubbers, *Rubber Chem. Technol.* 70 (1997) 202–210. doi:10.5254/1.3538425.
- [140] J.R. Luchini, A mathematical model for hysteresis in filled rubber, Ph.D. Dissertation, University of Michigan, 1977.
- [141] A. Becker, V. Dorsch, M. Kaliske, H. Rothert, A material model for simulating the hysteretic behavior of filled rubber for rolling tires, *Tire Sci. Technol.* 26 (1998) 132–148.
- [142] V.A. Coveney, S. Jamil, D.E. Johnson, M.A. Keavey, C. Menger, H.T. Williams, Implementation in Finite Element Analysis of a Triboelastic Law for Dynamic Behaviour of Filled Elastomers, in: D. Boast, V.A. Coveney (Eds.), *Finite Elem. Anal. Elastomers*, Professional Engineering Pub., United Kingdom, 1999.
- [143] C.M. Roland, Network Recovery from Uniaxial Extension: II. The Origin of the Mullins Effect, *Rubber Chem. Technol.* 62 (1989) 880–895. doi:10.5254/1.3536281.
- [144] A.N. Gent, M. Hindi, Effect of Oxygen on the Tear Strength of Elastomers, *Rubber Chem. Technol.* 63 (1990) 123–134. doi:10.5254/1.3538236.
- [145] E.H. Andrews, A generalized theory of fracture mechanics, *J. Mater. Sci.* 9 (1974) 887–894.
- [146] G.J. Lake, A.G. Thomas, The strength of highly elastic materials, *Proc. R. Soc. Lond. Ser. Math. Phys. Sci.* 300 (1967) 108–119.
- [147] K.A. Mazich, M.A. Samus, C.A. Smith, G. Rossi, Threshold fracture of lightly crosslinked networks, *Macromolecules.* 24 (1991) 2766–2769.
- [148] PR1401-Threshold-test-service-announcement, (n.d.).
- [149] G.J. Lake, O.H. Yeoh, Measurement of Rubber Cutting Resistance in the Absence of Friction, *Rubber Chem. Technol.* 53 (1980) 210–227. doi:10.5254/1.3535030.
- [150] I. Masquelier, Influence de la formulation sur les propriétés en fatigue d'élastomères industriels, phdthesis, Université de Bretagne Occidentale, 2014.
- [151] I.S. Choi, C.M. Roland, Intrinsic Defects and the Failure Properties of cis-1,4-Polyisoprenes, *Rubber Chem. Technol.* 69 (1996) 591–599. doi:10.5254/1.3538386.
- [152] C.M. Roland, C.R. Smith, Defect Accumulation in Rubber, *Rubber Chem. Technol.* 58 (1985) 806–814. doi:10.5254/1.3536094.

- [153] G.R. Hamed, N. Rattanasom, Effect of Crosslink Density on Cut Growth in Black-Filled Natural Rubber Vulcanizates, *Rubber Chem. Technol.* 75 (2002) 935–942. doi:10.5254/1.3547693.
- [154] E.S. Dizon, A.E. Hicks, V.E. Chirico, The Effect of Carbon Black Parameters on the Fatigue Life of Filled Rubber Compounds, *Rubber Chem. Technol.* 47 (1974) 231–249. doi:10.5254/1.3540429.
- [155] G.S. Fielding-Russell, R.L. Rongone, Fatiguing of Rubber-Rubber Interfaces, *Rubber Chem. Technol.* 56 (1983) 838–844. doi:10.5254/1.3538158.
- [156] J.-B. Le Cam, B. Huneau, E. Verron, L. Gornet, Mechanism of Fatigue Crack Growth in Carbon Black Filled Natural Rubber, *Macromolecules.* 37 (2004) 5011–5017. doi:10.1021/ma0495386.
- [157] M. Braden, A.N. Gent, The attack of ozone on stretched rubber vulcanizates. II. Conditions for cut growth, *J. Appl. Polym. Sci.* 3 (1960) 100–106.
- [158] G.J. Lake, Corrosive Aspects of Fatigue, *Rubber Age.* 104 (1972) 39.
- [159] G. Kraus, Reinforcement of Elastomers by Particulate Fillers, in: F.R. Eirich (Ed.), *Sci. Technol. Rubber*, Elsevier, 1978: pp. 291–338.
- [160] M. Morton, Polymerization, in: F.R. Eirich (Ed.), *Sci. Technol. Rubber*, Elsevier, 1978: pp. 291–338.
- [161] H. Chun, A.N. Gent, Strength of Sulfur-Linked Elastomers, *Rubber Chem. Technol.* 69 (1996) 577–590. doi:10.5254/1.3538385.
- [162] G.J. Lake, Aspects of fatigue and fracture of rubber, *Prog. Rubber Technol.* 45 (1983) 89–143.
- [163] Y. Fukahori, Estimation of fatigue life in elastomers. Theoretical analysis and applications of S–N curves with fracture mechanics, *Int. Polym. Sci. Technol.* 12 (1985).
- [164] D.G. Young, Dynamic Property and Fatigue Crack Propagation Research on Tire Sidewall and Model Compounds, *Rubber Chem. Technol.* 58 (1985) 785–805. doi:10.5254/1.3536093.
- [165] G.J. Lake, P.B. Lindley, Fatigue of rubber at low strains, *J. Appl. Polym. Sci.* 10 (1966) 343–351. doi:10.1002/app.1966.070100214.
- [166] J. De Eskinazi, K. Ishihara, H. Volk, T.C. Warholic, Towards predicting relative belt edge endurance with the finite element method, *Tire Sci. Technol.* 18 (1990) 216–235.
- [167] H.L. Oh, A Fatigue-Life Model of a Rubber Bushing, *Rubber Chem. Technol.* 53 (1980) 1226–1238. doi:10.5254/1.3535090.
- [168] S. Yamashita, Selecting damping materials (service environment, strain and endurance), *Int. Polym. Sci. Technol.* 19 (1992).

- [169] W.V. Mars, A. Fatemi, A novel specimen for investigating the mechanical behavior of elastomers under multiaxial loading conditions, *Exp. Mech.* 44 (2004) 136–146. doi:10.1007/BF02428173.
- [170] R.J. Harbour, A. Fatemi, W.V. Mars, Fatigue crack orientation in NR and SBR under variable amplitude and multiaxial loading conditions, *J. Mater. Sci.* 43 (2008) 1783–1794.
- [171] M. Kaliske, B. Näser, C. Meiners, Inelastic Fracture Mechanics for Tire Durability Simulations 4, *Tire Sci. Technol.* 35 (2007) 239–250.
- [172] M. Aït-Bachir, W.V. Mars, E. Verron, Energy release rate of small cracks in hyperelastic materials, *Int. J. Non-Linear Mech.* 47 (2012) 22–29. doi:10.1016/j.ijnonlinmec.2012.03.001.
- [173] T. Zarrin-Ghalami, A. Fatemi, Multiaxial fatigue and life prediction of elastomeric components, *Int. J. Fatigue.* 55 (2013) 92–101. doi:10.1016/j.ijfatigue.2013.05.009.
- [174] G. Ayoub, M. Naït-Abdelaziz, F. Zaïri, J.M. Gloaguen, P. Charrier, A continuum damage model for the high-cycle fatigue life prediction of styrene-butadiene rubber under multiaxial loading, *Int. J. Solids Struct.* 48 (2011) 2458–2466. doi:10.1016/j.ijsolstr.2011.04.003.
- [175] Y. Wang, W. Yu, X. Chen, L. Yan, Fatigue life prediction of vulcanized natural rubber under proportional and non-proportional loading, *Fatigue Fract. Eng. Mater. Struct.* 31 (2008) 38–48. doi:10.1111/j.1460-2695.2007.01199.x.
- [176] J.L. Poisson, S. Méo, F. Lacroix, G. Berton, N. Ranganathan, Multiaxial fatigue criteria applied to a polychloroprene rubber, *Rubber Chem. Technol.* 85 (2012) 80–91. doi:10.5254/1.3672431.
- [177] Y.S. Huang, O.H. Yeoh, Crack Initiation and Propagation in Model Cord-Rubber Composites, *Rubber Chem. Technol.* 62 (1989) 709–731. doi:10.5254/1.3536270.
- [178] I.S. Choi, C.M. Roland, L.C. Bissonnette, An Elastomeric Ejection System, *Rubber Chem. Technol.* 67 (1994) 892–903. doi:10.5254/1.3538720.
- [179] A. Stevenson, K.A. Malek, On the Puncture Mechanics of Rubber, *Rubber Chem. Technol.* 67 (1994) 743–760. doi:10.5254/1.3538707.
- [180] Timbrell, M. Wiehahn, A. Muhr, Simulation Of Crack Propagation In Rubber, in: J. Busfield, A. Muhr (Eds.), *Const. Models Rubber III Proc. Third Eur. Conf. Const. Models Rubber Lond. UK 15-17 Sept. 2003*, CRC Press, 2003: pp. 15–17.
- [181] W.V. Mars, Method and article of manufacture for estimating material failure due to crack formation and growth, US 2002/0139194 A1, n.d.
- [182] W.V. Mars, Heuristic approach for approximating energy release rates of small cracks under finite strain, multiaxial loading, in: V. Coveney (Ed.),

Elastomers Compon. Serv. Life Predict. - Prog. Chall., Woodhead Publishing, 2005: pp. 89–109.

- [183] W.V. Mars, A. Fatemi, Multiaxial fatigue of rubber: Part II: experimental observations and life predictions, *Fatigue Fract. Eng. Mater. Struct.* 28 (2005) 523–538.
- [184] W.V. Mars, A. Fatemi, Multiaxial fatigue of rubber: Part I: equivalence criteria and theoretical aspects, *Fatigue Fract. Eng. Mater. Struct.* 28 (2005) 515–522.
- [185] W.V. Mars, A. Fatemi, Nucleation and growth of small fatigue cracks in filled natural rubber under multiaxial loading, *J. Mater. Sci.* 41 (2006) 7324–7332. doi:10.1007/s10853-006-0962-2.
- [186] P.B. Lindley, Relation between hysteresis and the dynamic crack growth resistance of natural rubber, *Int. J. Fract.* 9 (1973) 449–462.
- [187] J.J. Busfield, C.H.H. Ratsimba, A.G. Thomas, Crack growth and predicting failure under complex loading in filled elastomers, in: D. Boast, V.A. Coveney (Eds.), *Finite Elem. Anal. Elastomers*, Professional Engineering Pub., United Kingdom, 1999: pp. 235–250.
- [188] H.J. Kim, G.R. Hamed, On the Reason that Passenger Tire Sidewalls are Based on Blends of Natural Rubber and cis-Polybutadiene, *Rubber Chem. Technol.* 73 (2000) 743–752. doi:10.5254/1.3547618.
- [189] C.M. Roland, J.W. Sobieski, Anomalous Fatigue Behavior in Polyisoprene, *Rubber Chem. Technol.* 62 (1989) 683–697. doi:10.5254/1.3536268.
- [190] R.J. Harbour, A. Fatemi, W.V. Mars, The Effect of a Dwell Period on Fatigue Crack Growth Rates in Filled SBR and NR, *Rubber Chem. Technol.* 80 (2007) 838–853. doi:10.5254/1.3539420.
- [191] A. Stevenson, J.R. Hawkes, J.A. Harris, P. Hansen, *Fatigue Life of Elastomeric Engineering Components Under Biaxial Loading Using Finite Element Analysis*, SAE Technical Paper, 1998.
- [192] A. Stevenson, Fatigue Crack Growth in High Load Capacity Rubber Laminates, *Rubber Chem. Technol.* 59 (1986) 208–222. doi:10.5254/1.3538194.
- [193] W.V. Mars, A. Fatemi, The Correlation of Fatigue Crack Growth Rates in Rubber Subjected to Multiaxial Loading Using Continuum Mechanical Parameters, *Rubber Chem. Technol.* 80 (2007) 169–182. doi:10.5254/1.3548164.
- [194] G. Andreini, P. Straffi, S. Cotugno, G. Gallone, G. Polacco, Compariso of Sine versus Pulse Waveform Effects on Fatigue Crack Growth Behavior of NR, SBR and BR Compounds, *Rubber Chem. Technol.* 83 (2010) 391–403. doi:10.5254/1.3512954.

- [195] C. Sun, A. Gent, P. Marteny, Effect of fatigue step loading sequence on residual strength, *Tire Sci. Technol.* 28 (2000) 196–208.
- [196] W.V. Mars, Identifying the damaging events in a multiaxial duty cycle, in: G. Heinrich, M. Kaliske, A. Lion, S. Reese (Eds.), *Const. Models Rubber VI*, CRC Press, 2009: p. 261.
- [197] M. Flamm, T. Steinweger, U. Weltin, Lifetime prediction of multiaxially loaded rubber springs and bushings, in: J. Busfield, A. Muhr (Eds.), *Const. Models Rubber III Proc. Third Eur. Conf. Const. Models Rubber Lond. UK* 15-17 Sept. 2003, CRC Press, 2003: pp. 49–53.
- [198] M. Braden, A.N. Gent, The attack of ozone on stretched rubber vulcanizates. I. The rate of cut growth, *J. Appl. Polym. Sci.* 3 (1960) 90–99.
- [199] G.J. Lake, P.B. Lindley, Ozone cracking, flex cracking and fatigue of rubber, Part I, *Rubber J.* 146 (1964) 24–28.
- [200] G.J. Lake, P.B. Lindley, Ozone cracking, flex cracking and fatigue of rubber, Part II, *Rubber J.* 146 (1964) 30–39.
- [201] G.J. Lake, P.B. Lindley, Role of Ozone in Dynamic Cut Growth of Rubber, *Rubber Chem. Technol.* 39 (1966) 1053–1064. doi:10.5254/1.3547116.
- [202] A.N. Gent, H. Hirakawa, Effect of temperature on the ozone cracking of butyl rubbers, *J. Polym. Sci. Part -2 Polym. Phys.* 5 (1967) 157–164.
- [203] W.V. Mars, Fatigue Life Prediction for Elastomeric Structures, *Rubber Chem. Technol.* 80 (2007) 481–503. doi:10.5254/1.3548175.
- [204] A.N. Gent, J.E. McGrath, Effect of temperature on ozone cracking of rubbers, *J. Polym. Sci. A.* 3 (1965) 1473–1482. doi:10.1002/pol.1965.100030416.
- [205] M.L. Studebaker, J.R. Beatty, The Oxidative Hardening of SBR, *Rubber Chem. Technol.* 45 (1972) 450–466. doi:10.5254/1.3544722.
- [206] S.G. Kim, S.-H. Lee, Effect of Crosslink Structures on the Fatigue Crack Growth Behavior of NR Vulcanizates with Various Aging Conditions, *Rubber Chem. Technol.* 67 (1994) 649–661. doi:10.5254/1.3538700.
- [207] G.R. Hamed, Materials and Compounding, in: *Eng. Rubber Des. Rubber Compon.*, Gent A., Carl Hanser Verlag, Munich, 1992: p. Chapter 6.
- [208] A.I. Medalia, Effect of Carbon Black on Ultimate Properties of Rubber Vulcanizates, *Rubber Chem. Technol.* 60 (1987) 45–61. doi:10.5254/1.3536121.
- [209] J. Zhao, G. Ghebremeskel, Reviewing fracture and fatigue factors, *Rubber Plast. News.* (2000) 14–21.

- [210] E.E. Auer, K.W. Doak, I.J. Schaffner, Factors Affecting Laboratory Cut-Growth Resistance of Cold SBR Tread Stocks, *Rubber Chem. Technol.* 31 (1958) 185–201. doi:10.5254/1.3542257.
- [211] A.Y. Coran, Vulcanization, in: F.R. Eirich (Ed.), *Sci. Technol. Rubber*, Elsevier, 1978: pp. 291–338.
- [212] J.J. Busfield, A.G. Thomas, M.F. Ngah, Application of fracture mechanics for the fatigue life prediction of carbon black filled elastomers, in: A. Dorfmann, A. Muhr (Eds.), *Const. Models Rubber*, CRC Press, 1999: pp. 249–256.
- [213] H.-H. Kausch, J.A. Hassell, R.I. Jaffee, eds., *Deformation and fracture of high polymers*, 1973.
- [214] A.N. Gent, M. Hindi, Heat Build-Up and Blowout of Rubber Blocks, *Rubber Chem. Technol.* 61 (1988) 892–905. doi:10.5254/1.3536225.
- [215] A.N. Gent, K.W. Scott, Dynamic Mechanical Properties, in: *Eng. Rubber Des. Rubber Compon.*, Gent A., Carl Hanser Verlag, Munich, 1992: p. Chapter 6.
- [216] Image J Introduction, ImageJ. (n.d.).
- [217] ENDURICA user's manual, (n.d.).
- [218] W.V. Mars, A. Fatemi, A Phenomenological Model for the Effect of R Ratio on Fatigue of Strain Crystallizing Rubbers, *Rubber Chem. Technol.* 76 (2003) 1241–1258. doi:10.5254/1.3547800.
- [219] E. Ostoja-Kuczynski, P. Charrier, E. Verron, L. Gornet, G. Marckmann, Influence of Mean Stress and Mean Strain on Fatigue Life of Carbon Black Filled Natural Rubber, in: P.-E. Austrell, L. Kari (Eds.), *Const. Models Rubber IV Proc. Fourth Eur. Conf. Const. Models Rubber ECCMR 2005 Stockh. Swed. 27-29 June 2005*, CRC Press, 2005: pp. 15–21.
- [220] K.L.G. Jago, X-RAY COMPUTED MICROTOMOGRAPHY OF RUBBER, *Rubber Chem. Technol.* 85 (2012) 387–407. doi:10.5254/rct.12.87985.
- [221] T. Zarrin Ghalami, *Fatigue life prediction and modeling of elastomeric components*, University of Toledo, 2013.
- [222] V. Le Saux, Y. Marco, S. Calloch, P. Charrier, Evaluation of the fatigue defect population in an elastomer using X-ray computed micro-tomography, *Polym. Eng. Sci.* 51 (2011) 1253–1263. doi:10.1002/pen.21872.
- [223] F.E. Ngolemasango, G.E. Nkeng, C. O'Connor, J. Manley, M. Bennett, J. Clarke, Effect of nature and type of flaw on the properties of a natural rubber compound, *Polym. Test.* 28 (2009) 463–469. doi:10.1016/j.polymertesting.2009.02.007.
- [224] M. Naït-Abdelaziz, F. Zaïri, Z. Qu, A. Hamdi, N. Aït Hocine, J integral as a fracture criterion of rubber-like materials using the intrinsic defect concept, *Mech. Mater.* 53 (2012) 80–90. doi:10.1016/j.mechmat.2012.05.001.

- [225] L. Mullins, N.R. Tobin, Theoretical Model for the Elastic Behavior of Filler-Reinforced Vulcanized Rubbers, *Rubber Chem. Technol.* 30 (1957) 555–571. doi:10.5254/1.3542705.
- [226] W.V. Mars, Analysis of stiffness variations in context of strain-, stress-, and energy-controlled processes, *Rubber Chem. Technol.* 84 (2011) 178–186. doi:10.5254/1.3570530.
- [227] M.C. Boyce, O. Yeh, S. Socrate, K. Kear, K. Shaw, Micromechanics of cyclic softening in thermoplastic vulcanizates, *J. Mech. Phys. Solids.* 49 (2001) 1343–1360. doi:10.1016/S0022-5096(00)00077-6.
- [228] G. Marckmann, E. Verron, L. Gornet, G. Chagnon, P. Charrier, P. Fort, A theory of network alteration for the Mullins effect, *J. Mech. Phys. Solids.* 50 (2002) 2011–2028. doi:10.1016/S0022-5096(01)00136-3.
- [229] S. Cantournet, R. Desmorat, J. Besson, Mullins effect and cyclic stress softening of filled elastomers by internal sliding and friction thermodynamics model, *Int. J. Solids Struct.* 46 (2009) 2255–2264. doi:10.1016/j.ijsolstr.2008.12.025.
- [230] H. Lorenz, M. Freund, D. Juhre, J. Ihlemann, M. Klüppel, Constitutive Generalization of a Microstructure-Based Model for Filled Elastomers, *Macromol. Theory Simul.* 20 (2011) 110–123. doi:10.1002/mats.201000054.
- [231] S.R. Rickaby, N.H. Scott, A cyclic stress softening model for the Mullins effect, *Int. J. Solids Struct.* 50 (2013) 111–120. doi:10.1016/j.ijsolstr.2012.09.006.
- [232] W.V. Mars, I. Mikel, A. Aitor, Loss of Stiffness During Fatigue and the Development of Crack Precursors, in: *Const. Models Rubber VIII*, CRC Press, London, 2013: pp. 355–360.
- [233] C.J. Derham, A.G. Thomas, Creep of Rubber under Repeated Stressing, *Rubber Chem. Technol.* 50 (1977) 397–402. doi:10.5254/1.3535153.
- [234] G.B. McKenna, L.J. Zapas, Response of Carbon Black Filled Butyl Rubber to Cyclic Loading, *Rubber Chem. Technol.* 54 (1981) 718–733. doi:10.5254/1.3535830.
- [235] M. Brieu, J. Diani, C. Mignot, C. Moriceau, Response of a carbon-black filled SBR under large strain cyclic uniaxial tension, *Int. J. Fatigue.* 32 (2010) 1921–1927. doi:10.1016/j.ijfatigue.2010.06.002.
- [236] J. Diani, Y. Merckel, M. Brieu, Modelling Mullins and cyclic stress-softening in filled rubbers, *Const. Models Rubber VII.* 229 (2011).
- [237] J. Gough, A.H. Muhr, Energy release rates for small cracks in rubber components, in: *Const. MODELS RUBBER IV*, Balkema, 2005: p. 51.

Appendix I

1. Characterization Tests Work Procedure

Table 1.1. Abbreviations of test types

Abbreviation	Test Type
FCN_EC	Fatigue Crack Nucleation - Strain Control
FCN_SC	Fatigue Crack Nucleation - Stress Control
CTET	Critical tearing Energy Test
FCG_2 H	Fatigue Crack Growth Pre-Test - 2 Hour
FCG_24 H	Fatigue Crack Growth - 24 Hour
FCG_NR	Fatigue Crack Growth - Non Relaxing
Hyper - ST	Hyperelastic - Simple Tension
Hyper - PT	Hyperelastic - Planar Tension
Hyper - SC	Hyperelastic - Simple Compression

Table 1.2. The waybill for planning the characterization tests

# Order	Name	Description	Specimen	Input	From Test	Output
1.1	MSB	Monotonic Strain to Break	S.T.			ϵ_{break}
1.2	FCN_EC	Fatigue Crack Nucleation - Strain Control	S.T.	ϵ_{break}	1.1 MSB	<i>N Life 100%</i>
				α	2.3 FCG	<i>N Life 150%</i>
				β	2.3 FCG	
1.3	FCN_SC	<i>Fatigue Crack Nucleation - Stress Control</i>	S.T.			
2.1	CTE	Critical tearing Energy	P.T. Notched			T_c
2.2	FCG_2 H	Fatigue Crack Growth - 2 Hour	P.T. Notched			
2.3	FCG_24 H	Fatigue Crack Growth - 20 Hour	P.T. Notched	T_c	2.1 CTE	r_c
				T_0		F
						$B(b); A; T_c$
2.4	FCG_NR	Fatigue Crack Growth - Non Relaxing	P.T Notched			
3.1	Hyper - ST	Hyperelastic - Simple Tension	S.T.			
3.2	Hyper - PT	Hyperelastic - Planar Tension	P.T.			
3.3	Hyper - SC	Hyperelastic - Simple Compression	S.C.			

Table 1.3. List of characterization tests and schedule time for one material

Material	Test #	Test Name	Test Condition	Cycles	Freq. / Rate	Replicates	Images	Pre-Test	TEST	ANALYSIS	Total (Hours)
Mat. 1	1.1.1	FCN_EC	100%	100000	2	01/05	50	3	13.89	1	87.44
	1.1.2				2	02/05	50	0.5	13.89	1	
	1.1.3				2	03/05	50	0.5	13.89	1	
	1.1.4				2	04/05	50	0.5	13.89	1	
	1.1.5				2	05/05	50	0.5	13.89	1	
	1.2.1	FCN_EC	200%	10000	2	01/05	50	3	1.39	1	24.94
	1.2.2				2	02/05	50	0.5	1.39	1	
	1.2.3				2	03/05	50	0.5	1.39	1	
	1.2.4				2	04/05	50	0.5	1.39	1	
	1.2.5				2	05/05	50	0.5	1.39	1	
	1.3.1	FCN_SC	Eq. Force 100%	100000	2	01/05	50	3	13.89	1	119.44
	1.3.2				2	02/05	50	0.5	13.89	1	
	1.3.3				2	03/05	50	0.5	13.89	1	
	1.3.4				2	04/05	50	0.5	13.89	1	
	1.3.5				2	05/05	50	0.5	13.89	1	
	1.4.1	FCN_SC	Eq. Force 200%	10000	2	01/05	50	3	1.39	1	56.94
	1.4.2				2	02/05	50	0.5	1.39	1	
	1.4.3				2	03/05	50	0.5	1.39	1	
	1.4.4				2	04/05	50	0.5	1.39	1	
	1.4.5				2	05/05	50	0.5	1.39	1	
	1.5.1	CTET	Tensile to Break	1	1%/sec	01/03	0	3	2	2	22
	1.5.2				1%/sec	02/03	0	0.5	2	1	
	1.5.3				1%/sec	03/03	0	0.5	2	1	
	1.6.1	FCG - 2 H	Cycling to Break	36000	5	01/03	50	3	2	5	58
	1.6.2				5	02/03	50	1	2	5	
	1.6.3				5	03/03	50	1	2	5	
	1.7.1	FCG - 24 H	Cycling to Break	432000	5	01/03	100	3	24	6	175
	1.7.2				5	02/03	100	1	24	6	
	1.7.3				5	03/03	100	1	24	6	
	1.8.1	FCG - NR	Cycling to Break	432000	5	01/03	100	3	24	10	267
1.8.2	5				02/03	100	1	24	10		
1.8.3	5				03/03	100	1	24	10		
1.9.1	Hyper - ST	0.10, 0.20, 0.50, 1.0, 1.5, 2.0, 3, 4	5	1%/sec	01/03	0	3	3.50	4	75.5	
1.9.2				1%/sec	02/03	0	1	3.50	4		
1.9.3				1%/sec	03/03	0	1	3.50	4		
1.10.1	Hyper - PT	0.10, 0.20, 0.50, 1.0, 1.5, 2.0, 3, 5	5	1%/sec	01/03	0	3	3.50	4	59.5	
1.10.2				1%/sec	02/03	0	1	3.50	4		
1.10.3				1%/sec	03/03	0	1	3.50	4		
1.11.1	Hyper - SC	0.10, 0.20, 0.50, 1.0, 1.5, 2.0, 3, 6	5	1%/sec	01/03	0	3	3.50	4	59.5	
1.11.2				1%/sec	02/03	0	1	3.50	4		
1.11.3				1%/sec	03/03	0	1	3.50	4		

2. Material Fatigue Behaviour Characterization

2.1. Critical Tearing Energy

Purpose: The strength of the material represents an upper limit that is used in planning subsequent fatigue tests. It also provides the Critical Tearing Energy, which is useful as a parameter in defining the fatigue crack growth law.

Specimen: Planar Tension with initial cut. 288 mm x 34.01 mm x 1.99 mm.

Initial Cut: 50 mm, inserted via razor blade.

Strain Rate: 1% / sec.

Ambient temperature: 23°C

Table 2.1. Strength parameters derived from edge cracked planar tension tests

Material	Engineering Stress at break, MPa	Engineering Strain at break	Strain Energy Density at break, mJ / mm ³	Critical Tearing Energy, kJ/m ²
MSB	2.105	1.274	1.596	54.30
MCN	1.634	0.641	0.6120	21.05

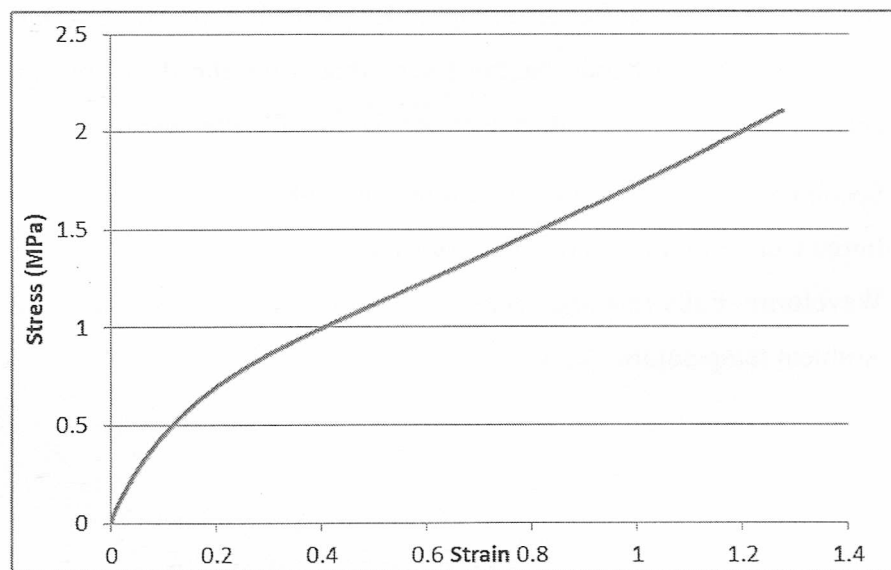


Figure 2.1. Comparison of strain to break experiments on edge pre-cracked planar tension specimen. Data for MSB. Specimen P3 was selected by Leartriker

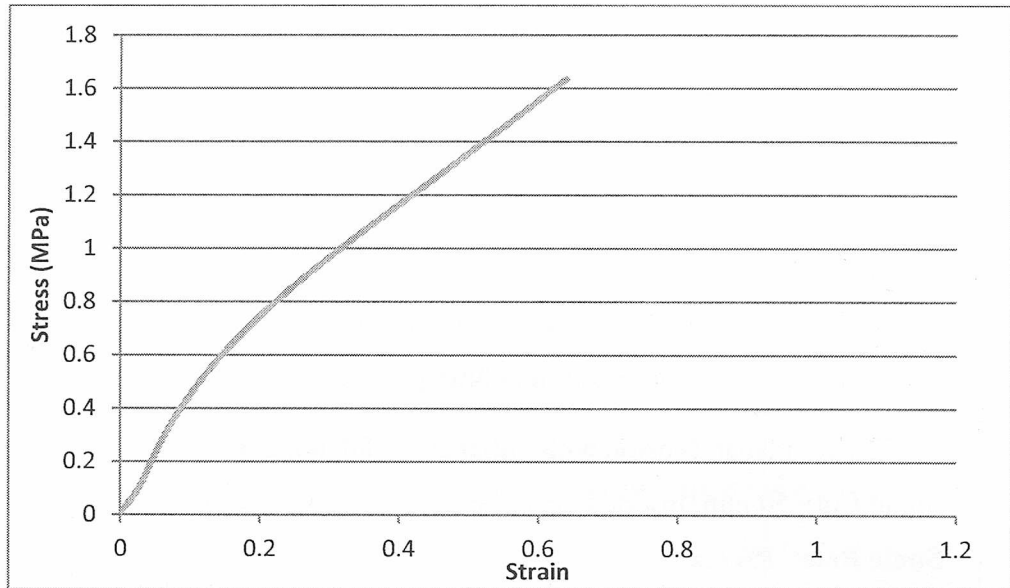


Figure 2.2. Comparison of strain to break experiments on edge pre-cracked planar tension specimen. Data for MCN. Specimen P2 was selected by Leartriker.

2.2. Fatigue Crack Growth

Purpose: The rate of growth of a crack indicates how quickly damage will accumulate in a material operating under particular conditions. Once we know how the growth rate depends on the forces that drive the development of microscopic crack precursors, we can then estimate fatigue life over a wide range of conditions.

Specimen: Planar Tension with initial cut. 288 mm x 34 mm x 1.98 mm.

Initial Cut: 50 mm, inserted via razor blade.

Waveform: Fully relaxing (minimum strain is held at zero), sine waveform

Ambient temperature: 23°C

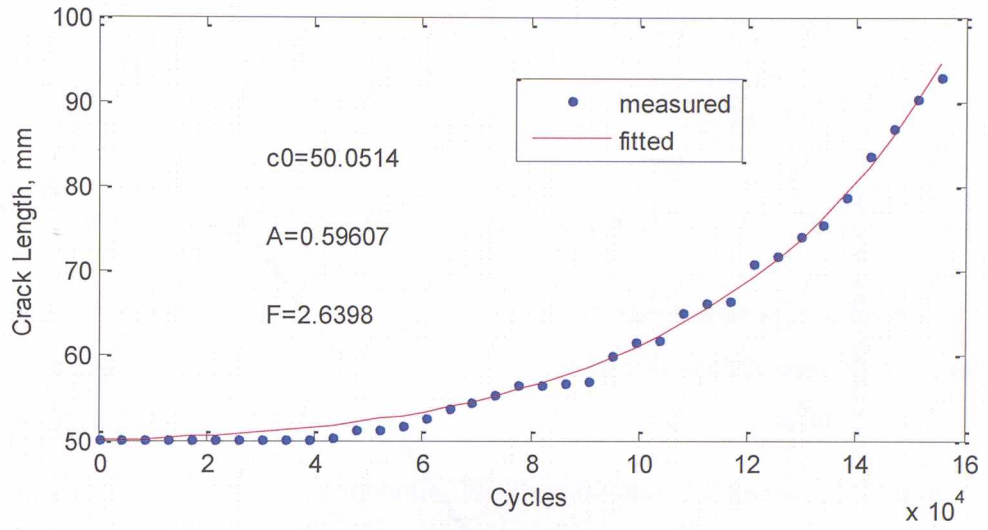


Figure 2.3. Crack length evolution during test for material MSB.

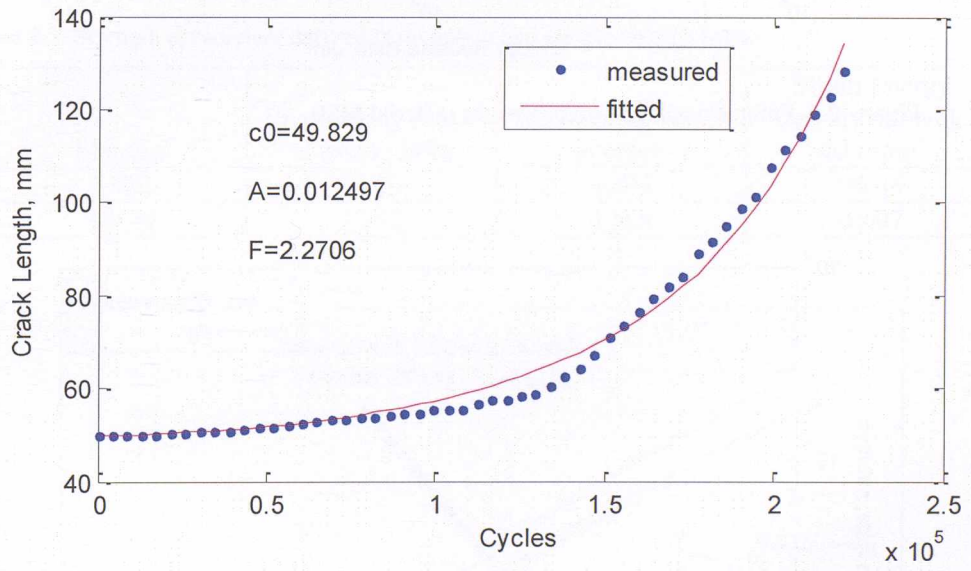


Figure 2.4. Crack length evolution during test for material MCN.

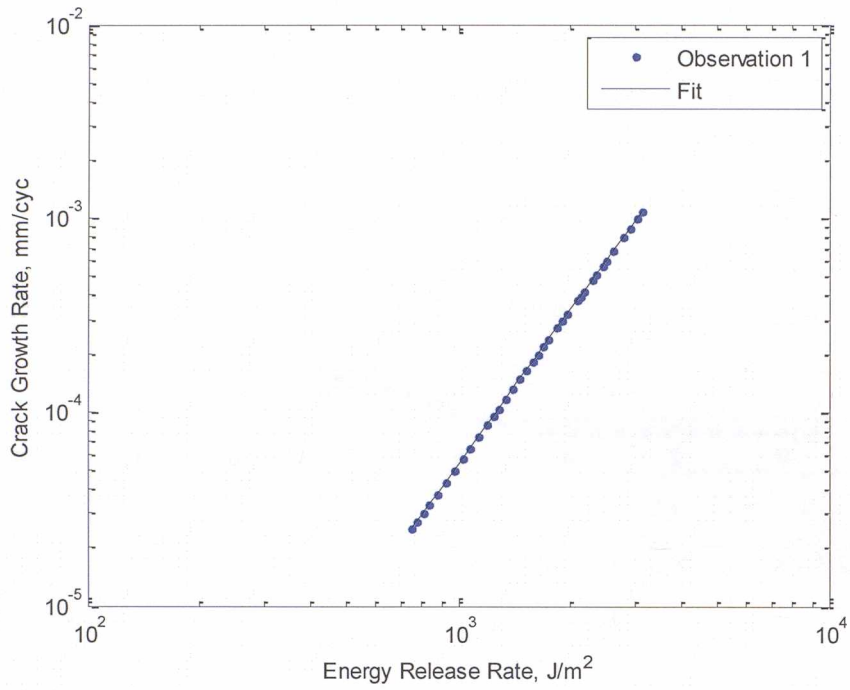


Figure 2.5. Fatigue crack growth curves for material MSB.

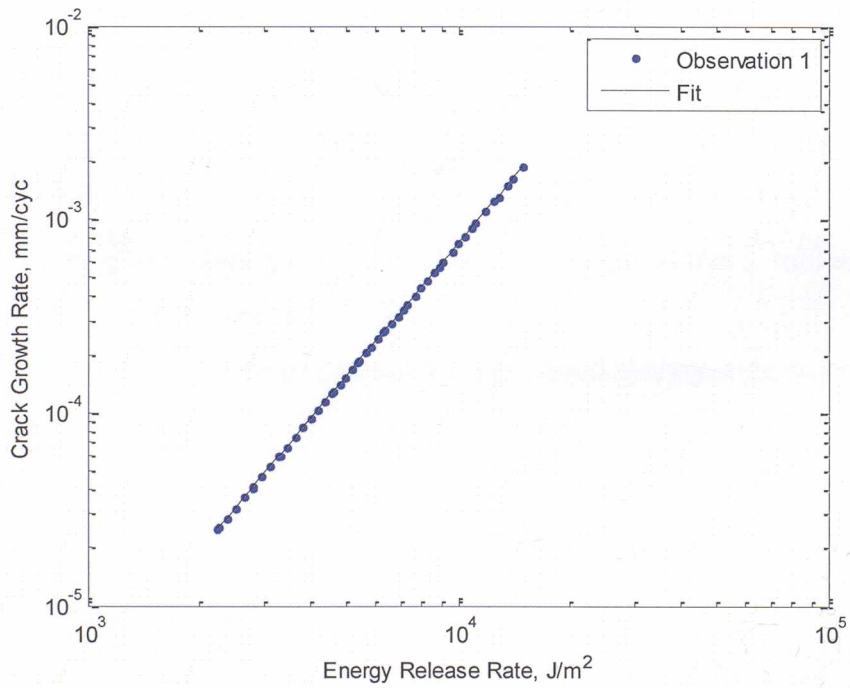


Figure 2.6. Fatigue crack growth curves for material MCN.

Table 2.2. Power law fatigue crack growth parameters (mm/cyc vs. J/m²).

Material	MSB	MCN
F	2.6398	2.2706
B	6.5010e-13	6.2524e-13

2.3. Monotonic simple tension, strain to break

Purpose: The strain at break in simple tension provides a starting point for planning crack nucleation experiments in simple tension, and it is widely used as a parameter for specifying rubber compounds.

Specimen: Simple Tension dumbbell. Width=6.01 mm, thickness = 1.98 mm.

Strain Rate: 1% / sec.

Ambient temperature: 23°C

Table 2.3. Strength parameters derived from unnotched simple tension tests.

Material	Engineering Stress at break, MPa	Engineering Strain at break	Strain Energy Density at break, mJ / mm ³
MSB	16.29	4.603	36.35
MCN	22.72	4.504	45.97

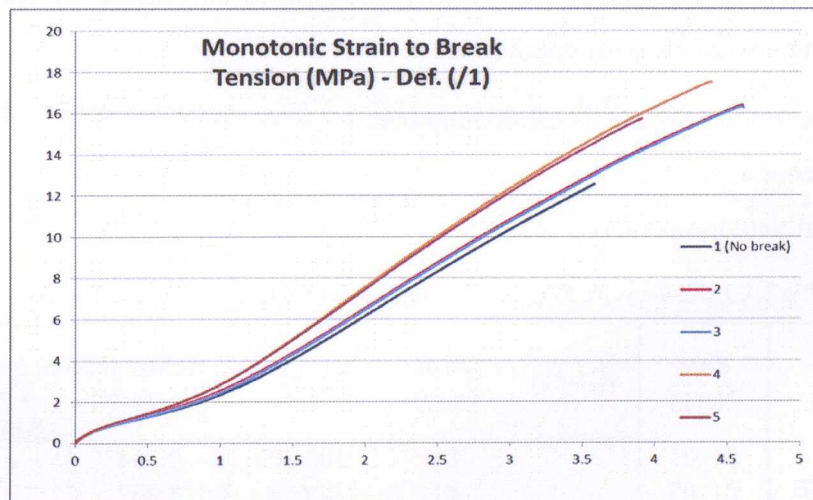


Figure 2.7. Simple tension stress-strain curves to break for material MSB. Replicate 3 chosen for analysis.

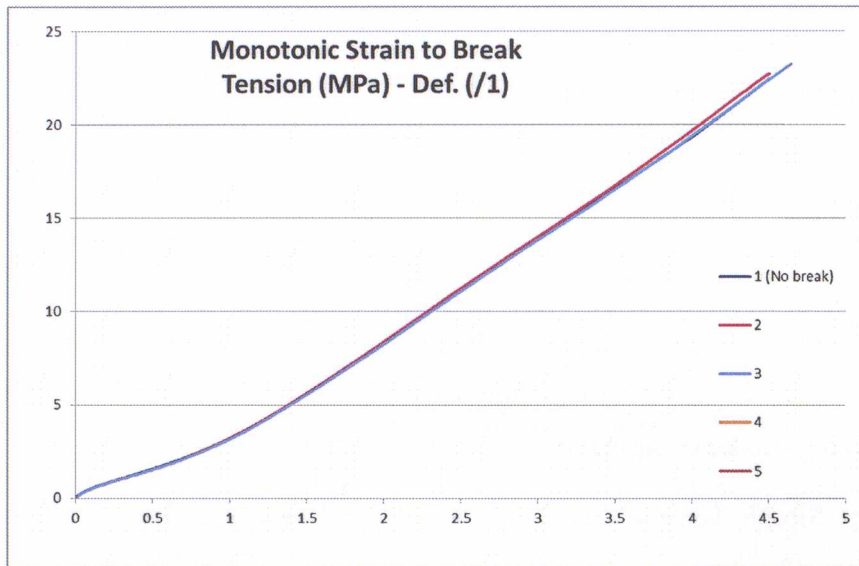


Figure 2.8. Simple tension stress-strain curves to break for material MCN. Replicate 2 chosen for analysis.

2.4. Fatigue Crack Nucleation

Purpose: This experiment provides the information needed for determining the effective intrinsic flaw size of the compound. When combined with the fatigue crack growth curve measured previously, it enables calculation of crack nucleation life over a wide range of conditions.

Specimen: Simple Tension dumbbell.

Frequency: 1 Hz.

Ambient temperature: 23 °C

Table 2.4. Fatigue cycles to failure in simple tension No pre-cut. Data for MSB

Strain Control	Test Name	EC (%)	Displ. (mm)	Life	Force at (Nf/2) (N)	Force (Average)	Life (Average)
	81_01	150		81	103225	3.264	3.41
81_02	81			40054	3.267		
81_03	81			149994	3.238		
81_04	81			18205	3.890		
81_05	81			97334	3.361		
100_01	180		100	1544	4.421	4.44	9524
100_02			100	37018	4.097		
100_03			100	4035	4.327		
100_04			100	1814	4.644		
100_05			100	3209	4.688		

Table 2.5 Fatigue cycles to failure in simple tension No pre-cut. Data for MCN.

Strain Control	Test Name	EC (%)	Displ. (mm)	Life	Force at (Nf/2) (N)	Force (Average)	Life (Average)
	81_01	150		81	18605	2.39	2.43
81_02	81			16495	2.41		
81_03	81			20095	2.46		
81_04	81			17239	2.47		
100_01	180		100	11734	2.71	2.68	11165
100_02			100	10265	2.69		
100_03			100	12795	2.64		
100_04			100	9789	2.70		
100_05			100	11244	2.69		

2.5. Crack Growth Law Parameters Analysis

Purpose: Fatigue crack growth generally follows a power-law function. Determining the parameters of this function enables calculation of strain-life curves over a range of conditions.

Table 2.6. Fatigue crack growth law parameters.

Material	MSB	MCN
T_c , kJ/m ²	54.302	21.0526
r_c , mm / cyc	2.0509	0.0041
F	2.6398	2.2706

2.6. Flaw size estimate and Computed strain-life curves

Purpose: By comparing observations of crack nucleation life with a family of computed strain-life curves, the intrinsic flaw size of the material can be determined. The natural variability inherent in fatigue crack nucleation measurements can then be rationalized in terms of the associated variations in flaw size.

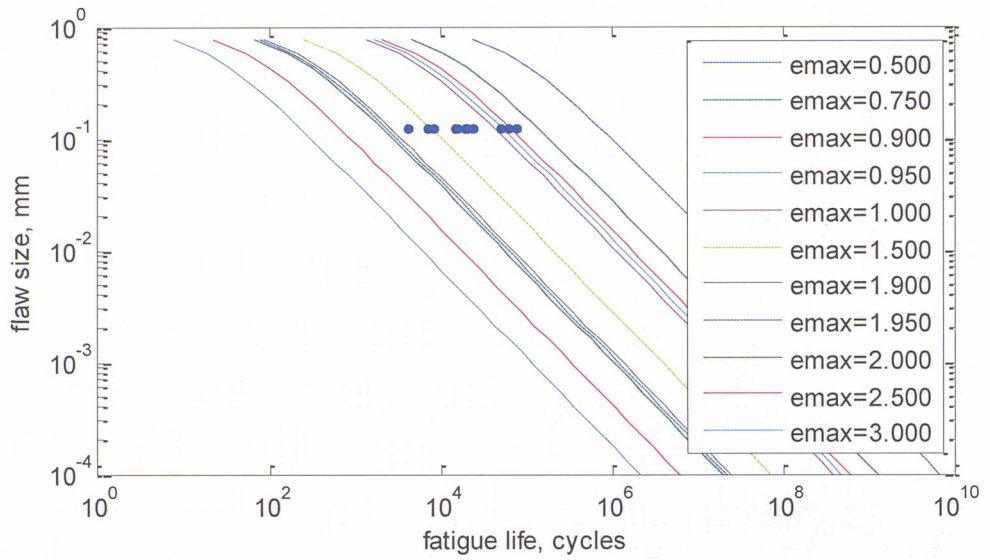


Figure 2.9. Computed dependence of life on flaw size, for various strain levels (ranging from 50% to 300% peak strain). Observations are plotted at actual life, and assumed flaw size of 0.009 mm. Data for MSB.

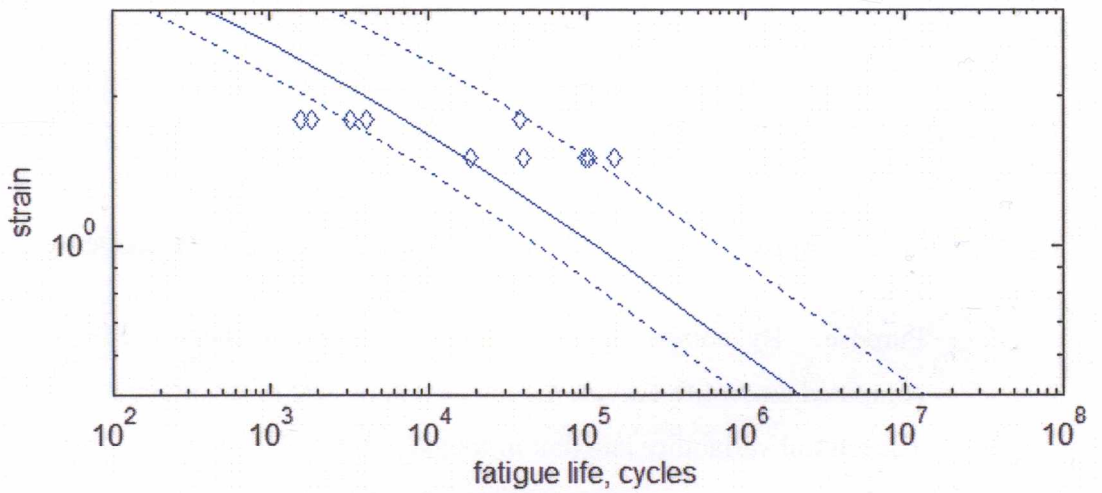


Figure 2.10. Comparison of observed fatigue life with Endurica-computed strain-life curves (solid curve is for flaw size of 0.009 mm, dashed curves are for ± 0.006 mm). Data for MSB.

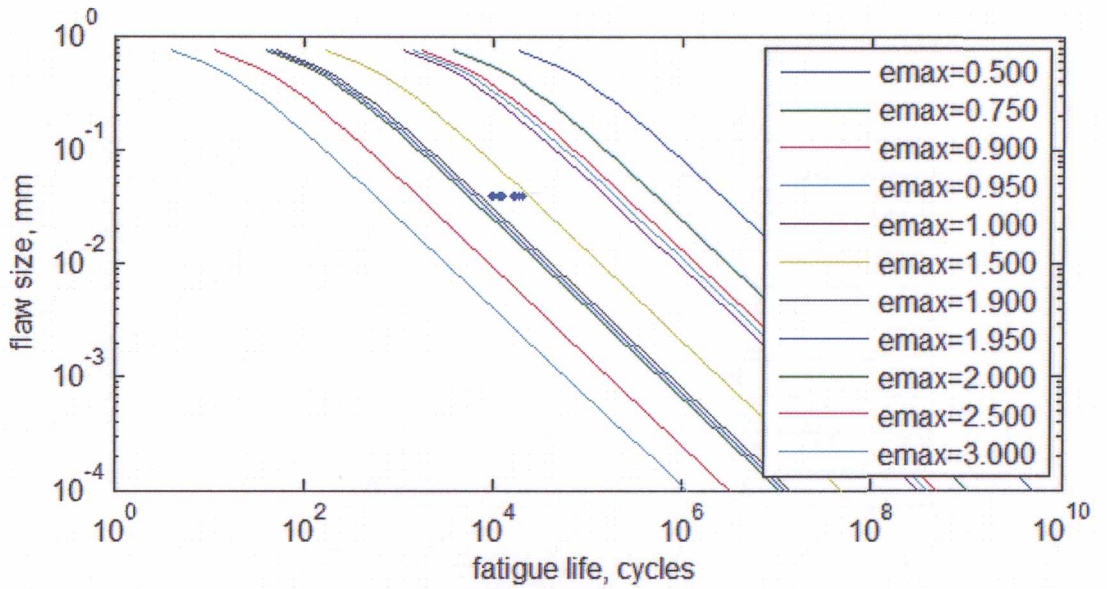


Figure 2.11. Computed dependence of life on flaw size, for various strain levels (ranging from 50% to 300% peak strain). Observations are plotted at actual life, and assumed flaw size of 0.04 mm. Data for MCN.

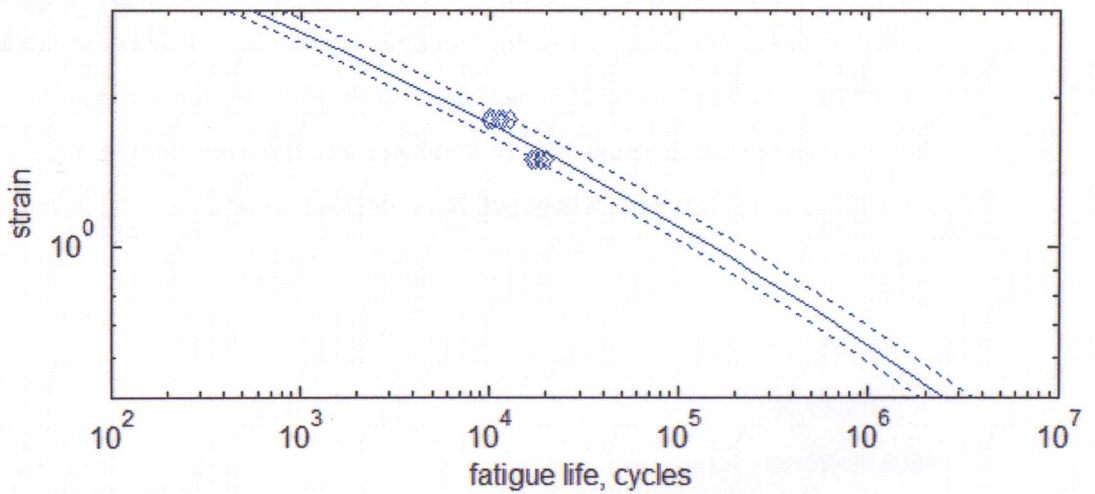


Figure 2.12. Comparison of observed fatigue life with Endurica-computed strain-life curves (solid curve is for flaw size of 0.04 mm, dashed curves are for +/- 0.01 mm). Data for MCN.

Table 2.7 Inferred crack precursor sizes.

	MSB	MCN
Crack precursor size, mm	0.009 +/- 0.006	0.040 +/- 0.010

Table 2.8. Computed strain-life

Strain	Fatigue Life, cycles MSB	Fatigue Life, cycles MCN
0.5	2.22E+06	2.49E+06
0.75	3.92E+05	5.07E+05
0.9	1.80E+05	2.38E+05
0.95	1.42E+05	1.89E+05
1	1.14E+05	1.51E+05
1.5	1.70E+04	2.32E+04
1.9	5.12E+03	6.99E+03
1.95	4.46E+03	6.10E+03
2	3.90E+03	5.33E+03
2.5	1.15E+03	1.56E+03
3	4.03E+02	5.42E+02

2.7. Crack Arrest Under Nonzero Minimum Strain

Purpose: Sometimes elastomers operate under conditions where the load is never removed fully during the duty cycle. Depending on elastomer type, this situation can strongly influence fatigue life by inducing strain crystallization at crack precursors. The effect can be efficiently characterized by studying the arrest of a growing crack when the maximum strain is held constant, and the minimum strain is ramped. This experiment is required whenever it is desired to analyze the effects of variable amplitude loading.

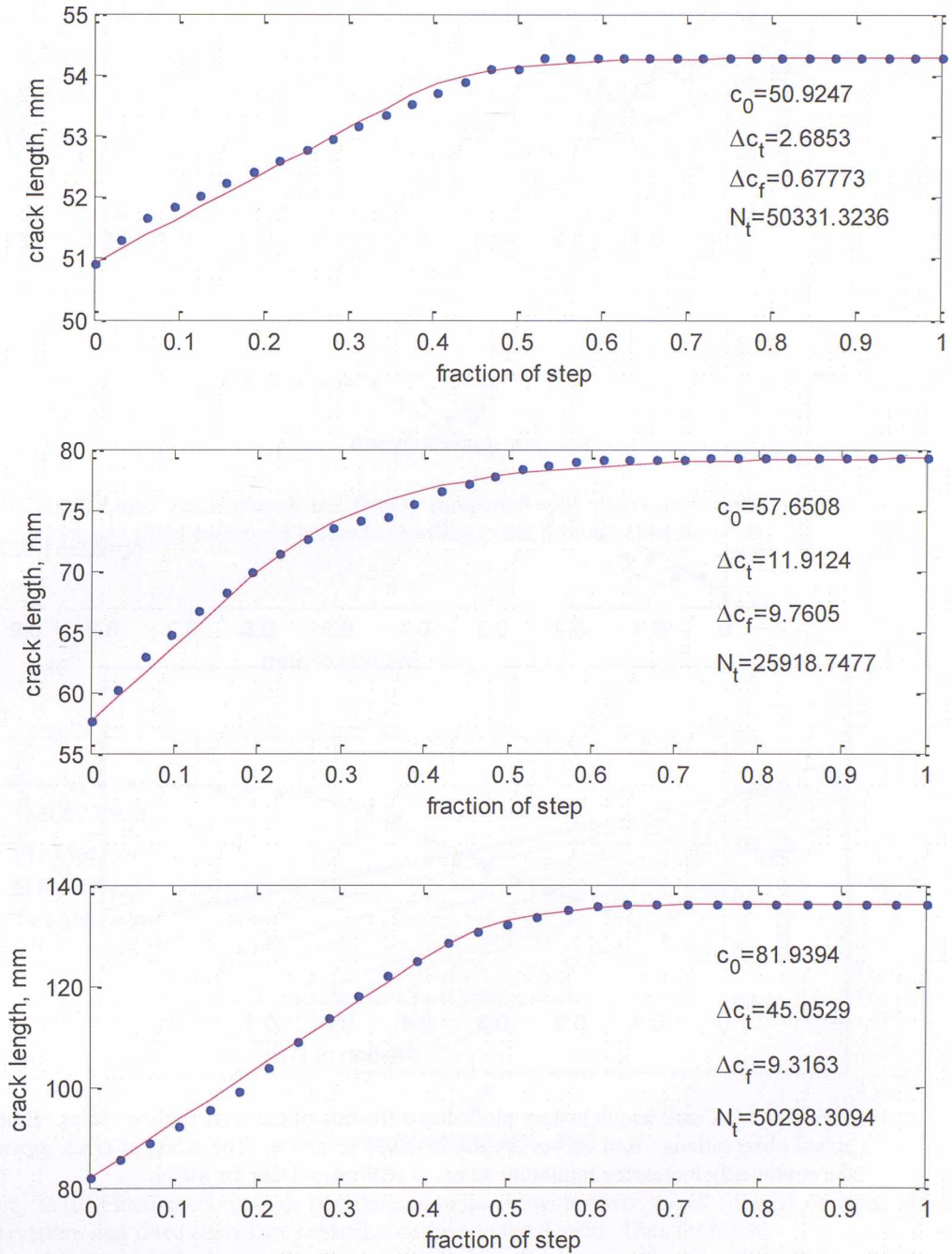


Figure 2.13. Crack length history plotted as a fraction of the total applied cycles. Blue datapoints are actual observations. Red curves are the modeled response. The arrest of crack growth is caused by the continually increasing minimum strain. 3 replicates. Data for MSB.

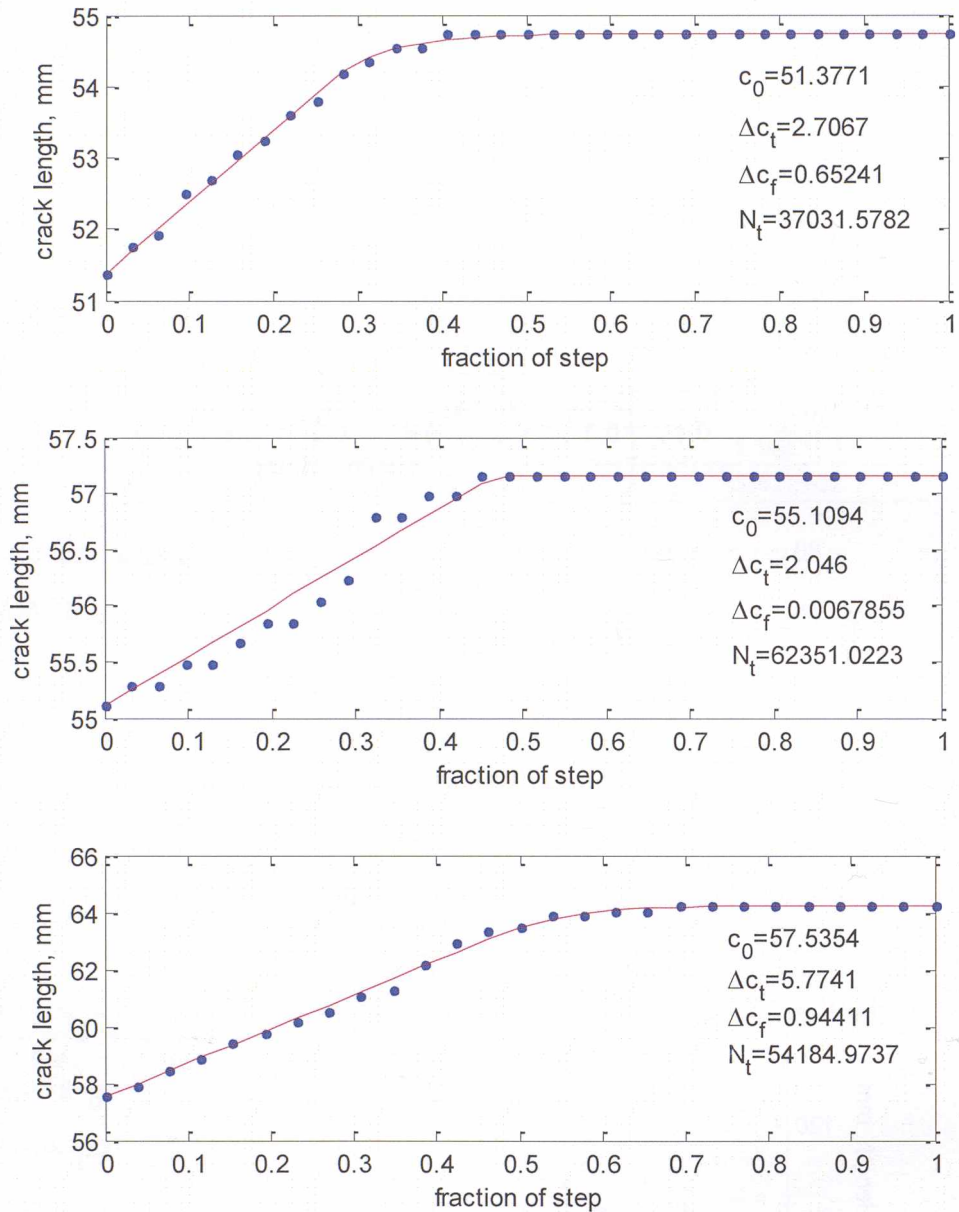


Figure 2.14. Crack length history plotted as a fraction of the total applied cycles. Blue datapoints are actual observations. Red curves are the modeled response. The arrest of crack growth is caused by the continually increasing minimum strain. 3 replicates. Data for MCN.

2.8. Crystallization Law

Purpose: The crack retarding effects of strain crystallization can be observed via the above experiment. In cases where the effect is significant, the parameters of the strain crystallization law can then be determined from the results. This information is essential when it is desired to analyze the effects of a variable amplitude duty cycle.

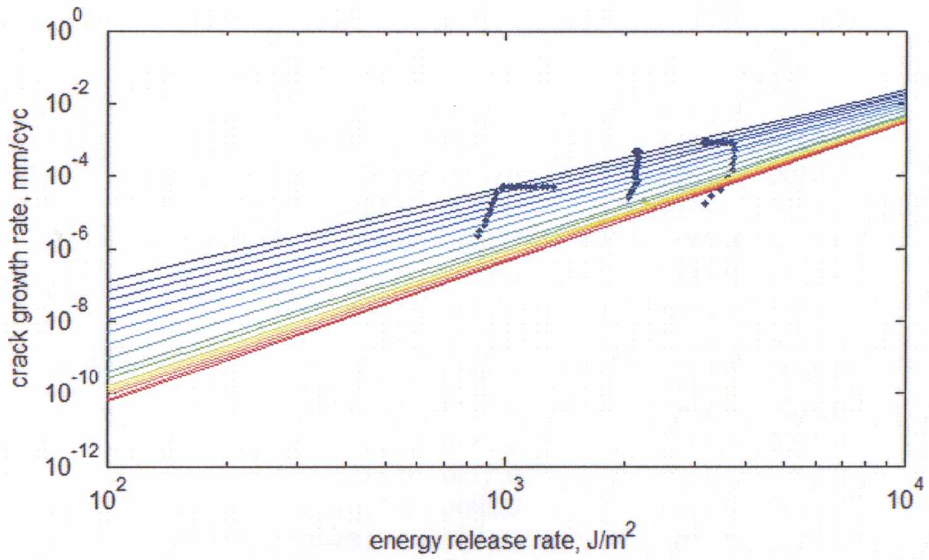


Figure 2.15. Fitted crack growth law (lines) compared with observations (points) of crack arrest. Observations and fitted curves are colored according to the R ratio. Data for MSB.

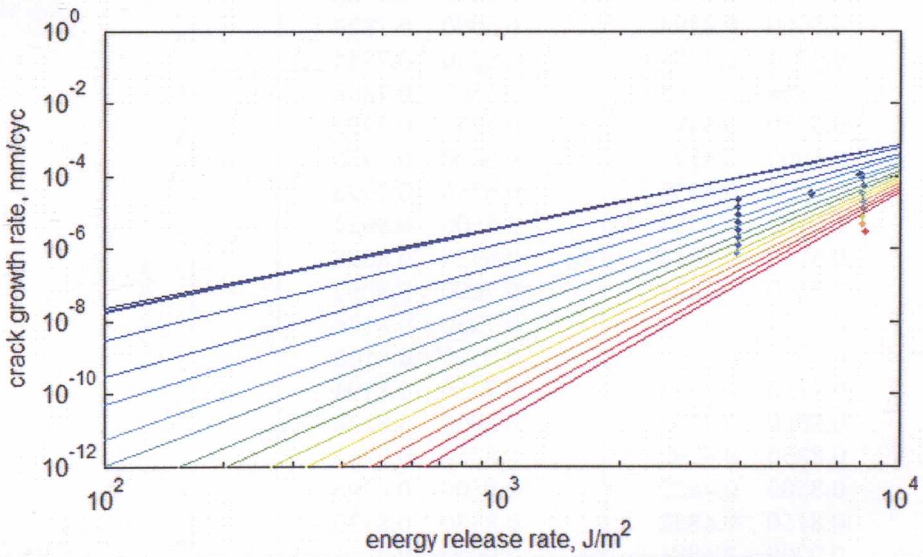


Figure 2.16. Fitted crack growth law (lines) compared with observations (points) of crack arrest. Observations and fitted curves are colored according to the R ratio. Data for MCN.

Table 2.9. Tabular crystallization law.

R, X(R) MSB		R, X(R) MCN	
0	0	0	0
0.0250	0.0643	0.0250	0.0191
0.0500	0.1286	0.0500	0.2628
0.0750	0.1929	0.0750	0.4054
0.1000	0.2572	0.1000	0.4955
0.1250	0.2837	0.1250	0.5509
0.1500	0.2965	0.1500	0.5922
0.1750	0.3103	0.1750	0.6287
0.2000	0.3192	0.2000	0.6566
0.2250	0.3285	0.2250	0.6797
0.2500	0.3391	0.2500	0.6994
0.2750	0.3490	0.2750	0.7162
0.3000	0.3583	0.3000	0.7301
0.3250	0.3666	0.3250	0.7445
0.3500	0.3746	0.3500	0.7559
0.3750	0.3845	0.3750	0.7650
0.4000	0.3953	0.4000	0.7684
0.4250	0.4033	0.4250	0.7718
0.4500	0.4113	0.4500	0.7752
0.4750	0.4203	0.4750	0.7786
0.5000	0.4294	0.5000	0.7820
0.5250	0.4381	0.5250	0.7854
0.5500	0.4465	0.5500	0.7888
0.5750	0.4495	0.5750	0.7922
0.6000	0.4525	0.6000	0.7956
0.6250	0.4555	0.6250	0.7990
0.6500	0.4584	0.6500	0.8024
0.6750	0.4614	0.6750	0.8058
0.7000	0.4644	0.7000	0.8092
0.7250	0.4673	0.7250	0.8126
0.7500	0.4703	0.7500	0.8160
0.7750	0.4733	0.7750	0.8194
0.8000	0.4762	0.8000	0.8228
0.8250	0.4792	0.8250	0.8262
0.8500	0.4822	0.8500	0.8296
0.8750	0.4852	0.8750	0.8330
0.9000	0.4881	0.9000	0.8364
0.9250	0.4911	0.9250	0.8398
0.9500	0.4941	0.9500	0.8432
0.9750	0.4970	0.9750	0.8466
1.0000	0.5000	1.0000	0.8500

3. Hyperelastic Behaviour Characterization

3.1. Hyperelastic Law Parameters

Purpose: The hyperelastic law is used to define reversible stress-strain behavior of an elastomer for finite element analysis.

I have used the simple tension, planar tension, and simple compression stress-strain measurements. We have chosen a three-term Reduced polynomial model to fit the data.

The resulting fit is overlaid with the simple tension measurements in Figure 3.1 and Figure 3.2. In this plot, the blue symbols and line represent simple tension and compression, the green line represents the planar tension prediction, and the red line represents the equibiaxial tension prediction. The curve fit parameters are given in Table 3.1.

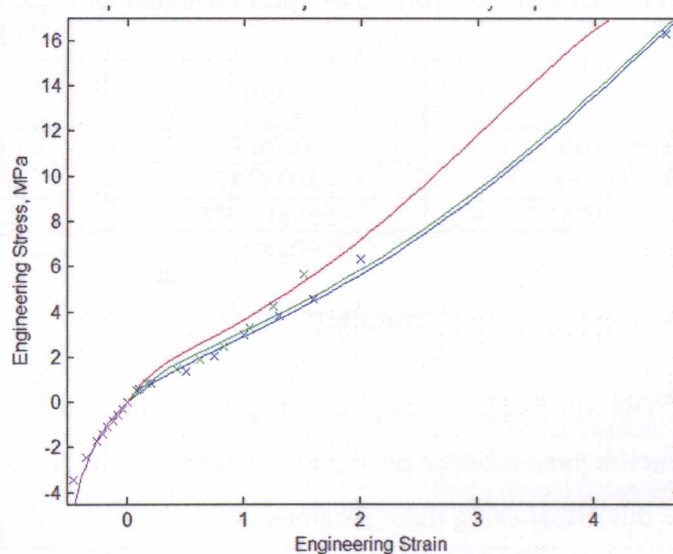


Figure 3.1. Fit of 3 term Reduced polynomial hyperelastic law to cyclic stabilized peak stress-strain observations. Blue is simple tension, green is planar tension, red is the computed equibiaxial tension, and magenta is simple compression. The cross marks are data used for the hyperelastic fit. The solid lines are the predicted response. Data for MSB.

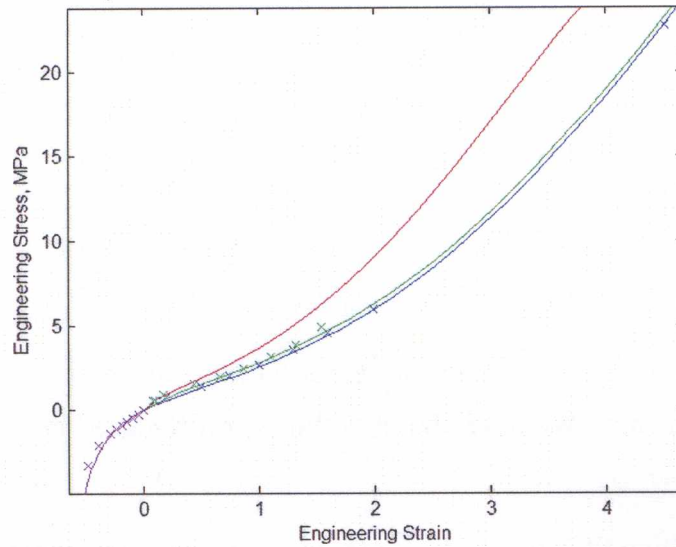


Figure 3.2. Fit of 3 term Reduced polynomial hyperelastic law to cyclic stabilized peak stress-strain observations. Blue is simple tension, green is planar tension, red is the computed equibiaxial tension, and magenta is simple compression. The cross marks are data used for the hyperelastic fit. The solid lines are the predicted response. Data for MCN.

Table 3.1. Three term Reduced polynomial model parameters for cyclic stabilized peak stress-strain observations.

	MSB	MCN
C10, MPa	0.7613	0.58279
C20, MPa	0.017187	0.036058
C30, MPa	-0.00010976	-0.00021584

3.2. Mullins Effect Parameters

Purpose: The Mullins law is used to define how an elastomer's stress-strain behavior depends on the most extreme prior loading event. Some finite element codes are able to capture this effect using these parameters.

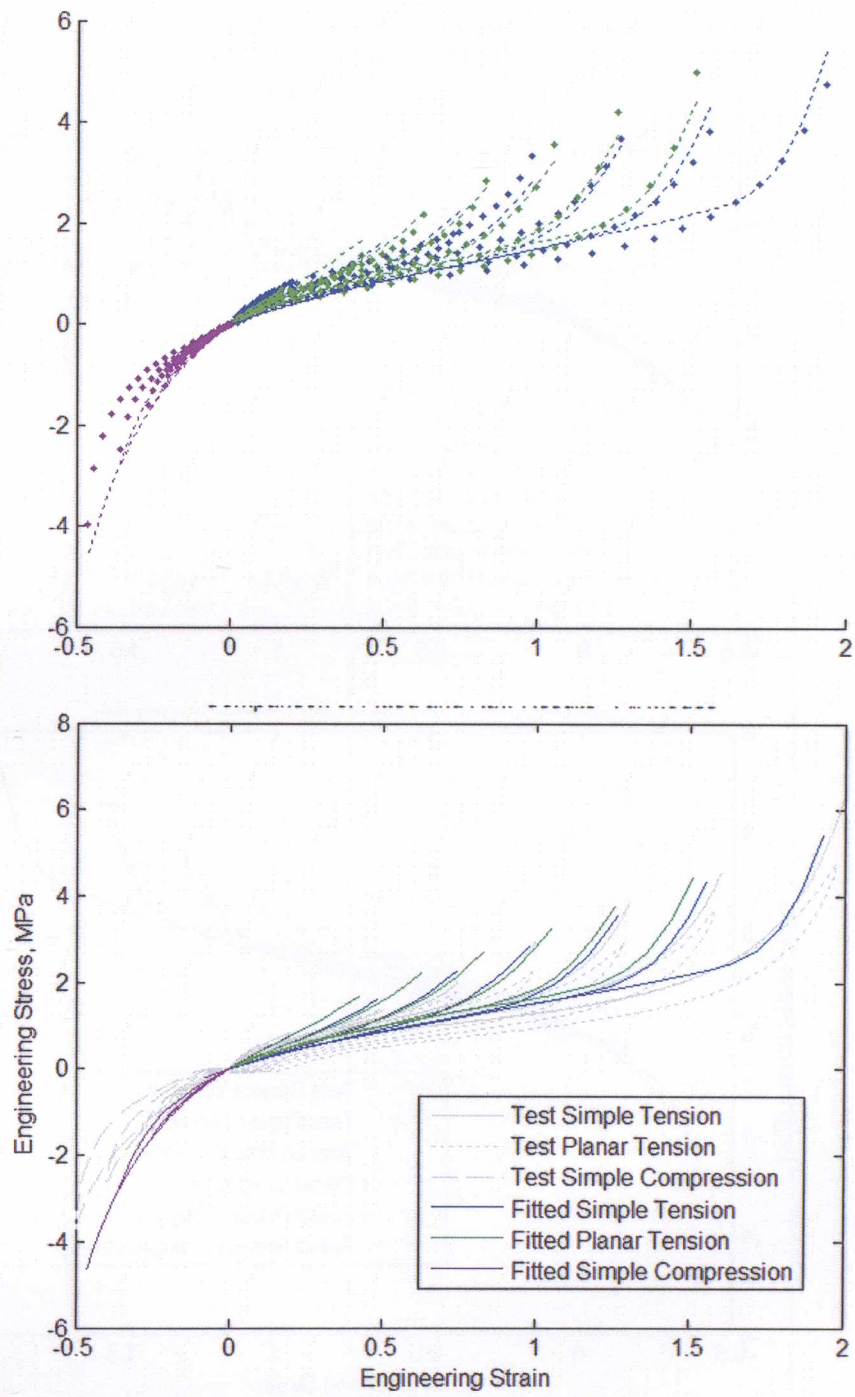


Figure 3.3. Fit of Mullins law to a series of cyclic stabilized unloading curves in planar tension and simple compression. Data for MSB.

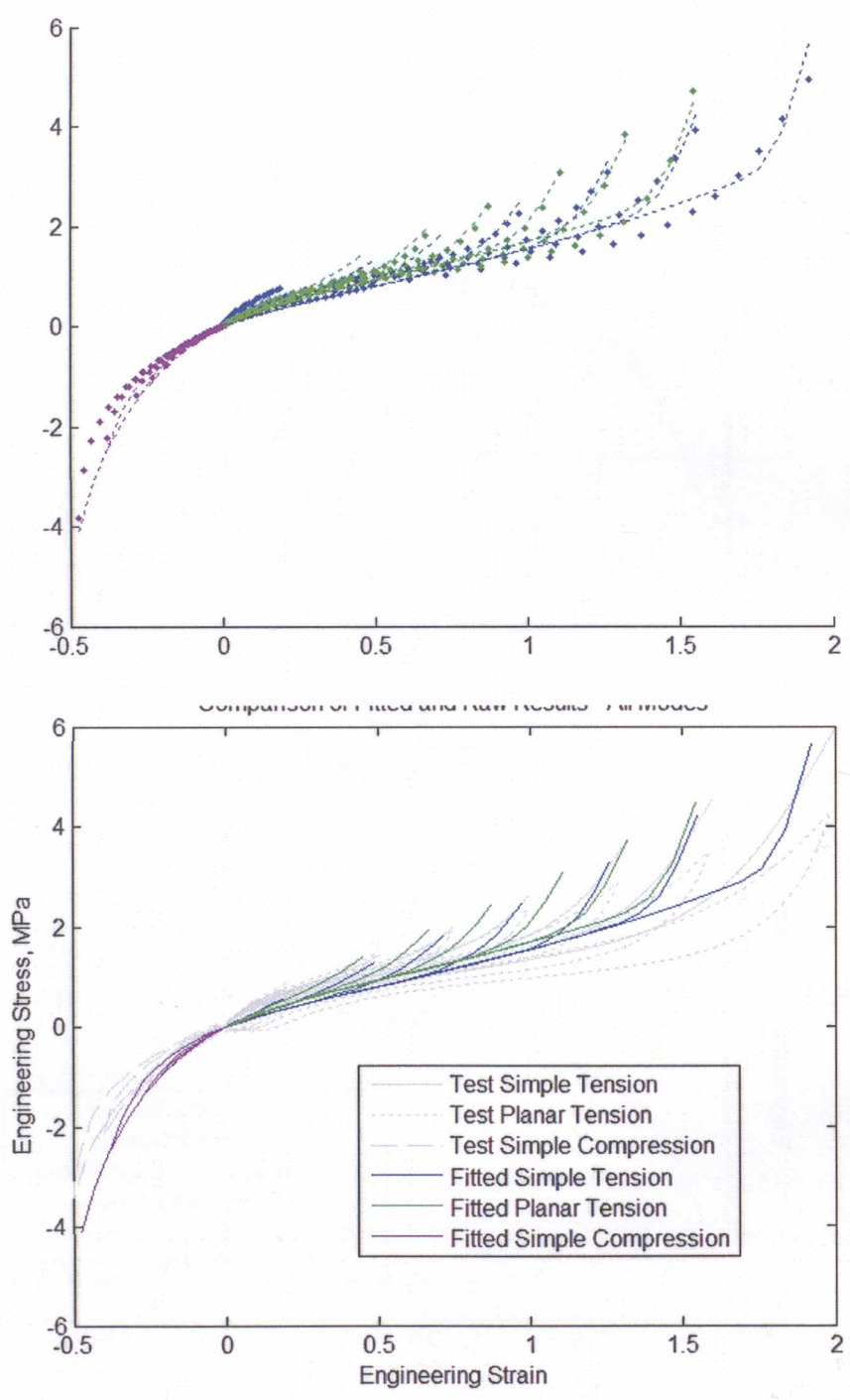


Figure 3.4. Fit of Mullins law to a series of cyclic stabilized unloading curves in planar tension and simple compression. Data for MCN.

Table 3.2. Mullins law parameters.

	MSB	MCN
r	2.1125	2.5504
m , MPa	0.77357	0.3822
β	0.027638	0.057019

4. Summary of Material Parameters for Endurica

The set of material parameters shown in Table 4.1 may be used to represent the subject material in the Endurica fatigue life solver.

Table 4.1. Material Properties for use in Endurica fatigue life solver.

MAT=MSB	MAT=MCN
ELASTICITY_TYPE=RP+MULLINS	ELASTICITY_TYPE=RP+MULLINS
C10=0.7613 ! MPa	C10=0.58279 ! MPa
C20=0.017187 ! MPa	C20=0.036058 ! MPa
C30=-0.00010976 !MPa	C30=-0.00021584 !MPa
MULLINSR=2.1125	MULLINSR=2.5504
MULLINSM=0.77357 !MPa	MULLINSM=0.3822 !MPa
MULLINSBETA=0.027638	MULLINSBETA=0.057019
BULK_MODULUS=1500 ! MPa	BULK_MODULUS=1500 ! MPa
FATIGUE_TYPE=THOMAS	FATIGUE_TYPE=THOMAS
TCRITICAL=54.30205882 ! kJ/m ²	TCRITICAL=21.05260469 !kJ/m ²
RC=2.0509 ! mm/cyc	RC=0.0041 ! mm/cyc
F0=2.6398	F0=2.2706
X(R)=LIST	X(R)=LIST
0	0
0.0643	0.0191
0.1286	0.2628
0.1929	0.4054
0.2572	0.4955
0.2837	0.5509
0.2965	0.5922
0.3103	0.6287
0.3192	0.6566
0.3285	0.6797
0.3391	0.6994
0.3490	0.7162
0.3583	0.7301
0.3666	0.7445
0.3746	0.7559
0.3845	0.7650
0.3953	0.7684
0.4033	0.7718
0.4113	0.7752
0.4203	0.7786
0.4294	0.7820
0.4381	0.7854
0.4465	0.7888
0.4495	0.7922
0.4525	0.7956
0.4555	0.7990
0.4584	0.8024
0.4614	0.8058
0.4644	0.8092
0.4673	0.8126
0.4703	0.8160
0.4733	0.8194
0.4762	0.8228
0.4792	0.8262
0.4822	0.8296
0.4852	0.8330
0.4881	0.8364
0.4911	0.8398
0.4941	0.8432
0.4970	0.8466
0.5000	0.8500

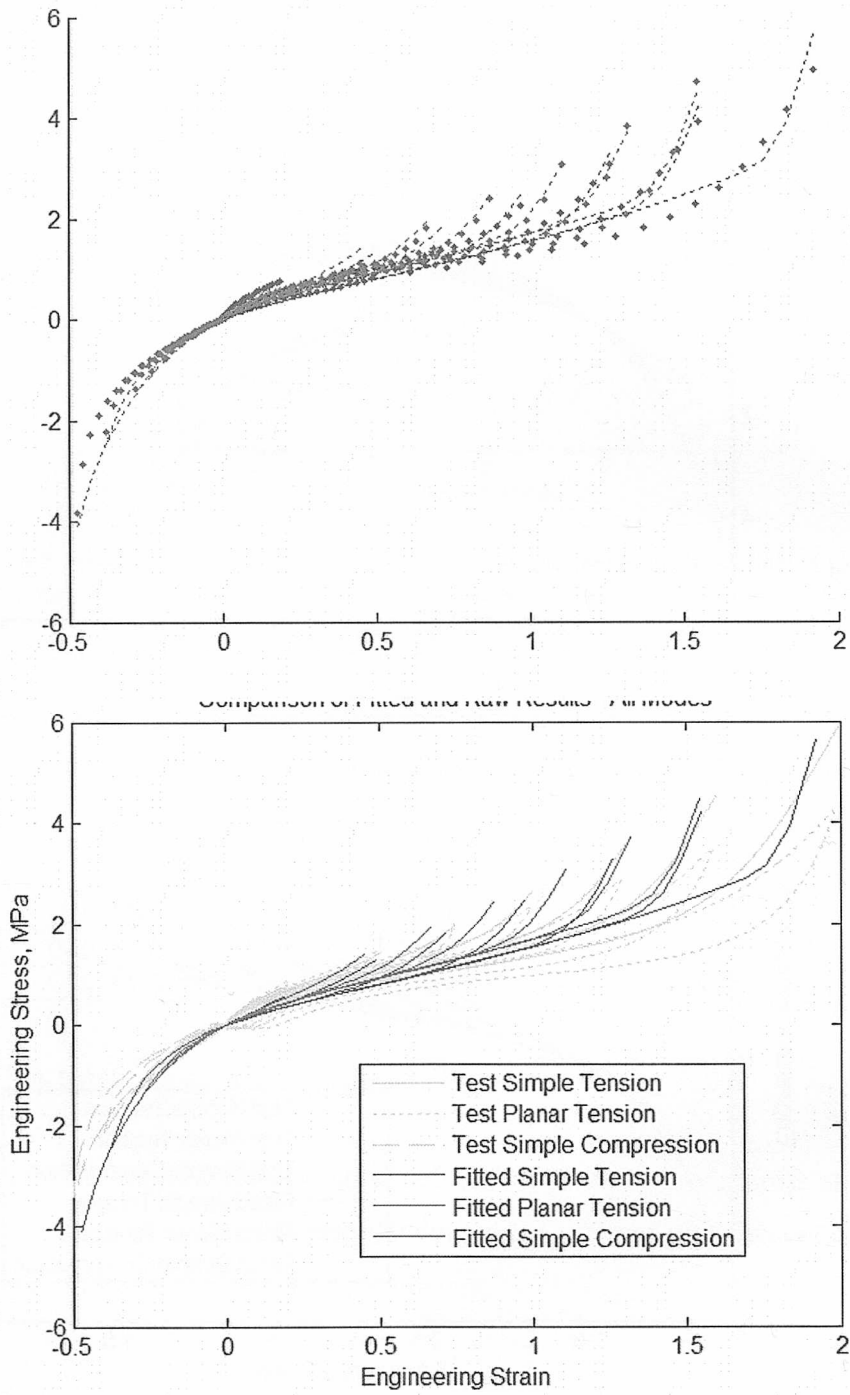


Figure 3.4. Fit of Mullins law to a series of cyclic stabilized unloading curves in planar tension and simple compression. Data for MCN.

Table 3.2. Mullins law parameters.

	MSB	MCN
r	2.1125	2.5504
m , MPa	0.77357	0.3822
β	0.027638	0.057019

4. Summary of Material Parameters for Endurica

The set of material parameters shown in Table 4.1 may be used to represent the subject material in the Endurica fatigue life solver.

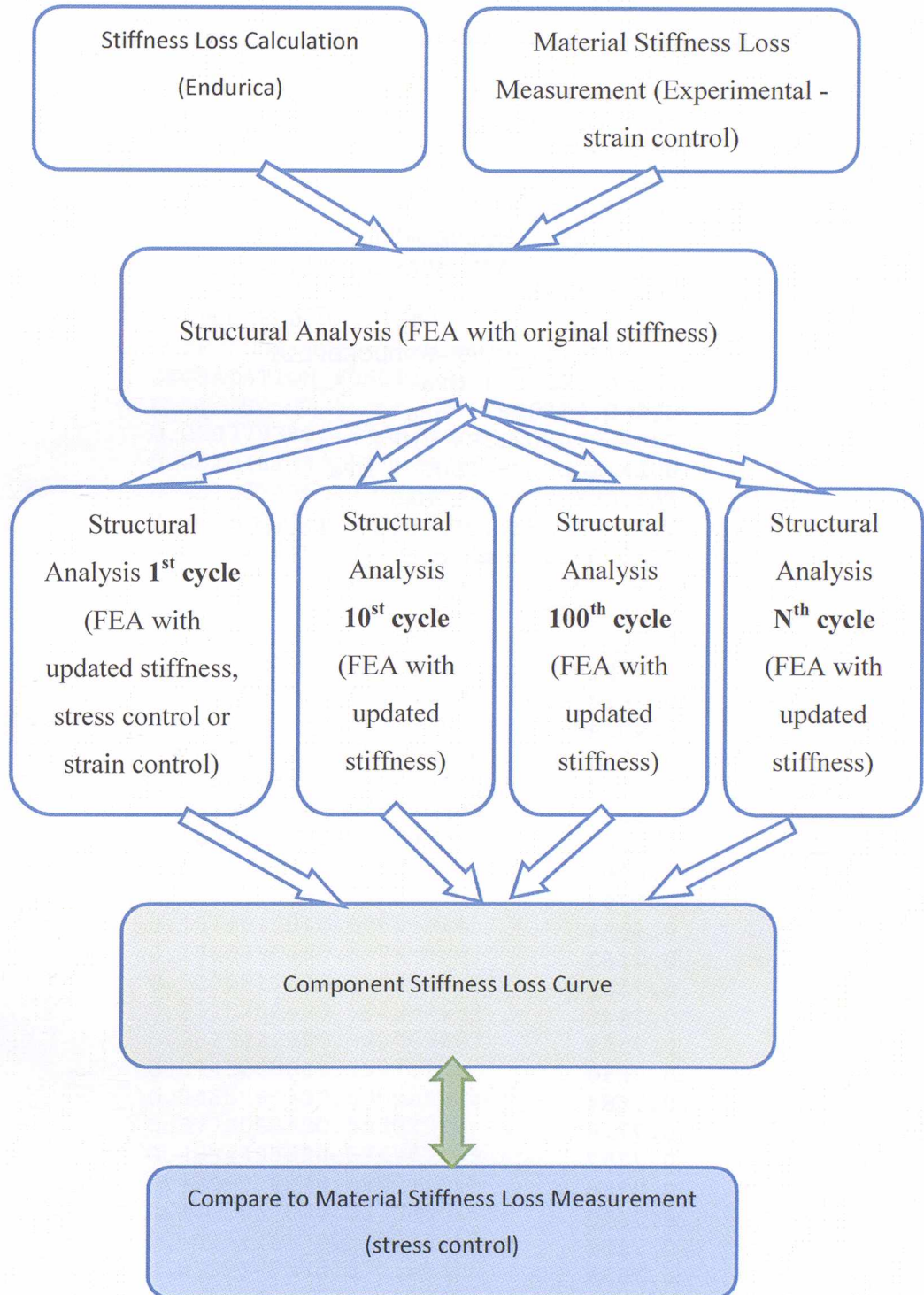
Table 4.1. Material Properties for use in Endurica fatigue life solver.

MAT=MSB	MAT=MCN
ELASTICITY_TYPE=RP+MULLINS	ELASTICITY_TYPE=RP+MULLINS
C10=0.7613 ! MPa	C10=0.58279 ! MPa
C20=0.017187 ! MPa	C20=0.036058 ! MPa
C30=-0.00010976 !MPa	C30=-0.00021584 !MPa
MULLINSR=2.1125	MULLINSR=2.5504
MULLINSM=0.77357 !MPa	MULLINSM=0.3822 !MPa
MULLINSBETA=0.027638	MULLINSBETA=0.057019
BULK_MODULUS=1500 ! MPa	BULK_MODULUS=1500 ! MPa
FATIGUE_TYPE=THOMAS	FATIGUE_TYPE=THOMAS
TCRITICAL=54.30205882 ! kJ/m ²	TCRITICAL=21.05260469 !kJ/m ²
RC=2.0509 ! mm/cyc	RC=0.0041 ! mm/cyc
F0=2.6398	F0=2.2706
X(R)=LIST	X(R)=LIST
0	0
0.0643	0.0191
0.1286	0.2628
0.1929	0.4054
0.2572	0.4955
0.2837	0.5509
0.2965	0.5922
0.3103	0.6287
0.3192	0.6566
0.3285	0.6797
0.3391	0.6994
0.3490	0.7162
0.3583	0.7301
0.3666	0.7445
0.3746	0.7559
0.3845	0.7650
0.3953	0.7684
0.4033	0.7718
0.4113	0.7752
0.4203	0.7786
0.4294	0.7820
0.4381	0.7854
0.4465	0.7888
0.4495	0.7922
0.4525	0.7956
0.4555	0.7990
0.4584	0.8024
0.4614	0.8058
0.4644	0.8092
0.4673	0.8126
0.4703	0.8160
0.4733	0.8194
0.4762	0.8228
0.4792	0.8262
0.4822	0.8296
0.4852	0.8330
0.4881	0.8364
0.4911	0.8398
0.4941	0.8432
0.4970	0.8466
0.5000	0.8500

FLAWSIZE=0.009 ! mm		FLAWSIZE=0.04 ! mm	
FLAWCRIT=1 ! mm		FLAWCRIT=1 ! mm	
TEMPREF=23 ! degC		TEMPREF=23 ! degC	
TEMPCOEF=0.0 ! 1/degC		TEMPCOEF=0.0 ! 1/degC	
STIFFLOSS_TYPE=TABULAR		STIFFLOSS_TYPE=TABULAR	
DEGRADATION_FUNCTION		DEGRADATION_FUNCTION	
0	1	0	1
0.000796506	0.925386087	0.000779381	0.847978423
0.001345821	0.899554637	0.001048134	0.820844397
0.001895136	0.888070773	0.001585638	0.791483938
0.002444451	0.875641112	0.002123142	0.766558489
0.002993765	0.866600675	0.005079416	0.718762538
0.00354308	0.861457565	0.00803569	0.698298421
0.004092395	0.859446374	0.010991964	0.686231512
0.004641709	0.855118928	0.013948238	0.683695468
0.005191024	0.84824457	0.017173265	0.673238124
0.037875251	0.79725125	0.020129539	0.667098195
0.070806669	0.785648348	0.023085813	0.668350613
0.103490895	0.772935003	0.026042087	0.651536168
0.136477245	0.767464227	0.028998361	0.655238786
0.169134005	0.764421086	0.031954635	0.648276399
0.202092889	0.759266515	0.063371765	0.629235943
0.234804581	0.756335537	0.09481577	0.618720787
0.267763465	0.753008936	0.126017899	0.61220676
0.300694883	0.753085137	0.157461904	0.608463341
0.333406575	0.748996215	0.188879035	0.597488062
0.366090802	0.747722639	0.220081163	0.598959321
0.39902222	0.750438718	0.251525169	0.592987197
0.431981104	0.743451657	0.282942299	0.592069807
0.464692796	0.740347915	0.314386304	0.59013171
0.497624214	0.74301705	0.345588433	0.590929273
0.53030844	0.745285962	0.377005563	0.58302971
0.56329479	0.746205017	0.408449569	0.576969109
0.595979016	0.741035196	0.439651697	0.580551619
0.628910434	0.742124722	0.471095703	0.577663616
0.661622126	0.734739603	0.502512833	0.578004053
0.69458101	0.732277965	0.533956838	0.571169416
0.727237771	0.742647374	0.565158967	0.57421338
0.760196655	0.738267207	0.596576097	0.575155182
0.792908347	0.730920117	0.628020103	0.57246002
0.825839765	0.73585202	0.659490983	0.571848822
0.858523991	0.737271871	0.690666237	0.568951288
0.891510341	0.730439426	0.722083367	0.573114531
0.924194567	0.728824032	0.753527372	0.566652363
0.957125985	0.729905901	0.784998253	0.566632758
0.989810212	0.731193549	0.816146631	0.571049067
0.990936307	0.727459323	0.847590637	0.564518389
0.992034936	0.727463143	0.879061517	0.566318019
0.992858909	0.725112203	0.910236771	0.562341262
0.993957538	0.731000028	0.941653901	0.548388759
0.99478151	0.72779178	0.973124782	0.528580159
0.99588014	0.726933932	0.978499825	0.522794582
0.996978769	0.72523304	0.983874869	0.526153566
0.997802741	0.720086715	0.989249913	0.508105605
0.998901371	0.717112995	0.994624956	0.489455174
1	0.700192724	1	0.440725244

Appendix II

1. Analysis Workflow



2. List of Scripts for Simulations

2.1. Material Data Header for Stiffness Loss Analysis at Endurica

2.1.1. MCN Material Data Header (*.hfi)

```
**HEADER
test of stiffness vs cycles output.
**OUTPUT
LIFE
CRACKGROWTH
STIFFNESS, NTIMES=100, PERCENTILE=0.02, UHYPER
CRITICAL_PLANE_SEARCH, TYPE=TRI3D, NMESH=3
**MATERIAL
MAT=MCN
ELASTICITY_TYPE=REDUCEDPOLY
C10=0.58279 ! MPa
C20=0.036058 ! MPa
C30=-0.00021584 !MPa
BULK_MODULUS=1500 ! MPa
FATIGUE_TYPE=THOMAS
TCRITICAL=21.05260469 !kJ/m^2
RC=0.0041 ! mm/cyc
F0=2.2706
X(R)=LIST
0
0.0191
0.2628
0.4054
0.4955
0.5509
0.5922
0.6287
0.6566
0.6797
0.6994
0.7162
0.7301
0.7445
0.7559
0.7650
0.7684
0.7718
0.7752
0.7786
0.7820
0.7854
0.7888
0.7922
0.7956
0.7990
0.8024
```

0.8058
0.8092
0.8126
0.8160
0.8194
0.8228
0.8262
0.8296
0.8330
0.8364
0.8398
0.8432
0.8466
0.8500
FLAWSIZE=0.04 ! mm
FLAWCRIT=1 ! mm
TEMPREF=23 ! degC
TEMPCOEF=0.0 ! 1/degC
STIFFLOSS_TYPE=TABULAR
DEGRADATION_FUNCTION
0 1
0.0007793810.847978423
0.0010481340.820844397
0.0015856380.791483938
0.0021231420.766558489
0.0050794160.718762538
0.00803569 0.698298421
0.0109919640.686231512
0.0139482380.683695468
0.0171732650.673238124
0.0201295390.667098195
0.0230858130.668350613
0.0260420870.651536168
0.0289983610.655238786
0.0319546350.648276399
0.0633717650.629235943
0.09481577 0.618720787
0.1260178990.61220676
0.1574619040.608463341
0.1888790350.597488062
0.2200811630.598959321
0.2515251690.592987197
0.2829422990.592069807
0.3143863040.59013171
0.3455884330.590929273
0.3770055630.58302971
0.4084495690.576969109
0.4396516970.580551619
0.4710957030.577663616
0.5025128330.578004053
0.5339568380.571169416
0.5651589670.57421338
0.5965760970.575155182
0.6280201030.57246002
0.6594909830.571848822
0.6906662370.568951288

```

0.7220833670.573114531
0.7535273720.566652363
0.7849982530.566632758
0.8161466310.571049067
0.8475906370.564518389
0.8790615170.566318019
0.9102367710.562341262
0.9416539010.548388759
0.9731247820.528580159
0.9784998250.522794582
0.9838748690.526153566
0.9892499130.508105605
0.9946249560.489455174
1      0.440725244
**HISTORY
HISTTYPE=6CNE3D
HISTPERIOD=1 ! sec
**FIELD

```

2.1.2. MSB Material Data Header (*.hfi)

```

**HEADER
test of stiffness vs cycles output.
**OUTPUT
LIFE
CRACKGROWTH
STIFFNESS, NTIMES=100, PERCENTILE=0.02, UHYPER
CRITICAL_PLANE_SEARCH, TYPE=TRI3D, NMESH=3
**MATERIAL
MAT=MSB
ELASTICITY_TYPE=REDUCEDPOLY
C10=0.7613 ! MPa
C20=0.017187 ! MPa
C30=-0.00010976 !MPa
BULK_MODULUS=1500 ! MPa
FATIGUE_TYPE=THOMAS
TCRITICAL=54.30205882 ! kJ/m^2
RC=2.0509      ! mm/cyc
F0=2.6398
X(R)=LIST
0
0.0643
0.1286
0.1929
0.2572
0.2837
0.2965
0.3103
0.3192
0.3285
0.3391
0.3490
0.3583
0.3666
0.3746

```

0.3845
0.3953
0.4033
0.4113
0.4203
0.4294
0.4381
0.4465
0.4495
0.4525
0.4555
0.4584
0.4614
0.4644
0.4673
0.4703
0.4733
0.4762
0.4792
0.4822
0.4852
0.4881
0.4911
0.4941
0.4970
0.5000
FLAWSIZE=0.009 ! mm
FLAWCRIT=1 ! mm
TEMPREF=23 ! degC
TEMPCOEF=0.0 ! 1/degC
STIFFLOSS_TYPE=TABULAR
DEGRADATION_FUNCTION
0 1
0.0007965060.925386087
0.0013458210.899554637
0.0018951360.888070773
0.0024444510.875641112
0.0029937650.866600675
0.00354308 0.861457565
0.0040923950.859446374
0.0046417090.855118928
0.0051910240.84824457
0.0378752510.79725125
0.0708066690.785648348
0.1034908950.772935003
0.1364772450.767464227
0.1691340050.764421086
0.2020928890.759266515
0.2348045810.756335537
0.2677634650.753008936
0.3006948830.753085137
0.3334065750.748996215
0.3660908020.747722639
0.39902222 0.750438718
0.4319811040.743451657
0.4646927960.740347915

```

0.4976242140.74301705
0.53030844 0.745285962
0.56329479 0.746205017
0.5959790160.741035196
0.6289104340.742124722
0.6616221260.734739603
0.69458101 0.732277965
0.7272377710.742647374
0.7601966550.738267207
0.7929083470.730920117
0.8258397650.73585202
0.8585239910.737271871
0.8915103410.730439426
0.9241945670.728824032
0.9571259850.729905901
0.9898102120.731193549
0.9909363070.727459323
0.9920349360.727463143
0.9928589090.725112203
0.9939575380.731000028
0.99478151 0.72779178
0.99588014 0.726933932
0.9969787690.72523304
0.9978027410.720086715
0.9989013710.717112995
1      0.700192724
**HISTORY
MODEDEFAULT=1
HISTTYPE=6CNE3D
HISTPERIOD=1 ! sec
**FIELD

```

2.2.Abaqus Scripts (*.inp)

The following script is an example of the structure of the *.inp file used to define the finite element analysis for the updated stiffness conditions in Abaqus. The stiffness is updated in function of the user defined material data specified by the UHYPER. Thus the desired number of cycle has to be defined in the script. The cycle number is specified in the third line of Material section. In the written script has been specified of being the first cycle with the number one. The number of simulations to be done depend on the amount of cycles that has been computed that component will last. At least ten simulations have to be done per loading level, to construct the stiffness loss behaviour curve.

```

** MATERIALS
*Material, name=MATERIAL-2
*Hyperelastic, user, type=COMPRESSIBLE, properties=1
1
**Dimensions are in mm. Material units are in MPa. So stress
**is in MPa, disp in mm, and force in N.
*Material, name=MATREDPOLY
*Hyperelastic, n=3, reduced polynomial
0.58279, 0.036058, 0.00021584, 0.000666667, 0.,
0.
** BOUNDARY CONDITIONS
** OUTPUT REQUESTS
** FIELD OUTPUT: F-Output-1
*Output, field, number interval=10
*Contact Output
CDISP, CSTRESS
** FIELD OUTPUT: F-Output-2
*Node Output
CF, RF, U
** FIELD OUTPUT: F-Output-3
*Element Output, directions=YES
LE, NE, PE, PEEQ, PEMAG, S
** FIELD OUTPUT: F-Output-4
*Node Output, nset=SET-4RIGIDRP
TF,
** HISTORY OUTPUT: H-Output-1
*Output, history
*Element Output
IRA2, IRF2
*Energy Output
ALLAE, ALLCD, ALLDMD, ALLEE, ALLFD, ALLIE, ALLJD, ALLKE,
ALLKL, ALLPD, ALLQB, ALLSD, ALLSE, ALLVD, ALLWK, ETOTAL
** HISTORY OUTPUT: H-Output-2
*Node Output, nset=SET-4RIGIDRP
RF2, U2
*End Step

```

Appendix III

1. Script to Output Nominal Strains from Ansys to Endurica,

```
/POST1
ESEL,S,TYPE,,1
*GET,ELNUM,ELEM,0,NUM,MAX
ALLSEL,ALL
*DIM,NUMEL,ARRAY,ELNUM
SET,LAST
*GET,lastset,ACTIVE,0,SET,NSET
*GET,finaltime,ACTIVE,0,SET,TIME
*DIM,TIMEARRAY,ARRAY,lastset
*DO,j,1,lastset
SET,,,,,j
*GET,TIMEARRAY(j),ACTIVE,0,SET,TIME
RSYS,SOLU
ETABLE,StrX,EPEL,X
ETABLE,StrY,EPEL,Y
ETABLE,StrZ,EPEL,Z
ETABLE,StrXY,EPEL,XY
ETABLE,StrYZ,EPEL,YZ
ETABLE,StrXZ,EPEL,XZ
*DIM,DEF_x%j%,ARRAY,ELNUM          *DIM,DEF_y%j%,ARRAY,ELNUM
*DIM,DEF_z%j%,ARRAY,ELNUM
*DIM,DEF_xy%j%,ARRAY,ELNUM
*DIM,DEF_yz%j%,ARRAY,ELNUM
*DIM,DEF_xz%j%,ARRAY,ELNUM
e=exp(1)
*DO,i,1,ELNUM
    NUMEL(i)=i
    *GET,DEF_x%j%(i),ELEM,i,ETAB,StrX
    DEF_x%j%(i)=e**(DEF_x%j%(i))-1
    *GET,DEF_y%j%(i),ELEM,i,ETAB,StrY
    DEF_y%j%(i)=e**(DEF_y%j%(i))-1
    *GET,DEF_z%j%(i),ELEM,i,ETAB,StrZ
    DEF_z%j%(i)=e**(DEF_z%j%(i))-1
    *GET,DEF_xy%j%(i),ELEM,i,ETAB,StrXY
    DEF_xy%j%(i)=e**(DEF_xy%j%(i))-1
    *GET,DEF_yz%j%(i),ELEM,i,ETAB,StrYZ
    DEF_yz%j%(i)=(e**(DEF_yz%j%(i))-1)*(-1)
    *GET,DEF_xz%j%(i),ELEM,i,ETAB,StrXZ
    DEF_xz%j%(i)=(e**(DEF_xz%j%(i))-1)*(-1)
*ENDDO
*ENDDO
!*VOPER,DEF_yz,DEF_yz,MULT,-1
!*VOPER,DEF_xz,DEF_xz,MULT,-1
*CREATE,ansuitmp
```

```

*CFOPEN,'dump3D','hfi'
*DO,i,1,lastset
timenum=timearray(i)
*VWRITE,'Time=%timearray(i)%'
(A10)
*VWRITE,NUMEL(1,1),DEF_x%i%(1,1),DEF_y%i%(1,1),DEF_z%i%(1,1),DEF_x
y%i%(1,1),DEF_yz%i%(1,1),DEF_xz%i%(1,1)
(f5.0,',','e12.4,', 'e15.4,', 'e12.4,', 'e12.4,', 'e12.4,', 'e12.4)
*ENDDO
*CFCLOS
*END
/INPUT,ansuitmp
/nopr
*DEL,NUMEL
*DEL,TIMEARRAY
*DO,j,1,lastset
  *DEL,DEF_x%j%
  *DEL,DEF_y%j%
  *DEL,DEF_z%j%
  *DEL,DEF_xy%j%
  *DEL,DEF_xz%j%
  *DEL,DEF_yz%j%
*ENDDO

```

2. Script to Input Life Results from Endurica to Ansys Model

RowN=304 !Number of lines on "life.txt" file minus one.
ColN=8 !Number of columns in the "life.txt"

```
*DIM,disp,TABLE,RowN,ColN
*TREAD,DISP,'life','txt',' ', ,
!*DIM,life,ARRAY,RowN
ETABLE,life,U,Y
*do,i,1,RowN
a=disp(i,1)
!life(i)=a
DETAB,i,LIFE,a
*enddo
PLETAB,LIFE,NOAV
```